DOE/MC/26253-7
Distribution Category UC-122

SCALE-UP OF MISCIBLE FLOOD PROCESSES

DOE/MC/26253--7

DE92 001042

Annual Report

By
F. M. Orr, Jr.

May 1992

Work Performed Under Contract No. FG21-89MC26253

Prepared for
U.S. Department of Energy
Assistant Secretary for Fossil Energy

Royal J. Watts, Project Manager
Morgantown Energy Technology Center
P. O. Box 880
Morgantown, WV 26505

Prepared by
Stanford University
Petroleum Engineering Department
Stanford, CA 94305-2220

Abstract

Results of a wide-ranging investigation of the scaling of the physical mechanisms of miscible floods are reported.

Advanced techniques for analysis of crude oils are considered in Chapter 2. Application of supercritical fluid chromatography is demonstrated for characterization of crude oils for equation-of-state calculations of phase equilibrium. Results of measurements of crude oil and phase compositions by gas chromatography and mass spectrometry are also reported.

The theory of development of miscibility is considered in detail in Chapter 3. The theory is extended to four components, and sample solutions for a variety of gas injection systems are presented. The analytical theory shows that miscibility can develop even though standard tie-line extension criteria developed for ternary systems are not satisfied. In addition, the theory includes the first analytical solutions for condensing/vaporizing gas drives.

In Chapter 4, methods for simulation of viscous fingering are considered. The scaling of the growth of transition zones in linear viscous fingering is considered. In addition, extension of the models developed previously to three dimensions is described, as is the inclusion of effects of equilibrium phase behavior.

In Chapter 5, the combined effects of capillary and gravity-driven crossflow are considered. The experimental results presented show that very high recovery can be achieved by gravity segregation when interfacial tensions are moderately low. We argue that such crossflow mechanisms are important in multicontact miscible floods in heterogeneous reservoirs. In addition, results of flow visualization experiments are presented that illustrate the interplay of crossflow driven by gravity with that driven by viscous forces.

Acknowledgements

The research effort described in this report is primarily the work of a talented team of graduate students and post-docs whose names are listed as authors of the individual sections: Birol Dindoruk, Karen Hagedorn, Russ Johns, David Schechter, Maurice Stadler, Hamdi Tchelepi, Marco Thiele, and Dengen Zhou. They have demonstrated conclusively that graduate students teach the faculty more than the faculty teach the students.

Our fellow faculty and students at Stanford have also contributed in many ways to the research effort. Khalid Aziz, Bill Brigham, John Fayers, Tom Hewett, André Journel and many of their students helped us to think about the complex flow problems we consider in this report. We are much indebted to all of them.

Two key sources of financial support made this work possible: the U.S. Department of Energy under Grant No. DE-FG21-89MC26253 and the Miscible Flooding Industrial Affiliates program of the Stanford University Petroleum Research Institute. Members of the Miscible Flooding Affiliates for 1990/91 include: Arco Oil and Gas Co., BP Exploration Co. Ltd., Chevron Oil Field Research Co., Conoco Inc., Exxon Production, Japan National Oil Corporation, Marathon Oil Company, Mobil R&D Corporation, Mobil E&P Services, Petronas, Shell Development Co., Texaco, Inc., and UNOCAL. We acknowledge with special thanks the support of all those organizations.

We are also indebted to Royal Watts, our technical project officer at DOE, for his longstanding interest and support of this work. Colleagues too numerous to name individually at the oil companies listed above have listened to, challenged, offered suggestions for, and thus helped us in many ways to develop the ideas outlined here. They also have our thanks.

This report was assembled with much assistance from Pat Ota and Yolanda Williams. They began with handwritten scraps of text, computer files, and plots beyond counting, and somehow produced the finished report. Russ Johns also deserves special thanks for guiding all of us in the use of LaTeX to format this report. They have the admiration and gratitude of all of us who participated in the writing.

Lynn Orr
Stanford
December 1991

Contents

List of Tables

List of Figures

1. Introduction

This report summarizes results of a wide-ranging investigation of the fundamental physical mechanisms that control displacement performance in miscible floods: phase behavior, viscous fingering, reservoir heterogeneity, viscous crossflow, capillary crossflow, and gravity segregation. The central objective of the research effort is to quantify scaling behavior of multicontact miscible (MCM) displacement processes, so that experimental observations at laboratory scale can be interpreted and translated with confidence to the much larger displacement scales appropriate to oil reservoirs.

The translation of scales requires an understanding of the flow processes that control displacement performance. Phase behavior, the partitioning of components between phases, and the resulting chromatographic separations that occur when phases flow at different rates are responsible for multicontact miscibility in one-dimensional flow settings. In reservoir flows, however, flow is anything but one dimensional. Permeability heterogeneities will induce nonuniform flow, as will viscous fingering. Crossflow, whether due to capillary, viscous or gravity forces, will induce mixing that cannot occur in one-dimensional flow. Thus, in reservoir scale flows, displacement performance will depend on the interplay of nonuniform flow, phase behavior and transverse mixing mechanisms. In this report we present new results that improve understanding of the physical mechanisms operating in all three areas.

In the interests of conciseness, we rely on the detailed descriptions given previously of experimental equipment, mathematical methods, and numerical techniques [51, 52] and focus on new results. Significant progress has been made in several areas. In Chapter 2, we demonstrate a new technique based on supercritical fluid chromatography (SFC) for characterization of a crude oil for phase behavior computations with an equation of state (EOS) and show that results of PVT experiments for a CO_2-crude oil are *predicted* with good accuracy. We also report results of detailed analyses by gas chromatography and mass spectrometry (GCMS) of hydrocarbons present in oil-rich and CO_2-rich phases. Those results illuminate the question of how crude oil composition influences the supercritical extraction that is an essential part of development of miscibility.

In Chapter 3, we explore development of miscibility in one-dimensional flow, the interaction of phase equilibrium with two-phase flow. In a significant extension of the well known three-component theory for vaporizing and condensing gas drives, we show that the standard criteria for miscibility, based on tie-line extensions through the initial and injection compositions, is not sufficient to explain displacement behavior in multicomponent systems. Instead, we use analytical solutions for four-component systems to show that an additional tie line, which we call the "crossover" tie line, can often control development of miscibility. We also show that the displacement behavior that has come to be known as a "condensing/vaporizing" gas drive [87, 69] is observed when a crossover tie line controls development of miscibility.

In Chapter 4 we turn to the question of nonuniform flow, and its impact on displacement performance. Nonuniform flow can arise from permeability heterogeneity or from viscous fingering. In most miscible floods, viscous fingering and permeability heterogeneity must interact to determine sweep efficiency. We have argued in past reports [1, 8, 2, 9] that permeability variations probably dominate fingering patterns in well developed flow. We use the particle-tracking simulator to study the scaling of finger growth as the length to width ratio for the flow system is changed. We also describe here continued development of the particle-tracking models used to investigate the interplay of fingering and heterogeneity. The development of a three-dimensional particle-tracking code and its potential for description of fingering patterns in realistically heterogeneous reservoirs is described. We also outline an approach that permits addition of the effects of phase behavior in such models.

In Chapter 5, we examine effects of crossflow in an experiment that combines the effects of gravity-driven flow, interfacial tension (IFT) gradients, and low IFT's. The experimental results reported show that significant crossflow can be expected when interactions of phase behavior and multiphase flow create mixtures on tie lines close to a critical tie line. Thus, crossflow will have significant impact on mixing of oil and injected gas in heterogeneous reservoirs if the displacement is MCM or nearly so. That result suggests that interactions of crossflow, heterogeneity and phase behavior will have significant impact on development of miscibility during MCM flow in heterogeneous reservoirs. Also presented in Chapter 5 are results of flow visualization experiments that illustrate how permeability heterogeneity, viscous crossflow, and gravity segregation interact to determine displacement performance. Those experiments also suggest that significant compositional effects are also possible when interactions of crossflow and equilibrium phase behavior are also present.

2. Phase Behavior

The partitioning of components between phases is responsible for the chromatographic separations of components that lead to the development of multicontact miscibility in CO_2 floods and other miscible gas injection processes. Hence, the prediction of equilibrium phase compositions is a fundamental part of any detailed description of a miscible flood process. This chapter reports results of two sets of experiments designed to improve understanding of the use of an equation of state (EOS) to predict phase equilibria.

Section 2.1 outlines the thermodynamic theory behind use of supercritical fluid chromatography as part of the experimental data used to characterize an oil for EOS calculations. The technique is then demonstrated for well characterized hydrocarbon systems and for a CO_2/crude oil system.

Section 2.2 reports results of experiments in which samples of equilibrium CO_2-rich and oil-rich phases were analyzed by gas chromatography and mass spectrometry (GC-MS). That technique permits identification of specific hydrocarbon molecules, and hence the analysis is much more detailed than that detained by gas chromatography alone. The detailed analyses are then used to explore how oil composition affects extraction by CO_2 and hence development of miscibility.

2.1 Prediction of CO_2/Hydrocarbon Phase Behavior Using SFC

Maurice P. Stadler

The traditional method of studying the phase behavior of reservoir fluids is by pressure-volume-temperature (PVT) experiments. A typical experiment requires loading a vessel with the mixture to be studied, controlling the pressure and temperature in the vessel, and sampling and analyzing the phases that result. The data are then used to tune an EOS representation of phase behavior, which can then be used to interpolate between known results and also to predict the phase behavior of new systems. However, PVT experiments are time-consuming, and sampling operations are difficult. Thus, the development of techniques to obtain appropriate PVT information more efficiently would reduce the cost of experimentation.

One such technique is supercritical fluid chromatography (SFC). SFC is similar to gas chromatography except that the carrier fluid is a relatively dense, supercritical fluid, in this case, high-pressure CO_2. Mixtures of hydrocarbons, such as crude oils, can be separated by SFC. Chromatography and thermodynamic theory are used to relate the time needed for a given compound to pass through the chromatograph to its interaction with the CO_2 carrier fluid. In other words, SFC elution times of the various hydrocarbon compounds can be used to help characterize CO_2/hydrocarbon systems. Three different applications are studied.

First, SFC is used to determine CO_2/hydrocarbon binary interaction parameters for the Peng-Robinson EOS. (Binary interaction parameters are used to improve the accuracy of the EOS.) An equation is derived that relates the SFC-elution time of a hydrocarbon to its interaction parameter with CO_2. Interaction parameters for several n-alkanes are measured using SFC.

The second application is the characterization of crude oils for predictions of phase behavior of CO_2/crude oil mixtures with an EOS. SFC is used in two different ways for this application. First, SFC is a natural tool for characterizing CO_2/oil mixtures because hydrocarbons that elute together during an SFC run are likely to partition together into CO_2. (See Section 2.2 for confirmation of this point.) Second, unknown CO_2/n-alkane binary interaction parameters, which are needed for the EOS calculations, are determined using the method described above. A method for prediction of CO_2/crude oil phase behavior is proposed and tested by comparing the results to PVT experiments.

Finally, SFC is used to determine the solubility of a hydrocarbon in dense CO_2. This application is based on the work of Bartle *et al.* [4].

2.1.1 SFC Apparatus

The apparatus, supplied by Applied Biosystems, is basically a GC that has been modified to accept supercritical CO_2 as the carrier fluid. This was done by placing a pump between the CO_2 supply vessel and the injection port. A schematic diagram of the apparatus is shown in Fig. 2.1.

The gas chromatograph used was a Hewlett-Packard (HP) Model 5890. A flame ionization detector was used to detect the material eluted from the column. This type of detector is ideal for analysis of hydrocarbons with a CO_2 carrier fluid because hydrocarbons burn easily, whereas CO_2 does not.

An SFC MicroGradient System pump (Applied Biosystems) delivered the CO_2 at high pressures. This pump is designed to deliver fluids accurately at low flow rates. The pump consists of two 10 ml syringe pump cylinders. An important feature of the pump is that it can be programmed to deliver fluid at fixed or steadily changing pressures. That feature is similar to temperature programming in gas chromatography. The maximum allowable pressure is 5500 psig.

The injector is a Valco Model C14W injection valve. Two different packed columns were used in this work. The first is a Polysiloxane PM, 20 cm × 1.0 mm, column (Applied Biosystems), which was used for simulated distillation and the binary interaction parameter work. The second column is a Spherisorb ODS2, 10 cm × 4.6 mm, column (Jones Chromatography), which was used for the solubility work. These columns were chosen due to their ability to separate hydrocarbons. For this study, an HP 3396A Integrator was used.

The experiments and data acquisition were partially automated by linking the components electronically. The HP 3396A Integrator and the HP 5890 GC were linked via the Instrument Network (INET). INET digitally transfers the raw detector data to the integrator. Also, the integrator can control all of the setpoints (oven temperature, detector temperature, etc.) of the GC.

The pump also has features for networking, relays for activating four external devices. Two of these event actuators were used in this study, one to activate the injector and one to start the integrator. Finally, the integrator was linked to an IBM Personal Computer AT through an RS232C port. This was done so that chromatographic runs could be stored on the hard drive of the PC since the memory of the integrator is limited. In other words, the PC was used as an external disc drive.

2.1.2 CO_2/Hydrocarbon Binary Systems

We begin with a description of a method for determination of CO_2/hydrocarbon binary interaction parameters. We present first a derivation that relates the binary interaction parameter between CO_2 and a hydrocarbon to the capacity factor (a chromatographic measurement). A test of the technique for well-characterized hydrocarbons follows.

Thermodynamic Development

In order to use SFC to measure properties of CO_2/hydrocarbon systems, equations that relate chromatography to thermodynamics are needed. The equation necessary to determine binary interaction parameters from SFC is derived in this section.

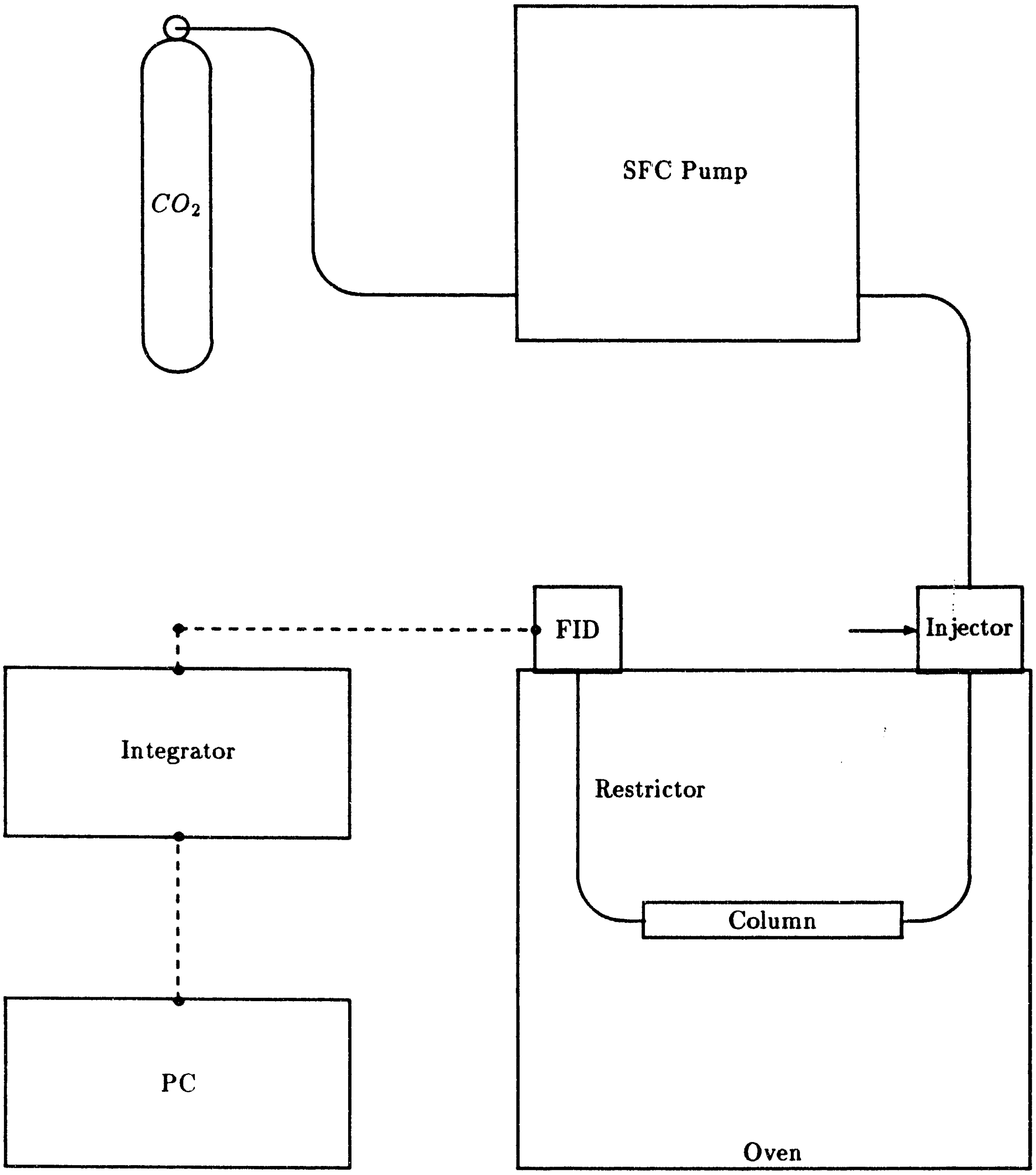

Figure 2.1: Experimental apparatus.

The chromatographic system to be considered consists of two phases: a mobile phase and a stationary phase. A schematic diagram of the chromatographic column is shown in Fig 2.2. The solute, component 1, is distributed between these two phases. The mobile phase consists almost entirely of CO_2, component 2.

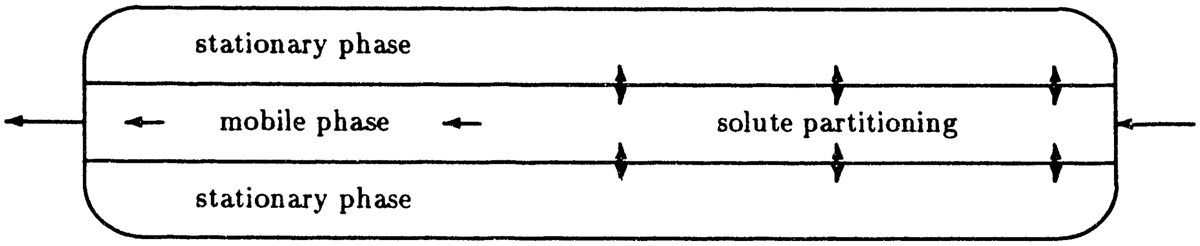

Figure 2.2: Schematic of column and partioning of solutes between phases.

The partial molar Gibbs function of the solute can be determined from [79]

$$d\bar{G}_1 = RT\,d\ln \hat{f}_1 \qquad (\text{const } T) \tag{2.1}$$

where $\bar{G}_1$ is the partial molar Gibbs function of the solute, R is the universal gas constant, T is the temperature, and $\hat{f}_1$ is the partial fugacity of the solute. Integration from any standard state of the solute at the mixture temperature to the state of the solute in solution at T and P gives

$$\bar{G}_1 - G_1^{\circ} = RT \ln \frac{\hat{f}_1}{f_1^{\circ}} \tag{2.2}$$

where the standard state is indicated by the superscript o. By addition and subtraction of $RT \ln x_1$ on the right, we obtain

$$\bar{G}_1 - G_1^{\circ} = RT \ln \frac{\hat{f}_1}{x_1 f_1^{\circ}} + RT \ln x_1 \tag{2.3}$$

where x_1 is the mole fraction of the solute. With the usual definition of an activity coefficient, $\gamma_1 \equiv \hat{f}_1 / x_1 f_1^{\circ}$, Eq. 2.3 becomes

$$\bar{G}_1 = G_1^{\circ} + RT \ln \gamma_1 x_1 \tag{2.4}$$

If the solute is locally at equilibrium in the column, then its partial molar Gibbs function will be equal in both the mobile (m) and stationary (s) phases.

$$G_1^{o,m} + RT \ln \gamma_1^m x_1^m = G_1^{o,s} + RT \ln \gamma_1^s x_1^s \tag{2.5}$$

If the solute is at infinite dilution, then its fugacity can be calculated from Henry's law, ($\hat{f}_1 = \hat{f}_1^{id} = f_1^{\circ} x_1$, where $\hat{f}_1^{id}$ is the ideal partial molar fugacity of the solute based on Henry's law). In this case, $\gamma_1^m = 1$ and $\gamma_1^s = 1$, and Eq. 2.5 now becomes

$$G_1^{o,m} + RT \ln x_1^m = G_1^{o,s} + RT \ln x_1^s \tag{2.6}$$

or

$$\ln \frac{x_1^{\mathrm{s}}}{x_1^{\mathrm{m}}} = \frac{1}{RT}(G_1^{\circ,\mathrm{m}} - G_1^{\circ,\mathrm{s}}) \tag{2.7}$$

From chromatography theory, the capacity factor, k_1', is given by [77]

$$k_1' \equiv \frac{x_1^{\mathrm{s}}}{x_1^{\mathrm{m}}} \frac{V^{\mathrm{m}}}{V^{\mathrm{s}}} \frac{V^{\mathrm{t,s}}}{V^{\mathrm{t,m}}} = \frac{t_1}{t_{\mathrm{o}}} - 1 \tag{2.8}$$

where V is the molar volume, V^{t} is the total volume, t_1 is the chromatographic retention time of the solute, and t_{o} is the time required for the carrier fluid to pass through the column, also called the "dead time." (The dead time is assumed to be equal to the elution time of methane.) The units of k_1' are

$$k_1' \, [=] \, \frac{\text{moles of solute in the stationary phase}}{\text{moles of solute in the mobile phase}} \tag{2.9}$$

These units become clear upon including the units in the definition in Eq. 2.8.

$$x_1 \quad [=] \quad \frac{\text{moles of solute}}{\text{moles of phase}} \tag{2.10}$$

$$V \quad [=] \quad \frac{\text{volume of phase}}{\text{moles of phase}} \tag{2.11}$$

$$V^{\mathrm{t}} \quad [=] \quad \text{volume of phase} \tag{2.12}$$

Eq. 2.8 is used to calculate the capacity factor experimentally. Combination of Eqs. 2.7 and 2.8 gives

$$\ln \left(k_1' \frac{V^{\mathrm{s}}}{V^{\mathrm{m}}} \frac{V^{\mathrm{t,m}}}{V^{\mathrm{t,s}}} \right) = \frac{1}{RT}(G_1^{\circ,\mathrm{m}} - G_1^{\circ,\mathrm{s}}) \tag{2.13}$$

Next, we take the partial derivative of Eq. 2.13 with respect to pressure. In addition, we assume that

$$\left[\frac{\partial}{\partial P} \left(\frac{V^{\mathrm{s}} V^{\mathrm{t,m}}}{V^{\mathrm{t,s}}} \right) \right]_T = 0 \tag{2.14}$$

Also, recall that

$$\left(\frac{\partial G_1^{\circ}}{\partial P} \right)_{T,x} = V_1^{\circ} \tag{2.15}$$

Eq. 2.13 now becomes

$$\left(\frac{\partial \ln k_1'}{\partial P} \right)_T = \frac{1}{RT}(V_1^{\circ,\mathrm{m}} - V_1^{\circ,\mathrm{s}}) + \left(\frac{\partial \ln V^{\mathrm{m}}}{\partial P} \right)_T \tag{2.16}$$

Recall that for Henry's law, $V_1^{\circ} = \bar{V}_1^{\infty}$, where $\bar{V}_1^{\infty}$ is the partial molar volume of the solute at infinite dilution. Also, $V^{\mathrm{m}} = V_2$ since the mobile phase is essentially pure CO_2. Making these substitutions, Eq. 2.16 becomes [5]

$$\left(\frac{\partial \ln k_1'}{\partial P} \right)_T = \frac{1}{RT}(\bar{V}_1^{\infty,\mathrm{m}} - \bar{V}_1^{\infty,\mathrm{s}}) + \left(\frac{\partial \ln V_2}{\partial P} \right)_T \tag{2.17}$$

Now, $\bar{V}_1^{\infty,\mathrm{m}}$ can be calculated from the expression

$$\bar{V}_1^{\infty,\mathrm{m}} = \lim_{n_1 \to 0} \left[\frac{\partial (n V^{\mathrm{m}})}{\partial n_1} \right]_{P,T,n_2} \tag{2.18}$$

$$= \lim_{n_1 \to 0} \left[-n \left(\frac{\partial V^{\mathrm{m}}}{\partial P} \right)_{n_1} \left(\frac{\partial P}{\partial n_1} \right)_{V^{\mathrm{m}}} \right]_{T,n_2} \tag{2.19}$$

where n_1 is the number of moles of the solute, n_2 is the number of moles of CO_2, and n is the total number of moles. Substitution of this expression into Eq. 2.17 yields [85]

$$\left(\frac{\partial \ln k_1'}{\partial P}\right)_T = -\frac{1}{RT}\left\{ n \lim_{n_1 \to 0}\left[\left(\frac{\partial V^m}{\partial P}\right)_{n_1}\left(\frac{\partial P}{\partial n_1}\right)_{V^m}\right]_{T,n_2} + \bar{V}_1^{\infty,s}\right\} + \frac{1}{V_2}\left(\frac{\partial V_2}{\partial P}\right)_T \tag{2.20}$$

or

$$\left(\frac{\partial \ln k_1'}{\partial P}\right)_T = -\frac{n}{RT}\lim_{n_1 \to 0}\left(\frac{\partial P}{\partial n_1}\right)_{V_2,T,n_2}\left(\frac{\partial V_2}{\partial P}\right)_T - \frac{\bar{V}_1^{\infty,s}}{RT} + \frac{1}{V_2}\left(\frac{\partial V_2}{\partial P}\right)_T \tag{2.21}$$

An EOS can be used to calculate the first and third terms on the right. For example, these derivatives for the Peng-Robinson EOS are used. (The binary interaction parameter between CO_2 and the solute, δ_{12}, is included in the limiting term.) If we substitute these expressions into Eq. 2.21, assume that δ_{12} and $\bar{V}_1^{\infty,s}$ are not functions of pressure, and integrate, Eq. 2.21 becomes

$$Y = \delta_{12}X_1 + \bar{V}_1^{\infty,s}X_2 + C, \tag{2.22}$$

where

$$\begin{aligned} Y &= \int_{P_i}^{P}\left[\frac{RT}{(V_2-b_2)} + \frac{RTb_1}{(V_2-b_2)^2} - \frac{2(1-\delta_{12})\sqrt{a_1a_2}}{V_2^2+2b_2V_2-b_2^2} + \frac{2a_2b_1(V_2-b_2)}{(V_2^2+2b_2V_2-b_2^2)^2} - \frac{RT}{V_2}\right] \\ &\quad \cdot\frac{1}{RT}\left[\frac{2a_2(V_2+b_2)}{(V_2^2+2b_2V_2-b_2^2)^2} - \frac{RT}{(V_2-b_2)^2}\right]^{-1} dP + \ln k_1', \end{aligned} \tag{2.23}$$

$$X_1 = -\int_{P_i}^{P}\frac{1}{RT}\left(\frac{2\sqrt{a_1a_2}}{V_2^2+2b_2V_2-b_2^2}\right)\left[\frac{2a_2(V_2+b_2)}{(V_2^2+2b_2V_2-b_2^2)^2} - \frac{RT}{(V_2-b_2)^2}\right]^{-1} dP, \tag{2.24}$$

$$X_2 = -\frac{P-P_i}{RT}, \tag{2.25}$$

$$C = \ln k_{1i}', \tag{2.26}$$

a_1, a_2, b_1, and b_2 are the Peng-Robinson EOS parameters. P_i is the lowest pressure at which the experiments are performed, and k_{1i}' is the capacity factor at the lowest pressure. The only unknowns in Eq. 2.22 are δ_{12} and $\bar{V}_1^{\infty,s}$. All of the other terms can be calculated using the EOS except for the capacity factors, which are determined using SFC. Eq. 2.22 is expressed in integral form because it is more accurate to integrate an analytical expression numerically than to differentiate discrete experimental data.

One way to obtain δ_{12} from Eq. 2.22 is to use SFC to measure the capacity factor of the solute at several pressures. The terms Y, X_1, X_2, and C can then be calculated using the measured capacity factors and the Peng-Robinson EOS. A least-squares, two-variable regression can then be performed to calculate δ_{12} and $\bar{V}_1^{\infty,s}$. However, this procedure was not found to be a very reliable method to determine δ_{12} because δ_{12} and $\bar{V}_1^{\infty,s}$ have a high statistical correlation.

A better way is to take advantage of the fact that binary interaction parameters for several CO_2/hydrocarbon pairs are reported in the literature. For these hydrocarbons, the capacity factors at several pressures were determined using SFC. Because δ_{12} is known, Eq. 2.22 becomes

$$(Y - \delta_{12}X_1) = \bar{V}_1^{\infty,s}X_2 + C \tag{2.27}$$

Now, $\bar{V}_1^{\infty,s}$ can be easily determined from a least squares fit. With several values of $\bar{V}_1^{\infty,s}$, a correlation can be made.

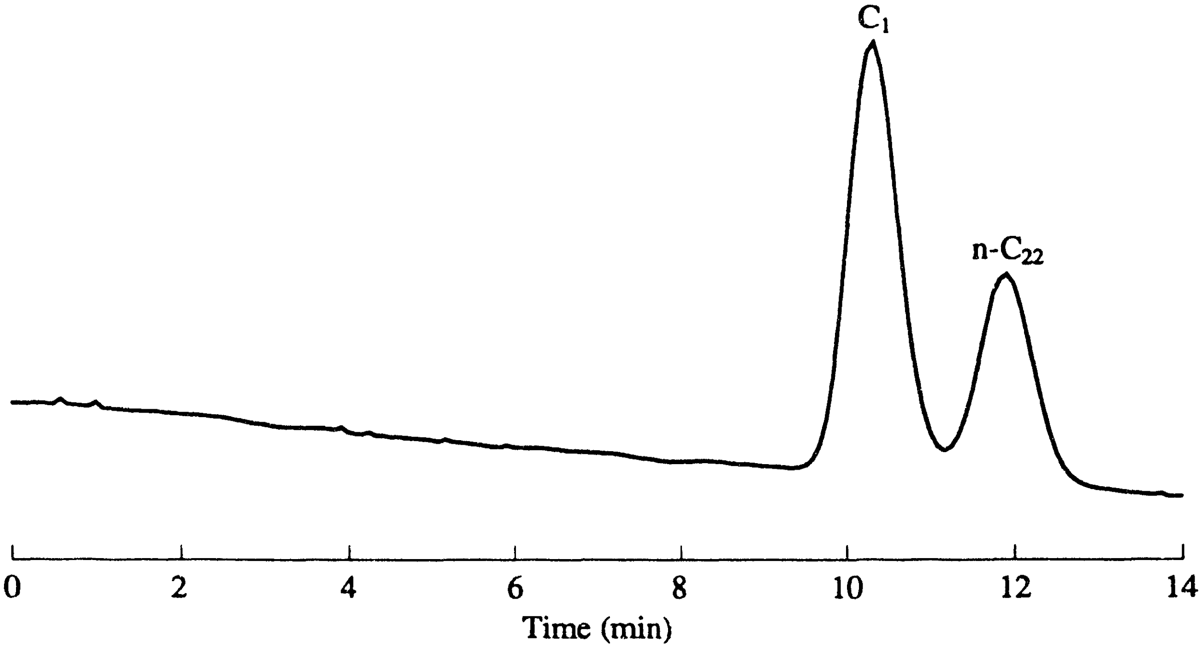

Figure 2.3: Example chromatogram of methane and docosane.

To determine δ_{12} for an unknown CO_2/hydrocarbon pair, $\bar{V}_1^{\infty,s}$ can be determined from the correlation, and Eq. 2.22 can be rearranged to yield

$$(Y - \bar{V}_1^{\infty,s}X_2) = \delta_{12}X_1 + C \tag{2.28}$$

A least squares fit can then be performed on capacity factor measurements to calculate δ_{12}.

Results and Discussion

A correlation is needed in order to calculate $\bar{V}_1^{\infty,s}$. The correlation was obtained using known CO_2/hydrocarbon binary interaction parameters, δ_{12}. For this purpose, the work of Deo *et al.* [15] was used because they list a consistent set of δ_{12}'s for a large number of hydrocarbons. For each hydrocarbon, SFC was used to measure the capacity factor at several pressures. An illustration of how the capacity factor was determined for docosane, n-C_{22}, at a particular temperature and pressure is given in Fig. 2.3.

The complete set of measurements for docosane at 131°F is reported in Table 2.1. Results of those measurements are also shown in Fig. 2.4.

The next step is to calculate $\bar{V}_1^{\infty,s}$ using a linear least square fit of Eq. 2.27 to the experimental data. The result of this regression for the data listed in Table 2.1 is that $\bar{V}_1^{\infty,s}$ = 848 ml/mole. As shown by the curve in Fig. 2.4, this procedure matches the capacity factor versus pressure data well, which partially vindicates the assumptions made in deriving Eq. 2.22.

Values of $\bar{V}_1^{\infty,s}$ were obtained by this procedure for many of the hydrocarbons included in the work of Deo *et al.* The results of these experiments and linear least squares regressions for $\bar{V}_1^{\infty,s}$ are given in Tables 2.2 and 2.3 and Fig. 2.5. The SFC experiments were performed at 131°F. Since Deo *et al.* list δ_{12}'s over a wide range of temperatures, interpolation was used where possible to obtain the δ_{12}'s of Tables 2.2 and 2.3. When interpolation of Deo *et al.*'s data was not possible, the δ_{12} at the temperature closest to 131°F was chosen. Nevertheless, the dependence of δ_{12} on temperature is not large.

Table 2.1: Capacity Factors for Docosane at 131°F.

Pressure (psia)	t_o (min)	t_1 (min)	$\ln k'_1$
1715	14.71	67.32	1.274
1915	15.59	33.66	0.148
2115	15.51	25.39	-0.451
2315	14.12	20.56	-0.785
2515	13.49	17.95	-1.107
2715	12.60	15.74	-1.388
2915	11.79	14.34	-1.535
3115	11.15	13.20	-1.694
3315	10.62	12.31	-1.838
3515	10.10	11.57	-1.927

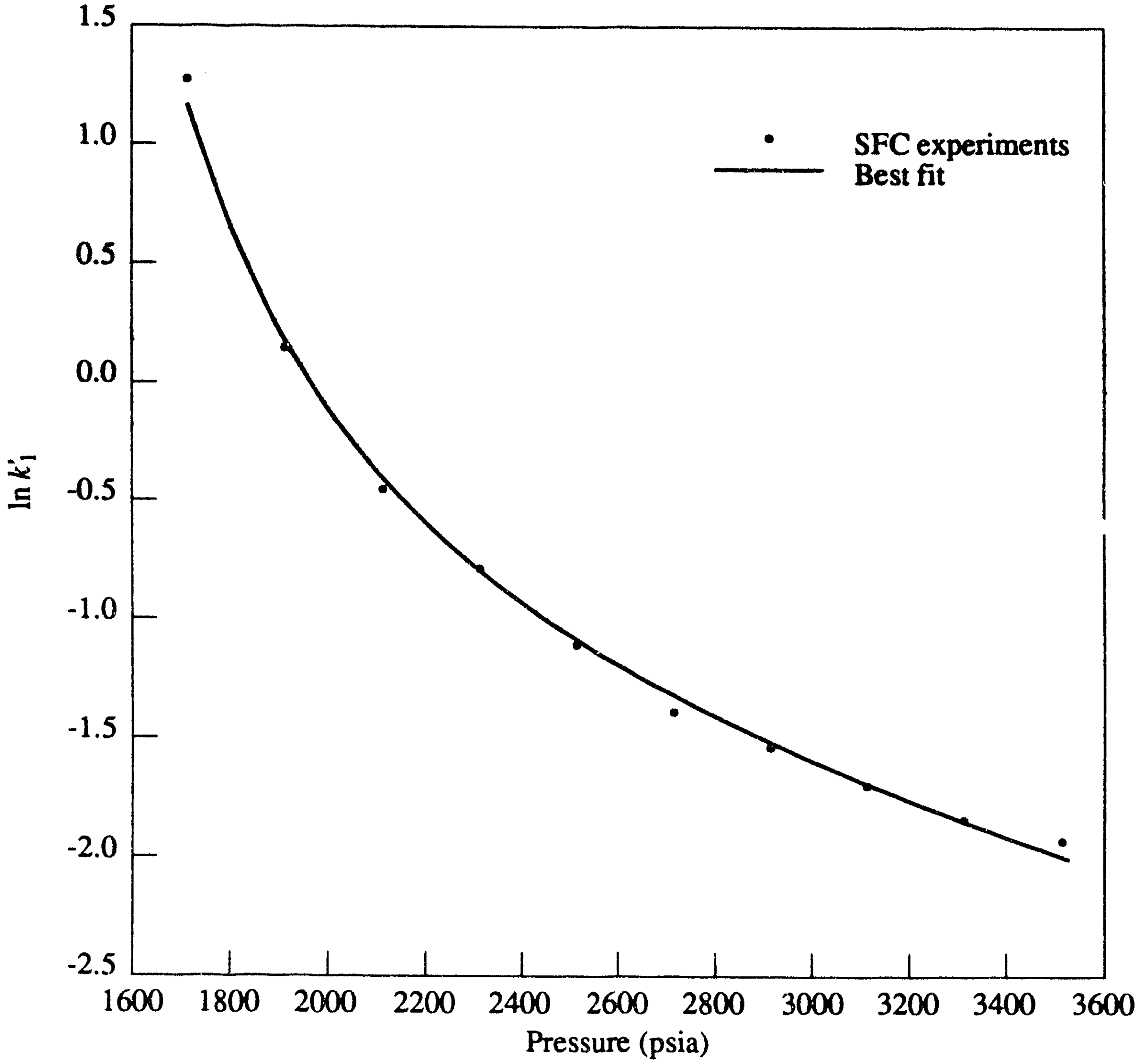

Figure 2.4: The effect of pressure on the capacity factor of docosane at 131°F.

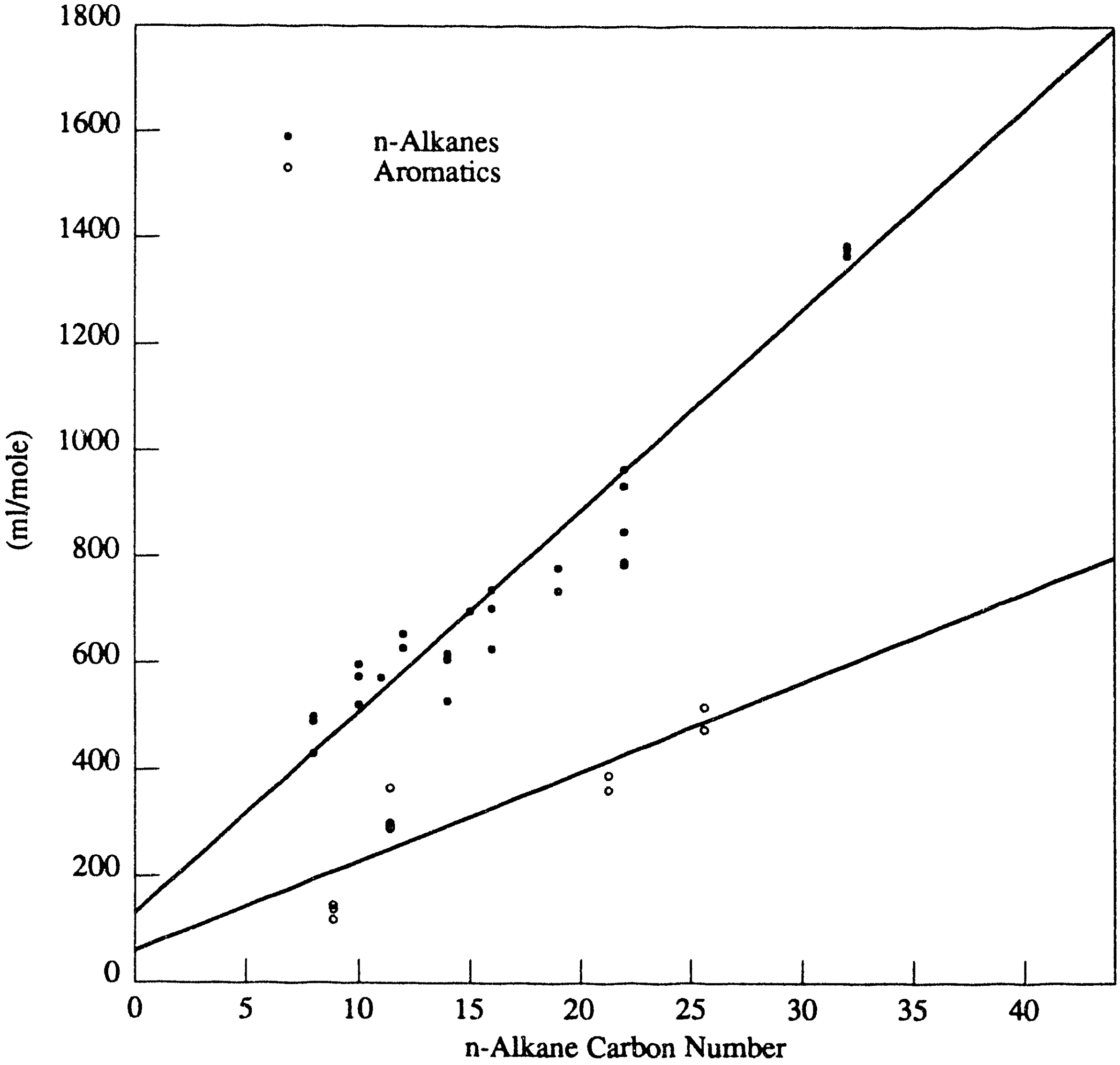

Figure 2.5: Correlation for $\bar{V}_1^{\infty,s}$. The equation for the line that passes through the n-alkane data is $\bar{V}_1^{\infty,s} = 37.9n + 131$ where n is the carbon number. For the aromatic data, the equation is $\bar{V}_1^{\infty,s} = 16.8n + 60.4$ where n is the apparent n-alkane carbon number.

As Table 2.2 shows, there is considerable scatter for the calculated values of $\bar{V}_1^{\infty,s}$ for a given component. Evidently, $\bar{V}_1^{\infty,s}$ is very sensitive to slight differences between different sets of capacity factor experiments. Therefore, multiple, sets of experiments, each yielding a value for $\bar{V}_1^{\infty,s}$, were performed for most of the solutes in order to improve the accuracy of the correlation.

As shown in Fig. 2.5, the results for the n-alkane data appear to fall more or less on a straight line. Deviations from this straight line may be due to the wide range of temperatures and experimental techniques at which the δ_{12}'s are reported. The line that passes through this data is a least squares line. Of course, this correlation may depend on temperature. However, this dependence is not important because the end result of our calculations, δ_{12}, does not depend strongly on temperature.

For the aromatic compounds, an "equivalent n-alkane carbon number" is determined by comparing the SFC elution of the aromatic to the elution of n-alkanes. For example, the SFC elution time of naphthalene is greater than that of undecane but less than that of docosane for a particular column temperature and pressure. Interpolation of these elution times results in an apparent n-alkane carbon number of 11.4. As Fig 2.5 shows, the aromatics have a smaller partial molar volume in the stationary phase than the n-alkanes, probably because aromatic molecules have a tighter molecular structure (fused rings) than n-alkanes (chains). The line passing through this data is also a least squares line.

Now, if we wish to obtain δ_{12} for a hydrocarbon that is not included in the work of Deo *et al.*, the following steps should be taken. First, the capacity factor is measured for the hydrocarbon over a range of pressures. Then, the correlation provided in Fig. 2.5 is used to obtain $\bar{V}_1^{\infty,s}$. The binary interaction parameter δ_{12} can now be obtained by fitting a least squares straight line to Eq. 2.28. The slope of this line is δ_{12}.

This procedure was applied to four hydrocarbons for which δ_{12} was not calculated by Deo *et al.* Table 2.4 lists the results of these experiments and calculations. $\bar{V}_1^{\infty,s}$ was taken from the correlation in Fig. 2.5. The SFC-determined δ_{12} for each hydrocarbon is the average of at least two separate δ_{12} determinations. The SFC experiments were performed at 131°F.

One way to check the validity of these measured δ_{12}'s is to use them in the Peng-Robinson EOS to try to calculate phase behavior data obtained in standard PVT experiments. Fig. 2.6 illustrates the results for the first three CO_2/hydrocarbon systems. The points are PVT data taken from Tsai and Yau [75] and Gasem and Robinson [24]. For each CO_2/hydrocarbon pair, two curves were calculated using the Peng-Robinson EOS. The solid line was calculated with a δ_{12} that results in a best fit of the EOS to the data while the dashed line was calculated with the δ_{12} determined using the SFC method outlined above. The data shown in these figures and for the CO_2/tetratetracontane are also listed in Tables 2.5–2.8. In these tables, x_2 is the mole fraction of CO_2 in the liquid phase and y_2 is the mole fraction of CO_2 in the vapor phase. Also required for the EOS calculations are the critical pressure, critical temperature, and acentric factor for each hydrocarbon (Table 2.4). The critical properties were calculated using the correlation of Twu [76], and the acentric factor was calculated using the correlation of Kesler and Lee [33]. Correlations were used for these hydrocarbons because the properties have not been determined experimentally.

As shown in Fig. 2.6, the SFC-determined δ_{12} improves the Peng-Robinson EOS prediction of the experimental data for the first three binary mixtures. In addition, for the CO_2/octacosane pair, the SFC-determined δ_{12} is very close to the best fit δ_{12}. Agreement is also good for the CO_2/hexatriacontane pair, as Fig. 2.6 and Table 2.4 show.

However, for the CO_2/tetratetracontane pair, the SFC method described above does not do a good job of predicting a useful δ_{12} for the Peng-Robinson EOS as Table 2.8 shows. Application of the linear correlation for $\bar{V}_1^{\infty,s}$ yields -0.266 for the value of δ_{12}. That value produces poor agreement with the phase equilibrium measurements summarized in Table 2.8. One possible explanation for this limitation is that determination of the critical properties, acentric factor, and

Table 2.2: Calculated $\bar{V}_1^{\infty,s}$ for n-alkanes with δ_{12} reported in Deo *et al.* [15].

Compound	δ_{12}	$\bar{V}_1^{\infty,s}$ (ml/mole)
Octane	0.109	491.
		500.
		431.
Decane	0.100	523.
		598.
		575.
Undecane	0.102	572.
Dodecane	0.104	655.
		628.
Tetradecane	0.110	618.
		607.
		612.
		529.
Pentadecane	0.093	698.
Hexadecane	0.098	703.
		627.
		738.
Nonadecane	0.105	737.
		799.
Docosane	0.093	791.
		848.
		785.
		934.
		965.
Dotriacontane	0.063	1386.
		1384.
		1381.
		1367.
		1380.

Table 2.3: Calculated $\bar{V}_1^{\infty,s}$ for aromatics with δ_{12} reported in Deo *et al.* [15].

Compound	"Apparent" n-alkane carbon number	δ_{12}	$\bar{V}_1^{\infty,s}$ (ml/mole)
m-Xylene	8.9	0.074	120.
			146.
			139.
Naphthalene	11.4	0.124	367.
			294.
			291.
			296.
			301.
Phenanthrene	21.3	0.154	364.
			391.
Pyrene	25.6	0.282	476.
			519.

Table 2.4: SFC-calculated δ_{12} for hydrocarbons not studied by Deo *et al.* [15]. The value for $\bar{V}_1^{\infty,s}$ was determined from the correlation.

Compound	$\bar{V}_1^{\infty,s}$ (ml/mole)	δ_{12}		P_c (bar)	T_c (K)	ω
		SFC	Best fit			
Tetracosane	1017	0.124	0.068	9.38	806	1.00
Octacosane	1165	0.080	0.079	7.95	836	1.11
Hexatriacontane	1460	0.006	0.020	5.99	884	1.27
Tetratetracontane	1794	-0.266	0.020	3.96	946	1.52

Table 2.5: Binary phase behavior for the CO_2/tetracosane mixture at 212°F. Comparison of published PVT data [75] with calculations using the Peng-Robinson EOS with the SFC-determined and best fit δ_{12}'s.

Pressure (psia)	Published		Calculated			
			$\delta_{12} = 0.124$ (SFC)		$\delta_{12} = 0.068$ (Best fit)	
	x_2	y_2	x_2	y_2	x_2	y_2
147.	0.0819	1.0000	0.0728	1.0000	0.0853	1.0000
294.	0.1720	1.0000	0.1397	1.0000	0.1635	1.0000
441.	0.2437	1.0000	0.2011	1.0000	0.2352	1.0000
588.	0.3004	1.0000	0.2574	1.0000	0.3008	1.0000
735.	0.3531	1.0000	0.3091	1.0000	0.3608	1.0000

Table 2.6: CO_2/octacosane phase behavior at 167°F. Comparison of published PVT data [24] with calculations using the Peng-Robinson EOS with the SFC-determined and best fit δ_{12}'s.

Pressure (psia)	x_2		
		Calculated	
	Published	$\delta_{12} = 0.080$ (SFC)	$\delta_{12} = 0.079$ (Best fit)
1120.0	0.551	0.556	0.557
1393.0	0.617	0.632	0.633

Table 2.7: CO_2/hexatriacontane phase behavior at 212°F. Comparison of published PVT data [24] with calculations using the Peng-Robinson EOS with the SFC-determined and best fit δ_{12}'s.

Pressure (psia)	x_2		
		Calculated	
	Published	$\delta_{12} = 0.006$ (SFC)	$\delta_{12} = 0.020$ (Best fit)
126.5	0.101	0.094	0.091
229.0	0.172	0.165	0.159
241.0	0.178	0.173	0.167
282.5	0.206	0.200	0.192
416.0	0.280	0.282	0.272
528.5	0.335	0.345	0.333
621.0	0.375	0.393	0.380
653.5	0.390	0.410	0.395
852.5	0.459	0.501	0.484

Table 2.8: CO_2/tetratetracontane phase behavior at 212°F. Comparison of published PVT data [24] with calculations using the Peng-Robinson EOS with the SFC-determined and best fit δ_{12}'s.

Pressure (psia)	x_2		
		Calculated	
	Published	$\delta_{12} = -0.266$ (SFC)	$\delta_{12} = 0.020$ (Best fit)
136.0	0.122	0.202	0.106
233.0	0.188	0.331	0.175
290.0	0.238	0.401	0.214
486.0	0.343	0.605	0.334
607.0	0.401	0.704	0.399
886.5	0.502	0.852	0.529

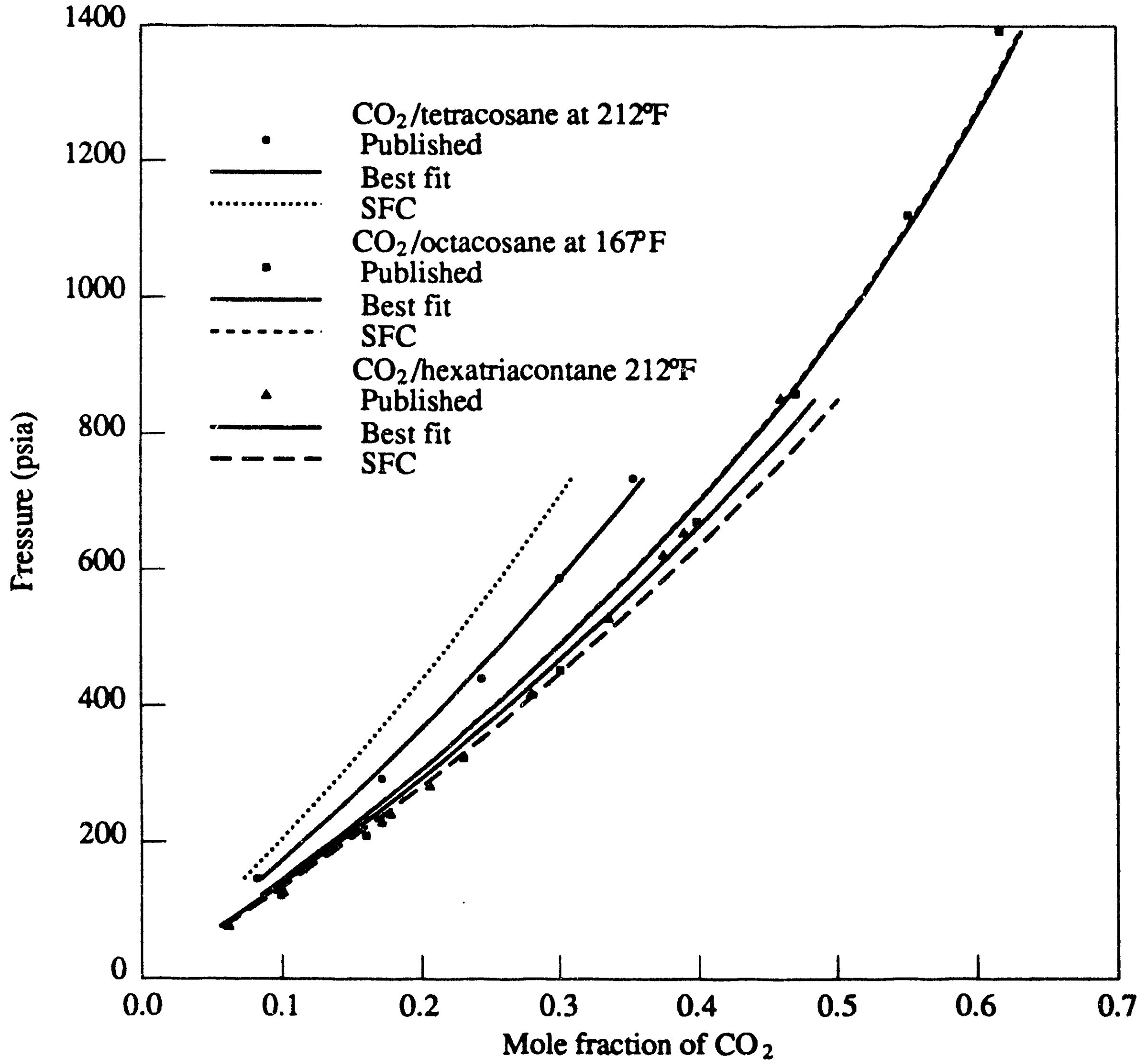

Figure 2.6: CO_2/tetracosane, /octacosane, and /hexatriacontane phase behavior. Comparison of literature PVT data [75, 24] with calculations using the Peng-Robinson EOS with the SFC-determined and best fit δ_{12}'s.

$\bar{V}_1^{\infty,s}$ all involve extrapolations of data for hydrocarbons much smaller than this large hydrocarbon. Thus, many of the properties needed to determine δ_{12} are not accurately determined, which in turn results in an inaccurate value for δ_{12}.

2.1.3 Crude Oil Characterization

Obtaining accurate CO_2/hydrocarbon binary interaction parameters is part of a larger problem: predicting the phase behavior of CO_2/crude oil mixtures. A typical crude oil contains hundreds of components. It is not practical to identify each pure component, and even if it were, calculations involving all the components would be prohibitively time-consuming. Instead, the hundreds of components of a crude oil are usually grouped into "pseudocomponents." The objective is to choose a small number of pseudocomponents while still being able to match experimentally determined phase behavior of the crude oil.

The approach to crude oil characterization taken here is specialized for mixtures with CO_2 and, with CO_2 enhanced oil recovery in mind, is based upon how the components of the crude oil partition from the oil-rich phase into the CO_2-rich phase. First, the lumping procedure will be described, and second, the results for an actual CO_2/crude oil system will be presented.

Characterization Procedure

The lumping procedure used was a two-stage process. First, the crude oil was divided into 30 to 40 single carbon number fractions by simulated distillation using SFC. Second, these carbon number fractions were grouped into a small number of pseudocomponents. A step-by-step description of this lumping procedure for a crude oil follows:

1. Acquire a few milliliters of the crude oil to be studied, and determine its carbon number distribution by simulated distillation using SFC. Although simulated distillation is usually performed with a gas chromatograph, SFC is used here because the elution order of the components during an SFC run depends on how the components partition into the CO_2 mobile phase. Thus, SFC is a natural tool for lumping because components that elute together partition into CO_2 together.

   Simulated distillation results in 37 or so carbon number fractions. These fractions are grouped into only a few pseudocomponents in the second stage of the lumping scheme.

2. Using an EOS, perform a flash calculation for a mixture of CO_2 with the crude oil (represented by carbon number fractions) at a temperature and pressure in the range of interest. Adjust the overall mole fraction of CO_2 so that a two-phase mixture results. The estimated K-value for each carbon number fraction is obtained from this calculation. (The critical pressure, critical temperature, acentric factor, and molecular weight assigned to each carbon number fraction were taken from correlations that are included in the EOS computer program.)

3. Group the carbon number fractions into a small number of pseudocomponents so that the difference between the K-value of each carbon number fraction and the K-value of the pseudocomponent to which they are assigned is minimized—the lumping scheme of Newley and Merrill [49] is used, except that they assigned K-values to the components of the crude oil based upon its dew point without any additional CO_2.

   This minimization procedure can be expressed mathematically. Assume that we wish to group N_c carbon number fractions (index i) into N_{pc} pseudocomponents (index j). The jth pseudocomponent group is given the label $m(j), j = 1, \ldots, N_{pc}$.

The objective function, σ, to be minimized is given by

$$\sigma = \sum_{j=1}^{N_{pc}} \sum_{i \in m(j)} \left(\frac{K_i - \bar{K}_j}{K_i} \right)^2 \tag{2.29}$$

$$K_i = \frac{y_i}{x_i} \tag{2.30}$$

$$\bar{K}_j = \frac{\sum_{i \in m(j)} y_i}{\sum_{i \in m(j)} x_i} \tag{2.31}$$

and y_i is the mole fraction of carbon number fraction i in the vapor phase and x_i is the mole fraction in the liquid phase.

4. The last step is to calculate the critical temperature, critical pressure, acentric factor, and molecular weight for these pseudocomponents. These mixing rules are also taken from Newley and Merrill [49]. Also, each CO_2/pseudocomponent must be assigned a binary interaction parameter.

Results and Discussion

The proposed lumping scheme was tested for mixtures of CO_2 with Means stock tank oil. The crude oil is characterized according to the scheme outlined above, and the Peng-Robinson EOS is used to generate a phase diagram, which is compared to experimental results.

The Means oil comes from the San Andres unit of the Permian Basin in Andrews County, Texas. Table 2.9 gives the simulated distillation results using SFC for Means. The first three components are specific compounds while the rest of the components are carbon number fractions. The weight % values come directly from the simulated distillation calculations and are converted to mole % values (z_i) using the molecular weight of each component or carbon number fraction. The C_{45} properties are used, arbitrarily, for the C_{41+} fraction.

The next step is to use the Peng-Robinson EOS to perform a flash calculation for a mixture of Means stock tank oil and 80 mole % CO_2 at 90°F and 1000 psia, conditions at which experimental data had been obtained previously [52, 71]. The results of this flash—the K-values and liquid phase mole fraction of each component—are given in Table 2.10.

Table 2.10 also includes the results of the pseudocomponent lumping scheme. Seven pseudocomponents were chosen because this is a number typically chosen for full reservoir simulations [49]. Each pseudocomponent group is enclosed in horizontal lines along with the critical temperature, critical pressure, acentric factor, and molecular weight calculated for each pseudocomponent. The binary interaction parameter between each pseudocomponent and CO_2 is simply that for one of the n-alkanes in or near the middle of the carbon number fraction group. This value is taken from Deo *et al.* or determined using the method discussed in Section 2.1.2. The source of these binary interaction parameters is indicated in the table.

The Peng-Robinson EOS and the pseudocomponent representation of the CO_2/Means stock tank oil were used to calculate a pressure-composition phase diagram. The results are presented as the solid lines in Fig. 2.7. Fig. 2.7 also shows the experimental data taken from Stessman [71]. The points are actual experimental data while the dashed lines indicate interpolation or extrapolation.

The overall agreement in Fig. 2.7 is fair. Large differences between the calculated and experimental results occur in the liquid-liquid region. No parameters were adjusted in calculating this phase diagram.

Table 2.9: Simulated Distillation Results for Means Stock Tank Oil.

Component	Composition (weight %)	z_i (mole %)
n-C_4	0.43	1.68
i-C_5	0.86	2.71
n-C_5	0.86	2.71
C_6	1.57	4.16
C_7	2.85	6.76
C_8	3.89	8.28
C_9	3.35	6.30
C_{10}	3.55	6.03
C_{11}	3.07	4.76
C_{12}	3.62	5.12
C_{13}	2.83	3.68
C_{14}	3.22	3.86
C_{15}	3.06	3.38
C_{16}	2.89	2.96
C_{17}	3.19	3.06
C_{18}	2.64	2.39
C_{19}	2.29	1.98
C_{20}	2.23	1.85
C_{21}	2.19	1.71
C_{22}	2.20	1.67
C_{23}	2.12	1.55
C_{24}	2.05	1.44
C_{25}	1.38	0.93
C_{26}	2.00	1.30
C_{27}	1.36	0.86
C_{28}	1.99	1.22
C_{29}	1.35	0.80
C_{30}	1.31	0.76
C_{31}	1.49	0.84
C_{32}	1.22	0.67
C_{33}	1.15	0.61
C_{34}	1.23	0.64
C_{35}	1.15	0.59
C_{36}	0.96	0.48
C_{37}	1.18	0.58
C_{38}	0.65	0.31
C_{39}	0.93	0.44
C_{40}	0.74	0.34
C_{41+}	25.0	10.6

Table 2.10: Results of the flash and lumping of Means stock tank oil with 80 mole % CO_2 at 90°F and 1000 psia.

Component	K_i	z_i (mole %)	x_i (mole %)	Lumping Results				
				P_c (K)	T_c (atm)	ω	MW	δ_{12}
CO_2	1.90×10^{0}	80.00	52.31	72.80	304.2	0.225	44.0	
n-C_4	1.98×10^{-1}	0.337	0.639	28.26	576.1	0.352	102.	0.109[a]
i-C_4	1.21×10^{-1}	0.543	1.126					
n-C_5	1.02×10^{-1}	0.543	1.152					
C_6	5.54×10^{-2}	0.831	1.875					
C_7	2.97×10^{-2}	1.352	3.158					
C_8	1.74×10^{-2}	1.655	3.933					
C_9	9.49×10^{-3}	1.261	3.029					
C_{10}	5.42×10^{-3}	1.206	2.915					
C_{11}	3.12×10^{-3}	0.951	2.306	19.43	699.4	0.556	179.	0.110[a]
C_{12}	1.77×10^{-3}	1.024	2.487					
C_{13}	1.05×10^{-3}	0.736	1.791					
C_{14}	6.06×10^{-4}	0.772	1.878					
C_{15}	3.47×10^{-4}	0.676	1.646					
C_{16}	2.04×10^{-4}	0.593	1.443					
C_{17}	1.25×10^{-4}	0.613	1.492	14.27	786.1	0.722	270.	0.099[a]
C_{18}	8.44×10^{-5}	0.479	1.166					
C_{19}	5.85×10^{-5}	0.396	0.965					
C_{20}	3.83×10^{-5}	0.369	0.899					
C_{21}	2.65×10^{-5}	0.343	0.834					
C_{22}	1.79×10^{-5}	0.334	0.813					
C_{23}	1.28×10^{-5}	0.309	0.753					
C_{24}	2.17×10^{-6}	0.288	0.702	11.37	844.2	0.999	347.	0.102[b]
C_{25}	1.29×10^{-6}	0.186	0.454					
C_{26}	8.29×10^{-7}	0.261	0.635					
C_{27}	5.32×10^{-7}	0.172	0.419					
C_{28}	3.40×10^{-7}	0.244	0.593					
C_{29}	2.38×10^{-7}	0.161	0.392	9.82	881.5	1.108	403.	0.063[a]
C_{30}	1.50×10^{-7}	0.151	0.369					
C_{31}	1.01×10^{-7}	0.168	0.409					
C_{32}	6.70×10^{-8}	0.134	0.326					
C_{33}	4.64×10^{-8}	0.123	0.299					
C_{34}	3.28×10^{-8}	0.128	0.312	7.26	954.1	1.317	520.	0.006[c]
C_{35}	2.37×10^{-8}	0.118	0.287					
C_{36}	1.67×10^{-8}	0.096	0.233					
C_{37}	1.26×10^{-8}	0.116	0.282					
C_{38}	8.88×10^{-9}	0.062	0.152					
C_{39}	6.81×10^{-9}	0.087	0.213					
C_{40}	4.85×10^{-9}	0.068	0.166					
C_{41+}	1.37×10^{-9}	2.112	5.143					

---

[a] Taken from Deo *et al.* [15] for an n-alkane near the middle of the pseudocomponent.

[b] The average of the two SFC-determined δ_{12}'s for n-C_{24} and n-C_{28}.

[c] The SFC-determined δ_{12} for n-C_{36}.

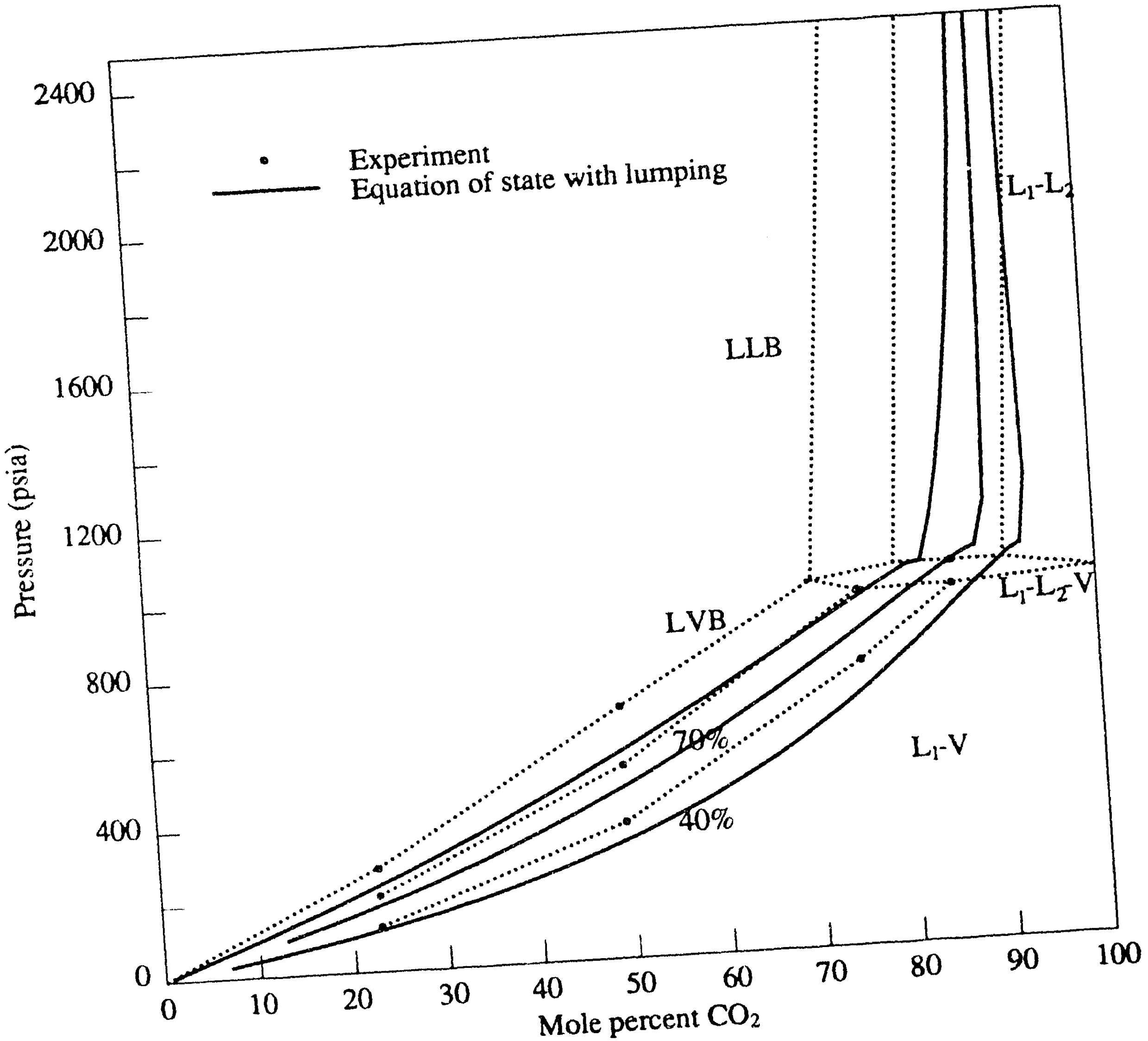

Figure 2.7: Pressure-composition phase diagram for the CO_2/Means stock tank oil mixture at 90°F. Comparison of experiments [71] and calculations.

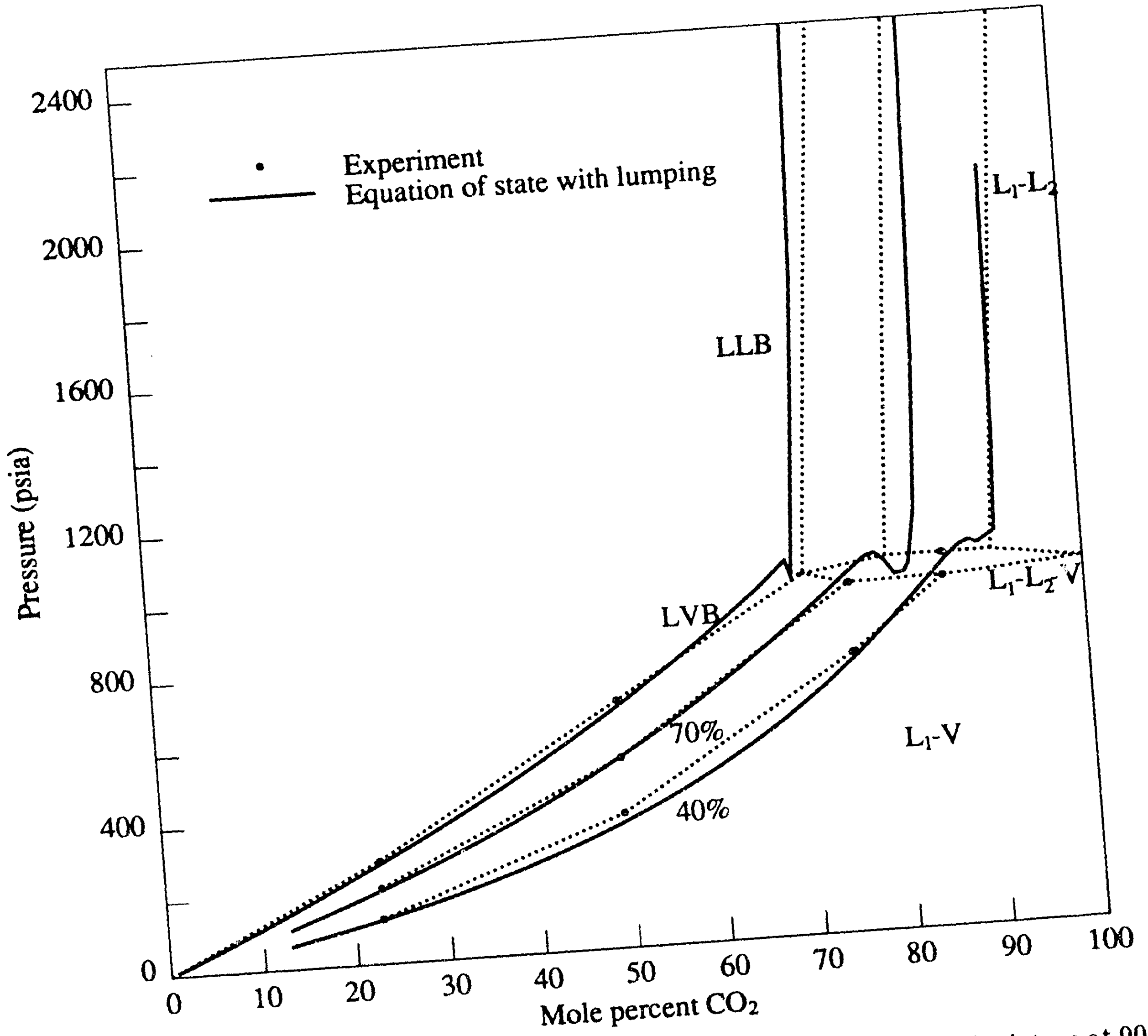

Figure 2.8: Pressure-composition phase diagram for the CO_2/Means stock tank oil mixture at 90°F. Comparison of experiments [71] and calculations with δ_{12} for the CO_2/heaviest pseudocomponent pair equal to 0.1.

Pressure-composition phase diagrams of the type shown in Fig. 2.7 are usually sensitive to the δ_{12} between CO_2 and the heaviest pseudocomponent. As discussed in Section 2.1.2, however, δ_{12} for very heavy hydrocarbons could not be determined accurately using SFC. As a result, another pressure-composition phase diagram was calculated with a modified value of the CO_2/heaviest pseudocomponent δ_{12}. A value of 0.1 was chosen because this number is roughly in line with the other binary interaction parameters. The results of this recalculated phase diagram are shown in Fig. 2.8.

As shown in Fig. 2.8, the overall agreement is much improved. The saturation (bubblepoint) line is predicted well, and the sharp change in slope of the constant volume fraction lines from the L_1-V to the L_1-L_2 region also agrees.

The three phase region was observed experimentally, but could not be found using the Peng-Robinson EOS. However, the EOS does correctly predict the transition from the L_1-V region to the L_1-L_2 region. In this transition zone, the equation-of-state calculations yield a peculiar "dip" in the lines. Here is one possible explanation for this quirk: the EOS computer program calculates a point on the saturation (or constant % volume line), by starting with the previously calculated point, increasing the mole % CO_2 by a small increment, and calculating the pressure iteratively until the equilibrium conditions are satisfied. When a mole % CO_2 addition places the mixture slightly out of the L_1-V region and into the L_1-L_2 region, the equation of state may still find a metastable, L_1-V equilibrium state, which will continue the line with the same trend. However, with additional increases in the mole % CO_2, the metastable state no longer exists and the equation of state will find the stable, L_1-L_2 equilibrium state. When this occurs, the pressure of the mixture will drop since a more stable equilibrium state has been found, and the calculated phase diagram line will exhibit a sharp bend. The prediction of false phase-equilibrium solutions using an equation of state is also explained by Baker *et al.* [3]. It is probable, therefore, that application of an appropriate technique for the three-phase flash [50] would produce the experimentally observed three-phase region at the appropriate range of compositions and pressures.

The above results show that the initialization scheme presented in this section can be used to predict the phase behavior of a CO_2/crude oil mixture. Slight adjustment of δ_{12} between CO_2 and the heaviest pseudocomponent can improve the agreement to experimental results.

Similar agreement was also observed for mixtures of CO_2 with Means stock tank oil at 105 and 120°F.

2.1.4 Solubility in Dense CO_2

In addition to CO_2 enhanced oil recovery applications, SFC and thermodynamic theory can also be used to convert the chromatographic capacity factor of a solute directly into its solubility in CO_2. This idea was described in the work of Bartle *et al.* [4], but they presented a limited amount of results. Here we extend their results.

First, an alternate derivation for the equation that relates the chromatographic capacity factor to solubility is presented, and then, experimentally determined solubilities are compared to published values.

Thermodynamic Development

We begin by rewriting Eq. 2.4 for the mobile CO_2 carrier fluid phase:

$$\bar{G}_1^{\mathrm{m}} = G_1^{\mathrm{o,m}} + RT \ln \gamma_1^{\mathrm{m}} x_1^{\mathrm{m}} \tag{2.32}$$

For an ideal mobile phase solution, $\gamma_1^{\mathrm{m}} = 1$. In this case,

$$\bar{G}_1^{\mathrm{id,m}} = G_1^{\mathrm{o,m}} + RT \ln x_1^{\mathrm{m}} \tag{2.33}$$

Substitution of this equation into Eq. 2.13 yields

$$\ln\left(k_1' \frac{V^{\mathrm{s}}}{V^{\mathrm{m}}} \frac{V^{\mathrm{t,m}}}{V^{\mathrm{t,s}}}\right) = \frac{1}{RT}(\bar{G}_1^{\mathrm{id,m}} - RT \ln x_1^{\mathrm{m}} - G_1^{\mathrm{o,s}}) \tag{2.34}$$

After some rearrangement, this equation becomes

$$x_1^{\mathrm{m}} = \frac{V_2}{k_1'}\left\{\frac{V^{\mathrm{t,s}}}{V^{\mathrm{s}} V^{\mathrm{t,m}}} \exp\left[\frac{1}{RT}(\bar{G}_1^{\mathrm{id,m}} - G_1^{\mathrm{o,s}})\right]\right\} \tag{2.35}$$

If the solute-rich phase remains in the pure solid state, then the expression in braces is approximately constant with respect to pressure. If we make this assumption, then this equation becomes [4]

$$x_1^{\mathrm{m}} = \frac{V_2}{k_1'} C(T) \tag{2.36}$$

where C is a constant that is a function of temperature and the identity of solute. This equation can also be written as

$$x_1^m = \frac{C(T)}{k_1' \rho_2} \tag{2.37}$$

where ρ_2 is the density of the CO_2 and $C(T)$, therefore, has different units from the $C(T)$ of Eq. 2.36.

Eq. 2.37 can be used to determine the solubility of a solute in CO_2 (x_1^m). The capacity factor of the solute (k_1') is determined using SFC, and the density of CO_2 (ρ_2) is determined using an EOS. Each term is evaluated at the temperature and pressure at which the solubility value is desired. In order to calculate C, Eq. 2.37 is rearranged to yield

$$C = k_1' x_1^m \rho_2 \tag{2.38}$$

One solubility measurement for the solute at the desired temperature must be be known.

Once the value of C is fixed, the solubility in CO_2 at the same temperature can be determined at any other pressure by simply measuring the capacity factor of the solute at that pressure and using Eq. 2.37 to convert this capacity factor to solubility.

Results and Discussion

The procedure described above will now be used to determine the solubility of naphthalene in CO_2, and the results will be compared to measured values. McHugh and Paulaitis [43] measured the solubility of naphthalene in CO_2 over a range of pressures at four temperatures: 95°, 131°, 141°, and 149°F. These values are given in Tables 2.11–2.14, one table for each of the four temperatures.

Table 2.11 will be used to illustrate the procedure of how SFC capacity factors are converted into solubility values. The first column lists the pressures at which the published solubility measurements are reported. At each of these pressures and at 95°F, an SFC experiment was performed to calculate the capacity factor of naphthalene. The third column gives the density of pure CO_2 at the stated pressure and temperature.

The next step is to calculate C using Eq. 2.38 and one of the published solubility measurements, the "match point," indicated in Table 2.11 as the row without a % error. All of the other SFC solubilities are calculated using Eq. 2.37. These SFC-derived solubilities are listed in the fourth column and compared to the measured solubilities.

The solubility results of Tables 2.11–2.14 are also presented in Fig. 2.9. At 95° and 131°F, SFC results agree well with the measured solubilities of naphthalene in CO_2. The errors are within ±10% except for the 95°F case where the solubilities approach zero at low pressures. Also, as the pressure difference between the match point and another solubility measurement gets larger, so does the error, in general.

However, at 140°F the agreement between the SFC results and the data of McHugh and Paulaitis is poor at pressures below the match point. Also, the errors at 149°F are large. This behavior can be explained by noting that the upper critical end point for the CO_2/naphthalene binary system is about 145°F and 3500 psi [43]. The upper critical end point exists for highly asymmetric binary mixtures and is the lowest temperature at which a solute-rich liquid phase may form (Fig. 2.10). As the CO_2/naphthalene mixture temperature approaches the upper critical point end point temperature, the solute-rich phase can no longer be approximated by a pure solid solute, which invalidates one of the assumptions made in the thermodynamic development. Thus, the proximity of the CO_2/naphthalene system to the upper critical end point explains why the SFC-determined solubilities are so different from the measured results at the higher temperatures.

Table 2.11: Solubility of naphthalene in CO_2 (x_1^m) at 95°F. Comparison of SFC and measured [43] results. $C = 0.0144$ g/ml.

Pressure (psia)	k_1'	ρ_2 (g/ml)	x_1^m (mole fraction) SFC	Published	% error
1260	3.989	0.628	0.00577	0.00750	-23.1
1424	2.967	0.703	0.00692	0.00975	-29.0
1545	2.008	0.733	0.00982	0.01066	-7.9
1930	1.449	0.791	0.01261	0.01410	-10.6
2452	1.104	0.837	0.01563	0.01605	-2.6
2894	0.976	0.866	0.01709	0.01709	
3226	0.894	0.883	0.01829	0.01830	-0.1
3517	0.837	0.897	0.01923	0.01908	0.8
3704	0.808	0.905	0.01976	0.01922	2.8

Table 2.12: Solubility of naphthalene in CO_2 (x_1^m) at 131°F. Comparison of SFC and measured [43] results. $C = 0.0404$ g/ml.

Pressure (psia)	k_1'	ρ_2 (g/ml)	x_1^m (mole fraction) SFC	Published	% error
1933	3.607	0.586	0.01912	0.02114	-9.5
2084	2.683	0.630	0.02390	0.02544	-6.1
2330	1.958	0.681	0.03030	0.03053	-0.8
2490	1.726	0.706	0.03316	0.03387	-2.1
2537	1.616	0.713	0.03509	0.03473	1.0
2750	1.393	0.739	0.03928	0.03928	
3051	1.177	0.768	0.04471	0.04224	5.8
3242	1.100	0.784	0.04689	0.04366	7.4
3449	1.008	0.799	0.05018	0.04586	9.4
3649	0.939	0.812	0.05297	0.04969	6.6
4174	0.830	0.842	0.05786	0.05382	7.5

Table 2.13: Solubility of naphthalene in CO_2 (x_1^m) at 140°F. Comparison of SFC and measured [43] results. $C = 0.0684$ g/ml.

Pressure		ρ_2	x_1^m (mole fraction)		
(psia)	k_1'	(g/ml)	SFC	Published	% error
1942	5.261	0.528	0.02461	0.01516	62.
2212	2.857	0.612	0.03914	0.02589	51.
2383	2.198	0.648	0.04799	0.03401	41.
2547	1.821	0.677	0.05551	0.04296	29.
2665	1.715	0.694	0.05746	0.04436	29.
2794	1.511	0.711	0.06370	0.05386	18.
2959	1.348	0.729	0.06956	0.05903	18.
2989	1.334	0.733	0.07000	0.06259	12.
3148	1.209	0.748	0.07559	0.06963	8.6
3154	1.223	0.749	0.07466	0.06990	6.8
3286	1.165	0.760	0.07720	0.07720	
3364	1.121	0.767	0.07960	0.07721	3.1
3422	1.079	0.771	0.08214	0.08306	-1.1
3599	1.024	0.785	0.08511	0.09064	-6.1
3699	0.994	0.792	0.08694	0.09204	-5.5
3739	0.983	0.794	0.08763	0.09583	-8.6
3964	0.939	0.808	0.09008	0.09756	-7.7
4227	0.882	0.823	0.09421	0.09802	-3.9

Table 2.14: Solubility of naphthalene in CO_2 (x_1^m) at 149°F. Comparison of SFC and measured [43] results. $C = 0.0583$ g/ml.

Pressure		ρ_2	x_1^m (mole fraction)		
(psia)	k_1'	(g/ml)	SFC	Published	% error
2202	3.579	0.561	0.02903	0.02427	19.6
2490	2.515	0.628	0.03691	0.03765	-2.0
2687	1.871	0.661	0.04707	0.04428	6.3
2790	1.717	0.676	0.05015	0.05015	
3089	1.400	0.713	0.05837	0.06440	-9.4
3264	1.272	0.731	0.06265	0.07309	-14.3
3369	1.185	0.741	0.06637	0.07902	-16.0
3476	1.139	0.750	0.06822	0.3206	-78.7
3714	1.035	0.768	0.07327	0.3237	-77.4
3989	0.960	0.787	0.07710	0.2999	-74.3

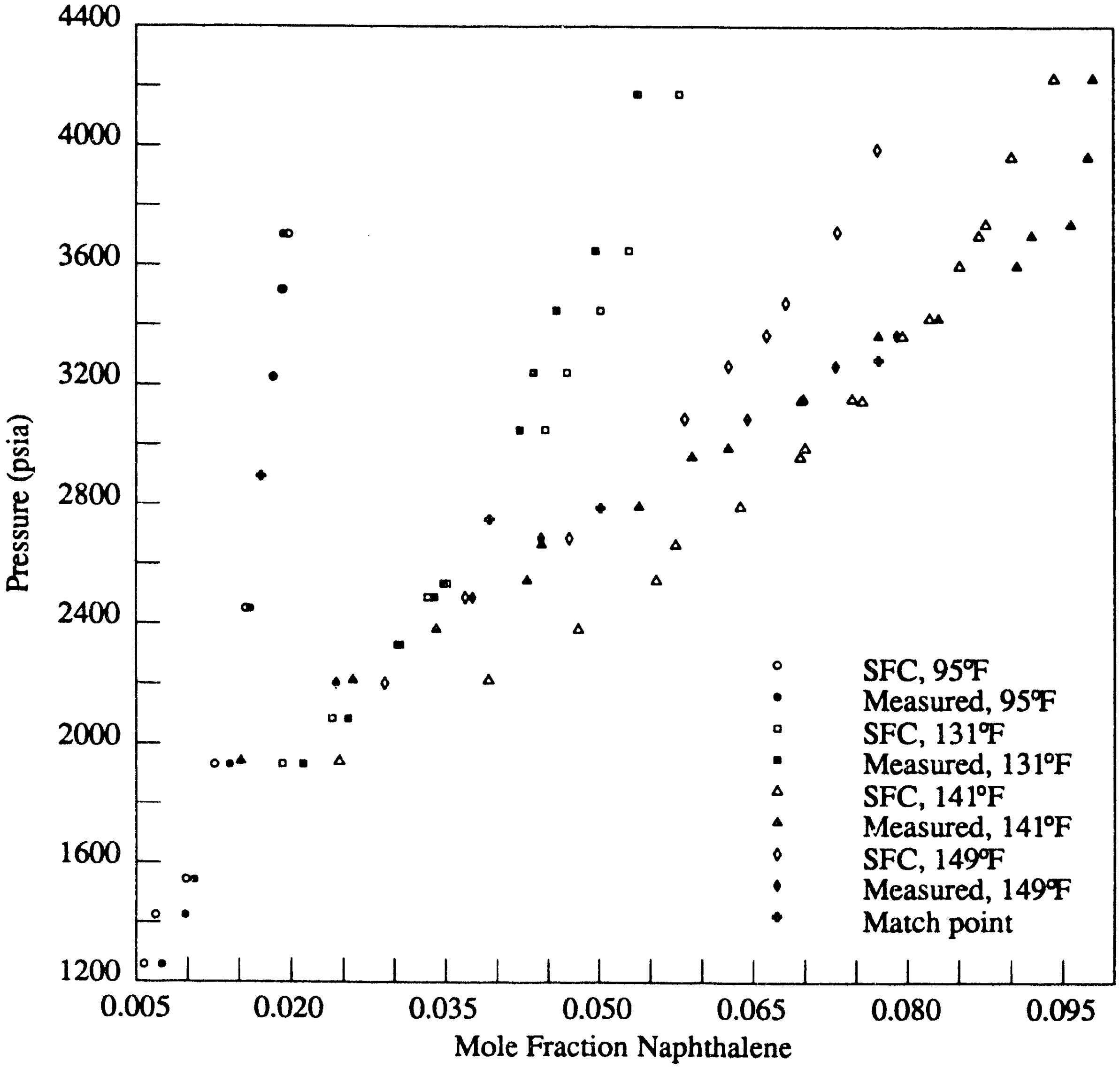

Figure 2.9: Solubility of naphthalene in CO_2. Comparison of SFC and measured [43] results.

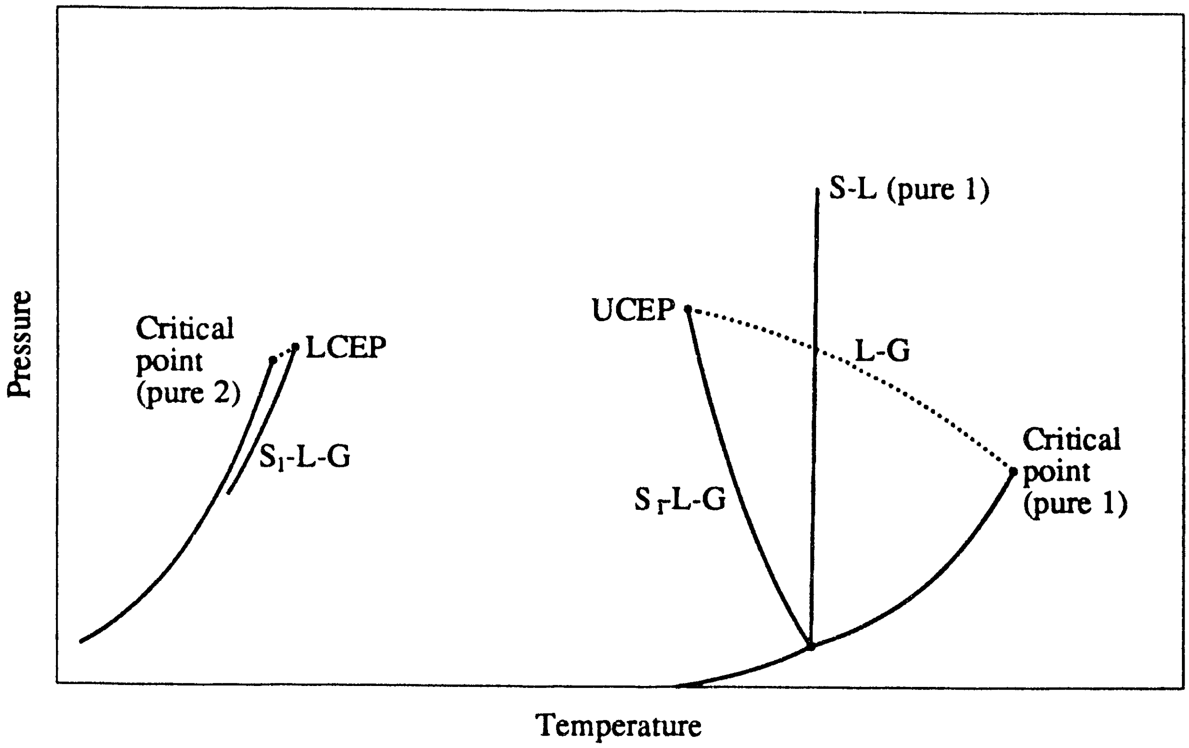

Figure 2.10: Pressure-temperature diagram for a highly asymmetric binary mixture indicating the upper critical end point (UCEP) [43].

Also note that the solubility of a solute becomes quite sensitive to changes in pressure and temperature in the region of the upper critical end point. Table 2.14 shows, for example, that the measured solubility of naphthalene increases considerably at about 3400 psi.

This SFC method of determining the solubility of solids in dense CO_2 has also been applied to biphenyl and phenanthrene with similar results and limitations.

2.1.5 Conclusions

1. A method for determining binary interaction parameters of n-alkanes using SFC has been demonstrated.

2. SFC is useful for characterizing crude oils because components that elute together also partition into CO_2 together. A characterization scheme is proposed and tested for mixtures of Means stock tank oil and CO_2.

3. SFC can also be used to measure solubility of individual hydrocarbons in dense CO_2 provided that the solubility at one pressure is known.

2.2 GC/MS Analysis of Crude Oils and CO_2/Crude Oil Phase Compositions

Karen D. Hagedorn

Predictions of miscible flood phase behavior with an equation of state (EOS) require a knowledge of an oil's composition and of certain physical properties associated with the compositional description, specifically critical properties and acentric factors. Typically, oil compositional analyses are obtained by true boiling point distillation or, more commonly, by simulated distillation (SIMDIS) using a chromatographic technique (Section 2.1). While these techniques give a quantitative analysis of the distribution of hydrocarbons on a size basis, they do not yield any information on the type of compounds present. Therefore, critical properties must be assigned to a grouping of compounds ("cuts") based on standard correlations. These cuts are generally selected based on the assumption that components that elute together from a chromatographic column behave similarly with regard to the process of interest, in this case extraction by CO_2. Exactly that assumption was used in Section 2.1 to obtain carbon number cuts, for example. The aims of this work are to determine the effect of molecular size and structure on the extractability of components in a crude oil by CO_2, and to examine how the overall compositional description of the oil affects phase behavior, specifically slim tube displacement performance. The technique employed for these analyses was gas chromatography/mass spectrometry (GC/MS).

2.2.1 Experimental Equipment and Procedures

The GC/MS equipment and operating conditions were described previously [52], as were the data analysis procedures for both phase samples and whole oils. Phase samples for the partitioning data were obtained from the PVT system described previously [71].

2.2.2 Results of Phase Sample Analyses

Partition coefficients were calculated for approximately 250 components in a Means crude oil/CO_2 system at 3000 psia, 105° F, and 85 mol percent CO_2. Partition coefficient, or K-value, is defined here as the weight fraction of a component in the upper phase divided by its weight fraction in the lower phase. Fig. 2.11 shows these K-values versus elution time from the GC. (It was shown in a previous report [52] that K-values correlate much better with elution time than with carbon number.) While the correlation is reasonably good, there are several classes of compounds that show significant deviations. The most significant of these are the two and three ring aromatics. Two ring aromatics in Fig. 2.11 are depicted by the spade symbol. They consistently fall below the curve defined by normal alkanes (circle symbols). While only one three ring aromatic was present in a substantial quantity, its K-value also falls well below the general trend of the data. This indicates that the "lumping" assumption that components eluting together from the GC also exhibit similar partitioning behavior may not necessarily be correct. Of course, if these components are not present in significant quantities, which is the case for many oils, then the assumption is acceptable. There are oils, however, that have a significant concentration of multi-ring aromatics for which the lumping procedure may have to be evaluated further. In addition, the multi-ring aromatics have significantly different properties (molecular weight, critical properties) from the alkanes they elute with. Their presence can be important in the assignment of cut properties for prediction purposes, as will be shown later. Finally, in terms of phase behavior, the presence of a significant quantity of multi-ring aromatics, which have been shown to be extracted less efficiently than similar sized normal alkanes, may have an effect on the phase behavior of an oil with CO_2, for example, low slim tube recoveries and/or a high MMP.

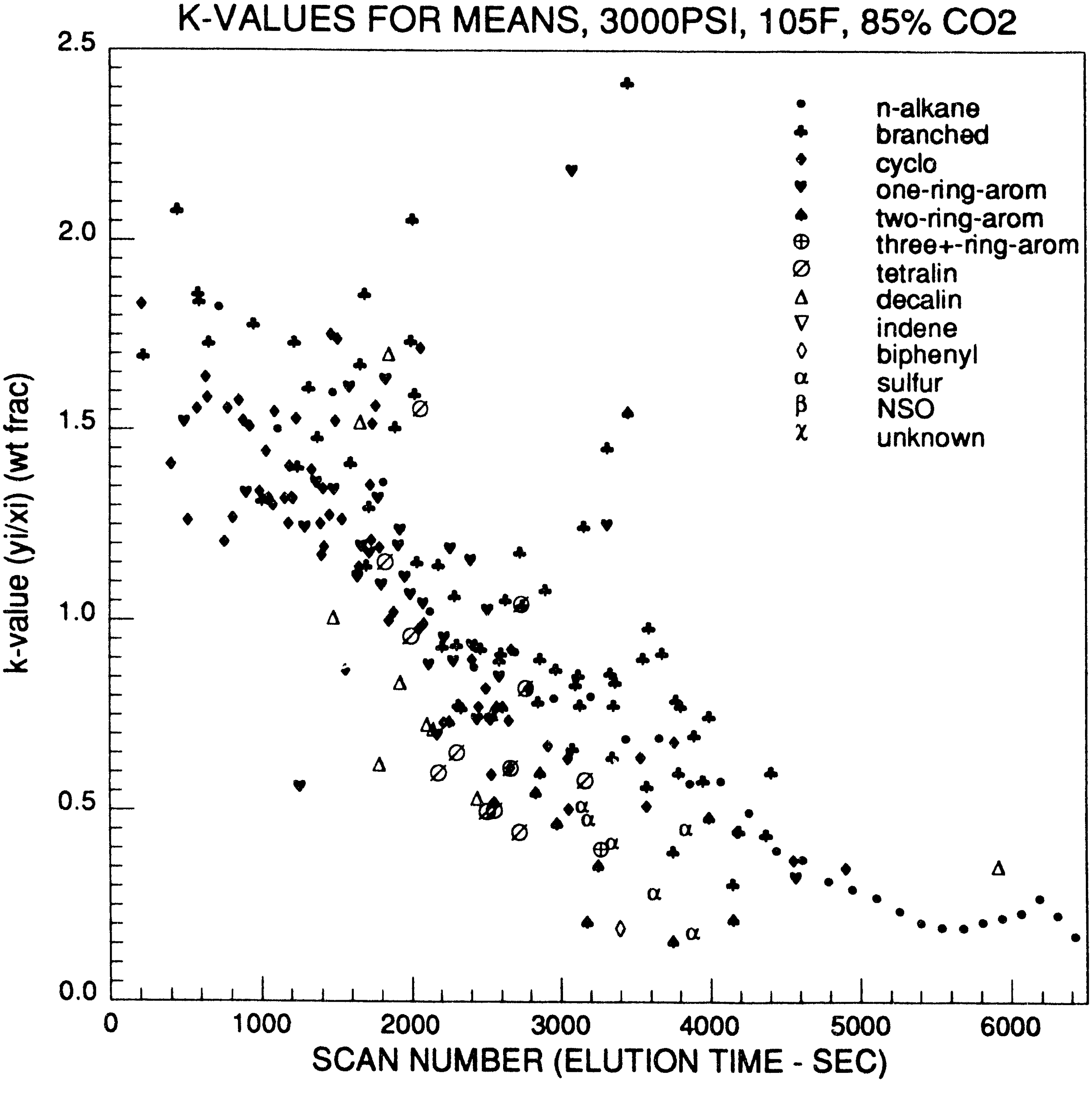

Figure 2.11: K-values for components of Means crude oil.

To show the effects of aromaticity on phase behavior, flash calculations were performed at 3000 psia and 125° F for two systems of 80% CO_2 and 20% synthetic oil. The synthetic oil for the alkane case consisted of 10% methane, 40% n-decane (C_{10}), 30% n-pentadecane (C_{15}), and 20% n-eicosane (C_{20}). For the aromatic oil, naphthalene ($C_{10}H_8$), phenanthrene ($C_{14}H_{10}$), and pyrene ($C_{16}H_{10}$) were substituted in equal molar amounts for the three normal alkanes. The methane concentration was the same in both oils. K-values for the three "heavy" components are plotted versus their true carbon number in Fig. 2.12. It is clearly shown that the K-values for the aromatic components are lower than those for the corresponding n-alkanes, even though the normal alkanes are actually heavier. It will be shown in Chapter 3 that the development of miscibility in 1-D systems is a function of the K-values of the intermediate components in the oil. Therefore, it appears that the presence of substantial quantities of multi-ring aromatic compounds in the oil will be detrimental to the development of miscibility.

2.2.3 Whole Oil Analyses

Two crude oils for which slim tube data were available were analyzed by GC/MS. The data reported here include only the carbon number range $C_5 - C_{35}$ (the limit of the GC operating conditions) and are based on weight percent. The crude oils are characterized by different carbon number distributions and have very different slim tube results. It was hoped that the partitioning data might explain the results from the slim tube displacements. Fig. 2.13 shows the chemical type distribution for Means crude oil, the oil that was used in the partitioning experiments. These data were compared to other Permian Basin oils in last year's report [52]. The composition of the Means oil was found to be quite similar to them, except that Means has a slightly larger fraction of normal alkanes in the intermediate range (C_{12} to C_{30}). Overall, this oil is predominantly paraffinic/naphthenic. Multi-ring aromatic compounds are present only in small quantities. Fig. 2.14 shows how the different chemical types are distributed with respect to carbon number. These carbon numbers are true carbon numbers obtained from mass spectra and are not related to elution time. Thus, this plot is not analogous to the GC trace. The peak carbon number for Means is C_9, and the distribution is rather broad through C_{20}, after which it tails off (some of this tailing is a function of the analytical technique). Note that cycloalkanes and single ring aromatics dominate the light range (C_5 to C_{12}), while branched and normal alkanes dominate the remainder. The peak depicted at C_{40} actually represents those compounds for which the carbon number is undetermined. The small amount of multi-ring aromatics lies in the C_{11} to C_{13} range.

Fig. 2.15 shows the slim tube recoveries at 1.2 PV injected for Means oil displaced by CO_2 at a temperature of 105° F. The slim tube behavior for Means is typical of West Texas oils. Recovery increases sharply with pressure until the curve "breaks over" at some pressure above which recovery increases much more slowly. This breakover point is commonly accepted as the MMP.

A second oil that was analyzed shows considerably different compositional and slim tube behavior from Means. Kubiki is a biodegraded Pacific Rim oil with a reservoir temperature of 125° F. Fig. 2.16 shows the chemical type distribution for Kubiki. Biodegradation is evidenced by the depletion of normal alkanes and some branched alkanes. However, the most notable property of this oil is the considerable amount of multi-ring aromatics present. Fig. 2.17 shows the carbon number distribution by type for Kubiki. The overall shape of the distribution differs from that of Means in several ways. The distribution is shifted somewhat towards higher carbon numbers, with C_6 and C_7 present in only very small quantities. The Kubiki distribution is also somewhat broader through the C_{11} to C_{21} range, mostly due to the multi-ring aromatic compounds. Kubiki does not tail out past C_{20} like Means, although it is not clear at this time how much the analytical technique affects this portion of the data. Overall, however, the two distributions are not all that different. The slim tube displacement results, however, are very different. Fig. 2.18 shows the slim tube data

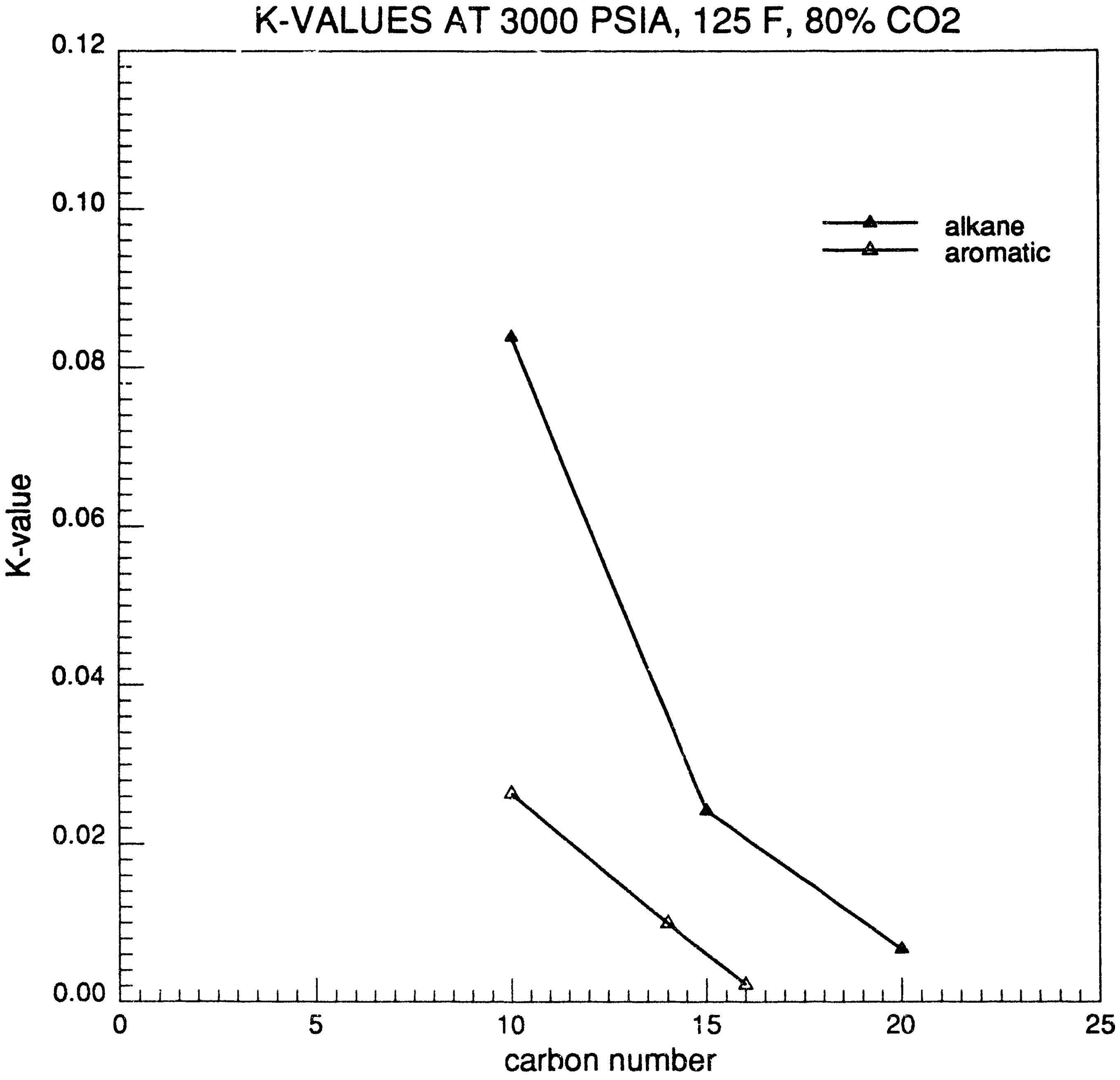

Figure 2.12: K-values for two-phase flash of "synthetic" oil.

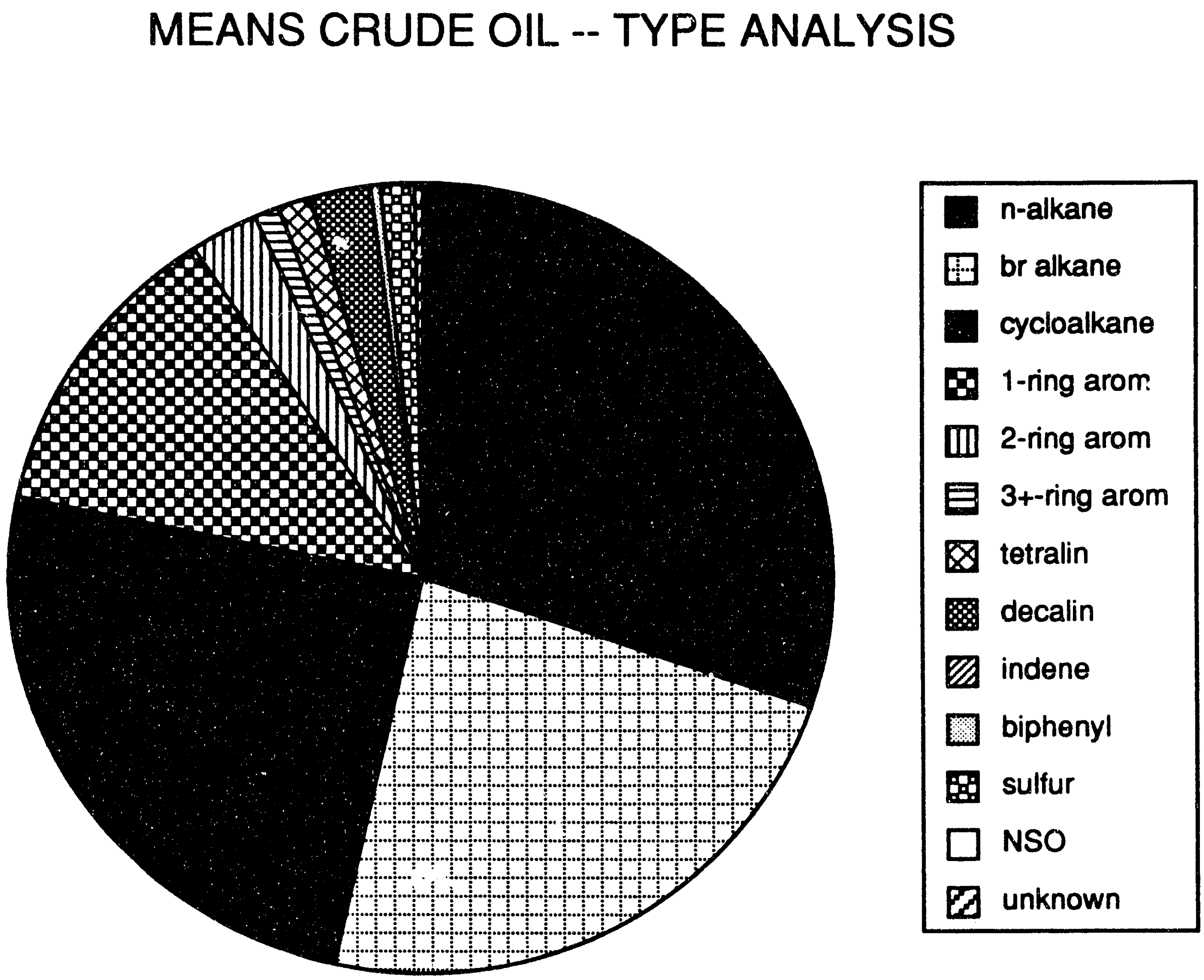

Figure 2.13: Means crude oil chemical type distribution.

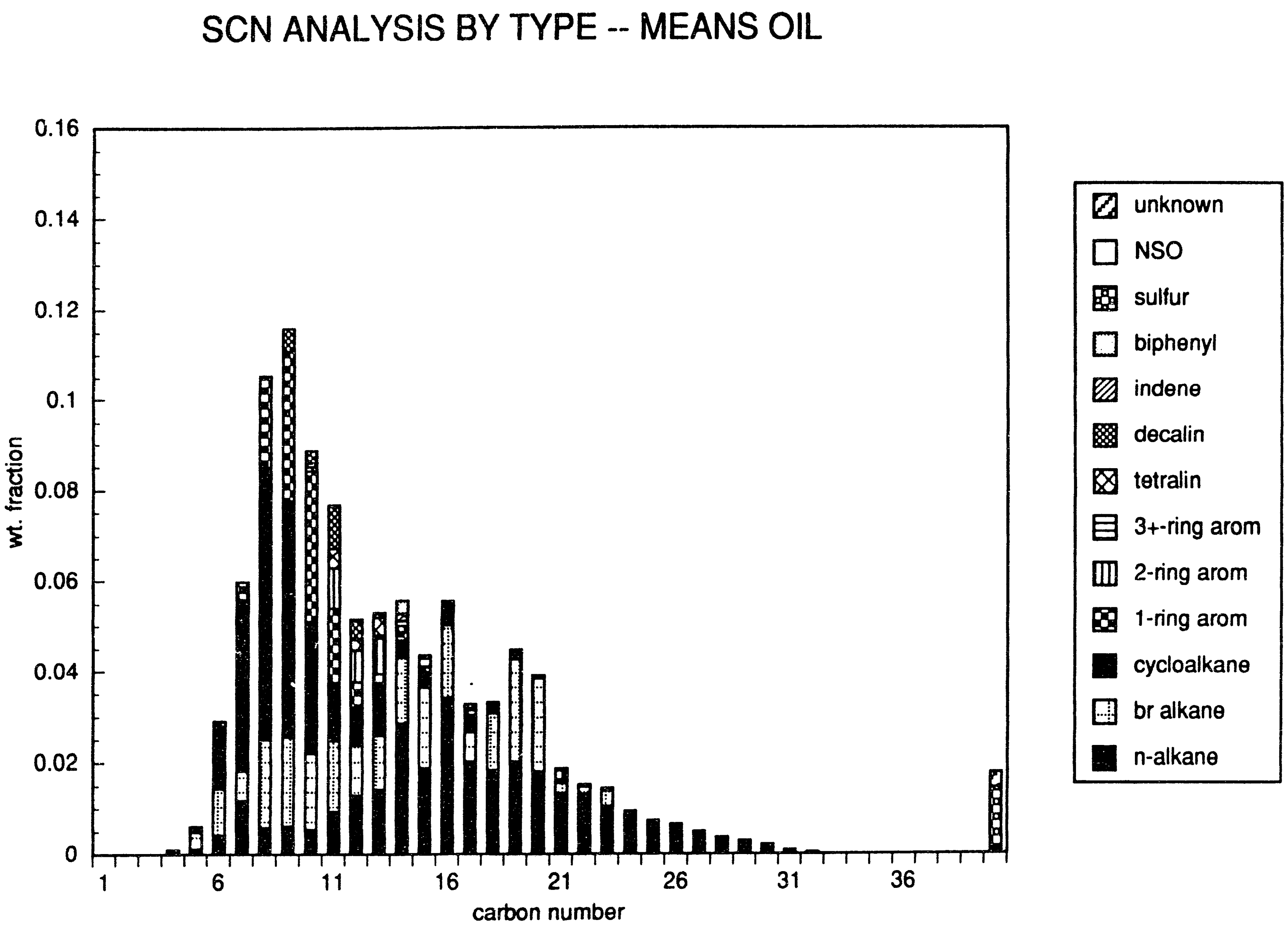

Figure 2.14: Means crude oil SCN analysis by type.

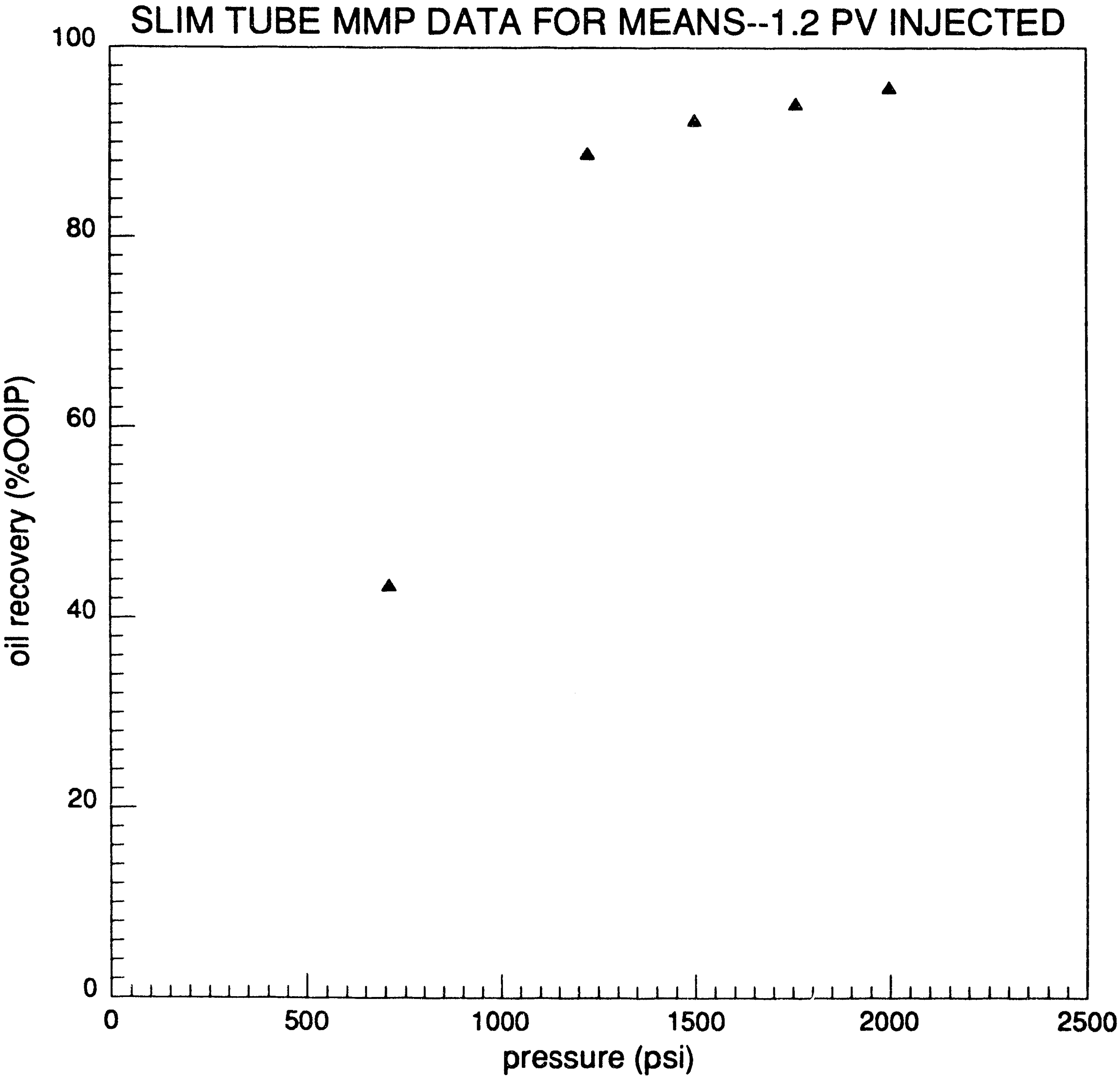

Figure 2.15: Means crude oil slim tube displacement data.

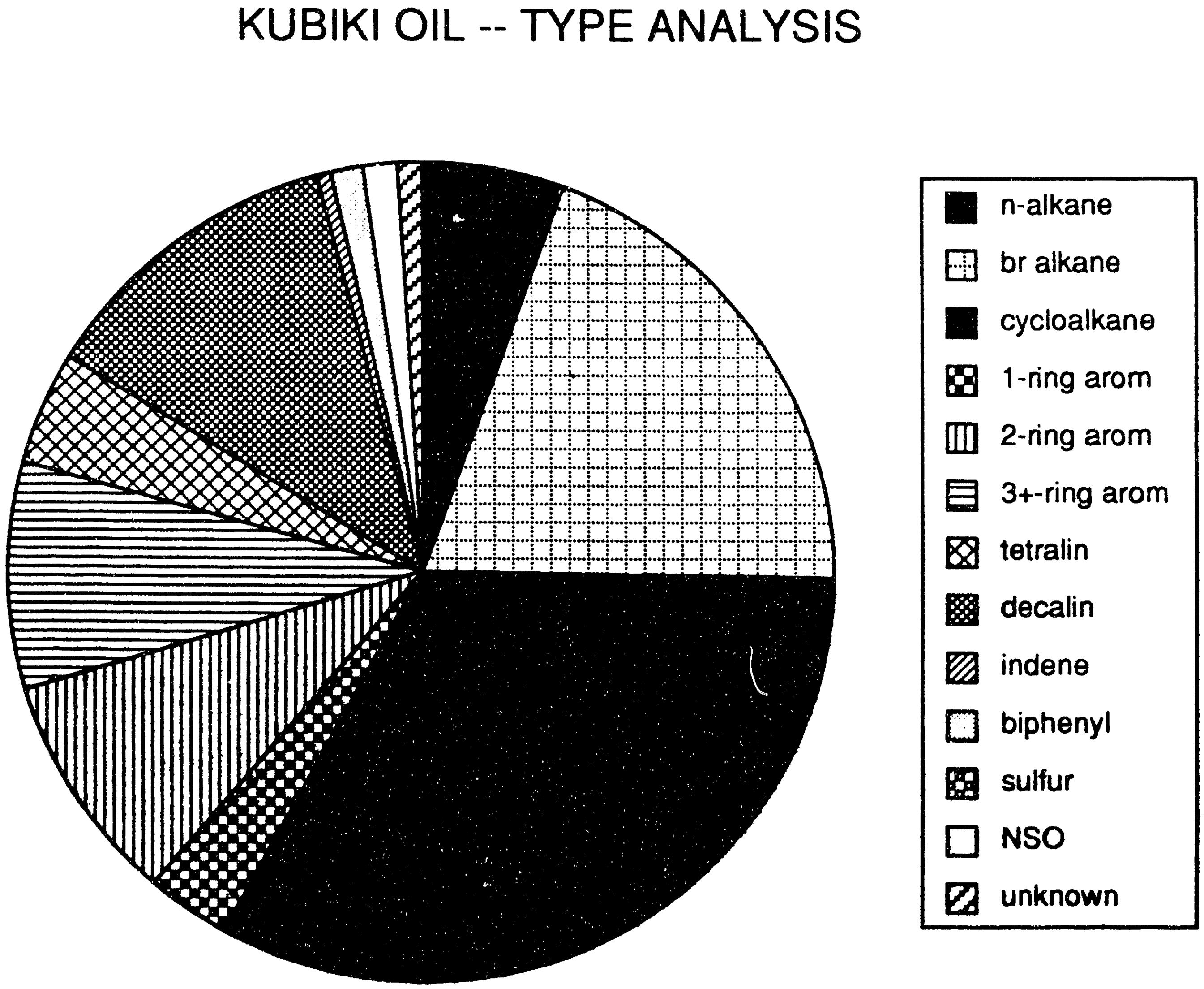

Figure 2.16: Kubiki crude oil chemical type distribution.

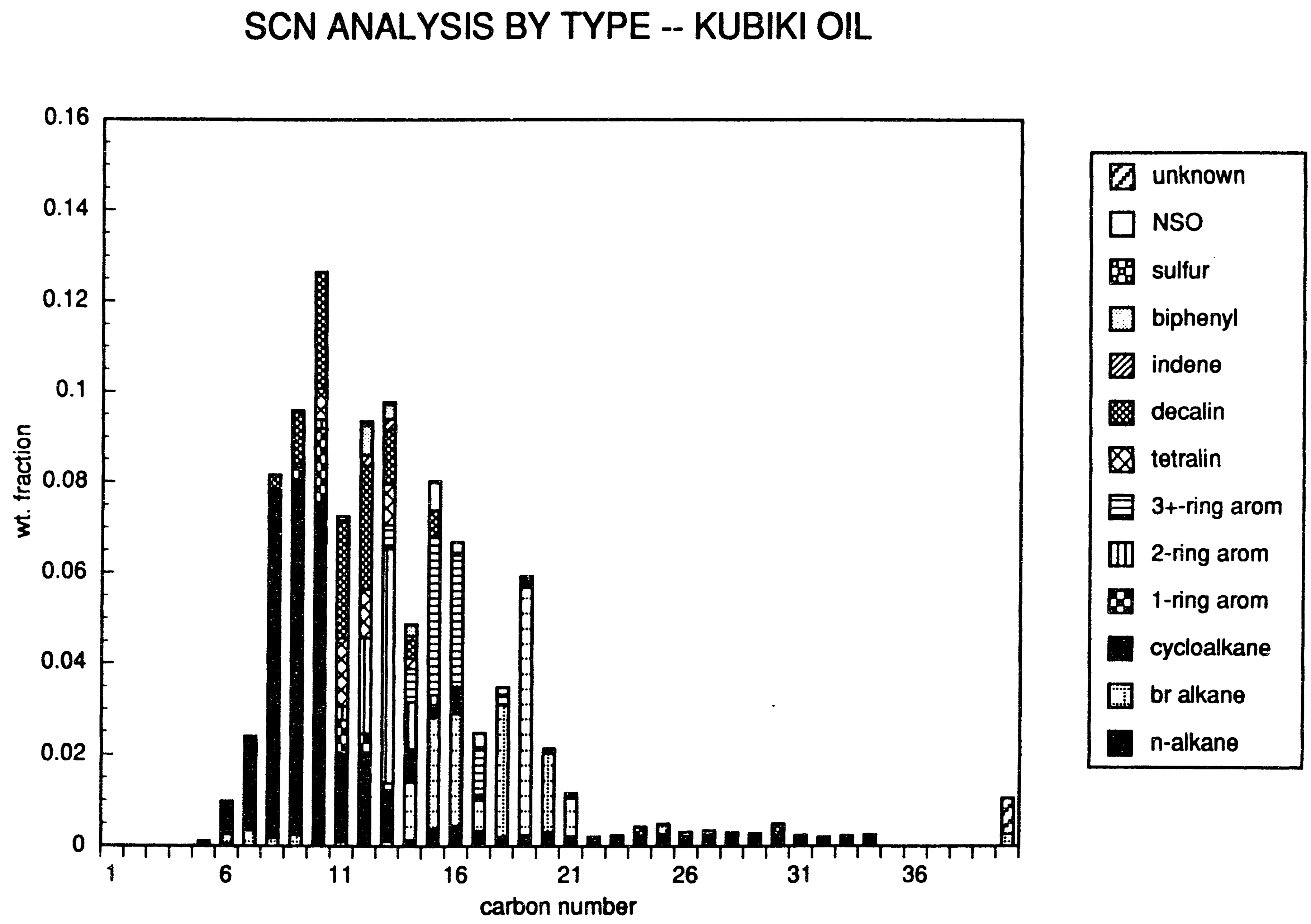

Figure 2.17: Kubiki crude oil SCN analysis by type.

for Kubiki at 125° F. The open triangle indicates a displacement for which a single phase appeared in the outlet sight glass. Clearly, no breakover point was seen in the range of pressures tested. Also, very high pressure was required to achieve the high recoveries (>85%) expected of a miscible displacement. Although it is uncertain whether this behavior is a function of the carbon number distribution or of the chemical type distribution (or both), the extraction data for Means clearly indicate that multi-ring aromatics are extracted less efficiently by CO_2. Therefore, the presence of a significant quantity of these compounds may be detrimental to the development of miscibility in Kubiki.

The critical properties of various cuts defined by SIMDIS are required for prediction purposes. These properties are generally obtained from standard correlations [32]. For oils such as Kubiki, however, these correlations may not necessarily be appropriate due to the significant deviation of aromatic critical properties from those of the paraffinic/naphthenic components eluting at the same time. While pure component critical temperatures and pressures are not available for most crude oil constituents, the effect of aromatics on cut properties can be seen by looking at cut-averaged molecular weights, which are easily determined from GC/MS data. Fig. 2.19 shows the average molecular weight for a given carbon number cut (defined as everything eluting between two normal alkanes, including the second normal alkane) compared to normal alkane values and the values suggested by Katz and Firoozabadi [32]. The Katz and Firoozabadi values are actually quite close to the normal alkane values, which is appropriate for oils like Means that have a very high percentage of these compounds. The correlation values are not very good, however, for Kubiki.

While it is true that Kubiki is an unusual case, the partitioning data and the whole oil analysis of Kubiki clearly show that for some oils, specifically those with a significant multi-ring aromatic fraction, the standard correlations for critical properties and even for MMP may not be appropriate. Knowledge of an oil's source and maturity (which affect aromatic content) can provide an indication that a more detailed analysis is required.

2.2.4 Conclusions

1. Multi-ring aromatic compounds are extracted less efficiently by CO_2 than the components they elute with.

2. The presence of a significant quantity of multi-ring aromatics may have a detrimental effect on the development of miscibility.

3. For oils with a significant aromatic content, standard critical property correlations, and probably MMP correlations, may not be appropriate.

2.3 Summary

The thermodynamic theory and experimental results presented in Section 2.1 show that supercritical fluid chromatography data can be tied to the characterization of a crude oil for calculations of phase equilibria with an equation of state. Thus, the approach presented is a step in the development of more advanced analytical techniques for miscible flood fluid systems. The goal of this work is to develop characterization methods that are much less time consuming than traditional PVT experiments. While many avenues remain to be investigated, the results obtained so far show that it is possible to add additional experimental constraints to a fluid characterization with little more effort than is required to obtain compositional information about the oil in the first place. Because that information is required anyway, the approach described is a significant improvement over existing techniques.

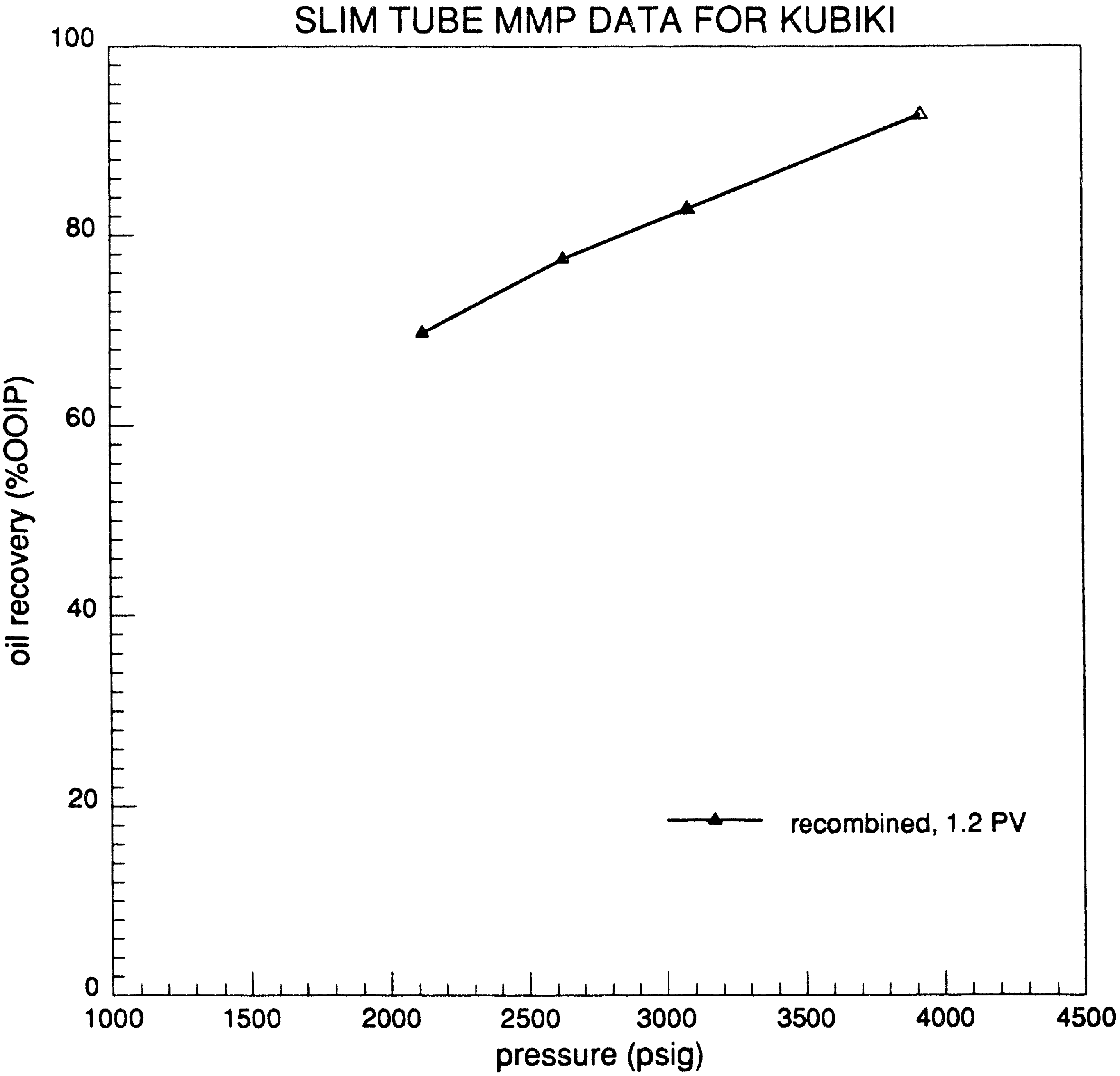

Figure 2.18: Kubiki crude oil slim tube displacement data.

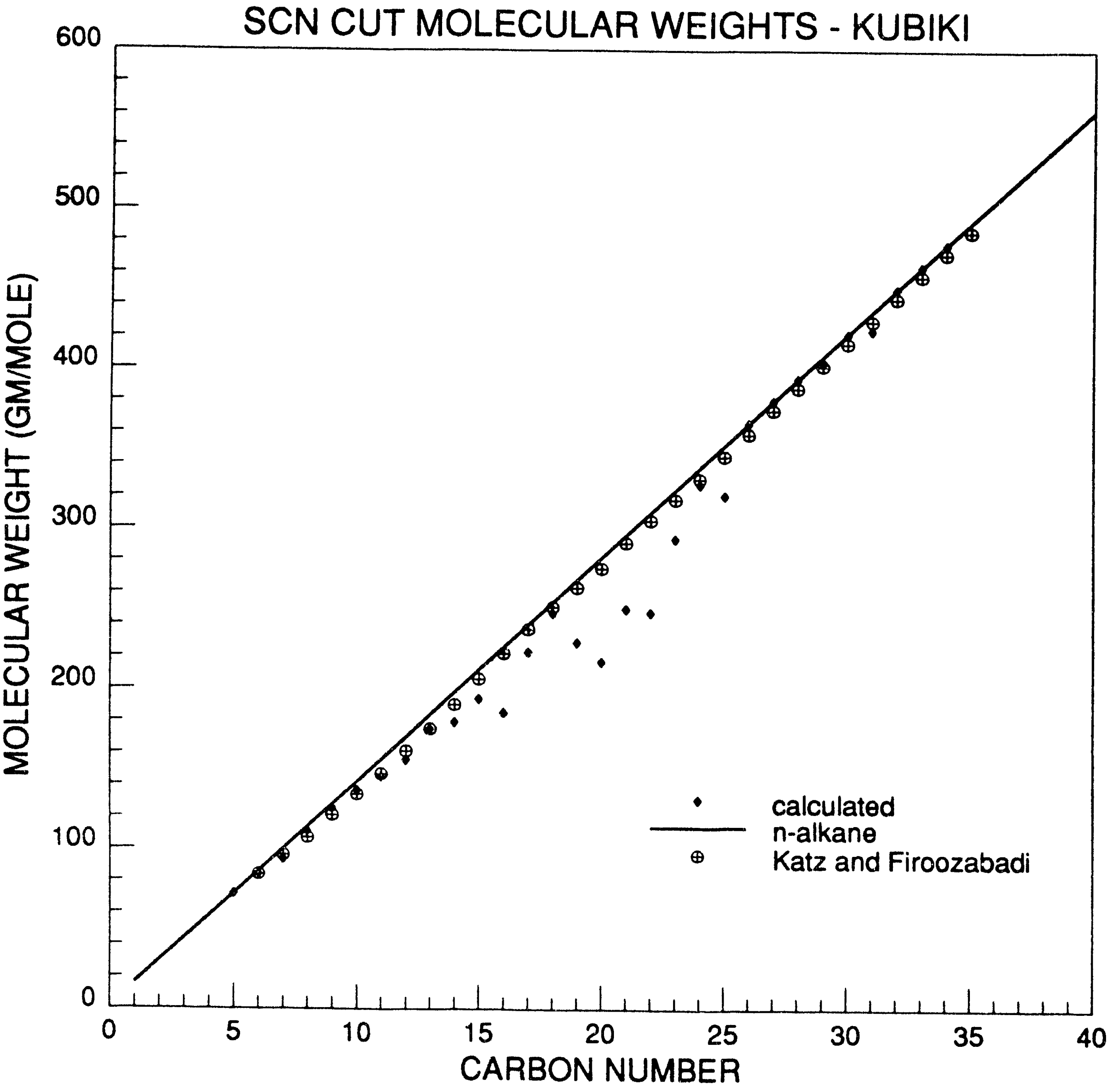

Figure 2.19: Single carbon number molecular weights for Kubiki.

The detailed compositional data obtained in the GC/MS analyses of crude oils and phases also demonstrate how information about the distribution of molecular types can be used to explain anomalous slim tube displacement behavior. The phase composition data show clearly that multiring aromatics are extracted less efficiently by dense CO_2 than are alkanes, whether branched or normal. The presence of such compounds in an oil results from the geochemistry of the origins of the oil and, of course, from the subsequent thermal and migratory history of the oil. The results presented suggest that geochemical information about sources and alteration of the oil, which is frequently obtained as part of the exploration process, can be used to advantage to determine when a detailed GC/MS analysis of the oil is needed.

3. Development of Miscibility in Four-Component Gas Drives

In this chapter we examine how phase behavior interacts with two-phase flow in one dimension. Because the flow is one-dimensional, effects of viscous fingering, heterogeneity and crossflow, all inherently two- and three-dimensional features, are necessarily absent. We also neglect dispersive mixing. In effect, we assume that there is sufficient diffusion to mix fluids at the pore level so that any phases present are in chemical equilibrium, but the level of diffusion is too low to cause growth of a significant dispersive transition zone during flow. Such an assumption only applies when the porous medium has minimal local variation in permeability, a situation that is approximated well in slim tube displacements, for example.

Under those assumptions, a minimum miscibility pressure (MMP) can be defined unambiguously. The traditional analysis of development of miscibility is based on ternary systems [61, 26, 44]. It is now well established that in ternary systems, multicontact miscibility can develop in only two ways. If the initial composition of the oil eventually lies on the extension of a critical tie line (a tie line tangent to the bimodal curve at the plait point) as the pressure is increased, the displacement is known as a vaporizing gas drive. If, on the other hand, the composition of the injected fluid is the one that lies on a critical tie-line extension as the pressure is increased or the composition of the injected mixture is changed, then the displacement is known as a condensing gas drive.

In this chapter we show that the ternary arguments used to describe development of miscibility do not tell the whole story if more than three components are present. Several investigators have argued that real miscible flood systems show important behavior that cannot be represented adequately on ternary diagrams. For example, Zick [87] and Stalkup [70] used composition simulations to show that multicomponent displacements have characteristics of both condensing and vaporizing gas drives. Jensen and Michelsen [28] used four-component systems to demonstrate that direct application of the critical tie-line criterion from ternary systems lead to incorrect estimates of the minimum miscibility pressure (MMP) in some cases. Stalkup [70] argued that quaternary phase diagrams were required in the analysis of displacements by nitrogen and methane (CH_4). However, none of the previous investigators has developed a rigorous extension of the three-component tie-line criterion for miscibility to systems with more than three components.

This work extends significantly the solution technique described by Monroe et al. [45] for one-dimensional, dispersion-free flow of four-component mixtures. Using the method of characteristics (MOC), analytical solutions can be found by geometric constructions not much more difficult than those performed in the Buckley-Leverett solution for displacement of oil by water. A more general tie-line extension criterion for development of miscibility in quaternary displacements is presented.

To illustrate the range of behavior possible in four-component systems, we consider several model systems. We begin in Section 3.1 with an analysis displacement of mixtures of methane (CH_4), butane (C_4), and decane (C_{10}) by CO_2. That analysis demonstrates a way that miscibility can develop that has not been previously identified. In Section 3.2, we examine a more general case of a four-component oil displaced by a mixture of CO_2 and solvent. In Sections 3.1 and 3.2 we simplify the analysis somewhat by assuming that there is no change in volume as components transfer between phases. We return to the model $CH_4/C_4/C_{10}$ system in Section 3.3, where we consider displacements by CO_2/C_4 mixtures and N_2. In Section 3.3 we also relax the assumption of no volume change as components transfer between phases, and we demonstrate the effects of numerical dispersion in comparisons of the analytical solutions with finite difference numerical solutions.

The analytical solutions presented here illustrate the variety of compositional behavior that can occur in four-component systems, and they provide considerable guidance about systems with more components. Hence, they represent a significant extension of the previously existing theory of the development of miscibility.

3.1 Displacement of $CH_4/C_4/C_{10}$ Mixtures by CO_2

Franklin M. Orr Jr., Russell T. Johns, and Birol Dindoruk

3.1.1 Mathematical Model

Consider one-dimensional, dispersion-free flow of four-component mixtures under the same assumptions stated by Monroe et al.[45] In this section we assume that components do not change volume as they transfer between phases, though we emphasize that the tie-line extension criteria presented below do not change if that assumption is relaxed.

The resulting material balance equations are

$$\frac{\partial C_i}{\partial t_D} + \frac{\partial F_i}{\partial x_D} = 0, \quad i = 1, \cdots, n_c \tag{3.1}$$

with,

$$C_i = \sum_{j=1}^{n_p} c_{ij} S_j, \quad F_i = \sum_{j=1}^{n_p} c_{ij} f_j, \quad c_{ij} = \frac{x_{ij}}{\rho_i} \Bigg/ \sum_{k=1}^{n_c} \frac{x_{kj}}{\rho_k},$$

where C_i and F_i are the overall volume fraction and fractional flow of component i, S_j is the saturation of phase j, c_{ij} and x_{ij} are the volume and mole fractions of component i in phase j, ρ_i is the density of component i, and x_D and t_D are dimensionless distance and time.

Phase equilibrium calculations were performed with the Peng-Robinson equation of state[60] (PREOS) with critical properties, acentric factors, and binary interaction parameters given in Table 3.1. Component densities used to convert mole fractions to volume fractions are also given in Table 3.1. Phase viscosities were calculated with the Lohrenz-Bray-Clark [40] correlation with values of the critical volumes reported in Table 3.1. Under the assumption of no volume change on mixing, phase densities calculated with the PREOS were not used to calculate phase saturations, but the PREOS densities were used in phase viscosity calculations. Volume translation parameters listed in Table 3.1 were used to improve estimates of phase density for use in those phase viscosity calculations. The fractional flow function was

$$f_g = \frac{S_g^{e_g}/\mu_g}{(1 - S_g - S_{or})^{e_o}/\mu_o + S_g^{e_g}/\mu_g}, \tag{3.2}$$

with $S_{or} = 0.20$, $e_o = 2.0$, and $e_g = 2.0$.

Eqs. 3.1 are a system of first-order hyperbolic equations. The solution is found by calculating the velocity at which each overall composition propagates through the porous medium[26]. Because dispersion is absent, the mixture compositions that form during the displacement lie on a single composition route that connects the initial composition to the injection composition. The problem then is to find the appropriate route for given initial and injection compositions. Potential solution routes or paths are obtained by solving an eigenvalue problem [26]. Path directions are given by eigenvectors and composition propagation rates (wave velocities) by eigenvalues. Tie lines, for

Table 3.1: Component Properties.

Component	M_w	P_c (psia)	T_c (deg F)	V_c (ft^3/mol)	ω	s_i (ft^3/mol)
CO_2	44.01	1071.0	87.90	1.5060	0.2250	0.0600
CH_4	16.04	667.8	-116.63	1.5899	0.0104	-0.0661
$n-C_4$	58.12	550.7	305.65	4.0828	0.2010	-0.0074
C_{10}	142.29	305.7	652.10	9.6610	0.4900	0.1602

Component	ρ_i (mol/ft^3)		δ_{ij}			
	1600 psia	1730 psia	CO_2	CH_4	$n-C_4$	C_{10}
CO_2	0.4237	0.4843	0.0000	0.1000	0.1257	0.0942
CH_4	0.2627	0.2848	0.1000	0.0000	0.0270	0.0420
$n-C_4$	0.5859	0.5886	0.1257	0.0270	0.0000	0.0080
C_{10}	0.3041	0.3045	0.0942	0.0420	0.0080	0.0000

example, are paths, and there are also two additional nontie-line paths through each composition point [26, 45]. The solution route must then be selected from the infinite set of composition paths subject to the additional "velocity constraint" that requires the propagation velocity for compositions within the two-phase region to increase monotonically as the solution route is traced from the injection composition to the initial composition.

The solution route that satisfies those constraints includes shocks (jumps from one composition to another), continuous variations (spreading waves) along a composition path, and zones of constant state, which arise when the solution route switches from one path to another. Shocks occur when it is impossible to satisfy the velocity constraint with continuous variations. A material balance for each component across a shock shows that the wave velocity of the shock is given by

$$\Lambda = \frac{F_i^I - F_i^{II}}{C_i^I - C_i^{II}}. \tag{3.3}$$

where I and II refer to opposite sides of the shock.

Eq. 3.3 can be used to prove that the solution route can enter or leave a two-phase region only via a shock in which the single-phase composition lies on an extension of an equilibrium tie line [26]. That proof establishes that the solution route will avoid the two-phase region if either the injection composition or the initial composition does not lie on any tie-line extension, and it applies to systems with any number of components. In other words, the displacement will be miscible in the multicontact sense.

In ternary systems, a displacement is multicontact miscible (MCM) only if either the initial or injection composition lies on the edge of or outside the region of tie-line extensions. Monroe et al.[45] showed that addition of CH_4 to a C_4/C_{10} mixture induces two-phase flow, but did not investigate how miscibility develops for the live oil. Instead they speculated that strict multicontact miscibility would develop only when that same criterion is met. For four-component systems, however, the three-component tie line extension criterion is too restrictive. Instead, it is possible to achieve miscibility when both the initial and injection compositions fall well within the region of tie-line extensions.

3.1.2 Solution Structure

Consider the displacement of an initial mixture containing 10% CH_4, 20% C_4 and 70% C_{10} by pure CO_2. Fig. 3.1 shows the composition path solution obtained by the method described in detail by Monroe et al.[45] The corresponding composition profiles are shown as solid lines in Fig. 3.2. The positions of compositions in the profiles in Fig. 3.2 are expressed in terms of wave velocity. To convert to actual position, the wave velocity is simply multiplied by the dimensionless time, in pore volumes. Table 3.2 reports the compositions and wave velocities of the points labeled **a**-**f** in Fig. 3.1.

From the initial composition, **a**, there is a shock to composition **b**, which is on the tie line in the $CH_4/C_4/C_{10}$ plane that extends through composition **a**. From point **b**, there is a second shock to point **c** on the $CO_2/C_4/C_{10}$ face. That shock occurs because wave velocities (eigenvalues) increase along the composition paths that connect the $CH_4/C_4/C_{10}$ face to the $CO_2/C_4/C_{10}$ face. Hence continuous variation along this nontie-line path is prohibited by the velocity constraint. Note that the CH_4 concentration increases in the shock from **a** to **b** and then drops to zero in the **b**→**c** shock. Hence all the CH_4 from hydrocarbons left behind the leading **a**→**b** shock appears in a CH_4 bank.

Point **c** lies on a very important tie line, which Monroe et al.[45] called the crossover tie line. Development of miscibility in four-component systems depends on the location of the crossover tie

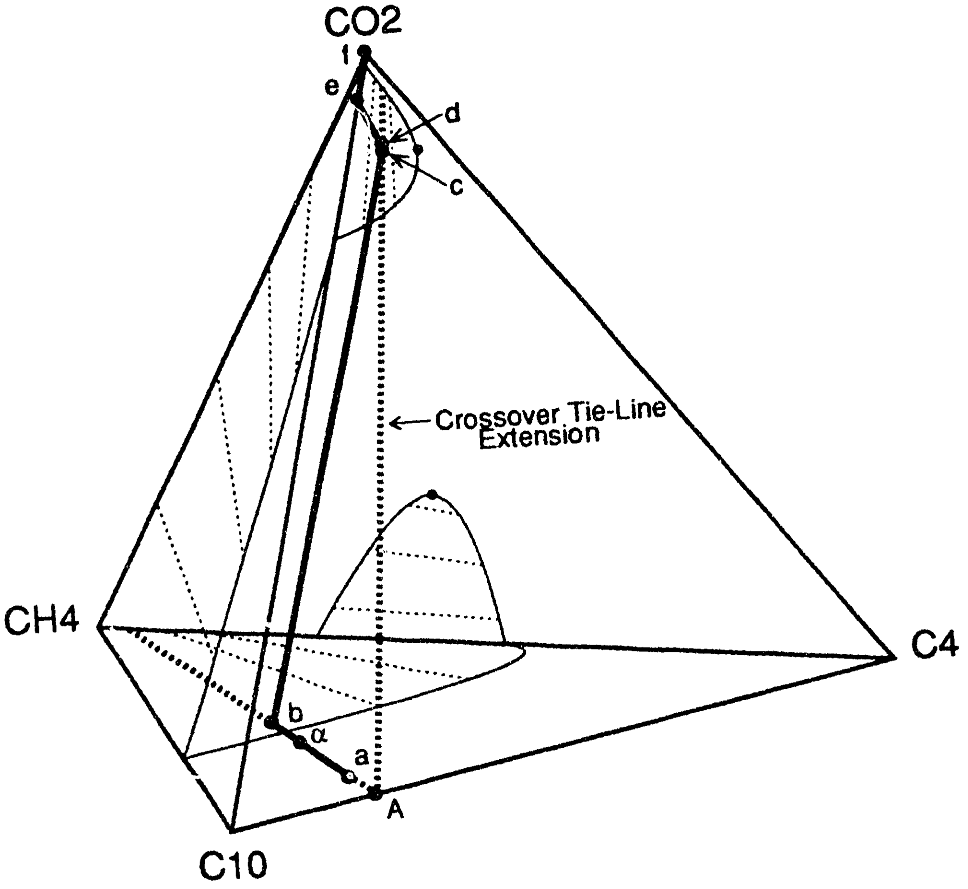

Figure 3.1: Composition route for displacement of a $CH_4/C_4/C_{10}$ mixture by pure CO_2 at 1600 psia, 160° F.

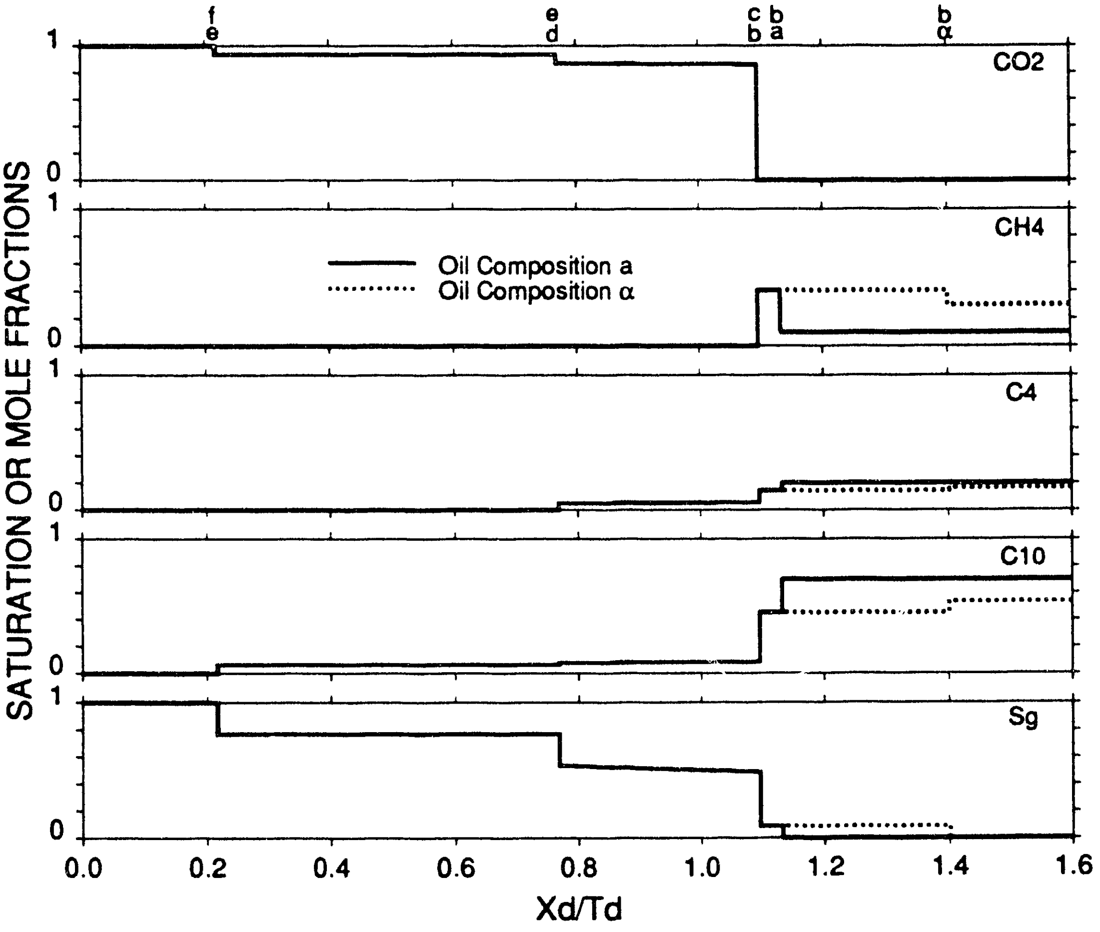

Figure 3.2: Composition profiles for the composition route at 1600 psia, 160° F.

Table 3.2: MOC Solution for the Composition Route at 1600 psia, 160° F.

Composition Label	Composition (Mole Fraction)				Gas Saturation (Vol. Fraction)	Wave Velocity
	CO_2	CH_4	$n-C_4$	C_{10}		
A	0.0000	0.0000	0.2188	0.7812	0.0000	-
a	0.0000	0.1000	0.2000	0.7000	0.0000	1.1308
b	0.0000	0.4046	0.1427	0.4527	0.0899	1.1308-1.0958
c	0.8615	0.0000	0.0531	0.0854	0.4893	1.0958
d	0.8698	0.0000	0.0515	0.0787	0.5379	0.7687
e	0.9376	0.0000	0.0000	0.0624	0.7685	0.7686-0.2166
f	1.0000	0.0000	0.0000	0.0000	1.000	0.2166
Oil Composition α						
α	0.0000	0.3000	0.1624	0.5376	0.0000	1.4013
b	0.0000	0.4046	0.1427	0.4527	0.0899	1.4013-1.0958

line with respect to the critical locus. Thus, a key result is to demonstrate a simple method for determination of the crossover tie line.

When the solution route reaches point **c**, only three components remain, and the composition route from point **c** to the injection composition, point **f** at the pure CO_2 apex, is the same as that described for a ternary vaporizing gas drive. Between **c** and **d** there is a continuous variation along the crossover tie line, the only continuous variation in the solution to this problem. It is the multicomponent equivalent of the region of continuous saturation variation in a Buckley-Leverett problem. At point **d**, the route jumps to point **e** on the injection tie line, and from point **e**, there is a shock to the injection composition. Hence in this example problem, the properties of the solution are largely governed by the behavior of the **a**→**b**, **b**→**c**, **d**→**e**, and **e**→**f** shocks.

Fig. 3.2 shows that the interplay of phase behavior and two-phase flow causes a chromatographic sorting of components present in the original oil into banks and waves in order of their equilibrium K-values. K-values depend on composition, but for the range of compositions investigated, the values were near 1.8 for CH_4, 1.3 for CO_2, 0.4 for C_4, and 0.09 for C_{10}. Hence, all of the CH_4, which has the largest K-value, appears in a leading bank. CO_2, with the next highest K-value, first appears at the shock in which the CH_4 disappears. Hence, in this example, no more than three components are present at any spatial location (Fig. 3.2). Because C_4 has the third highest K-value, hydrocarbons present between **c** and **d** are much richer in C_4 than is the original oil. C_4 then disappears at the **d**→**e** shock. C_{10}, with the lowest K-value, is the last to disappear at the slow-moving, trailing evaporation shock. The velocity of that shock is controlled by the solubility of C_{10} in the injected CO_2. That solubility is low when the C_{10} K-value is low.

3.1.3 Solution Construction

When the crossover tie line is connected to the initial and injection tie lines only by shocks (i.e. if the shocks **b** → **c** and **d** → **e** exist), the solutions illustrated in Figs. 3.1 and 3.2 can be constructed by the following sequence of straightforward calculations:

1. Find the crossover tie line for the given initial and injection compositions.
2. Calculate the composition **c** on the crossover tie line and hence the velocity of the **b**→**c** shock, Λ^{bc}.
3. Find composition **b** on the initial tie line and calculate the velocities of the **a**→**b** shock, Λ^{ab}.
4. Find the composition **d** on the crossover tie line and the composition **e** on the injection tie line and calculate the velocities of the **d**→**e** and **e**→**f** shocks, Λ^{de} and Λ^{ef}.

The crossover tie line can be found by a simple geometric construction:

1. Find the tie line in the $CH_4/C_4/C_{10}$ face that extends through the initial composition **a**. Extend that tie line further to find point **A** where it intersects the C_4/C_{10} edge of the ternary face (see Fig. 3.1).
2. The crossover tie line is the tie line in the $CO_2/C_4/C_{10}$ face that also extends through point **A**.

A detailed proof that the crossover tie line is so defined is given in the next section. For the example given here, there is only one tie line in the $CH_4/C_4/C_{10}$ face that intersects the initial composition **a**. Hence there is no question of uniqueness of composition paths for the solutions given here [30].

Point **c** on the crossover tie line is determined from a shock material balance on CO_2, as is shown in the next section. At point **c**,

$$\lambda_t^c = \frac{df_g^c}{dS_g} = \frac{F_{CO_2}^c}{C_{CO_2}^c}, \tag{3.4}$$

in which the eigenvalue for variation along the crossover tie line, λ_t, is simply given by $\frac{df_g}{dS_g}$. Eq. 3.4 is equivalent to the Welge tangent construction for the saturation at the shock that forms during displacement of oil by water.

Once point **c** is known, point **b** on the initial tie line can be found easily from a shock balance on CH_4.

$$\frac{F_{CH_4}^b}{C_{CH_4}^b} = \lambda_t^c \tag{3.5}$$

From composition **b**, the velocity of the leading **a**→**b** shock is given by a shock balance written for any of the three components present in the initial mixture, for example,

$$\Lambda^{ab} = \frac{F_{CH_4}^a - F_{CH_4}^b}{C_{CH_4}^a - C_{CH_4}^b}. \tag{3.6}$$

Points **d** and **e** can be found similarly. The wave velocity of the **d**→**e** shock satisfies another tangent construction of the form,

$$\lambda_t^d = \frac{df_g^d}{dS_g} = \frac{F_{C_4}^d}{C_{C_4}^d}. \tag{3.7}$$

When the composition **d** is known, point **e** is determined from a shock balance on CO_2 or C_{10}.

$$\frac{F_{CO_2}^d - F_{CO_2}^e}{C_{CO_2}^d - C_{CO_2}^e} = \lambda_t^d. \tag{3.8}$$

Finally, the wave velocity of the trailing shock can be found from

$$\Lambda^{ef} = \frac{F_{C_{10}}^e}{C_{C_{10}}^e}. \tag{3.9}$$

Thus, the full solution can be found easily if the crossover tie line is known. Hence, the simple geometric construction given for the determination of the crossover tie line simplifies construction of solutions significantly. We emphasize, however, that this procedure applies only when the crossover tie line is connected to the initial and injection tie lines by shocks. That happens when eigenvalues increase along nontie-line paths from points near **b** to points near **c** and also increase for paths from **d** to **e**. If eigenvalues decrease along either of those paths then a continuous variation along the nontie-line path will occur. In such cases, the crossover tie line must be found by integration along nontie-line paths.

3.1.4 Determination of the Crossover Tie Line

The wave velocity of the **a**→**b** shock is given by

$$\Lambda^{ab} = \frac{F_i^a - F_i^b}{C_i^a - C_i^b} \qquad i = CH_4, C_4, C_{10}. \tag{3.10}$$

Eq. 3.10 can be written for any two components and the velocity Λ^{ab} eliminated, which yields

$$\frac{F^a_{CH_4} - F^b_{CH_4}}{C^a_{CH_4} - C^b_{CH_4}} = \frac{F^a_i - F^b_i}{C^a_i - C^b_i} \qquad i = C_4, C_{10}. \tag{3.11}$$

Eq. 3.11 applies to any point **a** on the extension of the tie line through point **b**. In particular it applies in the limit as the concentration of CH_4 goes to zero, in which case the initial composition is the point **A**. The result for composition **A** is,

$$\frac{F^b_{CH_4}}{C^b_{CH_4}} = \frac{F^A_i - F^b_i}{C^A_i - C^b_i} \qquad i = C_4, C_{10}. \tag{3.12}$$

Now consider the material balances for the **b**→**c** shock. They have the form,

$$\lambda^c_i = \frac{df^c_g}{dS_g} = \frac{F^b_i - F^c_i}{C^b_i - C^c_i} \qquad i = CO_2, CH_4, C_4, C_{10}. \tag{3.13}$$

Because CH_4 is missing on the $CO_2/C_4/C_{10}$ face, $F^c_{CH_4} = 0$. Also, CO_2 is not present on the $CH_4/C_4/C_{10}$ face, so $F^b_{CO_2} = C^b_{CO_2} = 0$. Hence, for CH_4 and CO_2, Eq. 3.13 reduces to

$$\lambda^c_i = \frac{F^b_{CH_4}}{C^b_{CH_4}} = \frac{df^c_g}{dS_g}, \tag{3.14}$$

$$\lambda^c_i = \frac{F^c_{CO_2}}{C^c_{CO_2}} = \frac{df^c_g}{dS_g}. \tag{3.15}$$

Rearrangement of Eq. 3.13 written for C_4 or C_{10} gives

$$F^b_i = F^c_i + \lambda^c_i(C^b_i - C^c_i) \qquad i = C_4, C_{10}. \tag{3.16}$$

Rearrangement of Eq. 3.12 with substitution of Eq. 3.14 gives

$$F^b_i = F^A_i + \lambda^c_i(C^b_i - C^A_i) \qquad i = C_4, C_{10}. \tag{3.17}$$

Elimination of F^b_i from Eqs. 3.16 and 3.17 gives

$$\lambda^c_i = \frac{F^c_i - F^A_i}{C^c_i - C^A_i} = \frac{df^c_g}{dS_g} \qquad i = C_4, C_{10}. \tag{3.18}$$

Eqs. 3.18 are exactly equivalent to a set of material balances written for a tangent shock from point **A** to point **c**. Those shock balances require that points **A** and **c** lie on the same tie-line extension (Dumoré et al.[18]). Thus, point A, which lies on the extension of the tie line through point **b** by definition also lies on the extension of the tie line through **c**. Hence, the tie line through **A** and **c** is the crossover tie line.

3.1.5 Continuity

Now consider the effect of variations in the position of point **a** along the same tie-line extension. Once the crossover tie line has been determined for a given initial composition, **a**, the location of point **c** on that tie line is determined from Eq. 3.15 which is independent of the amount of CH_4 in the mixture **a** (because $\lambda^c_i = \frac{df^c_g}{dS_g}$, which depends only on S^c_g for overall composition variations along a single tie line). Once λ^c_i has been found from Eq. 3.15, point **b** is given by Eq. 3.14, which is also independent of the amount of CH_4 present at **a**. Hence points **b** and **c** are invariant for changes in the composition **a** as long as the compositions all lie on the same tie-line extension. Eqs. 3.7 and 3.8 are also independent of the CH_4 fraction in composition **a** as long as the crossover tie line is fixed, which it is as long as point **a** lies on the same tie line extension, and hence points **d** and **e** are also invariant.

Therefore, only the velocity of the leading shock, given by Eq. 3.10, changes if the CH_4 fraction is varied along the same tie line extension. The solutions given here must be continuous with respect to variations in the initial CH_4 fraction, and the solution reduces continuously to the three-component solution as **a** approaches **A**. In the limit as **a** approaches **A**, the wave velocity of the **A**→**b** shock from Eq. 3.14 is λ_t^c. The wave velocity of the **b**→**c** shock is also λ_t^c from Eq. 3.15. But λ_t^c is exactly the wave velocity of a shock from **A** to point **c**, the leading shock of the ternary solution. Thus, the **a**→**b** and **b**→**c** shocks merge and hence, the four-component solution reduces continuously to the three-component solution as the initial CH_4 fraction goes to zero.

3.1.6 Minimum Miscibility Pressure

Consider what happens to the crossover tie line as the displacement pressure is increased while the initial composition is held fixed. As the pressure increases, the two-phase region on the $CO_2/C_4/C_{10}$ face shrinks, and the crossover tie line becomes shorter as it approaches the plait point on that face. If the displacement is to be MCM, one of the three key tie lines (initial, injection, or crossover) must be a critical tie line. In the example considered here, the crossover tie line approaches the critical plait point at a lower pressure than do the initial and injection tie lines, and hence, the MMP for injection of pure CO_2 to displace $CH_4/C_4/C_{10}$ mixtures is the pressure at which the crossover tie line is the critical tie line in the $CO_2/C_4/C_{10}$ face. Thus, the MMP for a given initial composition can be found by the following steps:

1. Estimate the MMP. Extend the initial tie line in the $CH_4/C_4/C_{10}$ face at the estimated pressure to zero CH_4 concentration, point **A**.
2. Find the pressure at which the critical tie line in the $CO_2/C_4/C_{10}$ face extends through point **A**. That pressure is the updated estimate of the MMP.
3. If the new MMP differs significantly from the previous estimate repeat steps (1) and (2) to convergence.

The procedure outlined is illustrated in Fig. 3.3. in which the change in the MMP when a dead oil is saturated with CH_4 is determined. As Fig. 3.3 shows, a C_4/C_{10} mixture containing 48 mole % C_4 has an MMP of about 1600 psia. Addition of about 35% CH_4 to mixture **A** gives a saturated mixture, **a**, at 1600 psia. Extension of the tie line at 1600 psia through **a** gives composition **B** as Fig. 3.3 shows. Composition **B** lies on a critical tie line at about 1625 psia. Recalculation of the tie line through **a** at 1625 psia gives a new tie-line extension to the C_4/C_{10} axis. In this case, the new tie line differs only slightly from the previous one. Hence, convergence is achieved in only one step. Thus, addition of 35% CH_4 to the original oil changes the MMP, but for this system, in which tie lines in the $CH_4/C_4/C_{10}$ face cross the dilution line at a small angle, the magnitude of the change is small.

Fig. 3.3 shows that addition of CH_4 to a dead oil mixture at its MMP causes the composition route for displacement of the live oil at the same pressure to enter the two-phase region, as Monroe et al.[45] observed. Because the resulting crossover tie line lies quite close to the critical point at 1600 psia, however, the displacement is still quite efficient. The simple geometric construction for the tie line makes it clear why empirical correlations for MMP's call for use of the bubblepoint pressure as the MMP if the oil contains so much dissolved CH_4 that its bubblepoint exceeds the MMP estimated or measured for the dead oil. The dispersion free theory given here proves that the empirical proviso is not strictly correct, though it also shows that the change in the MMP is

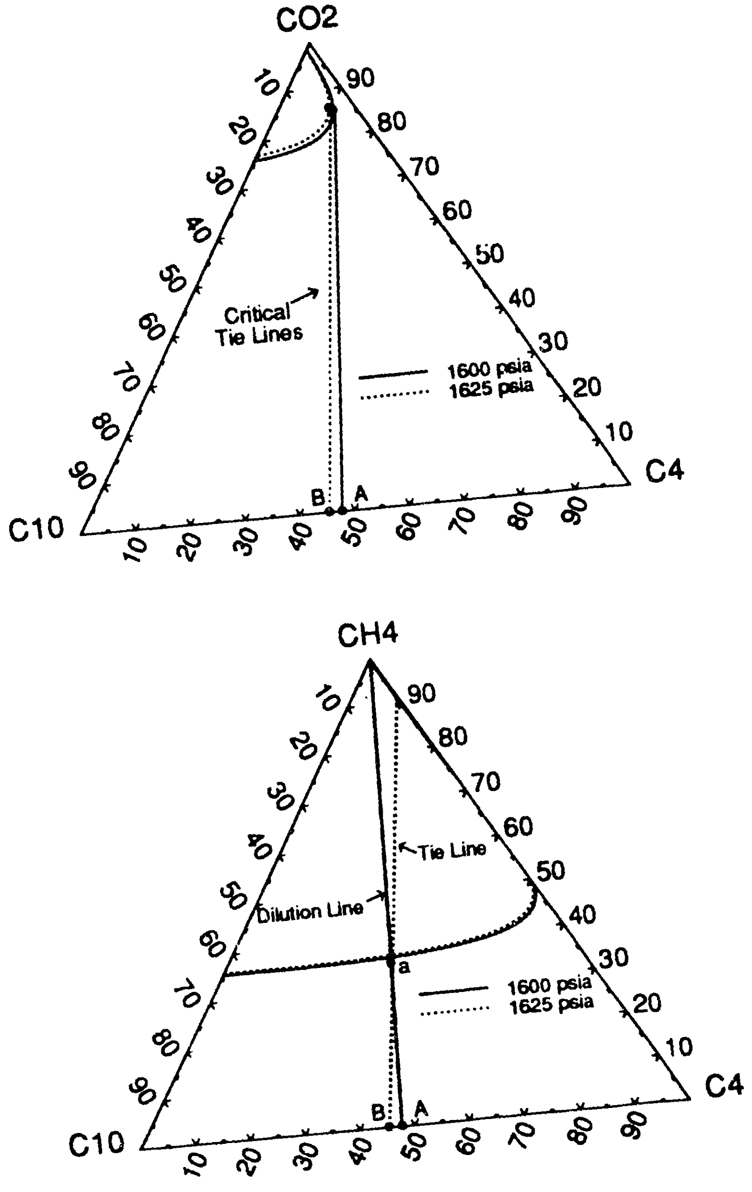

Figure 3.3: Determination of the MMP for initial mixture **a**.

likely to be small. In fact, the change in the MMP of 25 psia in the example given would be smaller than the typical pressure increment in slim tube tests, and hence below the typical resolution of an MMP measurement.

3.1.7 Development of Miscibility

When the crossover tie line is the critical tie line, Eq. 3.15 reduces to

$$\lambda_t^c = 1\,, \tag{3.19}$$

because $F^c_{CO_2} = C^c_{CO_2}$ at the critical point. Substitution of Eq. 3.19 into Eq. 3.14 shows that in that case,

$$F^b_{CH_4} = C^b_{CH_4}\,. \tag{3.20}$$

From the definitions of F_i and C_i, it is clear that Eq. 3.20 is satisfied in the two-phase region only when $f_g = S_g$. Now consider the local flow (not wave) velocity of the vapor and liquid phases,

$$v_g = \frac{q}{\phi A}\frac{f_g}{S_g}\,, \tag{3.21}$$

and

$$v_l = \frac{q}{\phi A}\frac{(1-f_g)}{(1-S_g)}\,. \tag{3.22}$$

Those phases have equal flow velocity when $v_g = v_l$. Rearrangement of Eqs. 3.21 and 3.22 shows that $v_g = v_l$ only when $f_g = S_g$. Hence, point **b** is on the equivelocity curve in the $CH_4/C_4/C_{10}$ face when the crossover tie line is the critical tie line.

Now consider the velocity of the leading shock. Because the initial composition is single-phase $F_i^a = C_i^a$. Substitution of that equality and Eq. 3.20 into Eq. 3.10 yields $\Lambda^{ab} = 1$. Thus, the leading shock has unit wave velocity for any composition **a** on the same tie-line extension.

Points **c** and **d** coincide at the plait point, so $\lambda_t^d = 1$ as well. Eq. 3.7 indicates, therefore, that the **d**→**e** shock also has unit velocity. Because point **d** is the plait point, $F^d_{CO_2} = C^d_{CO_2}$, and hence rearrangement of Eq. 3.8 shows that $F^e_{CO_2} = C^e_{CO_2}$. That result implies that point **e** lies on the binodal curve, which means that the trailing shock also moves with unit wave velocity. Hence, if the crossover tie line is the critical tie line in the $CO_2/C_4/C_{10}$ face, all shocks move with unit wave velocity, point **b** lies on the equivelocity surface, and hence the displacement is piston-like.

3.1.8 Sample Solutions

In the example given above, dilution of a C_4/C_{10} mixture with CH_4 changed the crossover tie line. If, however, the initial mixture is modified in such a way that the composition of the point **a** always remains on the same tie-line extension, only the wave velocity of the leading shock changes as, the continuity arguments that prove the invariance of points **b**, **c**, **d** and **e** for initial compositions on the same tie-line extension show. Fig. 3.2 also shows composition profiles for mixture α in Fig. 3.1, and the resulting velocity of the leading shock is given in Table 3.2. Composition α lies on the same tie-line extension, but it contains three times as much CH_4 as composition **a**. The profiles shown in Fig. 3.2 indicate that the leading CH_4 bank is larger for initial composition α, but the composition profiles upstream of the **b**→**c** shock are unchanged. Thus, the crossover tie line is fixed for all compositions that lie on the same tie-line extension in the $CH_4/C_4/C_{10}$ face.

Any change in initial composition or displacement pressure that results in a crossover tie line closer to the plait point in the $CO_2/CH_4/C_{10}$ face improves displacement efficiency. For example,

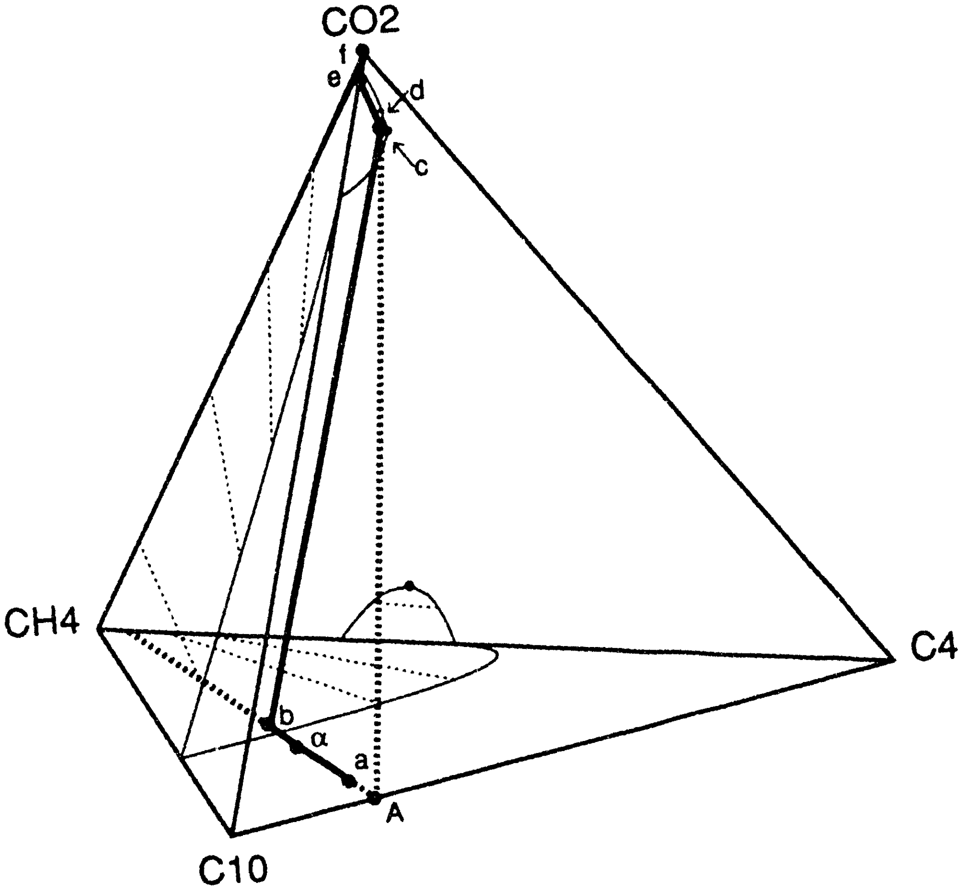

Figure 3.4: Composition route for displacement of oil mixture by pure CO_2 at 1730 psia, 160° F.

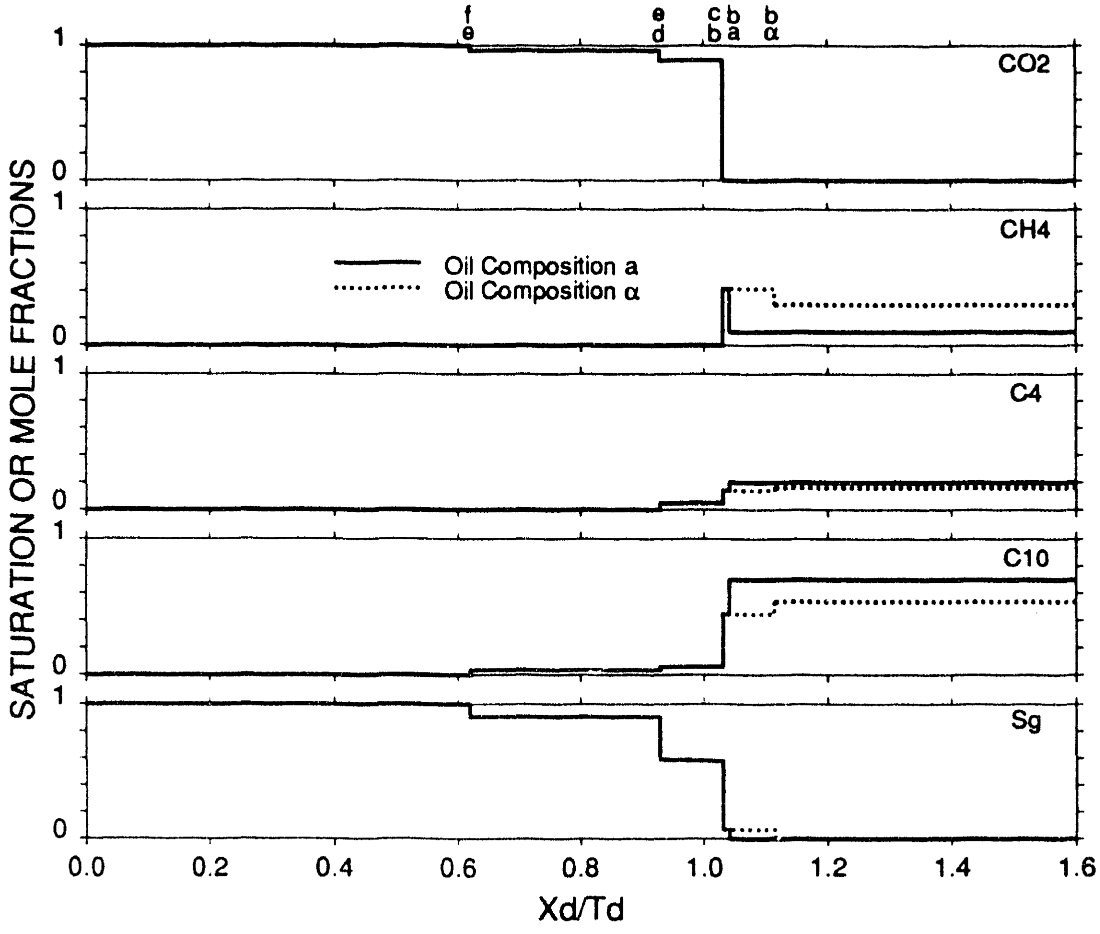

Figure 3.5: Composition profiles for the nearly miscible composition route at 1730 psia, 160° F.

Table 3.3: MOC Solution for the Composition Route at 1730 psia, 160° F.

Composition Label	Composition (Mole Fraction)				Gas Saturation (Vol. Fraction)	Wave Velocity
	CO_2	CH_4	C_4	C_{10}		
A	0.0000	0.0000	0.2189	0.7811	0.0000	-
a	0.0000	0.1000	0.2000	0.7000	0.0000	1.0405
b	0.0000	0.4160	0.1404	0.4436	0.0676	1.0405-1.0302
c	0.8934	0.0000	0.0475	0.0591	0.5784	1.0302
d	0.8942	0.0000	0.0473	0.0585	0.5919	0.9295
e	0.9643	0.0000	0.0000	0.0357	0.9081	0.9295-0.6200
f	1.0000	0.0000	0.0000	0.0000	1.000	0.6200
Oil Composition α						
α	0.0000	0.3000	0.1623	0.5377	0.0000	1.1142
b	0.0000	0.4160	0.1404	0.4436	0.0676	1.1142-1.0302

Fig. 3.4 shows the composition route for displacement of the initial mixture in Figs. 3.1 and 3.2 and Table 3.2, but this time at a pressure of 1730 psia. Details of the analytical solution are given in Table 3.3. As Fig. 3.4 shows, the crossover tie line is much closer to the plait point. Fig. 3.5 shows the resulting composition profiles. Comparison of Figs. 3.2 and 3.5 and Tables 3.2 and 3.3 indicates that at the higher pressure the leading shock is slower and the trailing shocks move faster. If the pressure were increased still further to 1750 psia, the MMP according to the crossover tie-line criterion, the trailing, intermediate and leading shocks would all merge, and a piston-like displacement would result.

3.1.9 Discussion

In the examples given here, it is the approach of the crossover tie line to the plait point that determines miscibility. In the next sections we will describe other systems in which either the initial tie line or the injection tie line will control development of miscibility. The examples shown indicate that the crossover tie-line MMP criterion is satisfied for mixture **a** at approximately 1750 psia. At that pressure, both the initial and injection compositions lie well within the region of tie-line extensions. Hence, the crossover tie-line criterion shows that miscibility can develop even when both initial and injection compositions are on tie-line extensions. Thus, the behavior of four-component systems contrasts sharply with that of three-component systems, in which either the injection or initial oil composition must lie outside the region of tie-line extensions if the displacement is to be MCM. For this system, the crossover tie-line criterion is less restrictive than the requirement that either the initial or injection composition be outside the region of tie-line extensions. For example, the injection composition, pure CO_2, lies on a critical tie line at 1870 psia, the $CO_2 - C_{10}$ critical pressure. The initial mixture **a** lies on a critical tie line at approximately 4500 psia. Hence, it is clear that the pressure given by the crossover tie line criterion is much lower than that obtained if the initial or injection composition is to be on a critical tie line. It is likely that many CO_2/crude oil systems containing dissolved CH_4 show similar behavior.

The solutions presented here allow interpretation of the experimental results reported by Metcalfe and Yarborough [44]. They performed displacement experiments for the $CO_2/CH_4/C_4/C_{10}$ system in a Berea sandstone core six feet in length. They reported displacement results at 1500 psia, 1700 psia, and 1900 psia, for an initial mixture containing 40% C_4 with 60% C_{10} and for the same mixture diluted with CH_4 (25 % CH_4, 30% C_4, 45% C_{10}). Phase diagrams calculated with the PREOS are shown in Fig. 3.6.

The displacements at 1500 psia for both initial compositions were immiscible according to the definition given here. Fig. 3.6 shows that composition **B**, the dead oil composition obtained by extending the initial tie line (at 1500 psia) to zero CH_4 concentration, yields a crossover tie line well inside the two-phase region on the $CO_2/C_4/C_{10}$ ternary diagram (Fig. 3.6). The live oil displacement at 1500 psia showed a significant CH_4 bank in effluent composition data, evidence of a chromatographic separation that can only occur if there is two-phase flow.

The live oil displacement at 1900 psia was first contact miscible as Metcalfe and Yarborough reported. A dilution line from the initial live oil composition to pure CO_2 passes close to the edge of the calculated two-phase region in the interior of the quaternary diagram, but does not penetrate it. No CH_4 bank was observed at 1900 psia, another indication that no two-phase flow occurred.

Metcalfe and Yarborough interpreted the displacements at 1700 psia to be MCM. According to the PREOS, at least, the composition **B** is outside the region of tie-line extensions (Fig. 3.6). Fig. 7 of Metcalfe and Yarborough indicates that the critical tie line in the $CO_2/C_4/C_{10}$ face intersects the C_4/C_{10} axis very close to composition **B**. Hence, the analytical theory supports their interpretation that the displacement was MCM. However, a small CH_4 bank was reported at 1700 psia, clear evidence that two-phase flow occurred somewhere in the core. There are several potential

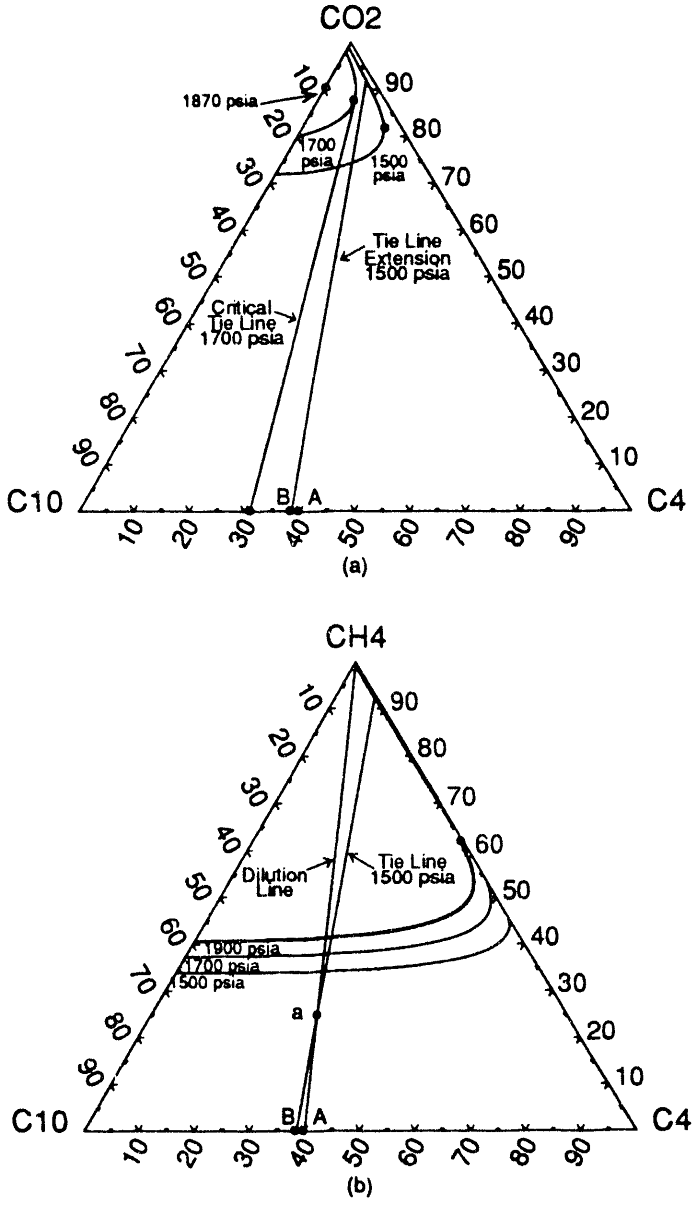

Figure 3.6: Comparison of experimental MMP results with the crossover tie-line criterion.

explanations for the existence of the CH_4 bank. For example, the PREOS may not represent the actual phase behavior adequately in the critical region. With a slight change in phase behavior, however, the analytical theory could predict a nearly MCM displacement, which would produce a small CH_4 bank. In addition, two-phase flow may have been caused by other displacement mechanisms not considered in the analytical theory. For example, physical dispersion can cause two-phase flow in a one-dimensional flow that is MCM without dispersion[80]. Furthermore, the experimental displacement was not strictly one-dimensional. Instead, viscous fingering, gravity segregation, and local permeability heterogeneity may have caused some nonuniform flow. As Pande and Orr[55, 56, 57] showed, if crossflow driven by viscous, capillary or gravity forces is also present, it can induce two-phase flow even when the corresponding one-dimensional displacement is MCM. In real displacements some two-phase flow is probably inevitable because dispersion, nonuniform flow, and crossflow are always present. In the limit where these physical mechanisms have small effect, however, as in slim tube displacements, the four component analytical theory allows unambiguous determination of the MMP.

3.1.10 Conclusions

Analysis of the behavior of dispersion-free MOC solutions for one-dimensional displacement of $CH_4/C_4/C_{10}$ mixtures by pure CO_2 injection shows that:

1. In four component systems, miscibility can develop even though both the injection and initial oil compositions lie on tie-line extensions.
2. Development of miscibility in displacements of $CH_4/C_4/C_{10}$ mixtures by CO_2 occurs when the crossover tie line is the critical tie line in the $CO_2/C_4/C_{10}$ face.
3. The crossover tie line can be found from a straightforward geometric construction when the crossover tie line is connected to the injection and initial tie line by shocks.
4. If the initial composition is varied along a single tie-line extension, only the velocity of the leading shock (and hence the size of the CH_4 bank) changes. All other portions of the solution remain fixed.
5. Interactions of phase behavior and two-phase flow cause a chromatographic sorting of components present in the initial oil into banks and waves in K-value order. All CH_4 in the zone of two-phase flow appears in a leading CH_4 bank.

3.2 Development of Miscibility in an Enriched-Gas Drive

Russell T. Johns

The four-component CO_2 flood solutions given in Section 3.1 were for an idealized system of pure hydrocarbon components, CH_4, C_4, and C_{10}. In this section, we extend the results of Section 3.1 in two ways. First, we examine a system in which the four components are not pure hydrocarbons, but instead are pseudocomponents, mixtures which have been lumped together for the purposes of calculation. The pseudocomponent representation more closely approximates the behavior of a crude oil system than does the well-characterized system of Section 3.1. Second, we consider more general initial and boundary conditions. We consider an initial oil that contains all four components, and an injected fluid that is a binary mixture. Example solutions are presented in which the injected fluid is a mixture of CH_4 and solvent, which in turn, is a mixture of CO_2 and hydrocarbon gases. The sample solutions presented illustrate the effect of enrichment levels

Table 3.4: Component Properties of Four Component Model.

Component	M_w	P_c (psia)	T_c (deg F)	V_c (ft^3/mol)	ω
CO_2+	41.0	769.81	142.79	2.540	0.1592
C_1N_2	16.0	71.17	-117.07	1.585	0.0130
C_5+	189.0	322.89	775.00	13.054	0.6736
$C_{30}+$	451.0	171.07	1136.59	30.644	1.0259

Component	ρ_i (mol/ft^3)	Interaction Parameters			
		CO_2+	C_1N_2	C_5+	$C_{30}+$
CO_2+	0.8184	0.0000	0..0286	0.0607	0.1268
C_1N_2	0.5472	0.0286	0.0000	0.0258	0.2000
C_5+	0.2848	0.0607	0.0258	0.0000	0.0000
$C_{30}+$	0.1226	0.1268	0.2000	0.0000	0.0000

in a system where the crossover tie line controls development of miscibility. Systems in which the other important tie lines, the initial and injection tie lines, control development of miscibility will be examined in the next section.

3.2.1 Selection of Four-Component Model

A four-pseudocomponent Peng-Robinson model was constructed using the approach suggested by Newley and Merrill [49] to represent the behavior of a multicomponent system. The initial reservoir fluid mixture used was that described by Lee, Lo and Dharmawardhana [39] and reported in their Table 1 as oil A. To apply the lumping procedure of Newley and Merrill, a feed composition close to the dew point curve (approximately 75% gas saturation) and along the dilution line of the oil and solvent compositions was chosen. The feed composition was used to determine input parameters such as K-values, for use in the pseudocomponent calculations. Methane (C_1) and nitrogen (N_2) were lumped into one separate pseudocomponent, so that solvent enrichment could be varied. The other pseudocomponents were defined as $CO_2 + C_2 + C_3 + C_4$, $C_5 + C_6 + C_7 + C_{10} + C_{14} + C_{20}$, and C_{30+}. C_{30+} forms a separate pseudocomponent because its K-value is much lower than the other components. Fig. 3.7 shows the phase diagram of the four-component model, and Table 3.4 lists the parameters used in the Peng-Robinson EOS representation of the phase behavior of the four-component system. Table 3.5 gives the initial solvent and reservoir oil compositions. The

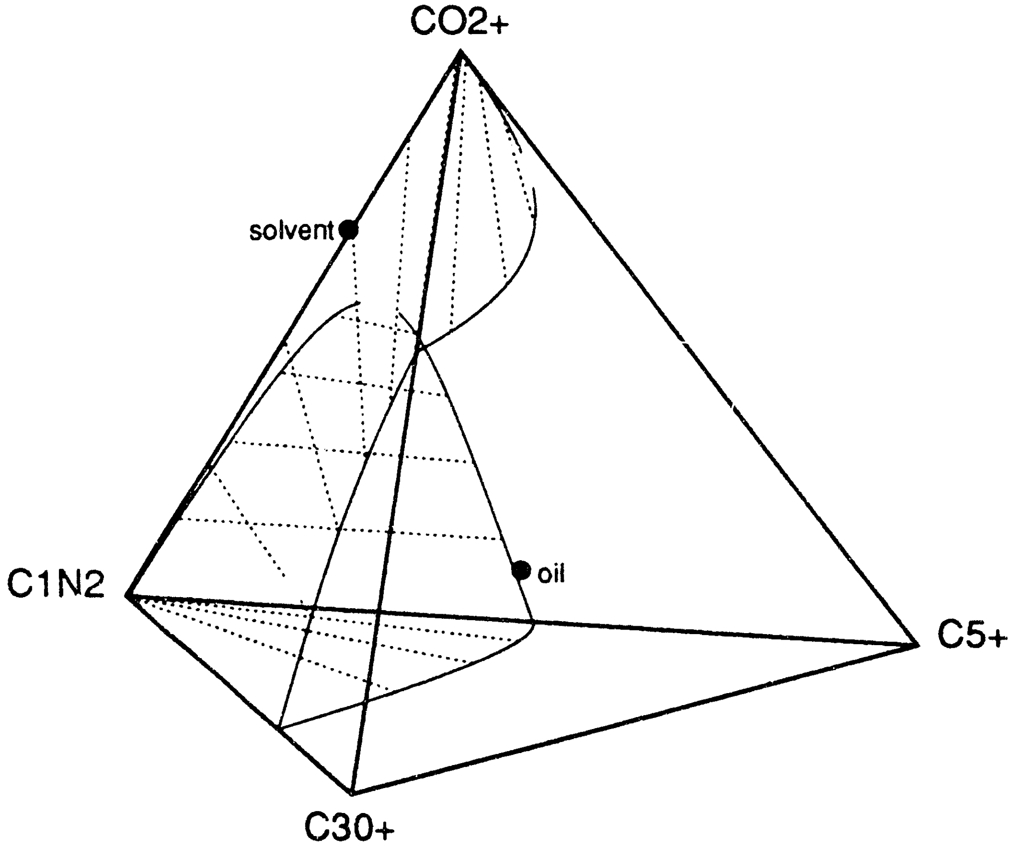

Figure 3.7: Phase diagram for the four-component model at 3650 psia and 200° F.

Table 3.5: Oil and Injection Gas Compositions For Four Component Model.

Component	Oil Mole Fraction	Injection Gas Mole Fraction	Feed Composition
CO_2+	0.11554	0.6723	0.587078
C_1N_2	0.36918	0.3277	0.334049
C_5+	0.42809	-	0.065526
$C_{30}+$	0.08719	-	0.013347

calculated bubblepoint for the four-component oil (11.554% CO_{2+}, 36.918% C_1N_2, 42.809% C_{5+}, 8.719% C_{30+}) is approximately 3325 psia at 200° F.

For convenience, all numerical and analytical calculations were performed based on the assumption of no volume change upon mixing (i.e. component densities, ρ_i, are the same in both the gas and liquid phases), which is a reasonable assumption at the pressure and temperature considered.

3.2.2 Analytic Results Using Four-Component Model

Four analytical solutions for varying CO_{2+} enrichment of the solvent were obtained. The solution technique consists of finding the crossover tie line and constructing tangent shocks along the crossover tie line. The analytical solutions consist of four shocks and three constant states. The solution is governed by the magnitude of the component K-values with the component with the largest K-value (C_1N_2) forming a fast "methane" bank, and the component with the smallest K-value (C_{30+}) disappearing at the slowest shock.

Fig. 3.8 shows the crossover tie line for an injected solvent composition of 67.23% CO_{2+} and 32.77% C_1N_2. It can be shown that the crossover tie line lies within the quaternary diagram, and its extension intersects both the initial oil tie line and solvent tie-line extensions. To test the correctness of the analytical solution, a numerical solution for the problem shown in Fig. 3.10 was obtained with a fully explicit finite difference calculation with 100 grid blocks and a time step size of one-tenth of the grid block spacing. If the number of grid blocks were increased, the numerical solution would be closer still to the analytical solution. Hence, in the limit of low numerical dispersion, the numerical solution reproduces the analytical solution. The numerical solution (Fig. 3.9) and the analytical profile (Fig. 3.10) agree very well.

Fig. 3.11 shows the production curves for this case. At breakthrough of the CO_{2+} component (t_d=.8455 pore volumes injected), 78 percent of the original moles in place for both C_{5+} and C_{30+} are recovered. At 5.0 pore volumes injected, 99% of the initial moles of oil in the core are recovered and only 12.7 percent of the initial moles of C_{30+} remain in the core.

Just as in Section 3.1, the crossover tie line controls the development of miscibility. If the crossover tie line extension intersects the critical plait point locus then the flood is at its MMP. For slightly higher pressures, the crossover tie line cannot be found and the flood is MCM or FCM.

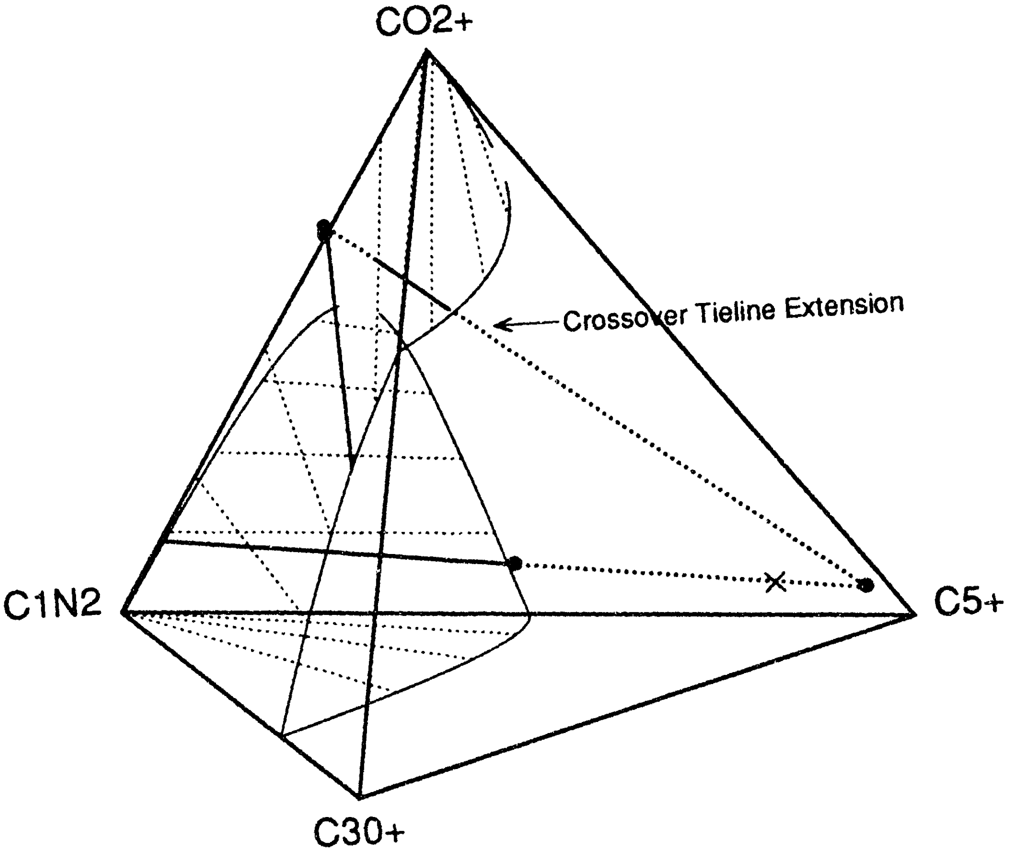

Figure 3.8: Crossover tie line for solvent composition of 67.23% CO_{2+} and 32.77% C_1N_2 at 3650 psia and 200° F. The "x" marks the intersection of the initial oil tie-line extension with the $CO_2/C_{5+}/C_{30+}$ ternary face.

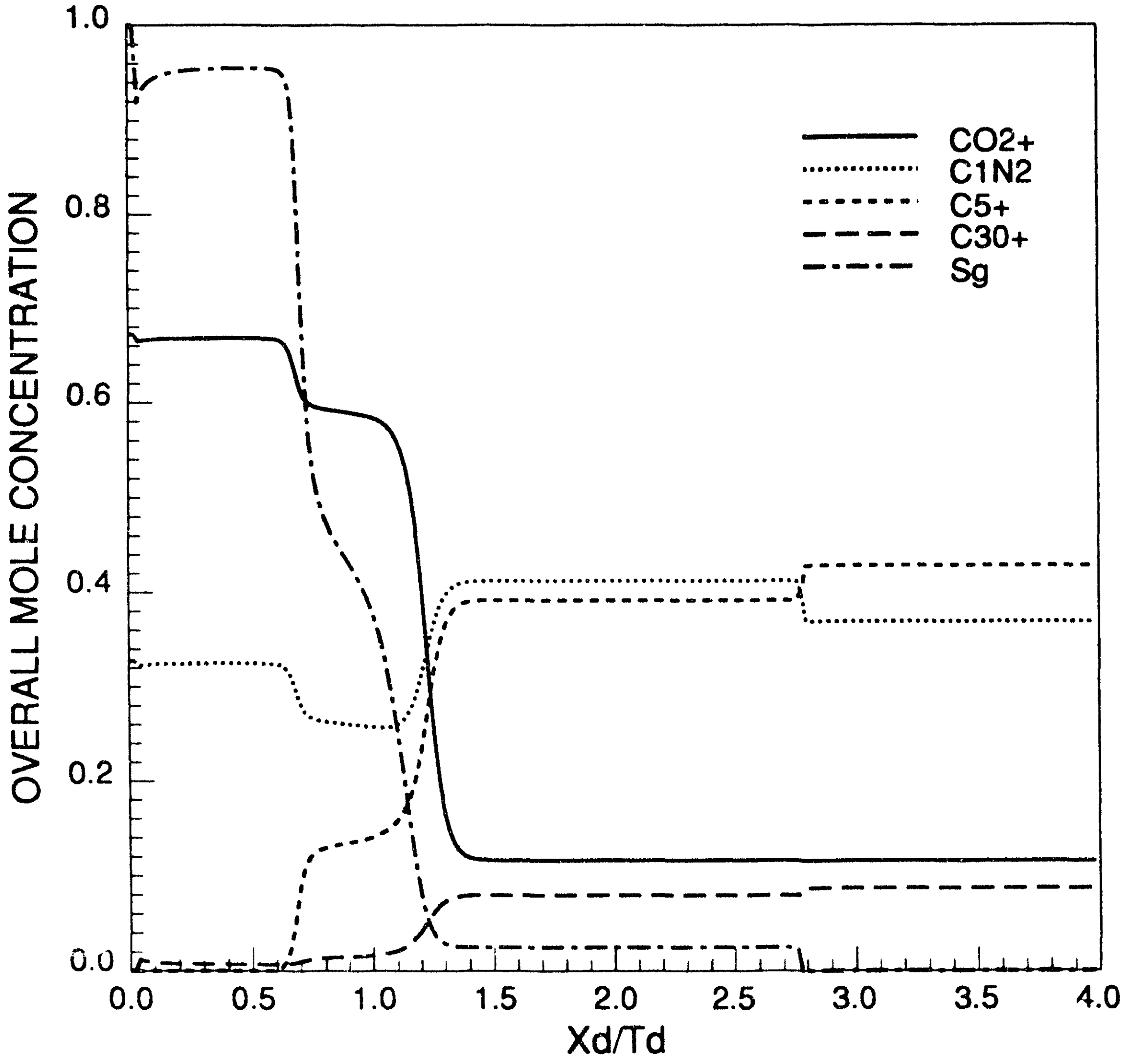

Figure 3.9: Four component numerical simulation at t_d=.50 PVI using 100 grid blocks (dx=.01, dt=.001) at 3650 psia and 200° F.

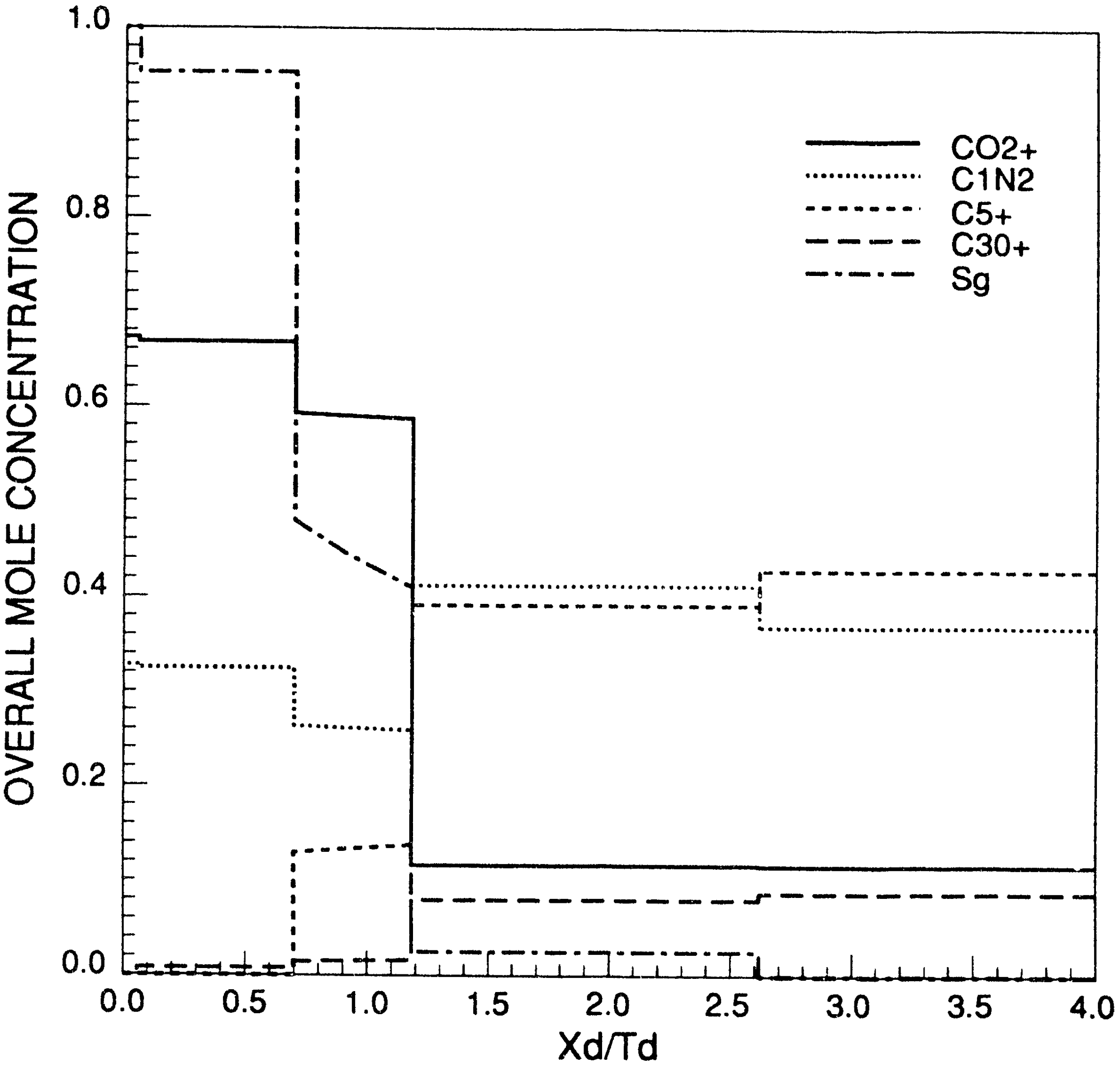

Figure 3.10: Analytical composition profiles for injection of 67.23/32.77 CO_2/C_1N_2 solvent.

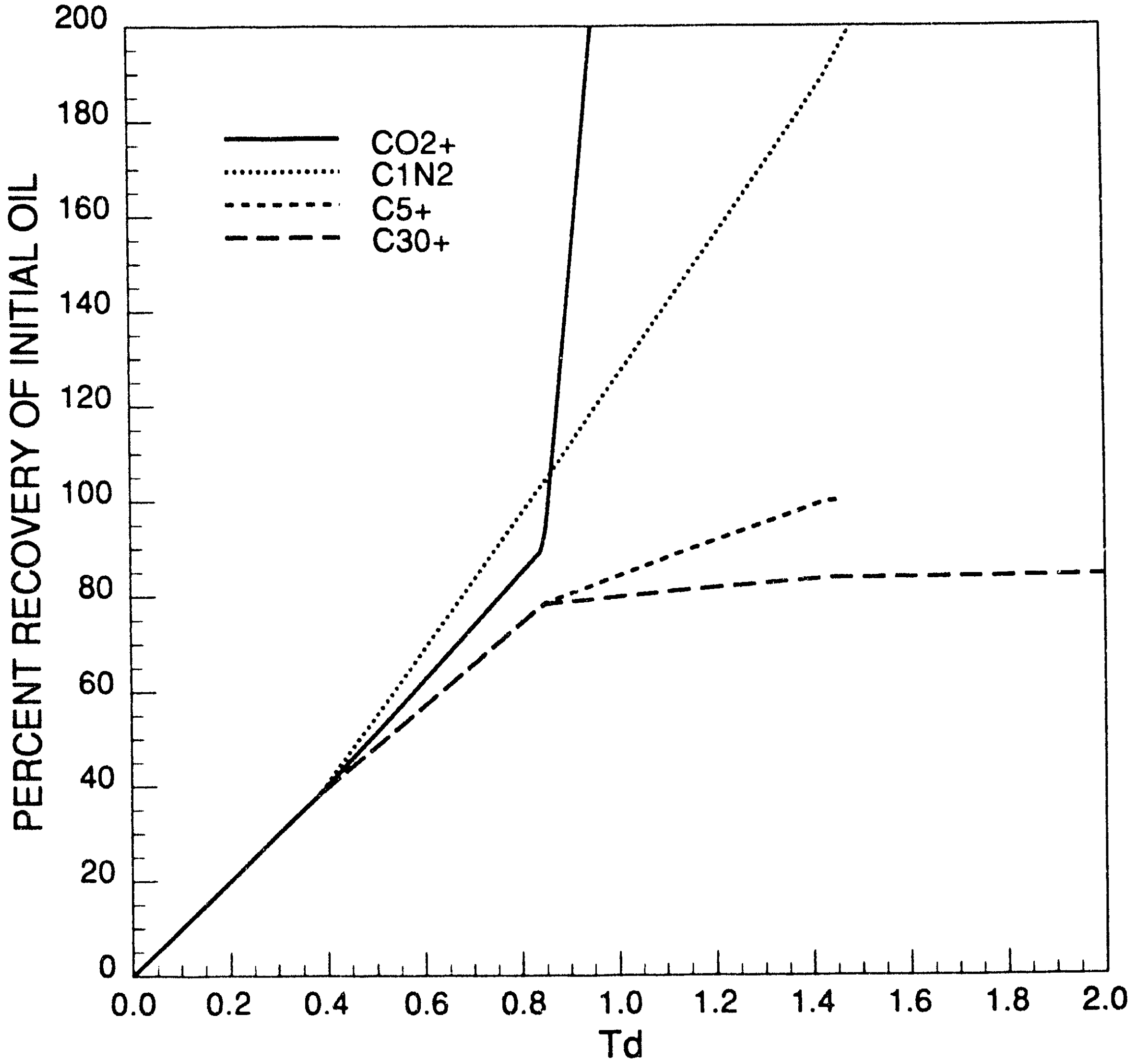

Figure 3.11: Analytical production curves for injection of 67.23/32.77 CO_2/C_1N_2 solvent.

For slightly lower pressures (i.e. as in this example), the flood is near miscible and two-phase flow exists.

The analytical and numerical solutions show features of a combined condensing and vaporizing gas drive mechanism. The middle intermediate component (C_{5+}) is condensed at the leading shock and vaporized at the trailing shock. A future paper is planned to discuss this condensing/vaporizing displacement mechanism.

3.2.3 Effects of Enrichment on Recovery

Three other analytical solutions were obtained to explore the sensitivity of the recovery with varying solvent enrichment. The analytical profile for a 70.5/29.5 mixture of CO_{2+} and C_1N_2 is shown in Fig. 3.12, a 70/30 mixture is shown in Fig. 3.13, and a 60/40 mixture is shown in Fig. 3.14. The production curves for these three cases are given in Figs. 3.15, 3.16 and 3.17.

Fig. 3.18 and 3.19 illustrate how sensitive recovery of the four-component oil is to the solvent enrichment. The recovery of the C_{5+} and C_{30+} components at breakthrough is approximately 91 percent for the 70.5/29.5 solvent mixture, 87 percent for the 70/30 mixture, and 65 percent for the 60/40 mixture. Recovery is slightly higher after 1.0 pore volume injected as shown in Fig. 3.19. Thus, a modest change in the solvent enrichment leads to a large change in the recovery of the middle and heavy components. The minimum enrichment required for multicontact miscibility is approximately a 71/29 mixture of CO_{2+} and C_1N_2. Thus, by adding only 4 percent CO_{2+} to the solvent, the incremental oil recovery would be 22 percent of the original oil in place at breakthrough of the solvent for a one-dimensional slim tube displacement.

Fig. 3.20 shows the phase densities and viscosities of compositions on the crossover tie line as multicontact miscibility is approached. These results also indicate that the minimum enrichment composition is a 71/29 mixture of CO_{2+} and C_1N_2.

3.2.4 Conclusions

The gas flood for the initial solvent mixture of 67.23% CO_{2+} and 32.77% CH_4N_2 is near miscible and achieves high oil recovery. Nevertheless, the four-component model suggests it is important to be very near the minimum enrichment necessary for multicontact miscibility. In the four-component model, the minimum solvent enrichment was determined to be a 71/29% mixture of CO_{2+} and C_1N_2. Further work will be done to explore the sensitivities of the recovery with varying pressure and with various levels of dispersion.

3.3 Development of Miscibility in CO_2/C_4, N_2 and CH_4/C_3 Displacements

Birol Dindoruk

In Sections 3.1 and 3.2 solutions for two model systems were presented. The displacement of $CH_4/C_4/C_{10}$ mixtures by pure CO_2 (Section 3.1) was the simplest because the injection fluid was pure CO_2, and the initial mixture did not contain any CO_2. Furthermore, the crossover tie line was connected to the initial and injection tie lines only by shocks. In that case, the crossover tie line could be found easily by a simple geometric construction. In the system of four pseudo components examined in Section 3.2, the initial mixture contained all four components, and the injected fluid was a mixture of two components. Again, however, the crossover tie line was also connected to the initial and injection tie lines by shocks only. In that case, the crossover tie line could also be found by a geometric construction as the only tie line that intersects the extensions of both the initial and injection tie lines.

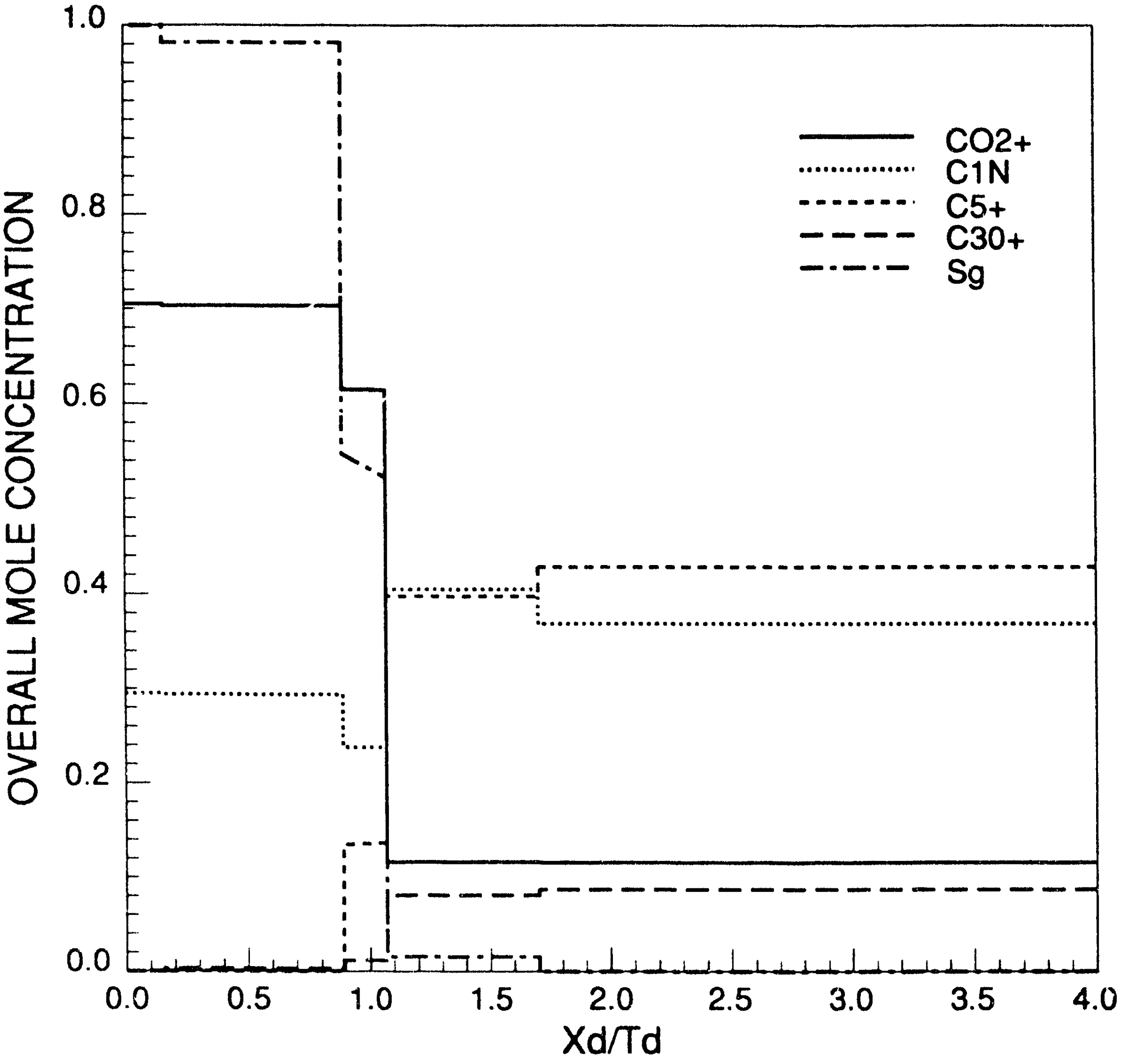

Figure 3.12: Analytical composition profiles for injection of 70.5/29.5 CO_2/C_1N_2 solvent.

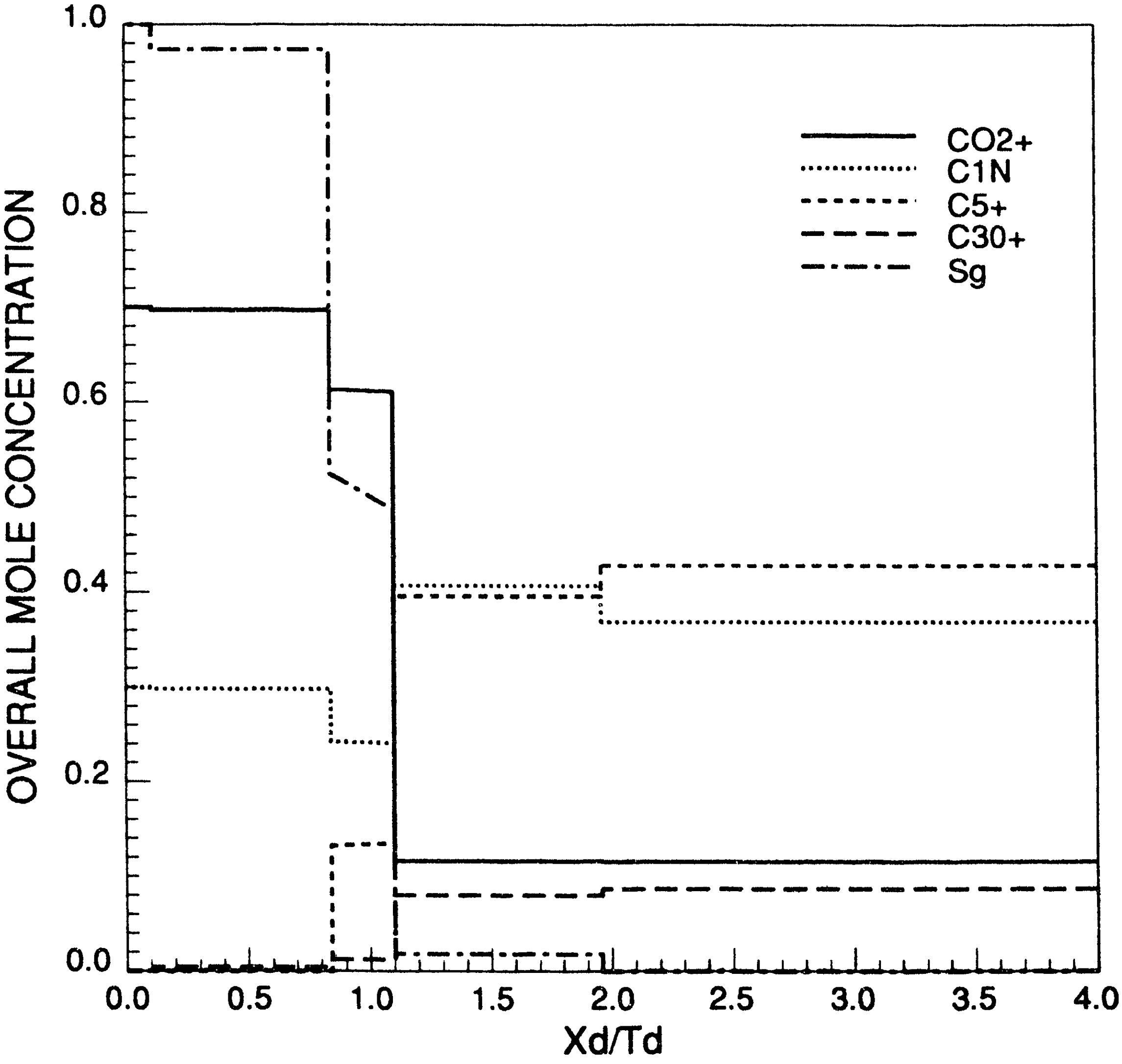

Figure 3.13: Analytical composition profiles for injection of 70/30 CO_2/C_1N_2 solvent.

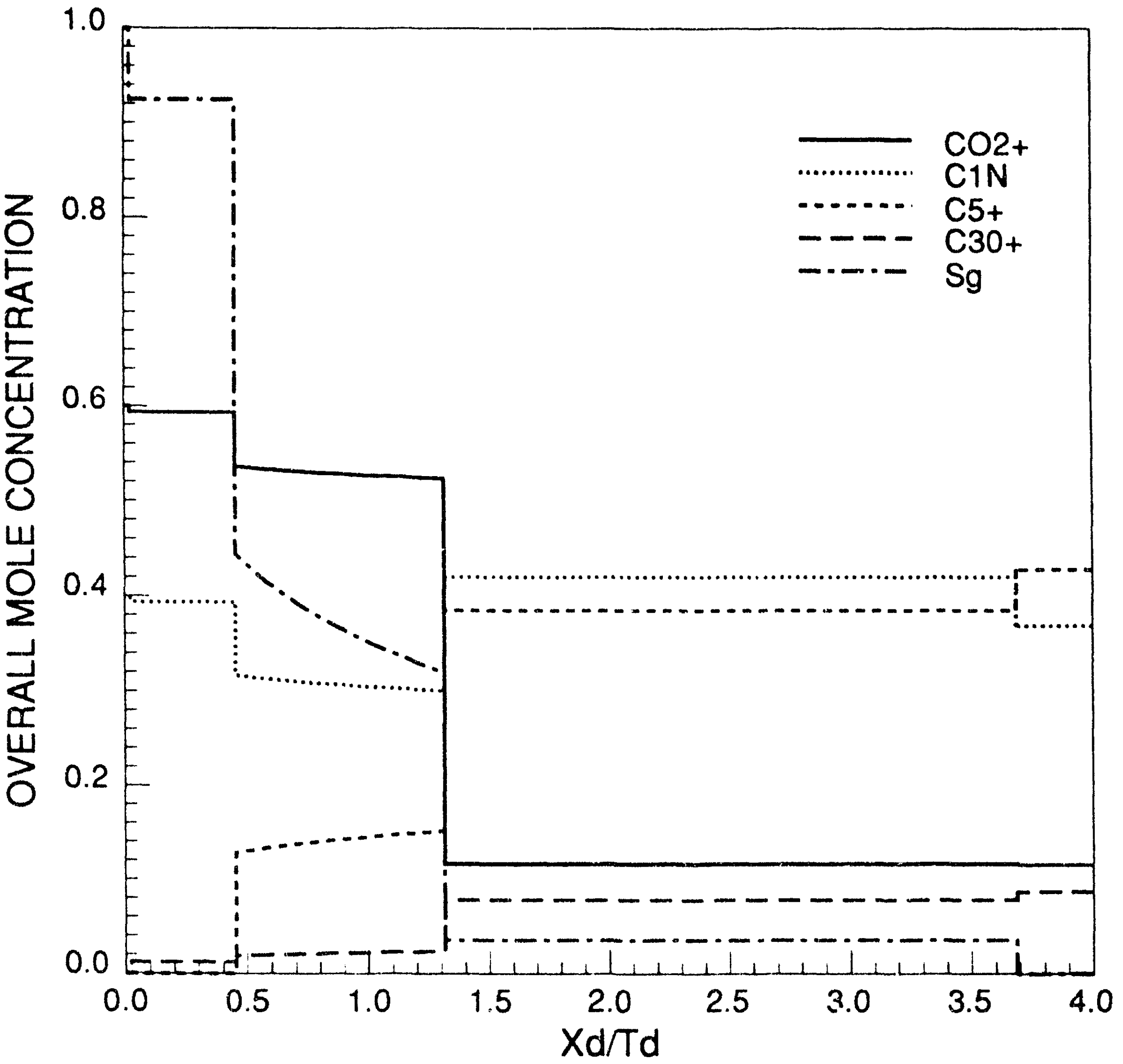

Figure 3.14: Analytical composition profiles for injection of 60/40 CO_2/C_1N_2 solvent.

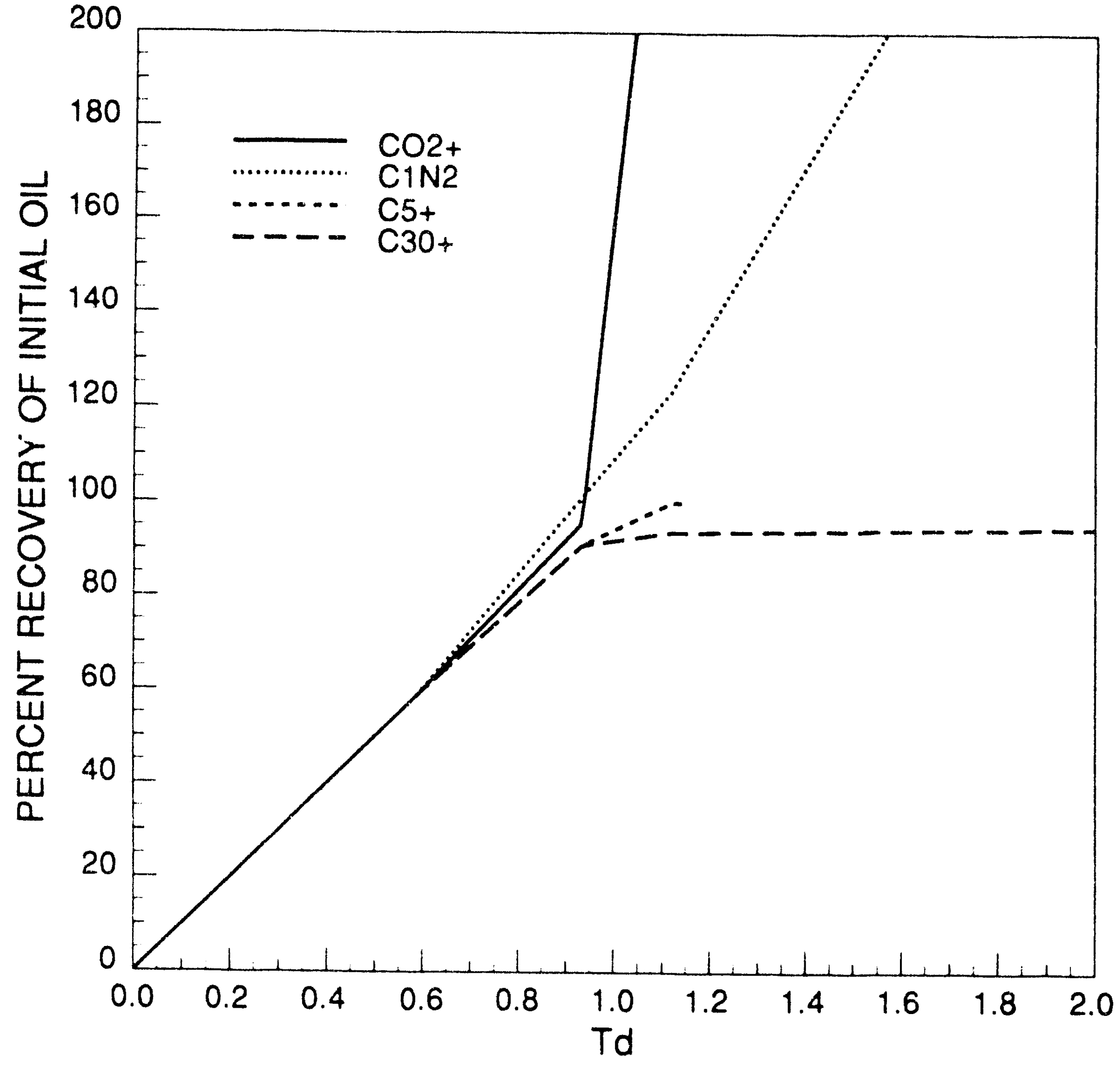

Figure 3.15: Analytical production curves for injection of 70.5/29.5 CO_2/C_1N_2 solvent.

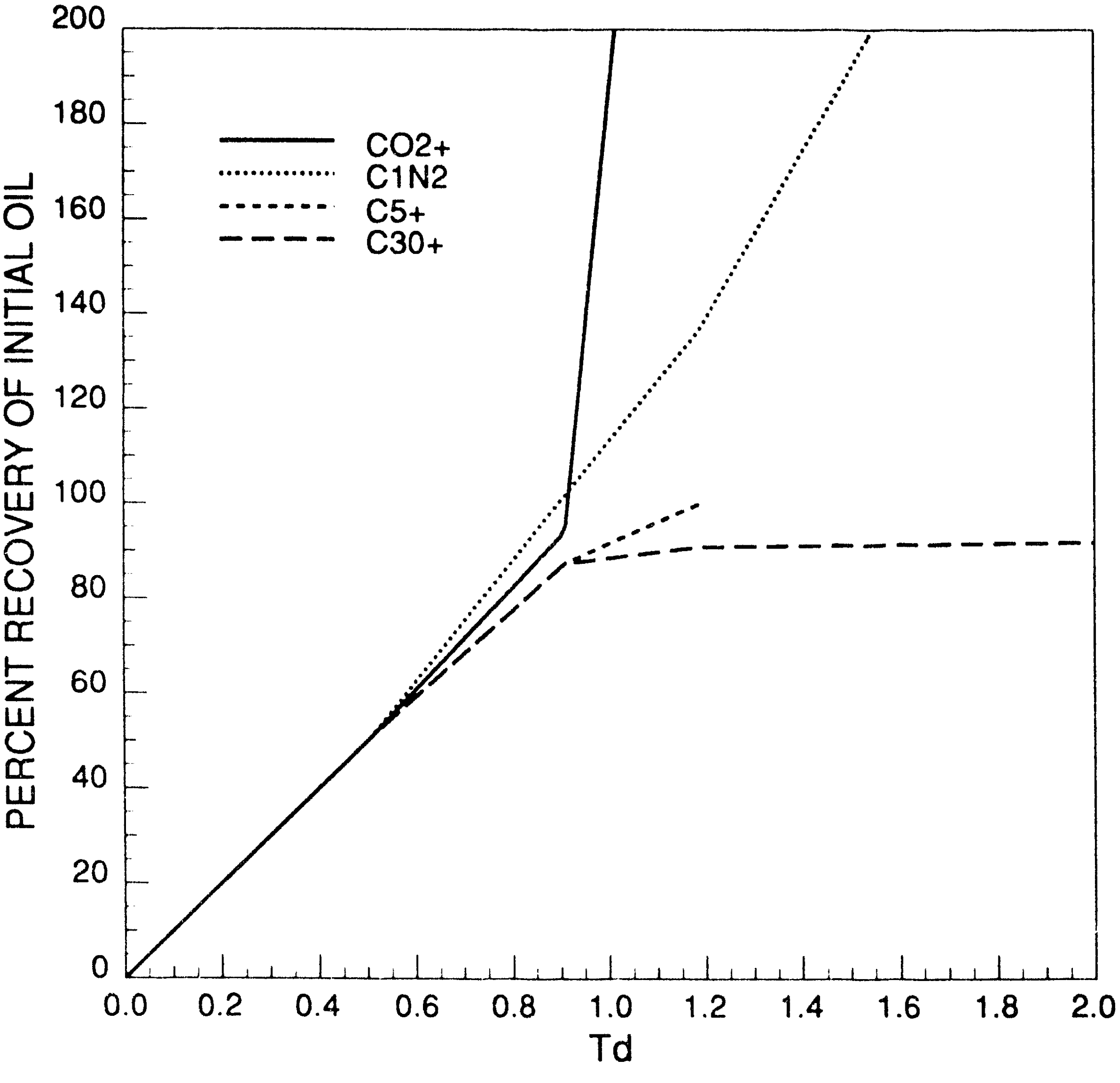

Figure 3.16: Analytical production curves for injection of 70/30 CO_2/C_1N_2 solvent.

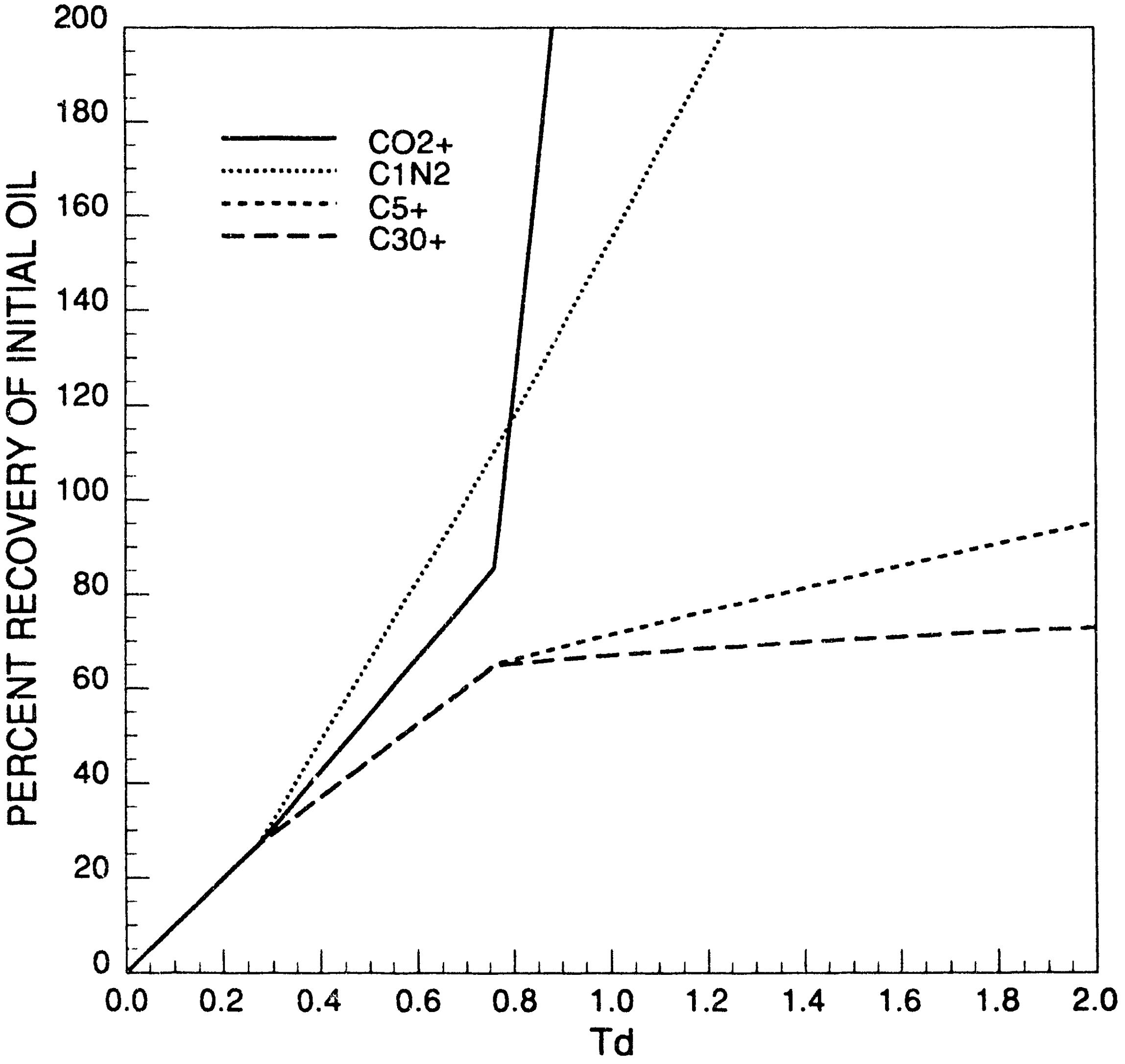

Figure 3.17: Analytical production curves for injection of 60/40 CO_2/C_1N_2 solvent.

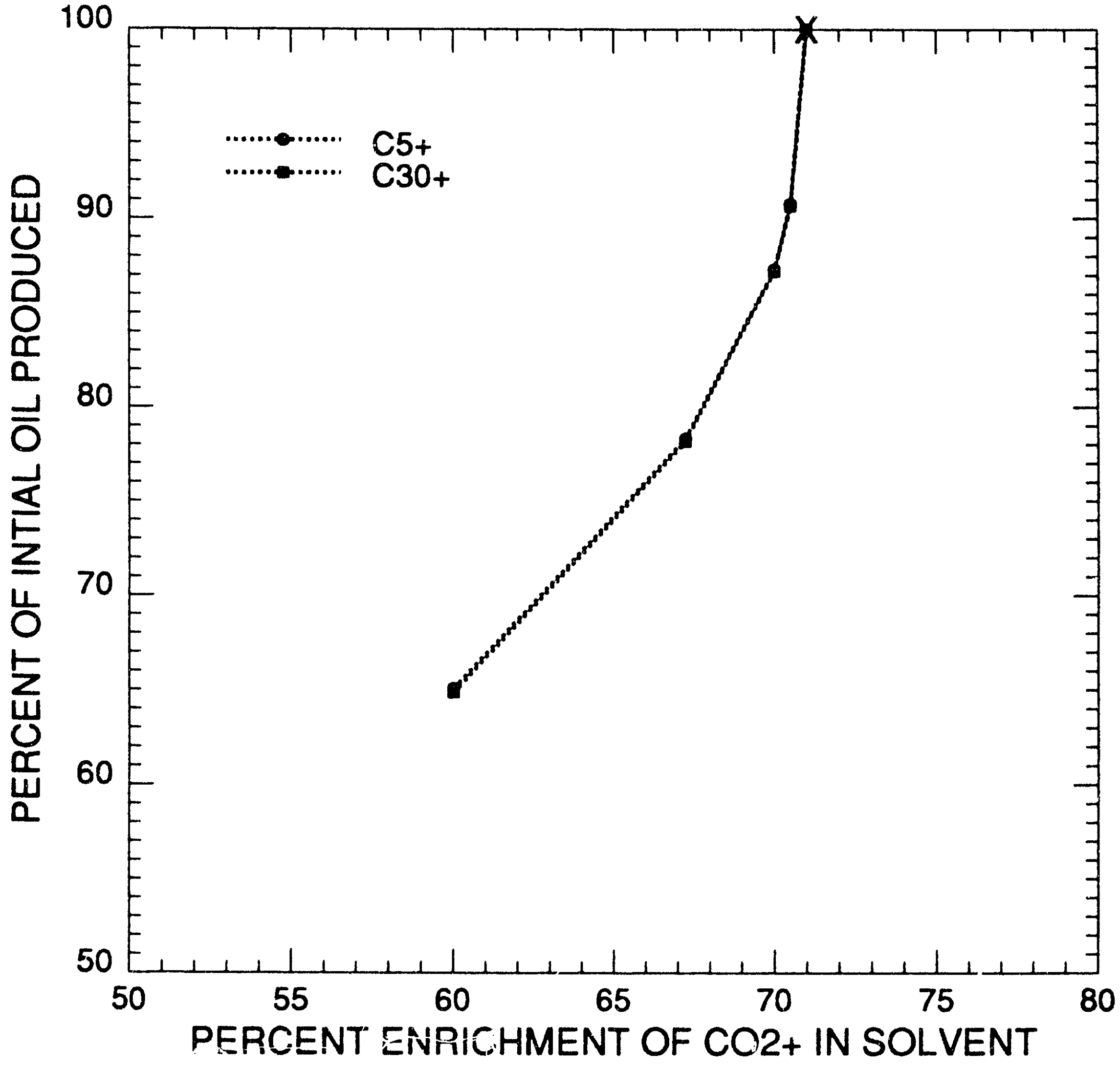

Figure 3.18: Analytical recovery versus enrichment of CO_{2+} at breakthrough. The minimum enrichment for multicontact miscibility is approximately 71/29 CO_{2+}/C_1N_2.

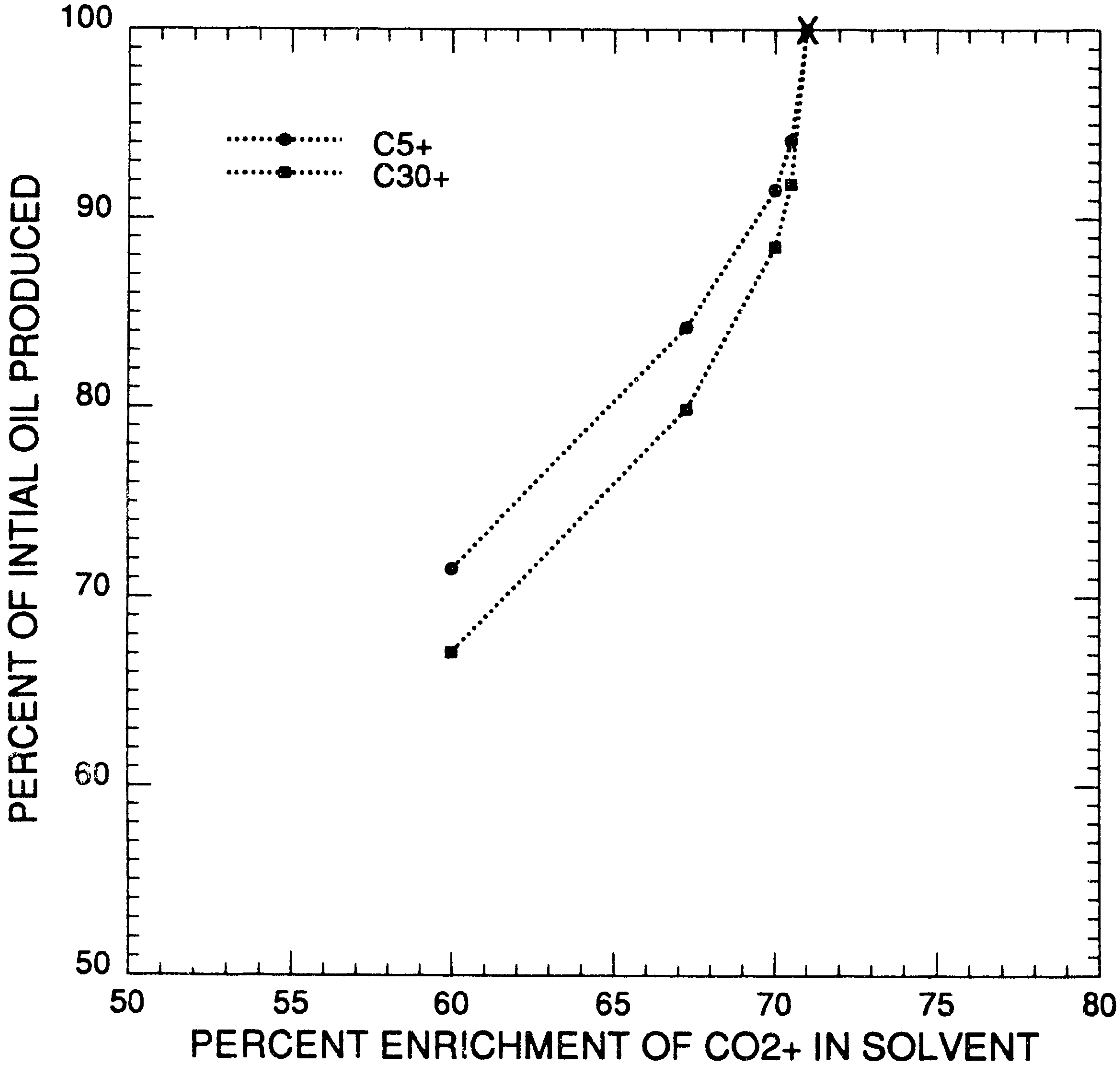

Figure 3.19: Analytical recovery versus enrichment of CO_{2+} at 1.0 PVI.

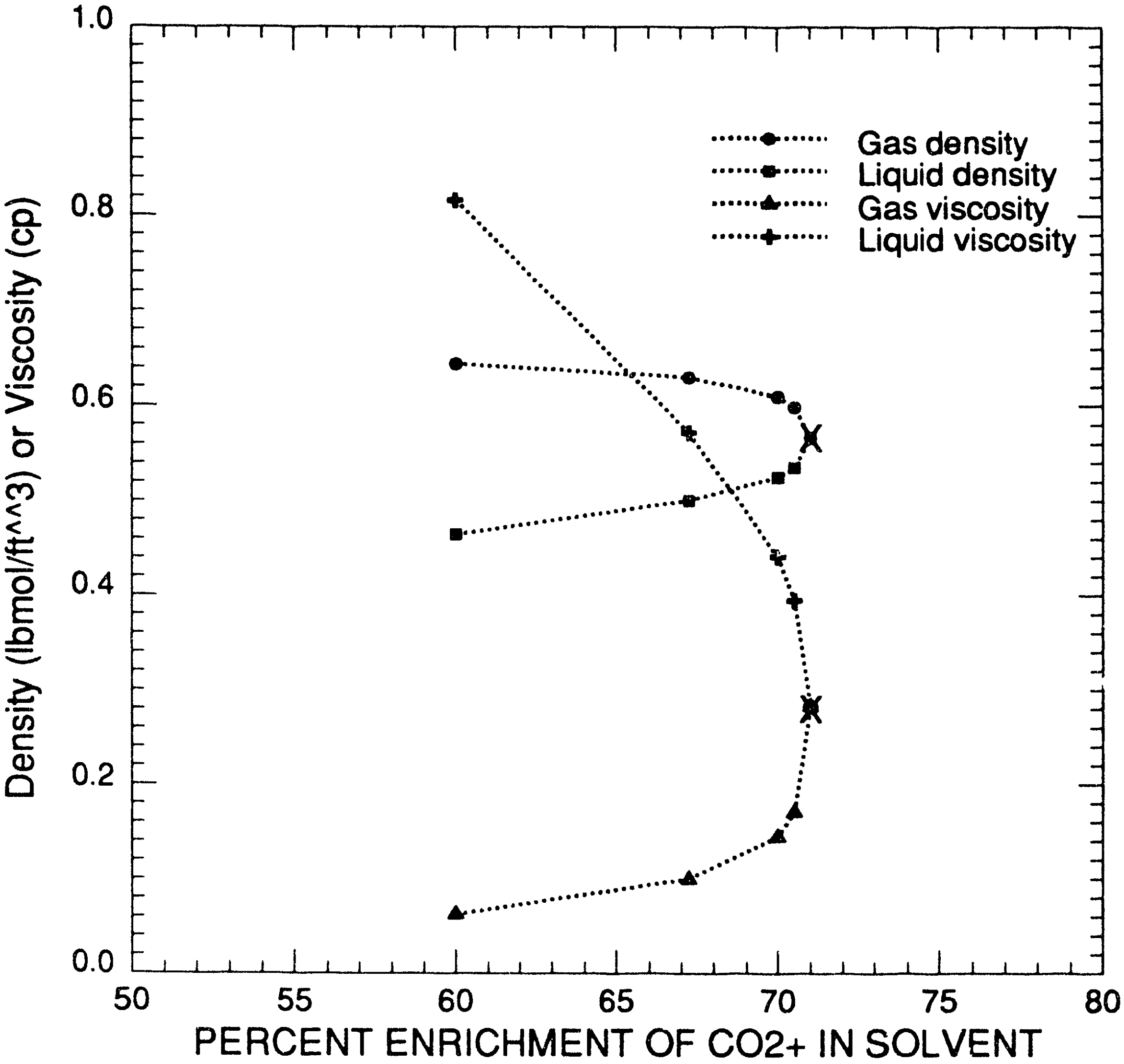

Figure 3.20: Gas and liquid properties on the crossover tie line versus enrichment of CO_{2+}. The minimum enrichment for multicontact miscibility is approximately 71/29 CO_{2+}/C_1N_2.

In this section we consider systems that are more complex in two ways. First, we relax the assumption of no volume change as components change phase since this assumption cannot yield late breakthrough times observed in experiments, and we demonstrate that the resulting flow velocity variations can be decoupled from the composition variations. Second, we consider solutions in which the portion of the solution that lies on the crossover tie line is reached by a continuous variation along a nontie-line path. In such cases, the crossover tie line is no longer found by extension of tie lines but by integration. The example solutions presented illustrate important variations in the patterns of behavior possible in multicomponent systems. They demonstrate, for example that miscibility can develop if any one of the initial, injection, or crossover tie lines is a critical tie line.

Analytical solutions for displacement of oil by CO_2/C_4, N_2 and CH_4/C_3 are presented. The analytical solutions are compared with the numerical solutions obtained with a 1-D compositional simulator. When effects of numerical dispersion are made small through use of fine grids, the analytical and numerical solutions agree well. The comparison of these solutions indicate how dispersion (numerical or physical) influences composition path behavior in multicontact miscible floods. We show also that variations in the local flow velocity induced by volume change can alter significantly the pattern of solution behavior from that observed for flow without volume change. Furthermore, the changes in the local flow velocity are found to be significant in all cases, particularly downstream of the leading shock.

Both the analytical and the numerical solutions agreed well within the limits of numerical dispersion. Numerical dispersion arises due to discrete time and space, and decreases as we refine the grids. We obtained that numerical dispersion, even in low levels, can alter the composition path significantly.

The example solutions given illustrate the patterns of behavior observed in condensing/ condensing, vaporizing/vaporizing and condensing/vaporizing gas drives. We show that the classification of the displacement in terms of condensing and vaporizing behavior is directly related with the key tie lines. Furthermore, one of these key tie lines can determine the limit of multicontact miscibility (MCM).

3.3.1 Mathematical Model

Under the assumptions stated by Monroe et al. [45], the governing mass balance equation for one dimensional multiphase multicomponent systems are

$$\frac{\partial G_i}{\partial \tau} + \frac{\partial F_i}{\partial \xi} = 0 \quad i = 1, n_c. \tag{3.23}$$

Explicit definition of the overall number of moles of component i is

$$G_i = G_i(\vec{Z}) = \sum_{j=1}^{n_p} x_{ij}\rho_{jD}S_j \quad i = 1, n_c, \tag{3.24}$$

and the overall molar fractional flow of component i is

$$F_i = F_i(\vec{Z}, v_D) = v_D \sum_{j=1}^{n_p} x_{ij}\rho_{jD}f_j \quad i = 1, n_c. \tag{3.25}$$

where

G_i = local overall number of moles of component i
F_i = overall fractional flow of component i
Z_i = overall mole fraction of component i

$\vec{Z}$ = vector of overall component mole fractions
n_c = number of components
n_p = number of phases
f_j = fractional flow of phase j
S_j = saturation of phase j
x_{ij} = mole fraction of component i in phase j
t = real time
ϕ = porosity
ξ = dimensionless distance, $\frac{x}{L}$
L = system length
τ = dimensionless time, $\frac{v_{inj}t}{\phi L}$, (pore volume)
ρ_{ini} = density of the original fluid in the system
ρ_j = molar density of phase j
ρ_{jD} = dimensionless molar density of phase j, $\frac{\rho_j}{\rho_{ini}}$
v = total flow velocity
v_D = dimensionless total velocity, $\frac{v}{v_{inj}}$
v_{inj} = injection velocity

The definition of Eq. 3.23 of the overall molar flux of component i differs from that stated in Eq. 3.1 in that it is a function of the local dimensionless flow velocity, v_D. The flow velocity varies with spatial location when components change volume as they transfer between phases.

Mathematically, the system of differential equations does not carry any information about the discontinuities. It applies only when there are continuous variations in the state space. Discontinuities in the solution must be introduced if the solution of the differential equations is multivalued at a given point in the one-dimensional porous medium. Finally, the components present at the discontinuity must also satisfy the integral material balance (Rankine-Hugoniot condition [67]). The convective velocity is eliminated from the following shock balance equations.

$$\Lambda_i^* = \frac{(F_i^{*II} - F_i^{*I})F_{n_c}^{*II} - (F_{n_c}^{*II} - F_{n_c}^{*I})F_i^{*II}}{(G_i^{II} - G_i^{I})F_{n_c}^{*II} - (G_{n_c}^{II} - G_{n_c}^{I})F_i^{*II}} \quad i = 1, n_c - 1. \tag{3.26}$$

where I and II indicates the upstream and downstream sides of the shock, and

$$F_i^* = \sum_{j=1}^{n_p} x_{ij}\rho_{jD} f_j \quad i = 1, n_c. \tag{3.27}$$

where,

F_i^* = scaled overall fractional flow of component i, $\frac{F_i}{v_D}$
Λ_i = shock wave velocity
Λ_i^* = scaled shock wave velocity, $\frac{\Lambda_i}{v_D}$

The shock speed is scaled with respect to upstream or downstream convective velocity depending on the logical direction of the solution.

$$\Lambda_i^* = \frac{\Lambda_i}{v_D^I} \tag{3.28}$$

The convective velocity of the unknown side can also be determined from the equation below once the speed of discontinuity is known.

$$\frac{v_D^{II}}{v_D^{I}} = \frac{\Lambda_i^*(G_{n_c}^{II} - G_{n_c}^{I}) + F_{n_c}^{*I}}{F_{n_c}^{*II}} \tag{3.29}$$

The equation system (3.23) can be solved using the method of characteristics, whereby it can be transformed into an eigenvalue problem to construct the continuous solution. The hyperbolic equation system is a Riemann problem [38, 63], where the initial data are prescribed by two different constant composition states connected by a discontinuity at $\xi = 0$,

$$Z_i(\xi, 0) = \begin{cases} Z_{i_{inj}} & \xi < 0 \\ Z_{i_{ini}} & \xi > 0. \end{cases} \tag{3.30}$$

$Z_{i_{ini}} =$ initial overall mole fraction of component i
$Z_{i_{inj}} =$ injected overall mole fraction of component i

The solution path in the composition domain must connect Z_{inj} and Z_{ini}. The first step toward solution of this problem is to calculate wave velocities for all the components. These velocities are the slopes of the characteristic lines in the $\xi - \tau$ plane. The continuous solution of this problem is always a rarefaction (specifically an expansion fan) wave at which the dependent variables are functions of $\eta = \xi/\tau$ (similarity variable). This type of functional dependence is due to self-similarity of the solution [38].

The original eigenvalue problem is stated by Monroe et al. [45]. It can be rearranged to decouple the flow velocity by row operations on the original form of the problem. This is accomplished on the posed eigenvalue problem without altering the eigenvector directions. The final form of the eigenvalue problem with the velocity decoupled is

$$\begin{pmatrix} [\mathcal{F} - \lambda^* \mathcal{G}] & \vec{0} \\ \vec{\mathcal{F}}^T - \lambda^* \vec{\mathcal{G}}^T & \frac{1}{v_D} \end{pmatrix} \begin{pmatrix} \vec{e} \\ \frac{dv_D}{d\eta} \end{pmatrix} = \begin{pmatrix} \vec{0} \\ 0 \end{pmatrix} \tag{3.31}$$

where,

$\vec{e}$ = eigenvector
η = similarity variable, $\frac{\xi}{\tau}$
λ = eigenvalue
λ^* = scaled eigenvalue, $\frac{\lambda}{v_D}$
λ_t = eigenvalue associated with composition variation along a tie line

First row elements of the matrix equation 3.31 are:

$$[\mathcal{F}] = \frac{\partial F_i^*}{\partial Z_j} - \frac{F_i^*}{F_{n_c}^*}\frac{\partial F_{n_c}^*}{\partial Z_j} \quad i = 1, n_c - 1 \quad j = 1, n_c - 1$$

$$[\mathcal{G}] = \frac{\partial G_i}{\partial Z_j} - \frac{F_i^*}{F_{n_c}^*}\frac{\partial G_{n_c}}{\partial Z_j} \quad i = 1, n_c - 1 \quad j = 1, n_c - 1 \tag{3.32}$$

and the second row elements are :

$$\vec{\mathcal{F}}^T = \left(\frac{1}{F^*_{n_c}} \frac{\partial F^*_{n_c}}{\partial Z_j} \quad j = 1, n_c - 1\right) \tag{3.33}$$

$$\vec{\mathcal{G}}^T = \left(\frac{1}{F^*_{n_c}} \frac{\partial G_{n_c}}{\partial Z_j} \quad j = 1, n_c - 1\right) \tag{3.34}$$

The matrix equation 3.31 is a 2x2 system with a submatrix of order $n_c - 1$ posing an eigenvalue problem of the form

$$[\mathcal{F} - \lambda^* \mathcal{G}]\,\vec{e} = \vec{0} \tag{3.35}$$

Eigenvectors are determined from the eigenvalue problem defined by Eq. 3.35. They indicate the characteristic directions in composition space and are given by

$$\vec{e} = \begin{pmatrix} \frac{dZ_1}{d\eta} \\ \frac{dZ_2}{d\eta} \\ \cdot \\ \cdot \\ \frac{dZ_{n_c-1}}{d\eta} \end{pmatrix} \tag{3.36}$$

Eq. 3.35 depends only on composition, not on local convective velocity. The last term is a scalar equation which can be integrated for the convective velocity along the composition path,

$$\left(\vec{\mathcal{F}}^T - \lambda^* \vec{\mathcal{G}}^T\right) \vec{e} = -\frac{1}{v_D} \frac{dv_D}{d\eta} \tag{3.37}$$

Integration of Eq. 3.37 (taking a small integration step size) for continuous variations yields

$$v_D = v_{D_o} e^{-cs} = v_{D_o}(1 - cs + \mathcal{O}(s^2)) \tag{3.38}$$

s = integration step size

where c is a product of the eigenvector calculated from Eq. 3.31,

$$c = \left(\vec{\mathcal{F}}^T - \lambda^* \vec{\mathcal{G}}^T\right) \vec{e}. \tag{3.39}$$

The expanded form of v_D in Eq. 3.38 is equivalent to the form without decoupling. The eigenvectors are defined as the changes of the composition along the path defined with a single parameter η. Since the dependence on η is not known explicitly, the integration along the eigenvector is performed numerically using an integration step size s.

The equations above include the effects of phase behavior through the phase compositions in the definitions of F_i and G_i. The equilibrium calculations were performed with the Peng-Robinson [60] equation of state. The phase densities were corrected using volume translation similar to that described by Peneloux et al. [59]. Phase viscosities were calculated with the correlation of Lohrenz et al. [40] from the phase composition data.

3.3.2 Sample Solutions

Three different quaternary model systems are considered. The quaternary systems selected show quite distinctive behavior. A CO_2/C_4 injection system is examined first to show that development of miscibility can be controlled by the injection tie line. Sample solutions for a N_2 displacement system show how the initial tie line can also control development of miscibility. In a displacement by a CH_4/C_3 mixture, however, development of miscibility is determined by the crossover tie line. Properties of the components used are shown in Table 3.6 [62, 15]. The volume translation parameters are calculated based on Jhaveri and Youngren [29], and Deo et al. [15]. where,

M_w = molecular weight
P_c = critical pressure
s_i = volume translation parameter
T_c = critical temperature
V_c = critical specific volume
ρ_i = molar density of component (pure) i
ω = acentric factor
δ_{ij} = binary interaction parameter of component i and j

In this study, simple functional forms of relative permeabilities have been used. For the vapor phase:

$$k_{rg} = k_{rge}\left[\frac{S_g}{1. - S_{or}}\right]^{n_g} \tag{3.40}$$

and for the liquid phase:

$$k_{rl} = k_{rle}\left[\frac{1. - S_g - S_{or}}{1. - S_{or}}\right]^{n_l} \tag{3.41}$$

where,

k_{rg} = relative permeability of gas phase
k_{rge} = end point of k_{rg}
k_{rl} = relative permeability of liquid phase
k_{rle} = end point of k_{rl}
n_g = gas relative permeability exponent
n_l = liquid relative permeability exponent
S_g = gas saturation
S_{or} = residual oil saturation

The relative permeability parameters used in this study are presented in Table 3.7. The fractional flow equations for the phases come from Darcy's law with no gravity and capillary pressure effects, and they are nonlinear functions of saturation (composition). The fractional flow equation for phase j is

$$f_j = \frac{\frac{k_{rj}}{\mu_j}}{\sum_{j=1}^{n_p} \frac{k_{rj}}{\mu_j}} \tag{3.42}$$

Table 3.6: Pure component properties and binary interaction parameters used in computations.

Component	M_w	P_c (psia)	T_c (° F)	V_c (ft^3/mol)	ω	s_i (ft^3/mol)
CO_2	44.01	1071.0	87.90	1.5060	0.2250	0.0600
N_2	28.01	493.0	-232.42	1.4403	0.040	-0.0014
CH_4	16.04	667.8	-116.63	1.5899	0.0104	-0.0661
C_3	44.09	615.7	205.95	3.2492	0.1520	-0.0768
C_4	58.12	550.7	305.65	4.0828	0.2010	-0.0744
C_{10}	142.29	305.7	652.10	9.6610	0.4900	0.1602
C_{20}	282.56	161.6	920.91	20.5390	0.9070	1.8418
Component	ρ_i (mol/ft^3)	δ_{ij}				
185° F	3100 psia	—	CH_4	C_3	C_{10}	C_{20}
CH_4	0.4735	—	0.0000	0.0200	0.0420	0.0540
C_3	0.6674	—	0.0200	0.0000	0.0100	0.0100
C_{10}	0.3054	—	0.0420	0.0100	0.0000	0.0000
C_{20}	0.1740	—	0.0540	0.0100	0.0000	0.0000
Component	ρ_i (mol/ft^3)	δ_{ij}				
160° F	1600 psia	N_2	CO_2	CH_4	C_4	C_{10}
N_2	0.2370	0.0000	—	0.0310	0.1200	0.1200
CO_2	0.4237	—	0.0000	0.1000	0.1257	0.0942
CH_4	0.2627	0.0310	0.1000	0.0000	0.0270	0.0420
C_4	0.5859	0.1200	0.1257	0.0270	0.0000	0.0080
C_{10}	0.3041	0.1200	0.0942	0.0420	0.0080	0.0000

Table 3.7: Relative permeability parameters for the example quaternary problems.

Parameter	Value
k_{rge}	0.8
k_{rle}	0.8
S_{or}	0.05
n_g	3.0
n_l	3.0

where,

k_{rj} = relative permeability of phase j
μ_j = viscosity of phase j

The type of the fractional flow functions selected yield a smooth S-shape curve with a single point of inflection. The character of the solution is directly related to the shape of the fractional flow curve. Because phase compositions are fixed for overall compositions on a single tie line, and because phase viscosities depend only on the composition of the phase, there is a single fractional flow curve for each tie line. Therefore, the family of fractional flow curves in the composition space constitutes a fractional flow surface. Hence, the properties (such as curvature) of this surface are also very important when a change from one tie line to another is considered.

In each of the four component solutions described below there are three key tie lines: (1) the one which passes, when extended, through initial composition, called the initial tie line, (2) the one which passes, when extended, through injection composition, the injection tie line, and (3) the crossover tie line. The first two are easy to obtain through a negative flash [83]. However, the crossover tie lines must be obtained differently in each case. A geometrical construction can be used in cases like those described in Sections 3.1 and 3.2. In all cases, however the crossover tie line is the intersection of two ruled surfaces[1] associated with the initial and injection tie lines. These surfaces are constructed by the tie lines that are traversed along the construction of the path.

The relative permeability functions depend only on the vapor saturation. However, the vapor saturation is a function of overall composition. For two-phase equilibrium conditions where gas and liquid are present,

$$S_g = \frac{V}{V + \frac{\rho_v}{\rho_l}(1 - V)} \tag{3.43}$$

where,

V = mole fraction of vapor phase
ρ_l = molar density of liquid phase
ρ_v = molar density of vapor phase

The mole fraction of vapor phase can be calculated from equilibrium phase compositions as

$$V = \frac{Z_i - x_{il}}{x_{iv} - x_{il}} \tag{3.44}$$

where,

x_{il} = mole fraction of component i in liquid phase
x_{iv} = mole fraction of component i in vapor phase

According to Eq. 3.43, the phase saturation is a function of the density ratio as well as phase compositions and overall composition. Therefore, correct estimation of phase densities will be important for the overall performance of the two-phase flow.

3.3.3 Displacement by a Carbon Dioxide and Butane Mixtures

Next, we consider displacement of an oil mixture of 10% CH_4, 10% C_4 and 80% C_{10} by 94% CO_2 and 6% C_4 at 1600 psia and 160°F. Fig. 3.21 illustrates the composition path for this

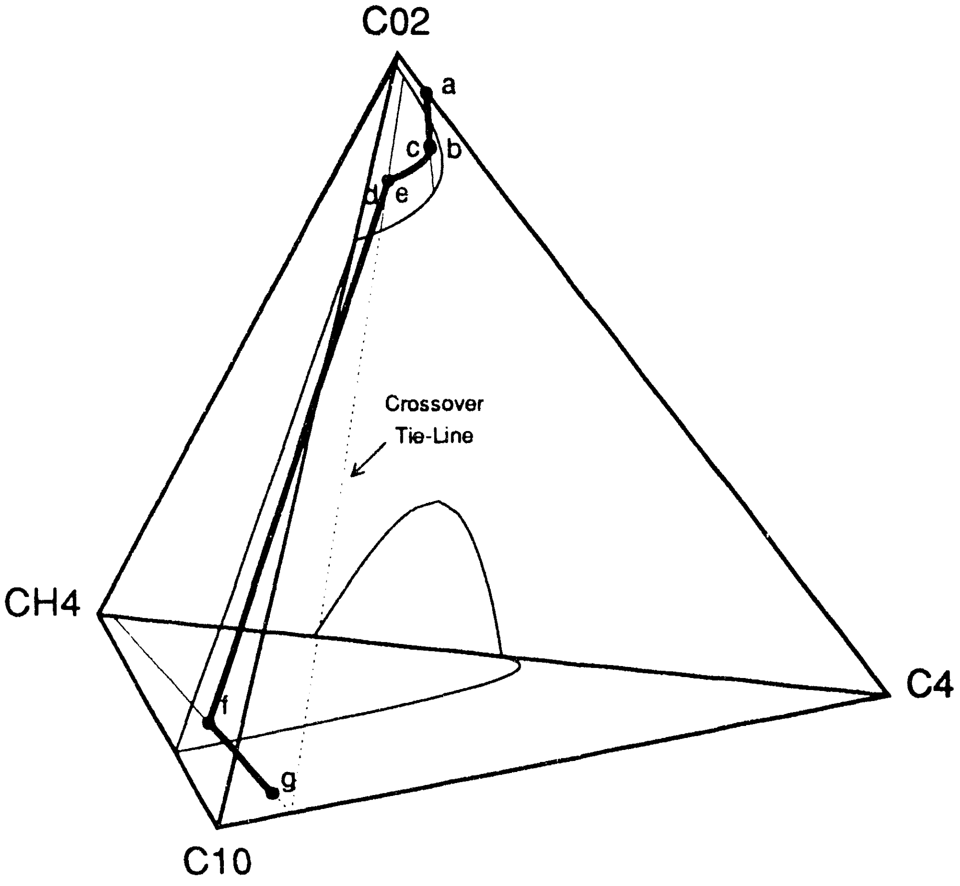

Figure 3.21: Composition route for displacement of a $CH_4/C_4/C_{10}$ mixture by a CO_2/C_4 mixture at 1600 psia and 160° F.

displacement along with the phase behavior. The relevant displacement profiles are shown in Fig. 3.22. The compositional coordinates of the key points in the solution are given along with the associated wave velocities in Table 3.8.

In this continuous drive, there is a trailing shock along the injection tie line from the injection composition, **a**, to point **b**. Then a continuous variation along the same tie line to point **c** follows, where the solution path switches from the tie-line path to nontie-line path. This segment extends until the crossover tie line is reached at point **d**. Until this point the solution route lies on the $CO_2/C_4/C_{10}$ face of the quaternary diagram (Fig. 3.21). On the crossover tie line, another path switch would be necessary if the solution route were to trace a path to the initial tie line. However, continuous variations from this point toward injection tie line have decreasing velocity, which violates the condition that requires monotonicity of the wave velocities. Therefore, the only compatible connecting path is via a shock to point **f**. Finally, the only possible wave is a fast shock from point **f** to the initial oil composition **g**.

The quaternary solution can be described as two subternary solutions connected through the crossover tie line. The solution segment on the $CO_2/C_4/C_{10}$ face as well as the segment on the ruled surface (ternary plane for this case) bounded by the initial tie line and the crossover tie line are typical of paths observed in four component condensing gas drives. Injected gas (94% CO_2 and 6% C_4) transfers the intermediates (C_4) into the fluid contacted in the transition zone portion between points **c** and **d**. Between points **e** and **f**, the CO_2 is the condensing component. Therefore, the behavior of this system can be classified as a condensing/condensing gas drive.

In this case, the crossover tie line can still be determined by the geometrical construction outlined in Section 3.1.3. The proof that the crossover tie line is so determined is quite similar to that given in section 3.1.4. In this case, however, the shock **e** → **f** is not a tangent shock (upstream intermediate discontinuity). Instead, the point **e** is determined by integration along the nontie-line path that departs from the injection tie line at the equal eigenvalue point, **c**. Point is the intersection of that path with the crossover tie line.

A finite difference solution for the same system was also obtained. The numerical and analytical solutions are compared in Fig. 3.23. The numerical scheme that was used is an explicit one point upstream weighting scheme. The numerical solution agrees well with the analytical solution for both figures, additional evidence that the analytical solution is correct. However, the numerical solution does differ in some ways from the analytical solution. Disagreement is the largest in the region of the solution where the path passes through an equal eigenvalue point (point **c** on Fig. 3.21). Evidently the small amount of numerical dispersion around the equal eigenvalue point smears the solution along the nontie-line path, and hence the switch in the numerical solution is poorly approximated. The strong shocks, on the other hand, show sharpening behavior as the injection progresses, and their agreement level with the analytical solution increases. Large constant states in the solution profile are also predicted very accurately in the numerical solution. In the numerical solutions, the total velocity is treated using a volumetric balance as suggested by Wattenbarger [82]. The total velocity in front of the leading shock (fastest moving discontinuity) was calculated indirectly based on the material balance at the outlet rather than direct numerical calculations. This was necessary because the velocity at the downstream of the leading shock fluctuates between two limits which were determined by the last point in the two phase portion of the profiles. Since the saturation of this last point changes at each time step, the total velocity at the downstream of this point changes. Calculation of this velocity is based on the shock point in the two phase, region as can seen from the shock balances.

In the first finite difference calculation (Fig. 3.23), the 2500 grid blocks were used, and the time step size was one fourth of the grid step size ($\frac{\Delta\xi}{\Delta\tau} = 4$). In the second finite difference

---

[1] Ruled Surface: A ruled surface is one that is generated by sequence of straight lines that are normal to a curve in three-dimensional space. A cylinder is the ruled surface with a circle as generating curve, for example.

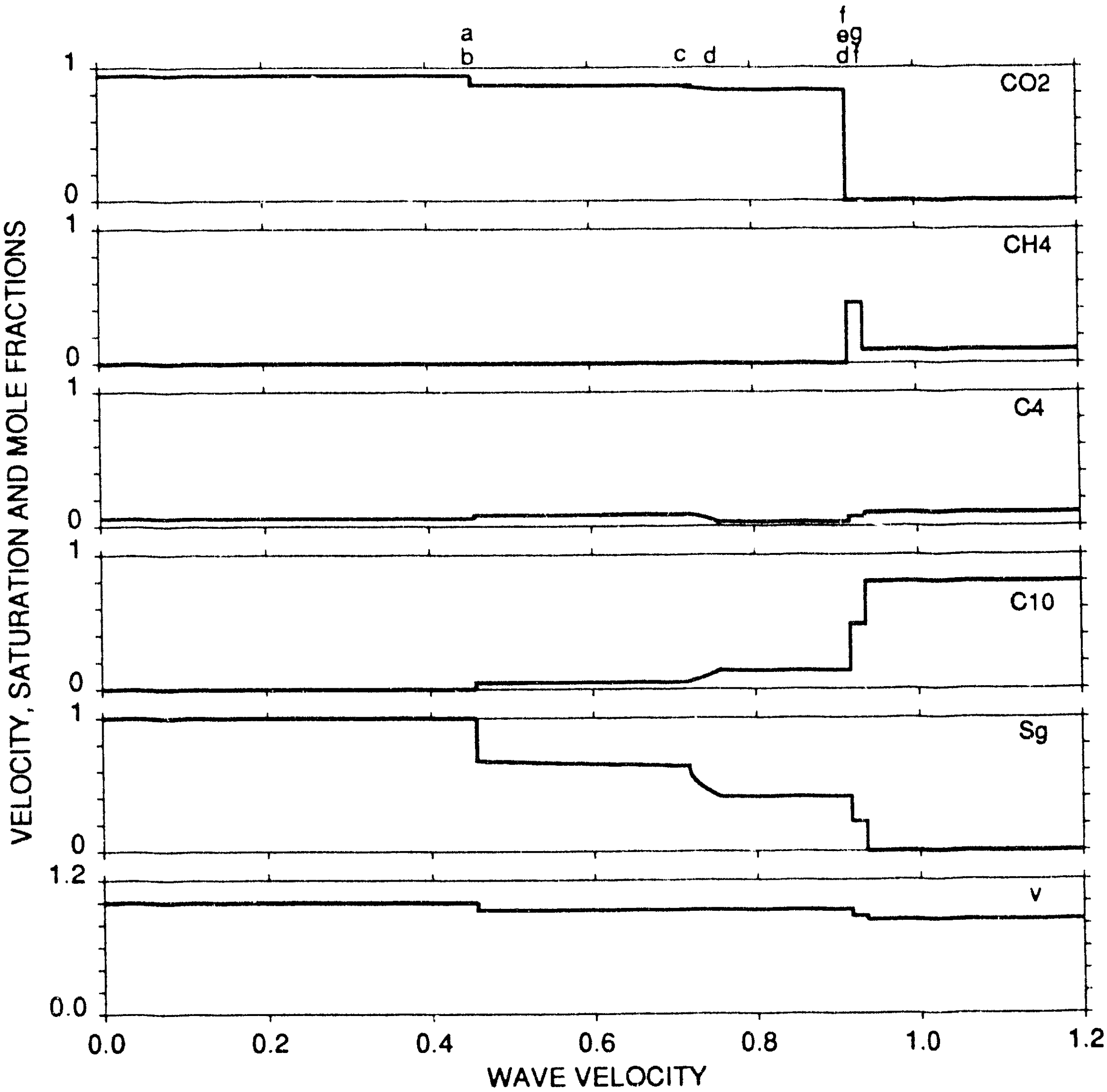

Figure 3.22: MOC profiles for displacement of $CH_4/C_4/C_{10}$ a mixture by a CO_2/C_4 mixture at 1600 psia and 160° F.

Table 3.8: MOC solution for the composition route of Fig. 3.3.1 at 1600 psia and 160° F.

Composition Label	Composition (Mole Fraction)				Total Flow Velocity	Gas Saturation (Vol. Fraction)	Wave Velocity
	CO_2	CH_4	C_4	C_{10}			
a	0.9400	0.0000	0.0600	0.0000	1.0000	1.0000	0.4559
b	0.8684	0.0000	0.0844	0.0472	0.9355	0.6785	0.4559
c	0.8641	0.0000	0.0858	0.0501	0.9355	0.6396	0.7176
d	0.8323	0.0000	0.0302	0.1375	0.9361	0.4067	0.7560
e	0.8323	0.0000	0.0302	0.1375	0.9361	0.4067	0.9167
f	0.0000	0.4518	0.4808	0.4808	0.8770	0.2216	0.9167-0.9355
g	0.0000	0.1000	0.1000	0.8000	0.8423	0.0000	0.9355

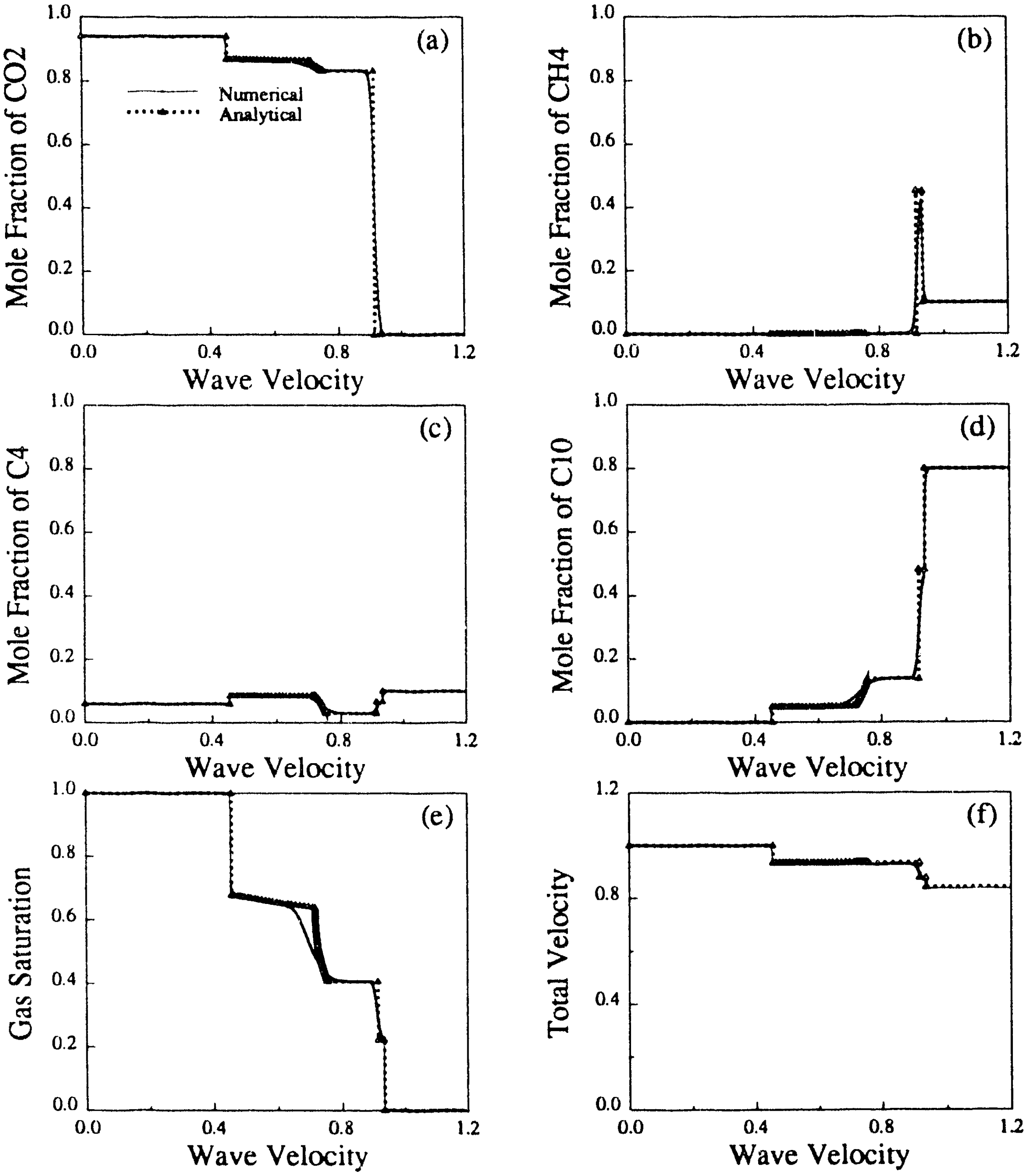

Figure 3.23: Comparison of MOC and **fine** grid FD solutions, $\frac{\Delta\xi}{\Delta\tau}$=4 and 2500 grid blocks, composition profiles (**a to d**), saturation profile (**e**) and velocity profile (**f**) for displacement of a $CH_4/C_4/C_{10}$ mixture by a CO_2/C_4 mixture at 1600 psia and 160° F.

calculation (Fig. 3.24), however, 500 grid blocks were used ($\frac{\Delta\xi}{\Delta\tau} = 5$). Both runs were terminated at 0.5 pore volumes of injection. Then the profiles were stretched by a factor of two for comparison with the analytical solution at one pore volume injected. In the composition profiles shown in Fig. 3.23b, there is a sharp, narrow CH_4 bank just behind the leading shock which disappears at the **f** → **g** shock as Fig. 3.22 and Table 3.8 show, the speeds of **e** → **f** and **f** → **g** shocks are nearly equal. Hence, the numerical dispersion preceding the **e** → **f** shock masks the zone of constant state behind the **f** → **g** shock, showing a merged shock. [2] Comparison of Figs. 3.23 and 3.24 indicates that as the grid size is refined, the numerical solution approaches the analytical solution. In the course grid run, the methane bank is not as large as it is in the analytical solution. Also, the numerical profile is smeared (dispersed) in a conservative fashion. Further inspection of this course grid solution (Fig. 3.24) also indicates smearing of all the shocks as well as a slower trailing shock (**a** → **b shock** in Fig. 3.21). In the numerical solutions, it is observed that the amount of smearing increases as one of the tie lines approaches the locus of plait points (or as the system approaches miscibility). That behavior is due to large changes in the properties and the equilibrium compositions that result from small changes in composition. Therefore, small errors in composition can change the other composition dependent properties more than the order of the error made in composition. In this system the injection tie line is close to the plait point which can be seen visually from Fig. 3.21 as well as from the large speed of the trailing shock.

3.3.4 Displacement by Pure Nitrogen

Next, consider displacement of the initial mixture, 10% CH_4, 20% C_4 and 70% C_{10} by pure nitrogen (N_2). Thus, the initial composition and displacement conditions are exactly the same as in the CO_2 flood example shown in Figs. 3.1 and 3.2 of Section 3.1. The composition path and the solution profiles for the system are given in Figs. 3.25 and 3.26. The labeled points and their associated wave velocities are presented in Table 3.9.

The labeling is done in the logical order of the solution construction. The solution structure for this case is quite different from that of the CO_2 flood example of section 3.1 previous case. This system can be classified as a vaporizing/vaporizing gas drive because it consists of two vaporizing sections connected through the crossover tie line on the CH_4 free face.

There is a leading shock from point **a** to point **b** along the initial tie line, followed by a continuous variation along the same tie line until the equal eigenvalue point, **c**, is reached. The curvature of the solution profiles change sharply at this point. A path switch occurs at **c**, followed by evolution along a nontie-line path. The nontie-line path extends until the crossover tie line is reached at point **d**. There is a large zone of constant state **d** → **d** because the wave velocity on the crossover tie line at **d** is greater than the wave velocity on the nontie-line path at point **d**. The constant state is followed by a continuous variation along crossover tie line to point **e**. That continuous variation is missing in the CO_2 displacement presented in Section 3.1. Point **e** is connected by a shock to **f** since smooth variations are not permissible due to the requirement for monotonocity of the wave velocity. Next, there is a continuous variation along the injection tie line to point **g**, where a trailing shock connects to the injection composition, **h**.

This system has continuous segments along all the key tie lines. As in the CO_2 displacement, the phase behavior dominates the spatial composition distribution. The most volatile (highest K-value)[3] in-situ component has the fastest bank in the transition zone. This is also observed by Johns [31] in constant-K simulations of pure component injection processes with no volume change on mixing. Upstream, in-situ components disappear in the order of their volatility, CH_4, C_4 and

---

[2] Shock-like structure would be a better term because it is not possible to have a sharp shock due to numerical dispersion. However, it is clear that there is actually a shock at the same location in the analytical solution.

[3] A K-value or K_i: equilibrium ratio for component i, x_{iv}/x_{il}

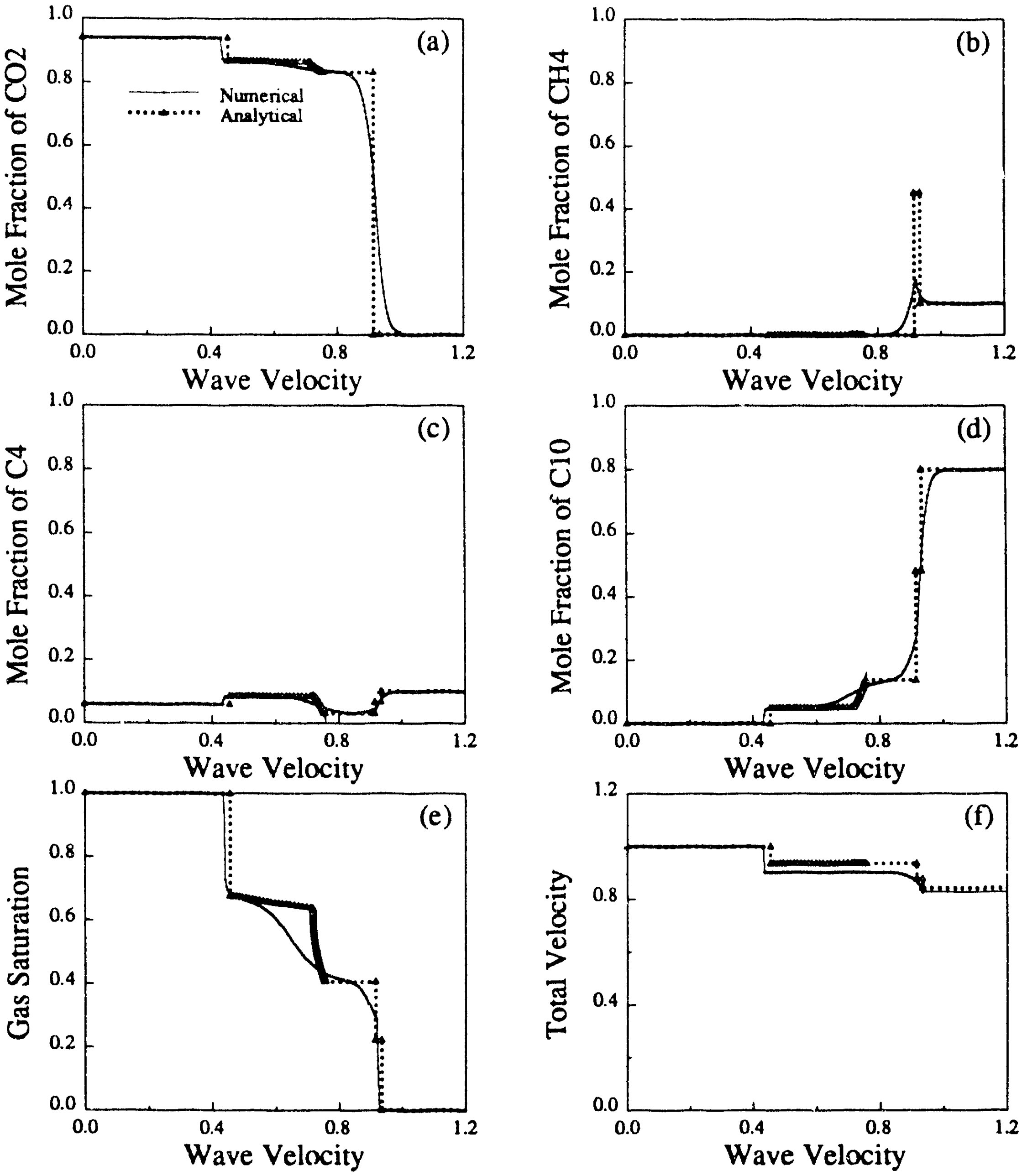

Figure 3.24: Comparison of MOC and FD solutions, $\frac{\Delta\xi}{\Delta\tau}$=5 and 500 grid blocks, composition profiles **(a to d)**, saturation profile **(e)** and velocity profile **(f)** for displacement of a $CH_4/C_4/C_{10}$ mixture by a CO_2/C_4 mixture at 1600 psia and 160° F.

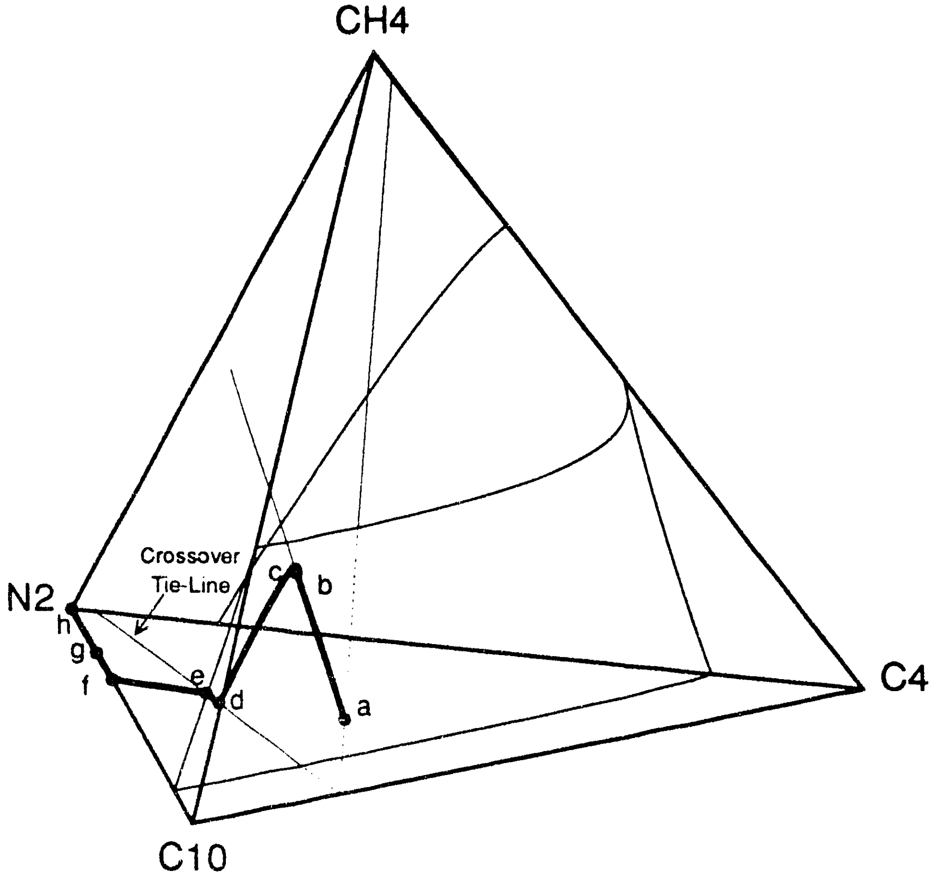

Figure 3.25: Composition route for displacement of a $CH_4/C_4/C_{10}$ mixture by pure N_2 at 1600 psia and 160° F.

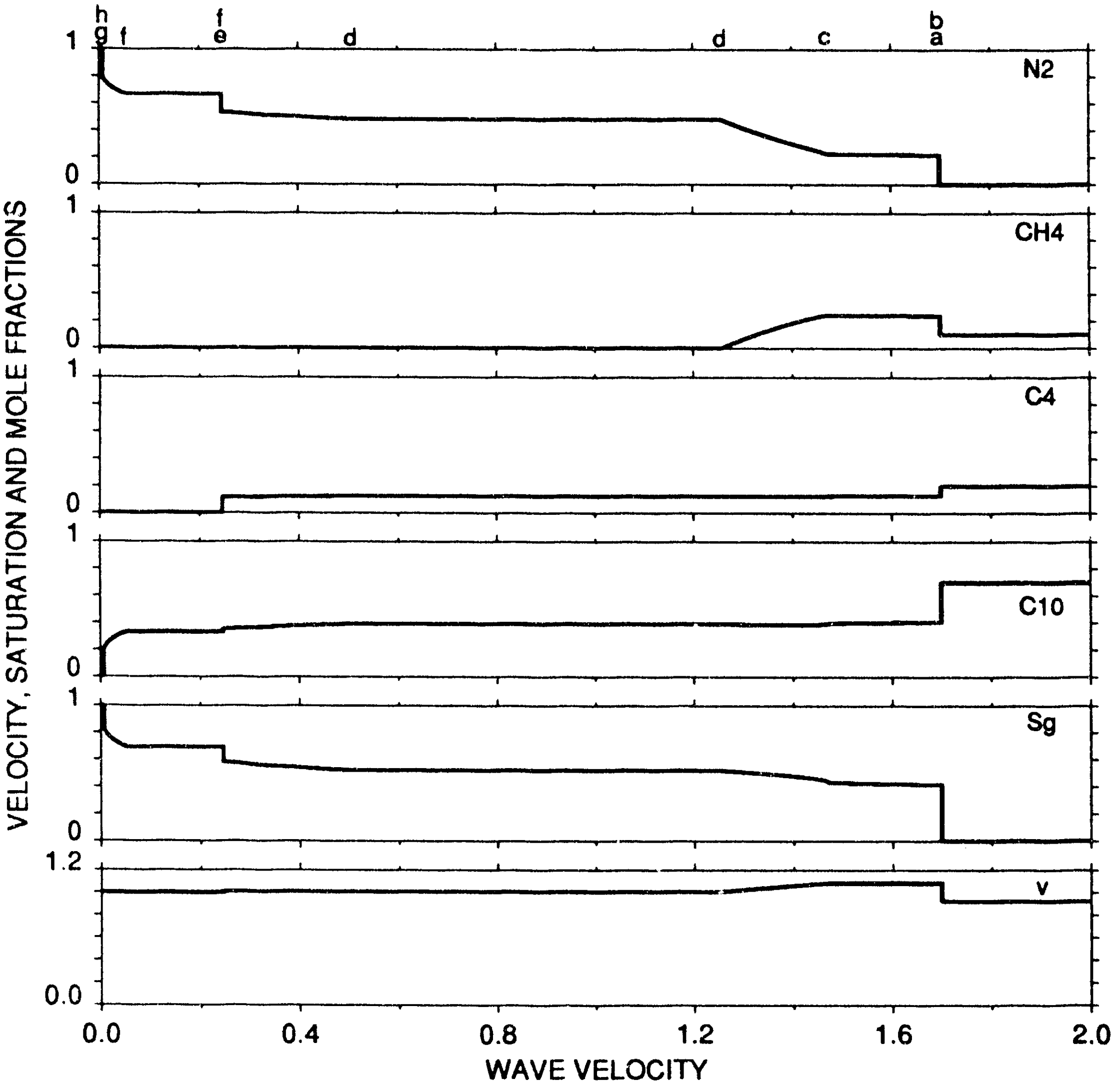

Figure 3.26: MOC profiles for displacement of a $CH_4/C_4/C_{10}$ mixture by pure N_2 at 1600 psia and 160° F.

Table 3.9: MOC solution for the composition route of Fig. 3.3.5 at 1600 psia and 160° F.

Composition Label	Composition (Mole Fraction)				Total Flow Velocity	Gas Saturation (Vol. Fraction)	Wave Velocity
	N_2	CH_4	C_4	C_{10}			
a	0.0000	0.1000	0.2000	0.7000	0.9209	0.0000	1.6987
b	0.2215	0.2415	0.1300	0.4069	1.0859	0.4150	1.6987
c	0.2271	0.2451	0.1283	0.3995	1.0859	0.4294	1.4721
d	0.4831	0.0000	0.1245	0.3923	1.0105	0.5193	1.2570-0.5082
e	0.5343	0.0000	0.1145	0.3512	1.0105	0.5822	0.2457
f	0.6677	0.0000	0.0000	0.3323	0.9996	0.6913	0.2457-0.0529
g	0.7940	0.0000	0.0000	0.2060	0.9996	0.8184	0.0070
h	1.0000	0.0000	0.0000	0.0000	1.0000	1.0000	0.0070

C_{10} respectively. The component with the lowest K-value, C_{10}, remains until the slowest shock arrives at the outlet.

The slopes of the tie lines, which are functions of the K-values, play important roles in the construction of the solution. The initial tie line in this example solution is not unique as long as the initial composition is strictly confined to the N_2 free face. In other words, two tie lines can be found that extend through the initial composition, **a**. Both are shown in Fig. 3.25. The first is the tie line in the interior of the quaternary diagram, along which the solution route is shown to enter the two-phase region. The second is a tie line that lies in the $CH_4/C_4/C_{10}$ face. A solution route similar to that described above can be found. It begins with a shock along the second tie line. That solution satisfies the monotonicity requirement and the requirement that the route follow paths. However, the second route can easily be eliminated by requiring that the solution be continuous with respect to the initial data, one of the conditions proposed by Hadamard [86] for a well-posed problem. This condition states that a slight variation of the initial data for the problem should cause the solution to vary only slightly. We also assume that Hadamard's first two conditions are satisfied, that is that a solution exists, and it is unique. Addition of an infinitesimal amount of N_2 to the initial composition will resolve the non-uniqueness issue, because two tie lines will not intersect at this new point. If the initial point **a** is the limit of such points as the N_2 concentration goes to zero, it is clear that the solution will be continuous with respect to adding N_2 only if the initial tie line is the tie line in the interior of the quaternary diagram. Therefore, the tie line in the interior of the quaternary diagram is selected.

For this system, the numerical solution shows very good agreement with the MOC results (Fig. 3.27). The performance of the numerical solution is a lot better than that obtained in CO_2/C_4 displacement because the system is far from being MCM, as the low trailing shock speed indicates. Furthermore, the shocks and the constant states are larger than the previous case, and this causes the numerical solution to correct itself in a finite range.

3.3.5 Displacement by a Methane and Propane Mixtures

Injection of CH_4 enriched with 10% C_3 into a mixture of 50% C_{10} and 50% C_{20} is considered at 160° F and 3185 psi. The composition path is shown in Fig. 3.28, and the relevant profiles are in Fig. 3.29. The key points along with the wave velocities are presented in Table 3.10.

This four component displacement is classified as a condensing/vaporizing gas drive, a type of displacement first described by Stalkup [68] and Zick [87]. They described such behavior based on inspection of numerical simulations. The section of the solution route between the initial tie line and the crossover tie line is the condensing part, and the section between the injection tie line and the crossover tie line is the vaporizing portion.

The equivalent behaviors can also be seen on the limiting faces of the quaternary diagram when the segments of the path are projected (Fig. 3 30) on the appropriate ternary faces. The solutions in Fig. 3.30 are actual solutions for the limiting cases rather than direct projections of the solution in Fig. 3.28, though the projections would look qualitatively the same. The primed points in Fig. 3.30 (a' to f') are equivalents of the ones shown in Fig. 3.28 (**a** to **f**). The condensing part is observed when the segment from the initial tie line to the crossover tie line is projected onto the C_{10}-free face (Fig. 3.30a). In Fig. 3.30a, coordinates of point **a** and a' are the same (same injection gas). However, point **f** is represented by f' with no C_{10} present. This sub-ternary system is a condensing gas drive in classical sense from point a' to point f'. Similarly, the continuous variation **d** $\rightarrow$ **e** in Fig. 3.28 is present for this sub-ternary case as $d' \rightarrow e'$

Similarly, the vaporizing part can be seen when the segment between the injection tie line and the crossover tie line is projected onto the C_3-free face (Fig. 3.30b). In this figure, coordinates of f and f' are the same (initial oil), and again the point **a** is represented as point a' with no

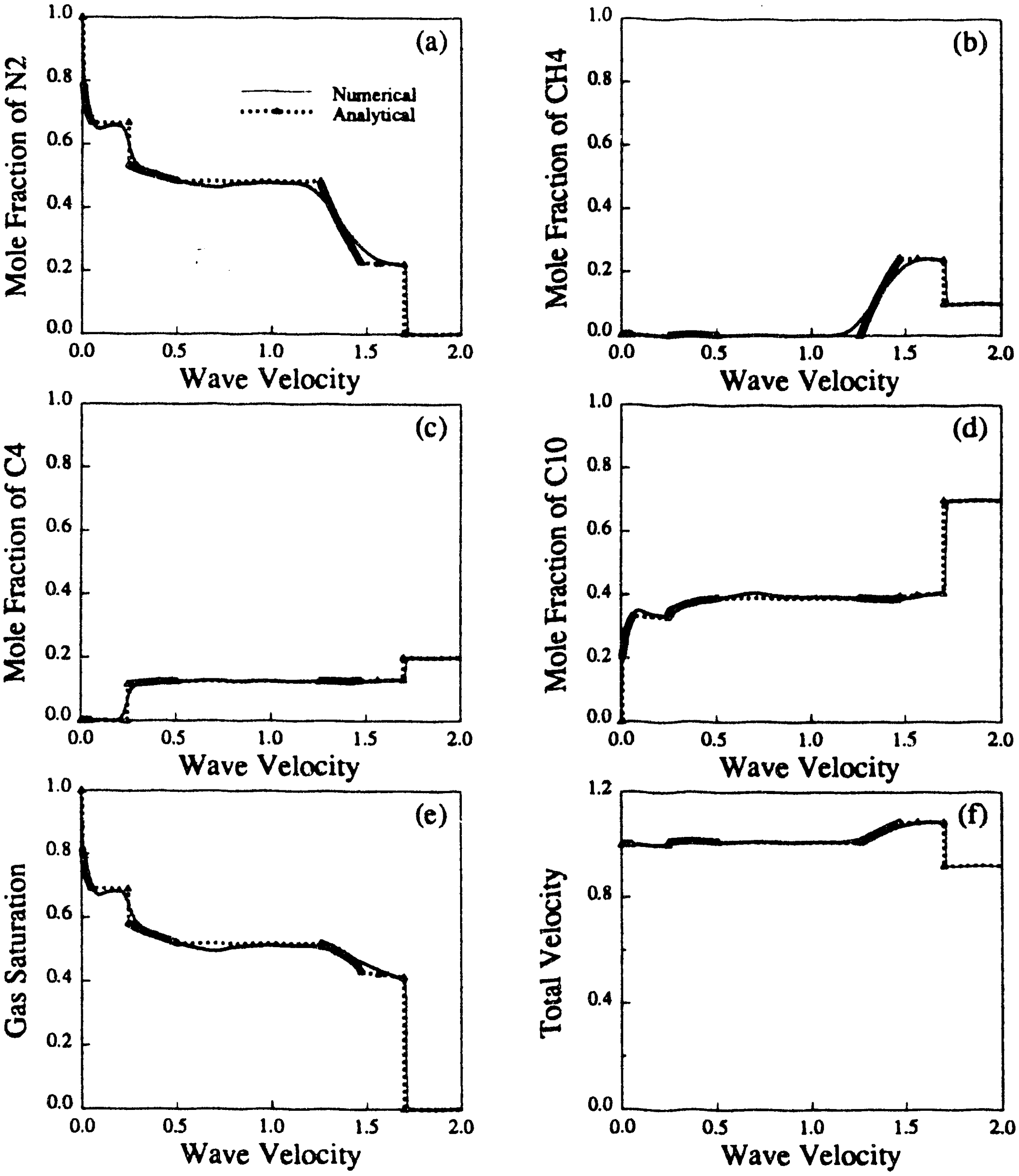

Figure 3.27: Comparison of MOC and FD solutions, $\frac{\Delta\xi}{\Delta\tau} = 5$ and 500 grid blocks, composition profiles (**a to d**), saturation profile (**e**) and velocity profile (**f**) for displacement of a $CH_4/C_4/C_{10}$ mixture by pure N_2 at 1600 psia and 160° F.

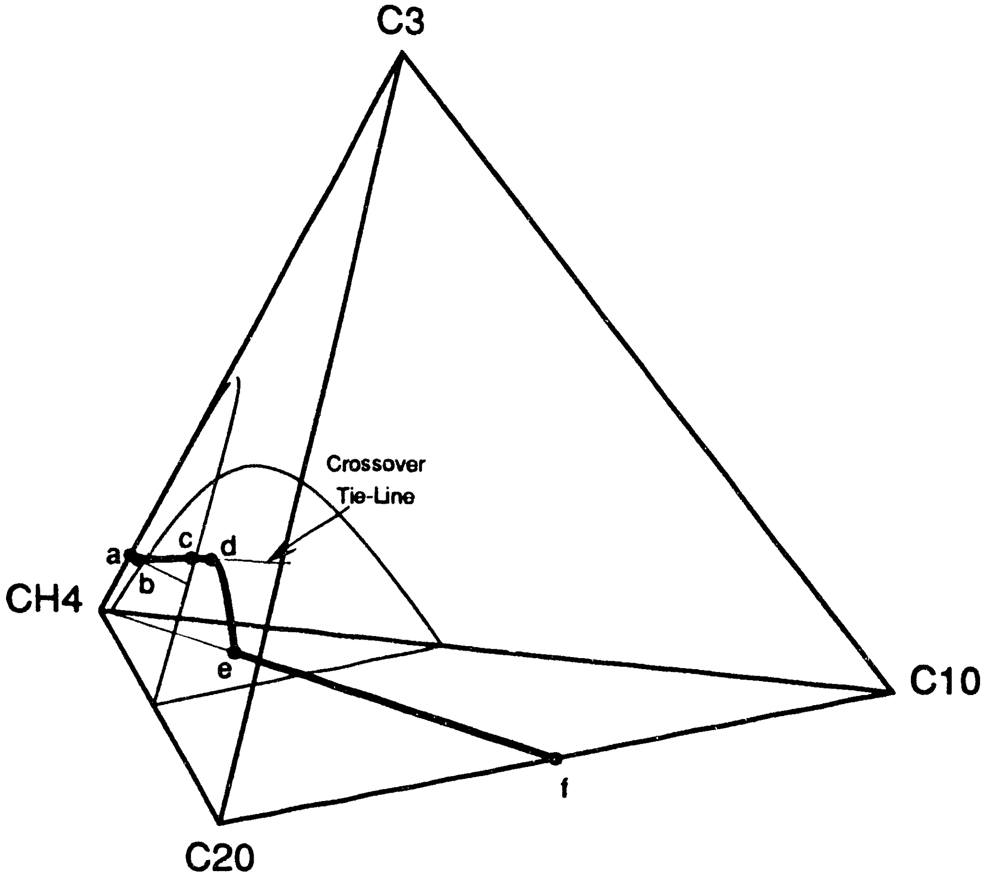

Figure 3.28: Composition route for displacement of a C_{10}/C_{20} mixture by a CH_4/C_3 mixture at 3100 psia and 185° F.

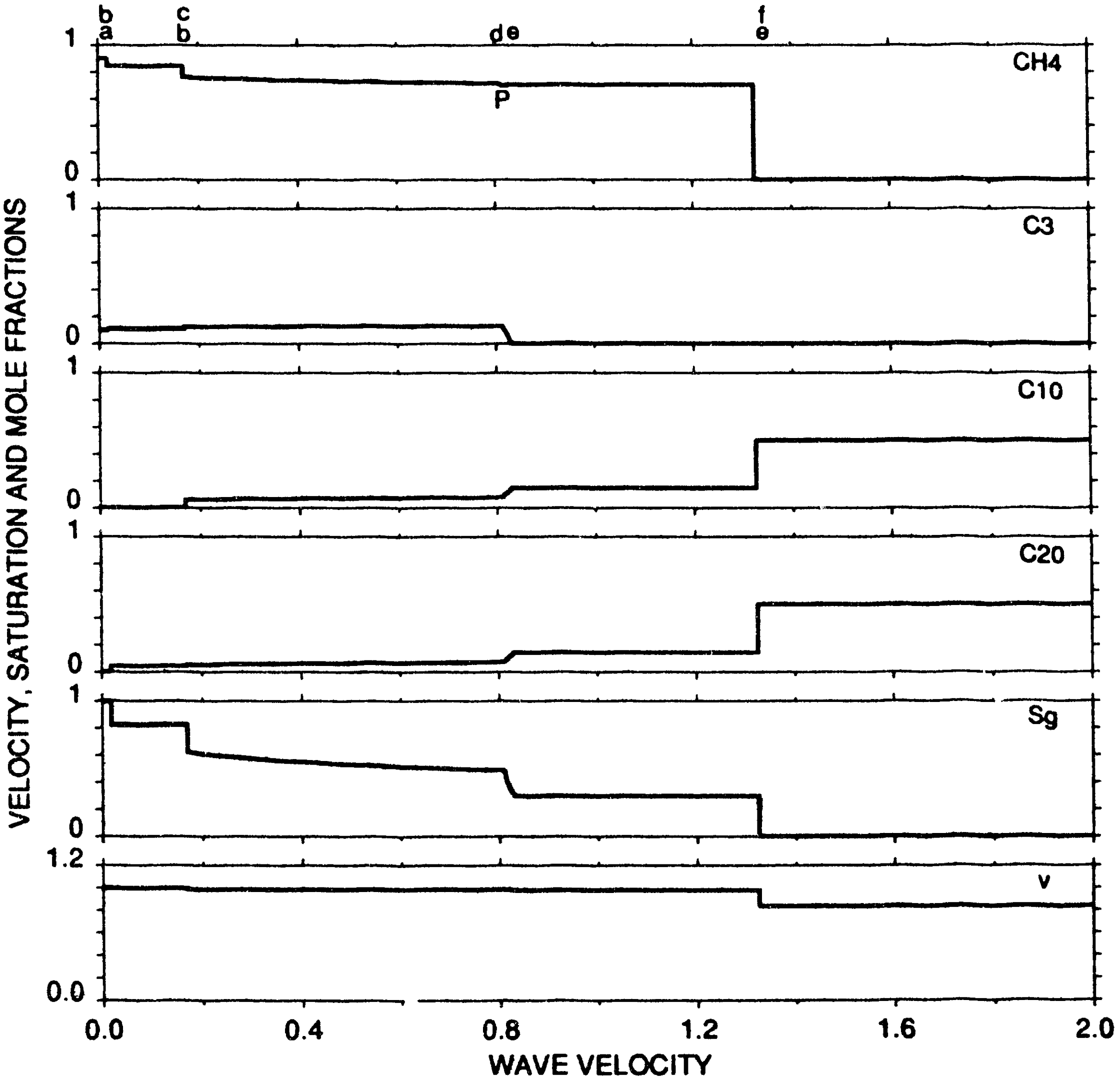

Figure 3.29: MOC profiles for displacement of a C_{10}/C_{20} mixture by a CH_4/C_3 mixture at 3100 psia and 185° F.

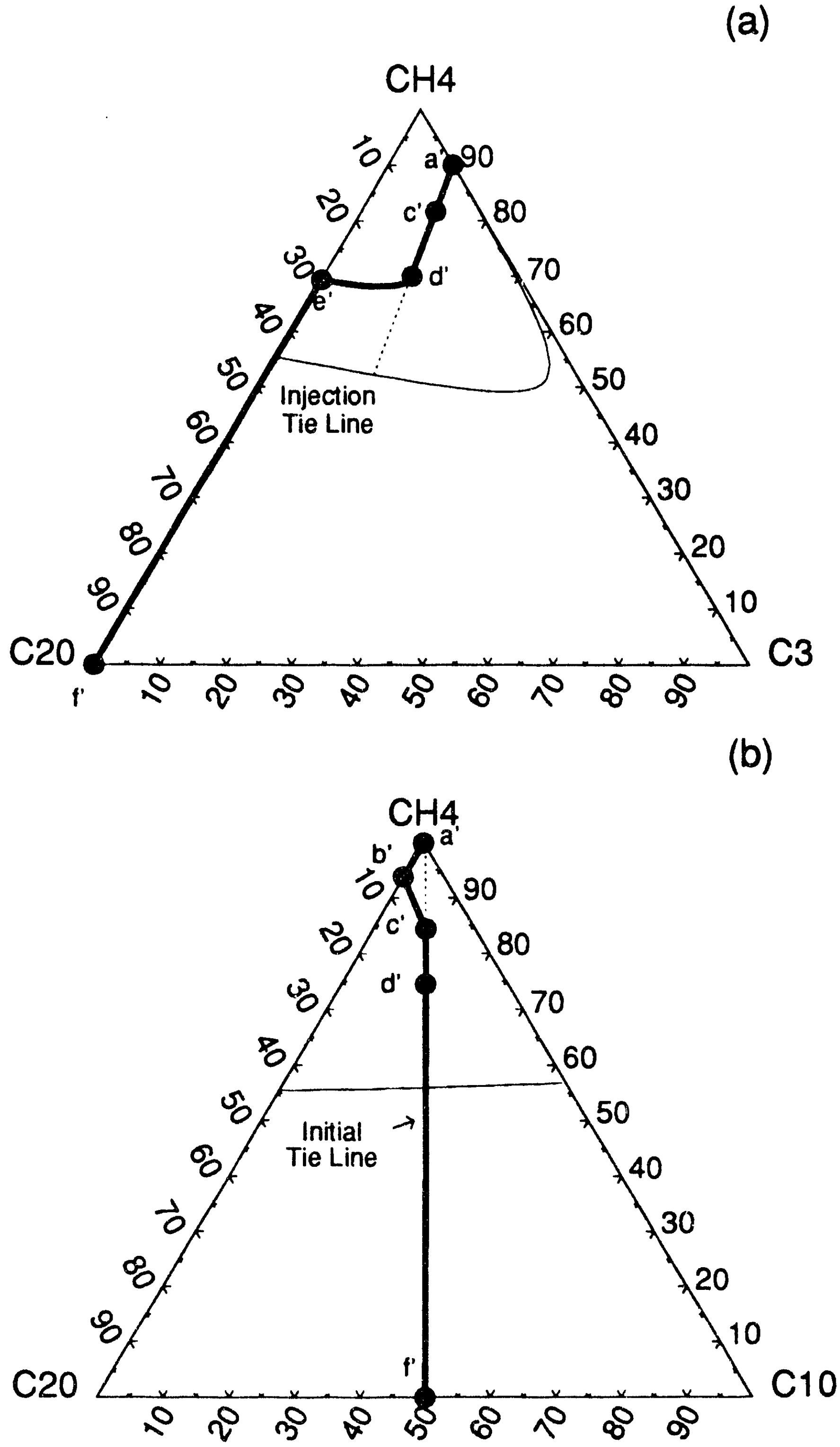

Figure 3.30: Limiting sub-quaternary composition routes for displacement of a C_{10}/C_{20} mixture by a CH_4/C_3 mixture at 3100 psia and 185° F.

Table 3.10: MOC solution for the composition route of Fig. 3.3.8 at 3100 psia and 185° F.

Composition Label	Composition (Mole Fraction)				Total Flow Velocity	Gas Saturation (Vol. Fraction)	Wave Velocity
	CH_4	C_3	C_{10}	C_{20}			
a	0.9006	0.0994	0.0000	0.0000	1.0000	1.0000	0.0184
b	0.8462	0.1090	0.0000	0.0448	0.9966	0.8238	0.0184-0.1724
c	0.7639	0.1235	0.0600	0.0525	0.9860	0.6218	0.1724
d	0.7162	0.1319	0.0797	0.0722	0.9860	0.4856	0.8127
e	0.7086	0.0000	0.1477	0.1438	0.9785	0.2974	0.8307-1.3463
f	0.0000	0.0000	0.5000	0.5000	0.8368	0.0000	1.3463

C_3 present. This sub-ternary system is a classical vaporizing gas drive from point f' to point a'. Similarly, the intermediate shock **c** → **b** in Fig. 3.28 is present for this sub-ternary case as $c' \rightarrow b'$ shock. The most useful aspect of such decoupling into two sub-ternary systems is that such subsystems can help determine the sharpening behavior of the nontie-line paths in the quaternary system as well as the qualitative features of the quaternary path topology. In other words, four-component systems can be examined as two sub-ternary cases linked through a key tie line, the *crossover* tie line. When two similar solutions are put together, however, there is no guarantee that the shocks on the entrance and/or exit tie lines (injection and initial tie lines) remain as tangent shocks. In the four component solutions two distinct parts of the solution are connected through the crossover tie line in such a way that the complete solution consists of a sequence of compatible waves. The compatibility condition requires that the solution be constructed as a sequence of shocks and spreading waves (smooth composition variations) in which slow compositions lie upstream of compositions with higher wave or shock velocities. For instance, in this CH_4/C_3 displacement there is no tangent shock along the entrance and exit tie lines, because a continuous variation along either tie lines to a tangent shock point, for example, would violate the compatibility condition.

The phase behavior of this system is quite different from that of the previous cases. The two-phase region is smaller and does not extend to the CH_4-free face as Fig. 3.28 shows. The solution also has different features. There is a jump from the injection composition **a** to point **b** along the injection tie line, where the jump is coupled to another jump from **b** to **c** on the crossover tie line. A continuous variation between these two tie lines is not possible because eigenvalues on nontie-line paths decrease slightly as the nontie-line path is traced from the injection to the crossover tie line. The type of the trailing shock is different because construction of the trailing shock as a limit of a continuous variation is not compatible with the **b** → **c** shock wave. This intermediate shock is followed by a continuous variation to point **d** on the same tie line. There is a path switch at this point. Point **d** is the equal eigenvalue point for the nontie-line path that is tangent to the crossover tie line and extends to point **e** on the initial tie line. The point **e** is connected to the injection composition **f** via a shock, because continuous variation after **e** is an incompatible wave.

The numerical solution (Fig. 3.31) for this case shows interesting behavior. The nontangent trailing shock creates a numerical artifact labeled as **U** in Fig. 3.31e. A very small underestimation of the saturation (labeled **U** in Fig. 3.31e) is observed just ahead of the trailing shock due to upstream weighting. In the numerical solutions, the transition zone propagates from the injection end to the production end. Therefore, the trailing shock tries to predict a tangent trailing shock,[4] which is incompatible with what lies ahead. Then the solution corrects itself due to mixing with the material ahead converging to the analytical solution.

Agreement of the two solutions is quite good. The numerical solution indicates the same dip in the CH_4 profile (labeled **P** in the top portion of Figs. 3.29a and 3.31a) though that zone is more dispersed in the numerical solution. The leading shock and the upstream zone of constant state are predicted with good accuracy.

3.3.6 Minimum Miscibility Pressure

The solutions presented in this chapter indicate that a new definition of MMP for general four component systems is required. This definition allows us to state a thermodynamic definition of the MMP for purely convective flow. Estimation of the minimum miscibility pressure (MMP) or minimum miscible enrichment (MME) in vaporizing/vaporizing, condensing/condensing and condensing/vaporizing gas drives will be based on different tie lines. In the CO_2/C_4 displacement, a condensing/condensing gas drive, it is the *injection* tie line that controls miscibility. In that system the displacement can be made MCM in two ways, by increasing the pressure or by increasing the enrichment level. In either case, though, the displacement is MCM when the injection tie line is tangent to the locus of plait points, a critical tie line. Thus the CO_2/C_4 displacement is MCM when the injection composition lies outside the region of tie line extensions. Hence, it is also consistent with the standard ternary definition of a condensing gas drive.

In the vaporizing/vaporizing N_2 displacement, the key tie line is the *initial* tie line. As pressure increases, among all the tie lines traversed along the solution, the initial tie line will have zero length at the lowest pressure. At the MMP it becomes tangent to the locus of plait points. Thus, the N_2 displacement satisfies the traditional definition of vaporizing gas drive miscibility based on ternary systems: the initial oil composition must lie outside the region of tie-line extensions.

The CH_4/C_3 displacement, a condensing/vaporizing gas drive, is not consistent with the ternary definitions of miscibility, however. In that system (and in the CO_2 displacements of Section 3.1), it is the *crossover* tie line that is a critical tie line at the lowest pressure or enrichment level. Thus, condensing/vaporizing gas drives do not satisfy any of the traditional ternary definitions of miscibility. The initial oil and injection fluid compositions in condensing/vaporizing gas drives lie well within the region of tie line extensions when the crossover tie line is a critical tie line. Hence, it is clear from the analytical solutions obtained here that mixing cell methods [21, 41, 28, 81], which detect whether the initial and injection compositions lie on tie line extensions at a given pressure and temperature, do not produce the correct result for condensing/vaporizing gas drives. Hence, such methods for MMP estimation should be used with caution unless it is known *a priori* that the displacement is not a condensing/vaporizing drive.

---

[4] A *tangent* trailing shock occurs when the speed of the trailing shock is identical to the eigenvalue on the downstream side.

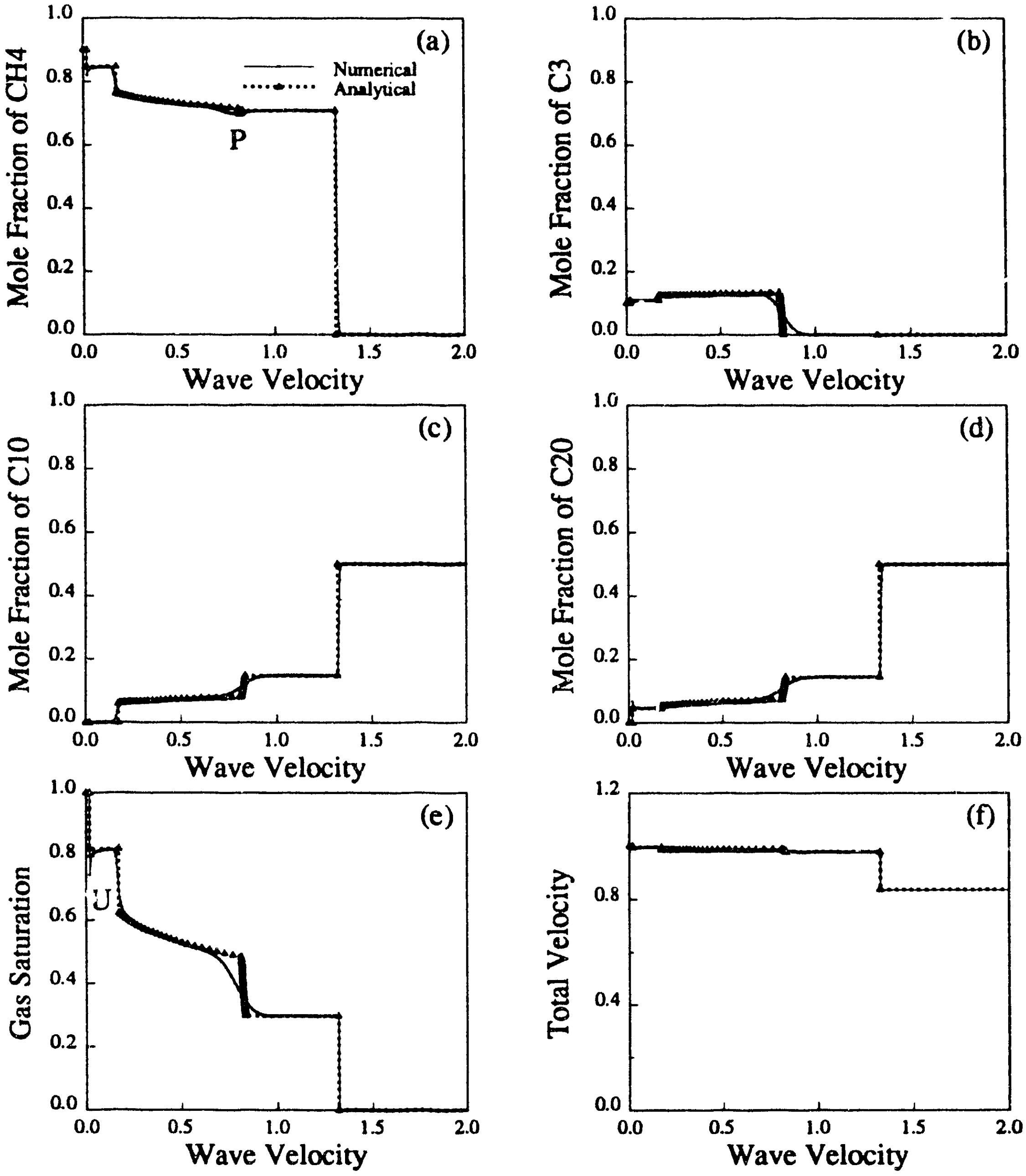

Figure 3.31: Comparison of MOC and FD solutions, $\frac{\Delta\xi}{\Delta\tau} = 5$ and 500 grid blocks, composition profiles (**a to d**), saturation profile (**e**) and velocity profile (**f**) for displacement of a C_{10}/C_{20} mixture by a CH_4/C_3 mixture at 3100 psia and 185° F.

3.3.7 Conclusions

The analytical and numerical solutions for a variety of miscible flood systems lead to the following conclusions:

1. A new method of decoupling the convective velocity from the rest of the solution has been developed.
2. Numerical solutions are in good agreement with the MOC results.
3. Three distinct behaviors are observed in the sample solutions, namely vaporizing/vaporizing, condensing/condensing and condensing/vaporizing drives.
4. In each system, a different tie line will determine the miscibility as pressure is increased. In the condensing/condensing system, the injection tie line becomes a critical tie line when the displacement is MCM. A vaporizing/vaporizing system is MCM when the initial tie line is a critical tie line. In a condensing/vaporizing system the crossover tie line controls the development of miscibility.
5. In the finite difference solutions equal eigenvalue points and nontangent trailing shocks are approximated least accurately.
6. Equilibrium ratios are the governing parameters in formation of the component banks.

3.4 Summary

Analytical solutions for displacement of $CH_4/C_4/C_{10}$ and C_{10}/C_{20} mixtures by a variety of injection gas systems are presented in this chapter. Displacements by CO_2, by a mixture of CO_2 and C_4, and by N_2 illustrate a fascinating range of behavior. The solutions presented illustrate clearly that the standard ternary description of development of miscibility is too simple. The four-component theory developed here explains the behavior of condensing/vaporizing gas drives, and it shows when and why mixing cell methods for MMP estimation fail. The analytical solutions also permit detailed testing of the accuracy of compositional simulations (such as those proposed in Section 4.3). Thus, the four-component theory represents a significant advance in understanding of the behavior of real miscible flood systems.

4. Modeling of Viscous Fingering

In most miscible floods, the viscosity of the injected gas will be substantially less than that of the oil being displaced. Hence, the displacement will be unstable, and viscous fingering will result. In such cases, displacement performance will depend on a complex interplay of viscous fingering, heterogeneity, crossflow, and phase behavior. Past work has focussed on the interaction of viscous fingering with permeability heterogeneity. A particle-tracking simulator developed originally by Araktingi [1, 2] and extended by Tchelepi [52] was applied by Brock [8, 9] to show that the simulation technique does a good job of capturing the transition from (1) flow dominated by viscous forces in homogeneous or randomly heterogeneous porous media to (2) flow dominated by the spatial distribution of permeability when there is significant correlation of high and low permeability. Thus, there is good evidence that the particle-tracking technique can be used to explore scaling issues that involve viscous fingering and heterogeneity.

In this chapter, we extend the previous results in three areas. In Section 4.1, we report results of a study of the scaling of finger growth in linear displacements. That study provides guidance on how simplified empirical models must be modified if they are to reflect physical observations of the effects of changes in length to width ratio on displacement performance. Section 4.2 describes briefly our continuing effort to extend the particle-tracking technique in this case, to model unstable flow in three-dimensional heterogeneous porous media. In Section 4.3 we outline what will be required to extend the particle-tracking technique to model the effects of phase equilibrium. The resulting code will be the first available that performs compositional particle-tracking simulations. When we can perform three-dimensional, compositional particle-tracking calculations, we will be able to assess more accurately than ever before the effects of the complex interactions that determine the efficiency of a miscible flood.

4.1 Scaling of the Growth of Viscous Fingers in Linear Flow

Hamdi Tchelepi

The influence of the scale of the flow domain of interest on unstable miscible displacement behavior is the target of this investigation. This influence will be considered in terms of absolute individual dimensions and as a ratio of length to width. The objective is better understanding of the scaling of the growth of viscous fingers.

In their benchmark experiments, Blackwell et al. [6] observed that for a particular mobility ratio, the breakthrough recovery increased as the length to width ratio (L/W) of the model used increased. For example, they reported that for a mobility ratio of 20, the breakthrough recoveries were 35, 45 and 67% in physical models with L/W of 3, 12 and 144 respectively. Unfortunately, complete recovery curves were only provided for models with L/W of 3.

Christie and Bond [13] obtained the recovery curve of Handy's experiment, first reported by Dougherty [16], which was performed in a model with L/W = 17 at a mobility ratio of 16.7. Their fine grid simulation agreed well with Handy's experimental recovery curve. Christie and Bond [13] made another simulation run at the same mobility ratio of 16.7, but for a system of L/W = 3. As a consequence of the agreement between their fine grid simulations and the experiments of Blackwell et al. [6] at mobility ratios of 5 and 86 in systems with L/W = 3, they ran a simulation at a mobility ratio of 16.7 and L/W = 3 and assumed that it was representative of Blackwell et al.'s data. They plotted Handy's experimental curve and the simulation of it, and the simulation at L/W = 3. The L/W = 3 case showed earlier breakthrough and lower recovery at a particular value of injected pore volumes after breakthrough as compared to the L/W = 17 case. They concluded that the length to width ratio is the dominant factor in the production behavior. High resolution particle-tracking random walk simulations made here confirm the findings of Christie and Bond.

They also showed the recovery curves predicted by Koval's [36] empirical viscous fingering model for a mobility ratio of 16.7. Koval's model prediction was good for the L/W = 3 case. Similar results were obtained with Fayers' model [19] with his unmodified parameters. Koval's model is based on a fractional flow formula assuming straight line relative permeability curves. In the formula, an effective viscosity ratio is used. This ratio is obtained from the quarter power mixing rule assuming constant concentrations. The concentrations were obtained from a fit to experimental data. Fayers' model is also based on a simple fractional flow expression. As in Koval's model, the viscosity of the displacing fluid is obtained from the quarter power mixing rule. However, concentrations within an idealized finger are used to calculate local mobilities. Moreover, the relative permeabilities are described in terms of a function that describes the width of the idealized finger.

Because of the insensitivity of the empirical models to variations in the length to width ratio, they naturally disagree with the L/W = 17 case. Fayers et al. [20] stated that "it is the asymptotic results [$L/W < 3$] for which the parametric values in the three empirical models are confirmed." The three empirical models referred to are those of Koval [36], Todd and Longstaff [74], and Fayers [19].

Gardner and Ympa [23] described what they called a "synergistic interaction" between phase behavior and macroscopic bypassing due to viscous fingering coupled with the influence of the lateral boundaries. The results shown in their Fig. 5 (which plots the oil saturation at 1.1 PVI vs. residence time, L/v), however, do not isolate the influence of the lateral boundary. The absolute value of the transverse dispersion coefficients in the experiments may explain the observed behavior. The lower the transverse dispersion coefficient, the higher the remaining oil saturation. This is in line with their description of the influence of transverse dispersion on the initiation and maintenance of fingers. The transverse dispersion coefficient D_T can be expressed as

$$D_T = D_m + \alpha_T v \tag{4.1}$$

where D_m is the effective molecular diffusion coefficient, α_T is the transverse dispersivity of the porous medium, and v is the flow velocity.

Gardner and Ypma used a linear stability analysis to examine the growth behavior of perturbations as a function of the wavelength of the disturbance. According to the linear theory, small fingers are damped by transverse dispersion before they can grow. They showed that the cutoff wavelength, λ_c, for a linear viscosity-concentration relationship is given by

$$\lambda_c = 2^{5/2}\left(\frac{\mu_o + \mu_s}{\mu_o - \mu_s}\right)\left(\frac{D_T}{v}\right) \tag{4.2}$$

where μ_o and μ_s are the viscosities of the oil and solvent respectively. Substitution of Eq. 4.1 into Eq. 4.2 gives

$$\lambda_c = 2^{5/2}\left(\frac{\mu_o + \mu_s}{\mu_o - \mu_s}\right)\left(\frac{D_m}{v} + \alpha_T\right) \tag{4.3}$$

For a fixed value of molecular diffusion coefficient D_m, the cutoff wavelength, λ_c, decreases as the flow velocity, v, increases. The dependence on velocity becomes more significant as the contribution of molecular diffusion, D_m, to the transverse dispersion coefficient, D_T increases. Obviously, if $D_m = 0$, λ_c is independent of v. Gardner and Ympa used the reciprocal Peclet Number, $Pe_T = D_T L / v W^2$, as a measure of the transverse dispersion level. It is the ratio of the time it takes a fluid particle to travel the length of the domain by convection, L/v, to the time it takes to disperse a particle the width of the domain, W^2/D_T. Using the expression for D_T in Eq. 4.1 we have

$$Pe_T = \frac{D_m}{v}\frac{L}{W^2} + \alpha_T \frac{L}{W^2} \tag{4.4}$$

As the flooding rate increases, Pe_T decreases. Consequently, transverse dispersion has less time to eliminate concentration gradients. Pe_T is independent of rate if molecular diffusion is negligible.

It is worth noting here that the contribution of the molecular diffusion term in the expression for the transverse dispersion coefficient ranges from 92% to 52% for flood rates ranging from 0.80 to 8.2 ft/day respectively in the experiments of Gardner and Ypma. As a result, we argue that the lateral boundary effect in those experiments was probably a strong function of the relatively high molecular diffusion levels.

Thus, the reported results of Blackwell et al. [6] , Christie and Bond [13], and Fayers et al. [20], as well as detailed particle-tracking simulations indicate clearly that the L/W ratio plays an important role in the physics of fingering, and the results of Gardner and Ypma [23] also point indirectly to that influence. While detailed numerical simulations seem to capture the influence of L/W on displacement behavior, no explanation has yet been provided as to how the physics of fingering during the displacement is affected by variations in length to width scales. Such an understanding will enable us to modify the empirical models so that we can use them to predict the performance of unstable miscible displacements in domains with $L/W > 3$.

4.1.1 Simulation Considerations

The wavelength of the smallest unstable mode when a less viscous fluid displaces a more viscous one miscibly is mainly determined by the transverse dispersion coefficient [72]. This physically determined cutoff is much smaller than a centimeter for most dispersion levels. It can be shown that not all initially unstable wavelengths continue to grow [72, 13]. As a result, the tolerated cutoff is greater than the physical limit of initial growth. The need for detailed numerical simulations to model unstable displacement behavior stems from the fact that longitudinal and transverse grid Peclet numbers $(\Delta_x/\alpha_L, \Delta_y/\alpha_T)$ control the cutoff wavelengths for the smallest unstable modes. These Peclet numbers must be small enough such that we allow as small a cutoff as is tolerated physically. Practically, the tolerated cutoff is the grid size below which no appreciable changes in fingering patterns occur.

The simulator used here employs a random walk particle-tracking method [1, 73, 10]. The elliptic pressure equation is solved on fine mesh for the boundary conditions of interest. Particles are used to represent the displacing component in order to minimize numerical dispersion. The velocity field is then used to calculate the convective displacement for the particles. Dispersion is modeled as a random process; as a result, the dispersive displacement that a particle undergoes is obtained from a random walker scaled by the dispersivities of the medium. The net displacement for a particle is the sum of the convective and dispersive components. In order to isolate the effect of the length to width ratio, all the simulations performed for this study assume negligible molecular diffusion contributions to the dispersion coefficients. As a result, the displacement behavior of the unstable miscible simulations is independent of injection rate.

Moving Boundaries

Varying grid Peclet numbers above the tolerated level will change the cutoff wavelength. This will alter the fingering mode at initiation and could affect the displacement behavior at later times. As a result, numerical simulations in domains of different sizes must all use the same grid Peclet numbers so that comparisons are possible. With this in mind and the fact that we are looking at scaling questions regarding the length to width ratio, it is obvious that our overall mesh size will grow as the size of the domain of interest increases for the chosen grid Peclet numbers. To comply with the requirement that the grid Peclet numbers remain the same for all simulations, moving boundaries were implemented in the simulator code. The motivation was one of both convenience and necessity. The convenience comes from much smaller CPU times. High resolution simulations in long domains may require gridblock numbers in the hundreds to represent length. That is inconvenient and most often prohibitive.

The first step was to examine the influence of the outlet boundary on displacement behavior. That effect is demonstrated in Figs. 4.1 - 4.3 for a mobility ratio of 12.5. On each plot, concentration maps are shown for two domains with the same width but different lengths. The comparisons are made in absolute time. Figs. 4.1 - 4.3 show successively larger times. At a particular time, the concentration maps for the short and long systems are almost identical. Some differences are detectable after the shorter system breaks through. Similar results are obtained for different higher and lower mobility ratios. The differences, albeit very small, do increase as the mobility ratio increases.

One may conclude that the influence of the proximity of the outlet on fingering behavior is negligible. This is in agreement with the fact that pressure differences between the resident fluid and the fingers are small. This finding justifies the use of a moving outlet boundary without sacrificing the high resolution of the numerical simulation.

The idea behind the moving boundary approach is that one finds the maximum penetration length at the end of a time step, pad it with a safe distance and place the outlet boundary at the resultant distance. This means that the system of equations to be solved is smaller than the mesh size representing the full physical model. Obviously, this brings about CPU time gains by reducing the solver's computational effort. As the displacement proceeds, the penetration length increases at a rate proportional to the effective mobility ratio and the size of the system of equations to be solved increases.

The inlet boundary condition implemented in the simulator is that of a constant total rate. The individual rates into the inlet blocks are solved for simultaneously with the gridblock pressures of the columns beyond the inlet.

As Figs. 4.1 - 4.3 indicate, the fingered zone stretches in the course of the displacement. The trailing edge of that zone moves with a certain velocity in homogeneous and mildly heterogeneous systems. As a result, a completely swept zone behind the trailing edge usually develops. This zone does not influence the displacement behavior ahead of it. As a result, one can implement a moving inlet boundary that discards such a region. The fact that the individual rates at the inlet face (which is now moved inward) are responsive to the details of the mobility distribution in the domain, means that we are not sacrificing the accuracy or resolution of the simulation.

In this case two gains are achieved. First, the system of equations is smaller than that required to represent the full length of the physical model. In contrast to the moving outlet boundary, this gain increases as the displacement progresses since the swept zone grows in proportion to the velocity of the trailing edge of the fingered zone. Second and more importantly, all the particles in the swept region will no longer be tracked. The savings are significant. For homogeneous and mildly heterogeneous (small correlation lengths) domains of interest, CPU time savings due to discarding the particles in the swept zone typically range from 2 to 7 fold as compared to using a fixed inlet boundary for mobility ratios ranging from 30 to 5 respectively. A disadvantage of this technique is that the ability to predict absolute pressures is lost when moving boundaries are used. However, the corrections required are easily obtained.

Figs. 4.4 - 4.8 are for an unstable displacement at M = 12.5 and L/W = 22, with 20 particles per block. Each plot compares, at a particular time, the concentration maps obtained using fixed and moving boundaries respectively.

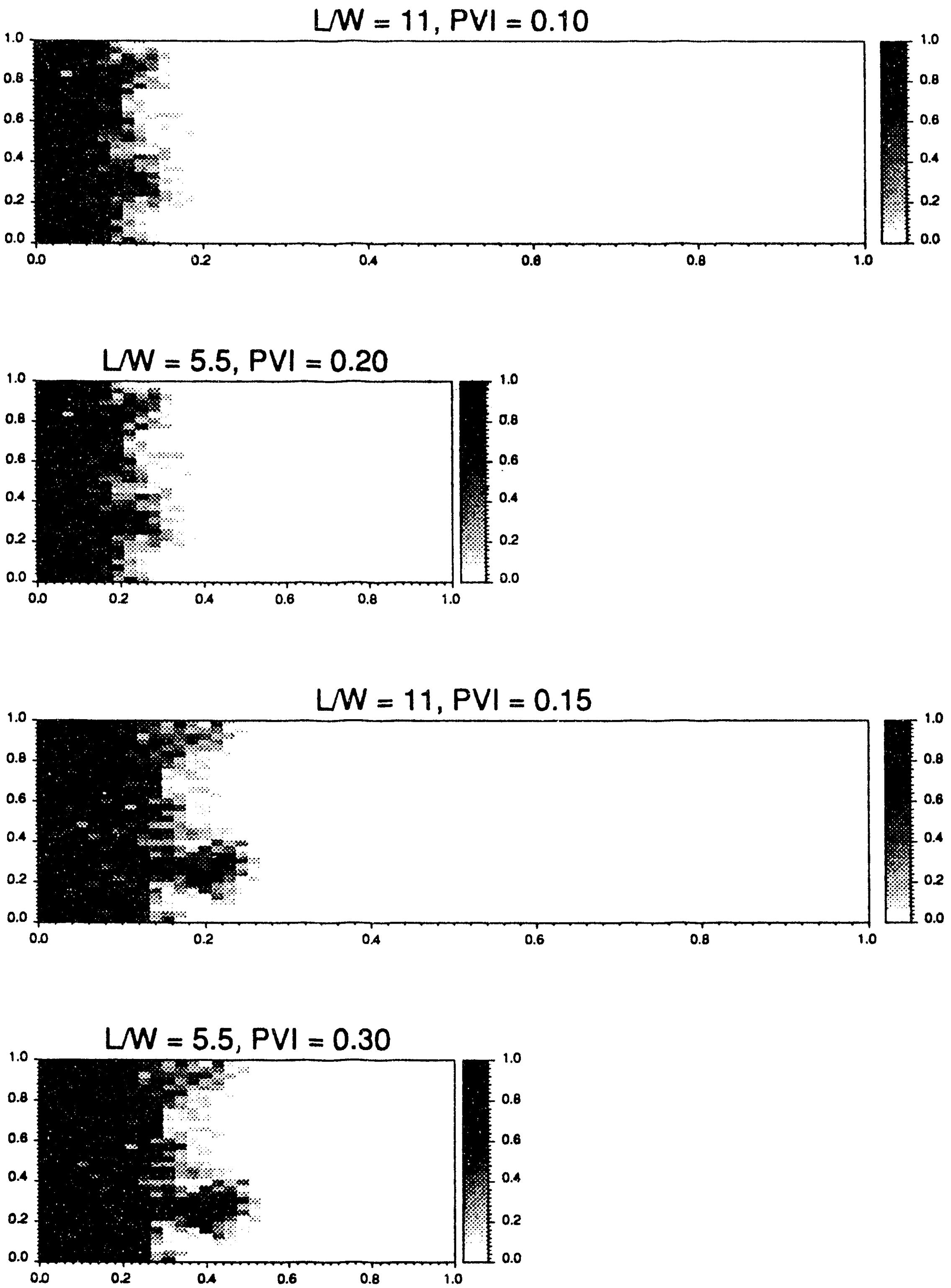

Figure 4.1: Comparison of the concentration grayscale maps for two systems with L/W of 5.5 and 11 at two absolute times corresponding to 0.1 and 0.15 PVI in the long model. Mobility ratio = 12.5.

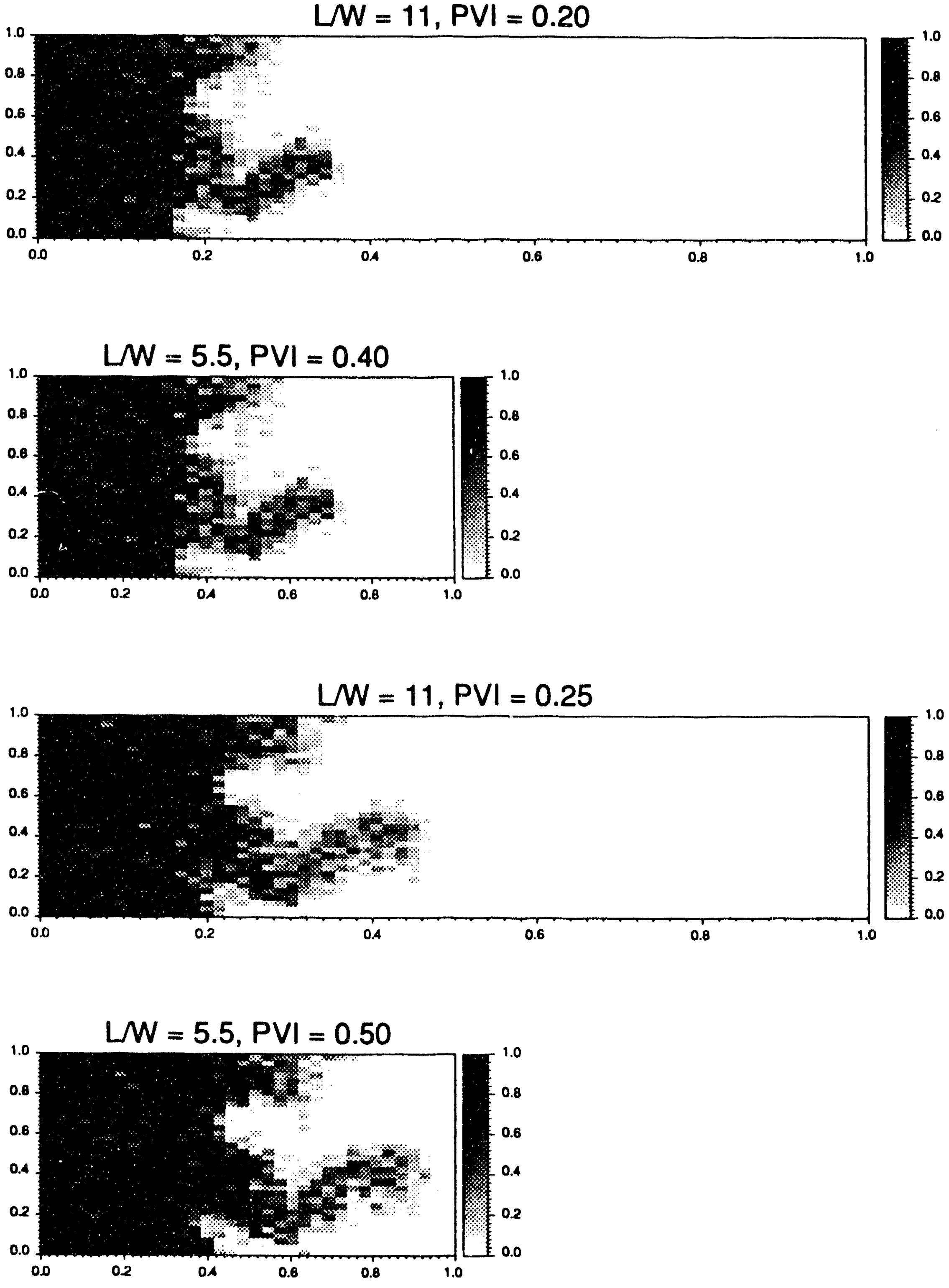
L/W = 11, PVI = 0.20

L/W = 5.5, PVI = 0.40

L/W = 11, PVI = 0.25

L/W = 5.5, PVI = 0.50

Figure 4.2: Comparison of the concentration grayscale maps for two systems with L/W of 5.5 and 11 at two absolute times corresponding to 0.2 and 0.25 PVI in the long model. Mobility ratio = 12.5.

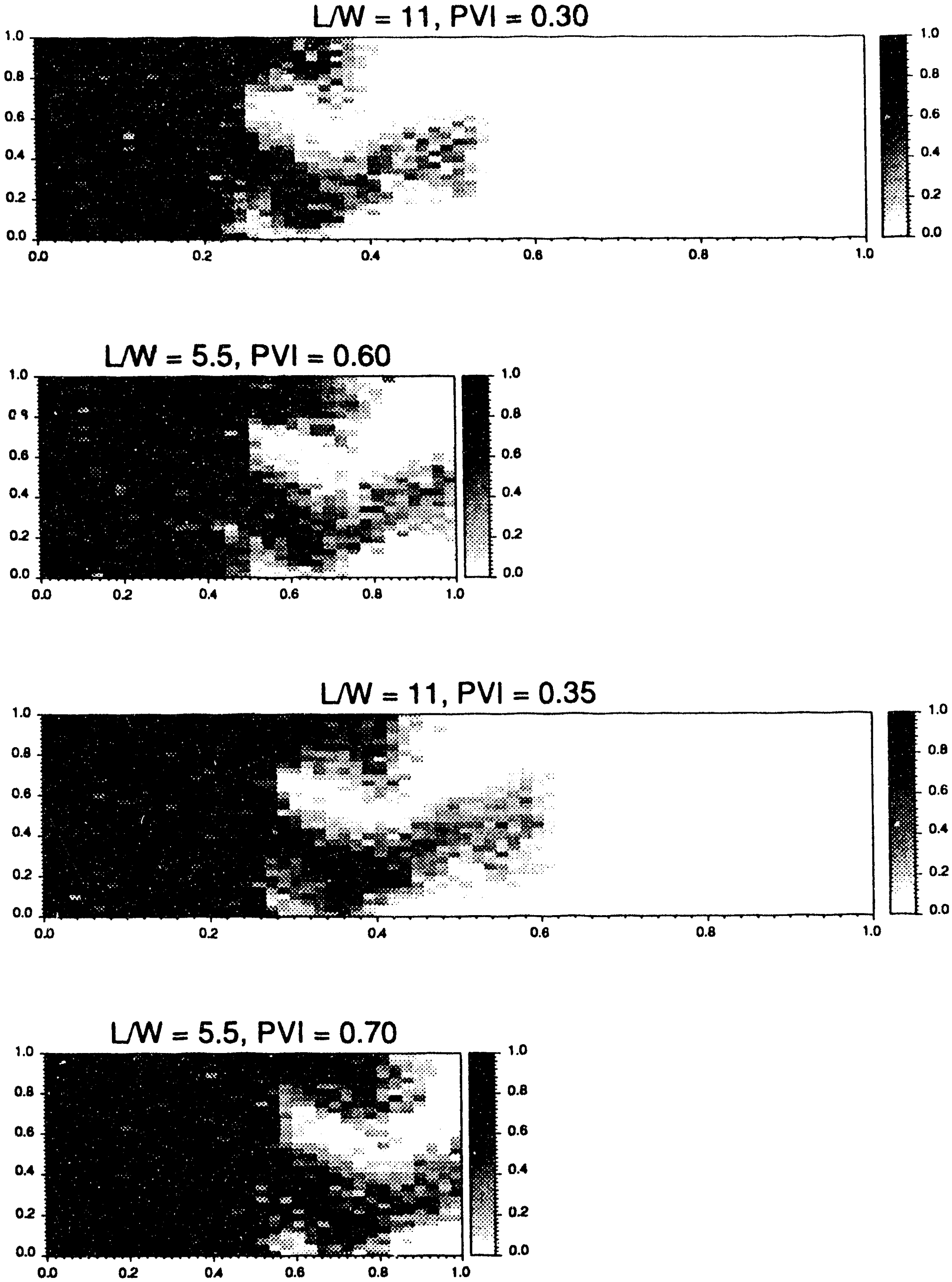

Figure 4.3: Comparison of the concentration grayscale maps for two systems with L/W of 5.5 and 11 at two absolute times corresponding to 0.3 and 0.35 PVI in the long model. Mobility ratio = 12.5.

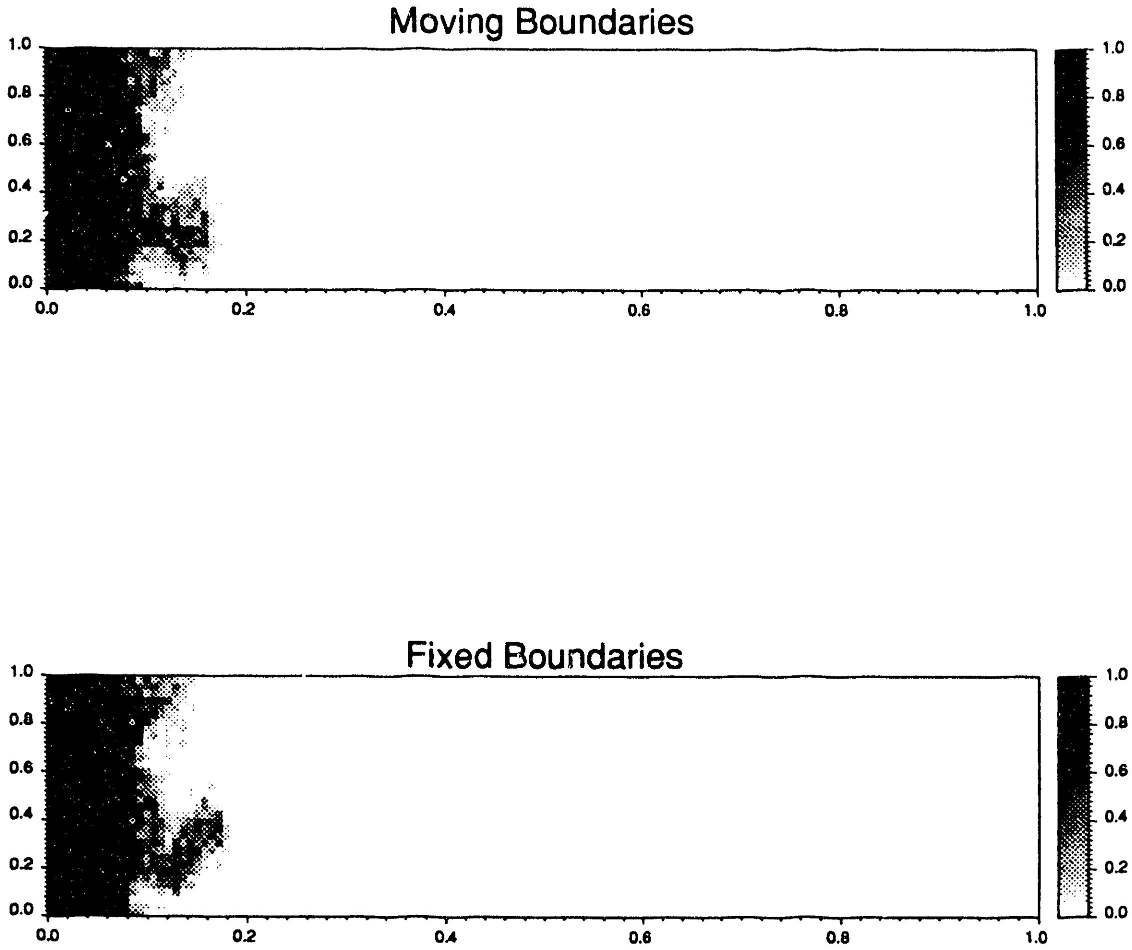

Figure 4.4: Comparison between fixed and moving boundaries simulations, M = 12.5, L/W = 22, PVI = 0.1.

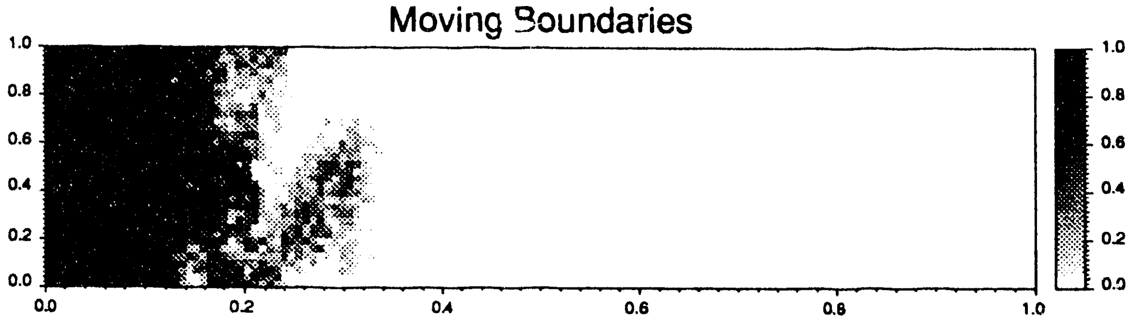
Moving Boundaries

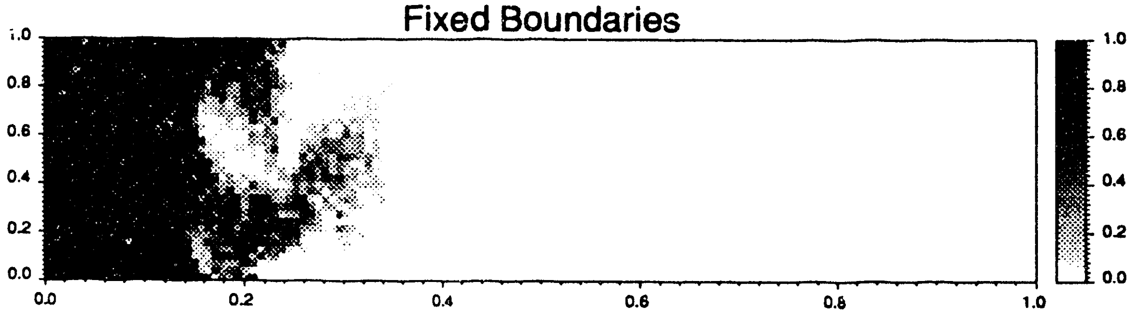
Fixed Boundaries

Figure 4.5: Comparison between fixed and moving boundaries simulations, M = 12.5, L/W = 22, PVI = 0.2.

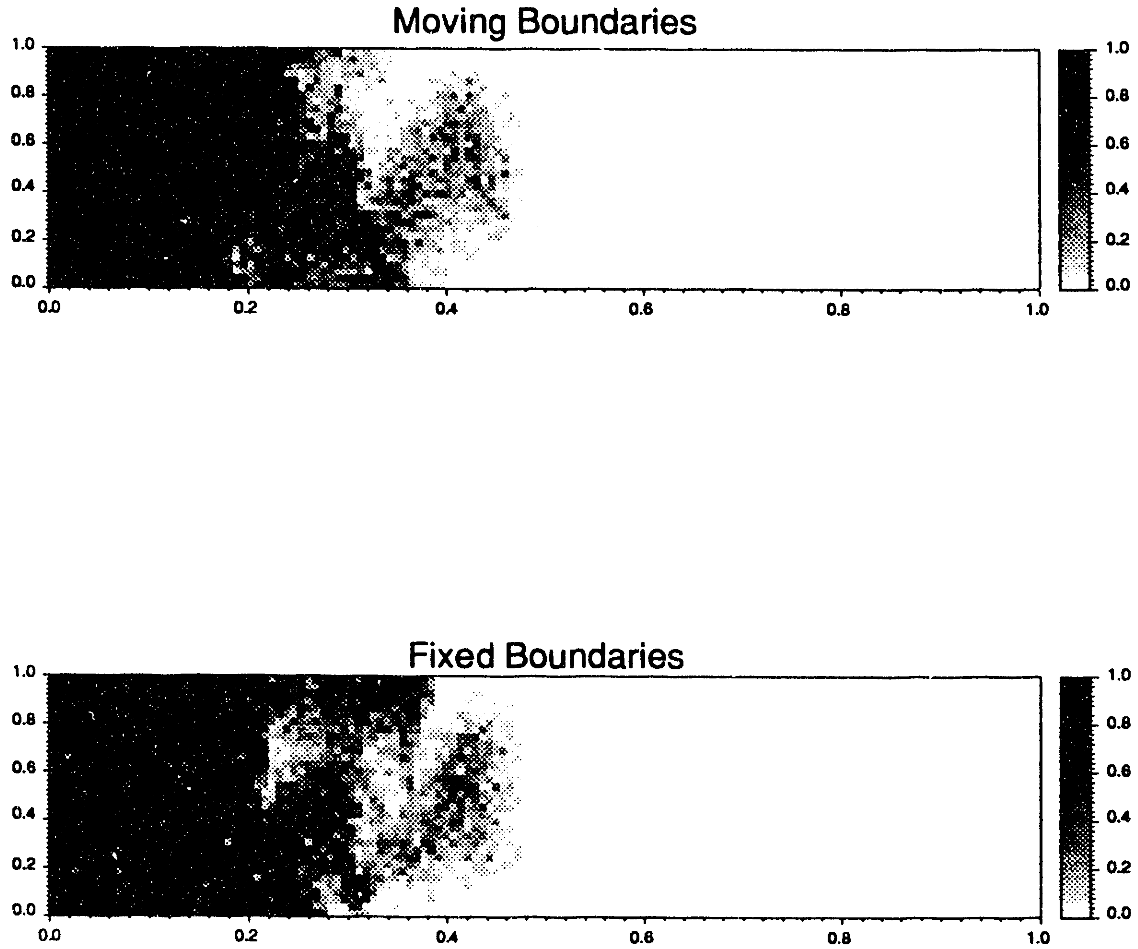

Figure 4.6: Comparison between fixed and moving boundaries simulations, M = 12.5, L/W = 22, PVI = 0.3.

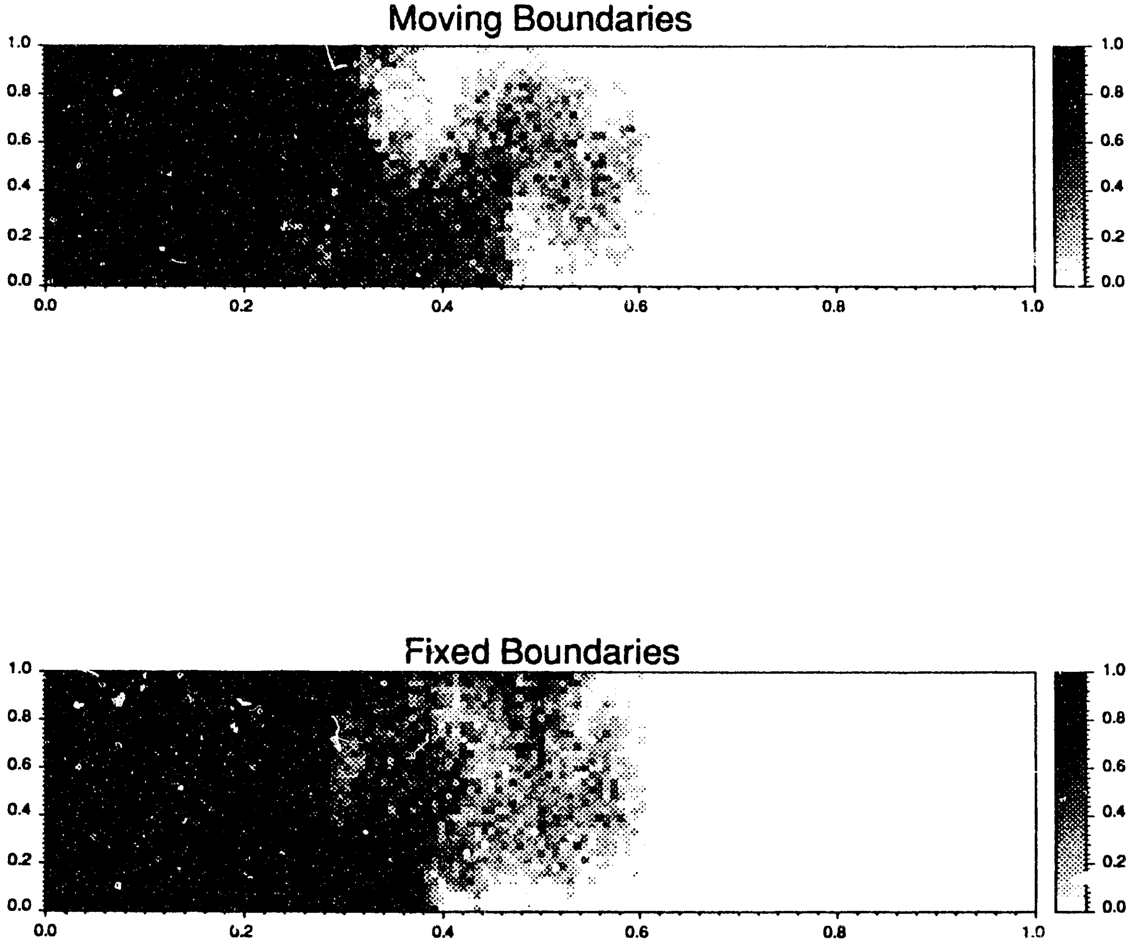

Figure 4.7: Comparison between fixed and moving boundaries simulations, M = 12.5, L/W = 22, PVI = 0.4.

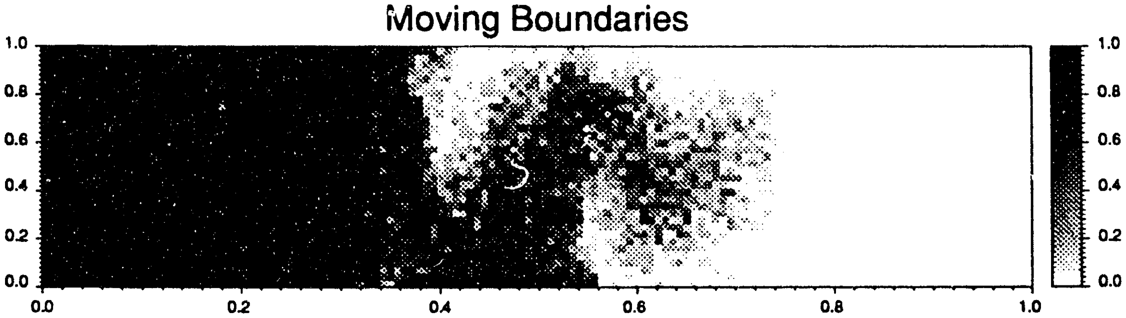

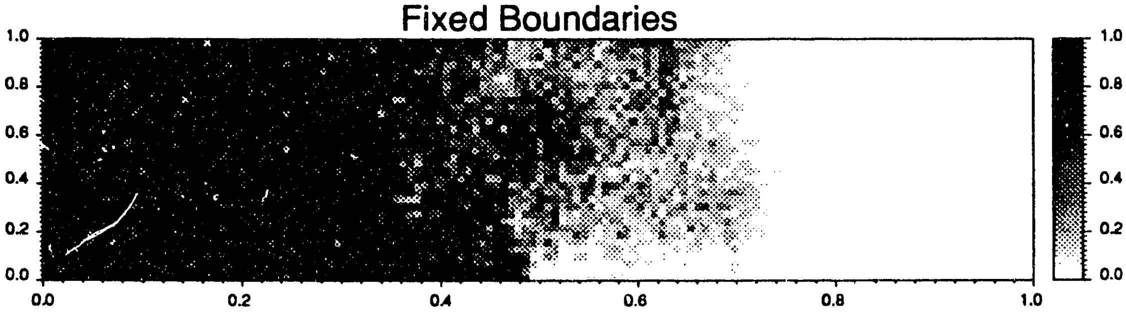

Figure 4.8: Comparison between fixed and moving boundaries simulations, M = 12.5, L/W = 22, PVI = 0.5.

The agreement demonstrated in Figs. 4.4 - 4.8 is excellent. Note that this is a tough test because we are comparing here the spatial distributions of concentration and not some integrated quantity that could possibly mask the effects of using moving boundaries. It is crucial that we do not lose any significant detail in the displacement behavior since that would defeat the purpose of the high resolution simulations we are after.

The algorithm used to implement moving inlet and outlet boundaries follows:

1. Choose a threshold concentration above which a column is considered fully swept, c_{min}.
2. Decide on safe distances:
   - (a) nc_{so} = number of columns ahead of the max penetration length
   - (b) nc_{si} = number of columns with a concentration more than c_{min} taken as a safe distance for the inlet boundary.
3. Find the number of consecutive columns, nc_i , with an average injection fluid concentration greater than c_{min}. Calculate $nc_{min} = nc_i - nc_{si}$.
4. Discard all particles with $x < \Delta x \; nc_{min}$.
5. Find the column position, nc_o, of the maximum penetration length.
   Calculate $nc_{max} = nc_o + nc_{so}$.
6. Calculate the coefficient matrix for:
   $j = 1, nr$
   $i = nc_{min} + 1, \; nc_{max} - 1$.
7. Assemble the right hand side and submit the system of equations to the solver.
8. Introduce the new particles at $nc_{min} + 1$, make sure that the velocity interpolation routine knows where the new boundaries are.
9. Advance the particles in the domain of interest.
10. At the end of the time step, go back to step 3.

4.1.2 The Influence of Variations in L/W

Now, we consider the mechanisms by which the physics of the fingering patterns is affected by the L/W ratio. Figs. 4.9, 4.10, and 4.11 are plots of recovery vs. PVI for mobility ratios of 6.25, 12.5, and 25 respectively. Each of these plots shows the recovery curves for three length to width ratios, namely 5.5, 11 and 22. Early breakthrough and lower recovery are evident at a given PVI as L/W decreases in Figs. 4.9 - 4.11. These effects are more pronounced for the higher mobility ratios.

Fig. 4.12 shows the dimensionless penetration length vs. PVI at a mobility ratio of 12.5 for three length to width ratios. The dimensionless quantities plotted correspond to the individual domains investigated. Note that the width is the same for the three domains; as a result, a plot of the corresponding absolute quantities will yield one curve for the three L/W cases. The curve for a longer model would simply exist beyond the breakthrough of a shorter model.

At the time the domain is first subjected to the pressure gradient, the viscosity contrast between the fluids is at its highest. As a result, small wavelengths are unstable. The transverse

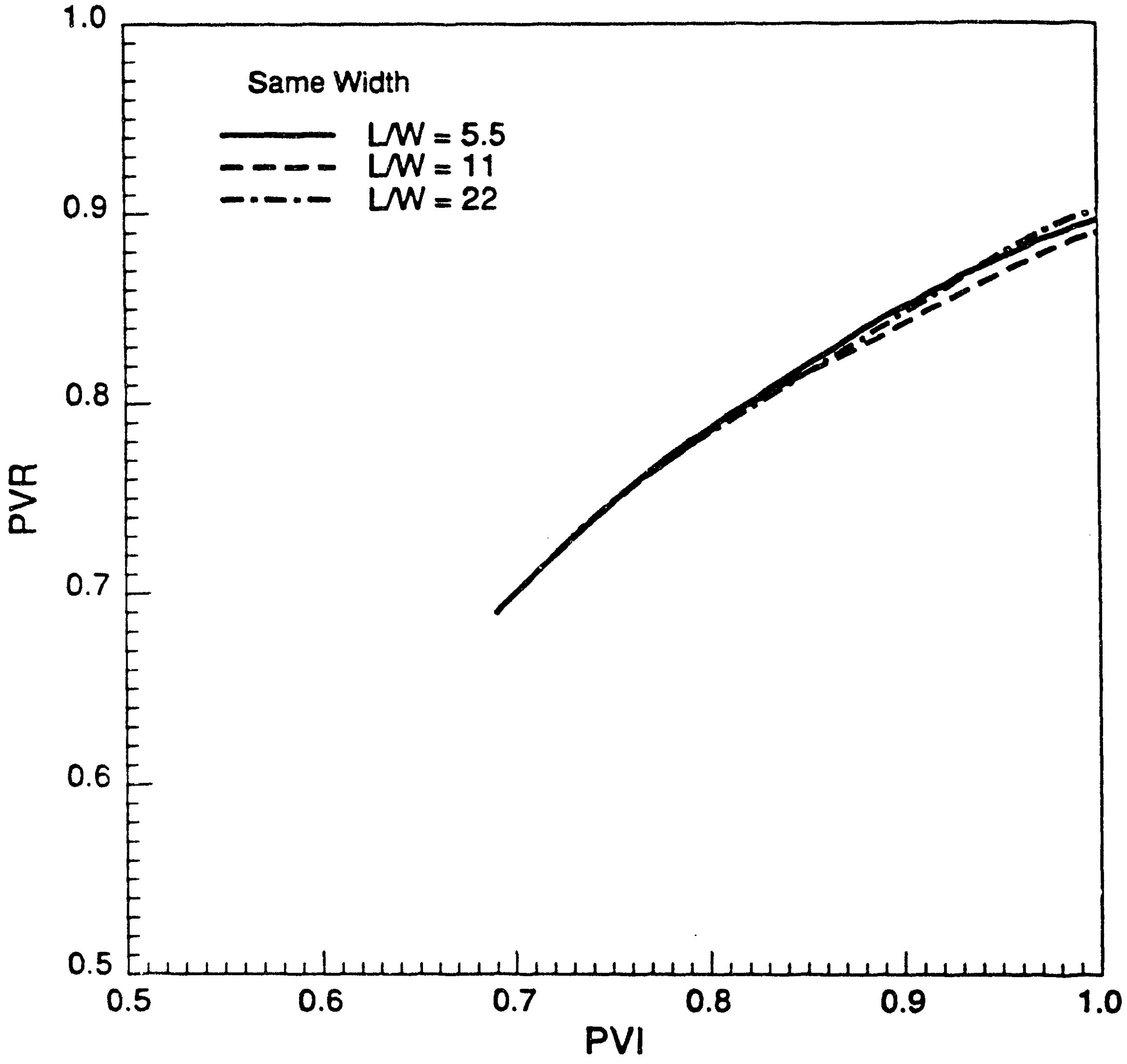

Figure 4.9: Effect of L/W on recovery for M = 6.25.

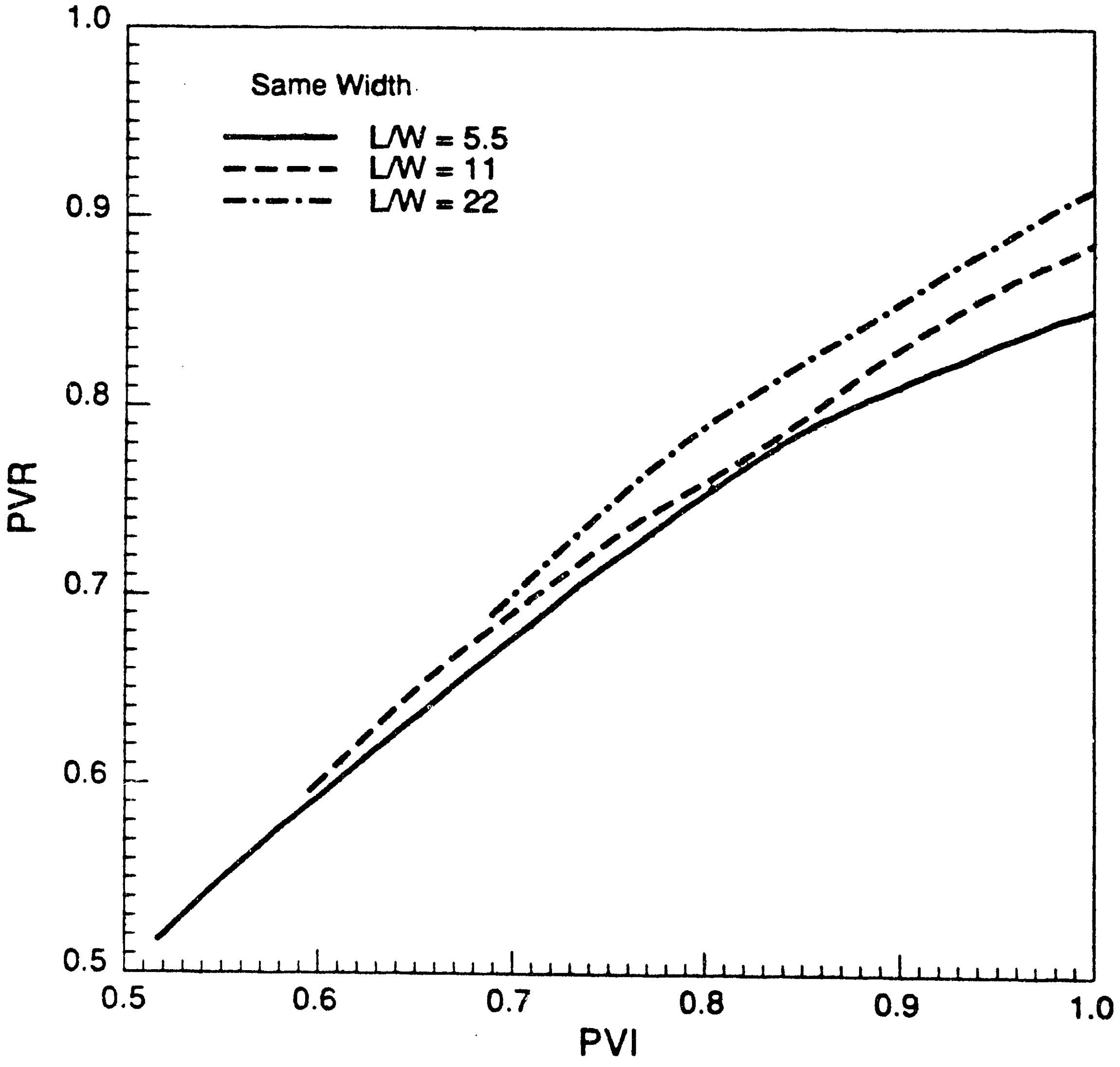

Figure 4.10: Effect of L/W on recovery for M = 12.5.

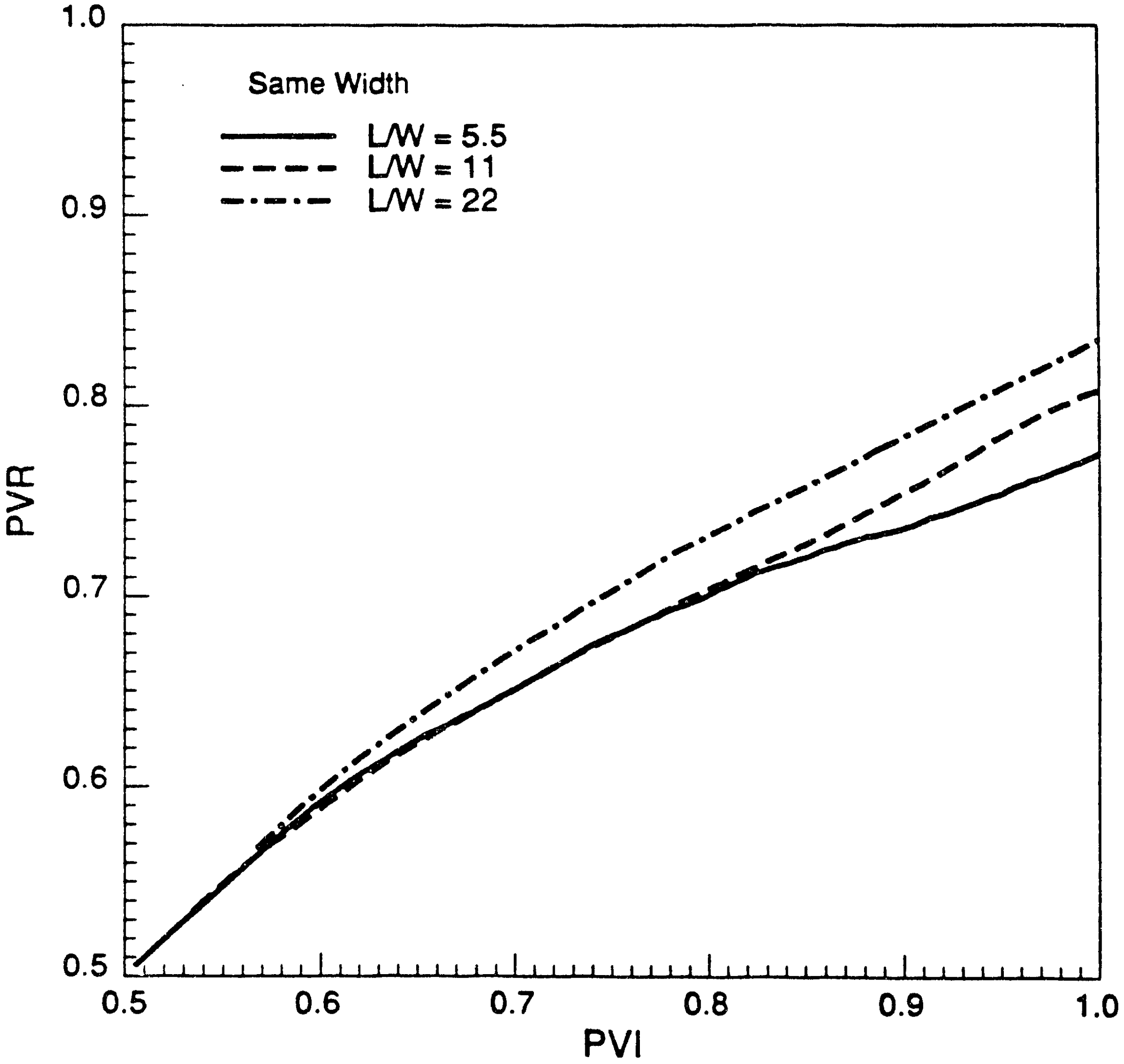

Figure 4.11: Effect of L/W on recovery for M = 25.

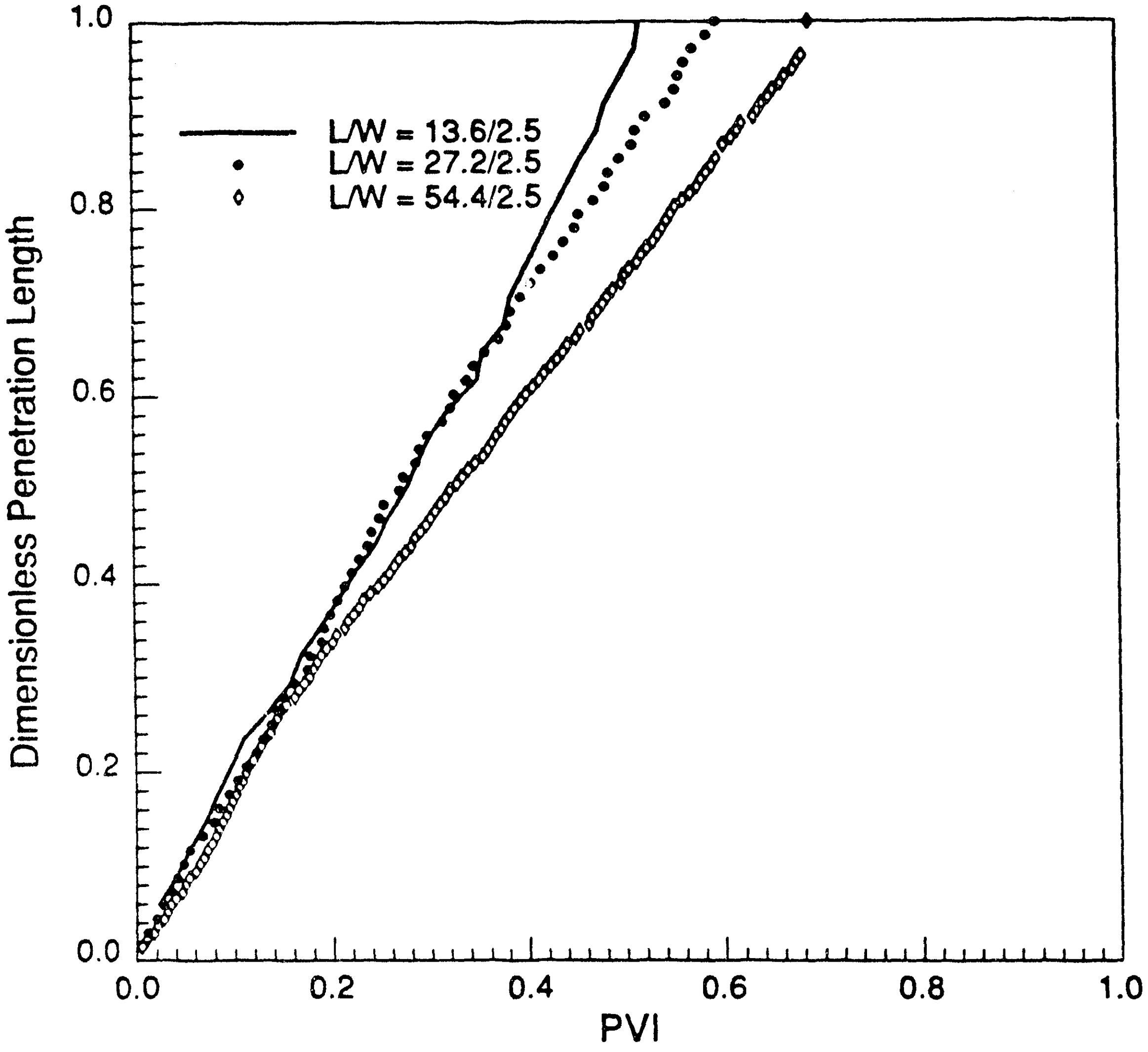

Figure 4.12: Dimensionless penetration length vs. PVI for three length to width ratios at M = 12.5.

dispersion coefficient (grid size in numerical simulations) determines the cutoff. Early in the displacement, transverse dispersion continues to work to eliminate the concentration gradients and suppresses the growth of some small wavelengths that were initially unstable. However, steep viscosity differences over short lengths still exist allowing for unstable growth; as a result, fingers develop.

As the displacement proceeds, the pressure field in the flow domain allows for crossflow into the growing fingers at their bases and out of the fingers at their tips. This convective crossflow coupled with dispersion (microscopic convective mixing) results in building up the concentration of the displaced fluid in the fingers. Consequently, the viscosity contrasts at finger boundaries are moderated. And since the rate of advance of a fluid front (leading or trailing edge) depends on the viscosity contrast, the velocities of the leading edges of the fingers decrease, while those at the trailing ends increase. This behavior is demonstrated in Fig. 4.13, which plots the relative velocities of the leading and trailing edges of the fingered zone for three mobility ratios, namely, 6.25, 12.5, and 25 in a system with L/W = 23.

These mechanisms allow larger fingers to overtake smaller ones, resulting in fewer dominant fingers. This lateral spreading continues until the lateral physical boundaries of the domain are felt. At this stage, one or a few large fingers of comparable length and width compete to organize the pressure field in the flow domain and dominate the displacement behavior. Lateral spreading due to dispersion continues; however, convective crossflow due to the pressure distribution in the flow domain is minimal. Consequently, further moderation of the viscosity contrasts around the boundaries of the fingered zone is inhibited. As a result, the velocities of the leading and trailing fronts of the fingered zone stabilize and hold at nearly constant values. This is clearly seen in Fig. 4.13.

If the dispersivities are constant, longer flow lengths are needed for the frontal velocities to reach stable values as the mobility ratio at which the displacement takes place increases. Moreover, the magnitude of change in the leading edge velocity with flow length is greater for the higher mobility ratio (see Fig. 4.13). One then would expect the differences in displacement behavior as L/W varies to increase as the mobility ratio increases. Experimental evidence to support this is lacking. However, the larger changes in the relative velocities at high mobility ratios may explain the increased deviation between empirical model predictions and experiments, even those with L/W = 3, as the mobility ratio reaches values in the hundreds.

It is important to remember that Fig. 4.13 also applies to all systems with $L/W < 23$. This is a consequence of the lack of influence of the outer boundary demonstrated earlier. Simulations in systems with L/W of up to 33 indicate that once the velocities of the leading and trailing edges stabilize, they experience no further change as the flow length increases. This points to the interesting possibility that the plane moving with the average flood velocity will move more slowly than the leading edge even after very long flow lengths, thus precluding dispersive growth. This possibility can only exist if the molecular diffusion contribution to the dispersion coefficient is negligible. Blackwell et al.'s [6] reported number of 67% breakthrough recovery for a system with L/W = 144 at a mobility ratio of 20 may be indicative of the absence of dispersive behavior in long systems when the mobility ratio is unfavorable. The detailed simulations for L/W = 33, for the mobility ratios investigated here, however, indicate that the displacement always reaches the stage where one finger spans the width of the model. The reason for continuing to call it a finger is that it moves with the stabilized leading edge velocity.

The reason for the insensitivity of the empirical models to variations in the length to width ratio can now be explained. The viscous fingering empirical models of Koval [36] and Todd and Longstaff [74] are based on the assumption that concentrations move with constant velocities. The fractional flow curves constructed using straight line relative permeabilities and the effective mobility ratio yield characteristic concentration velocities that decrease with the concentration

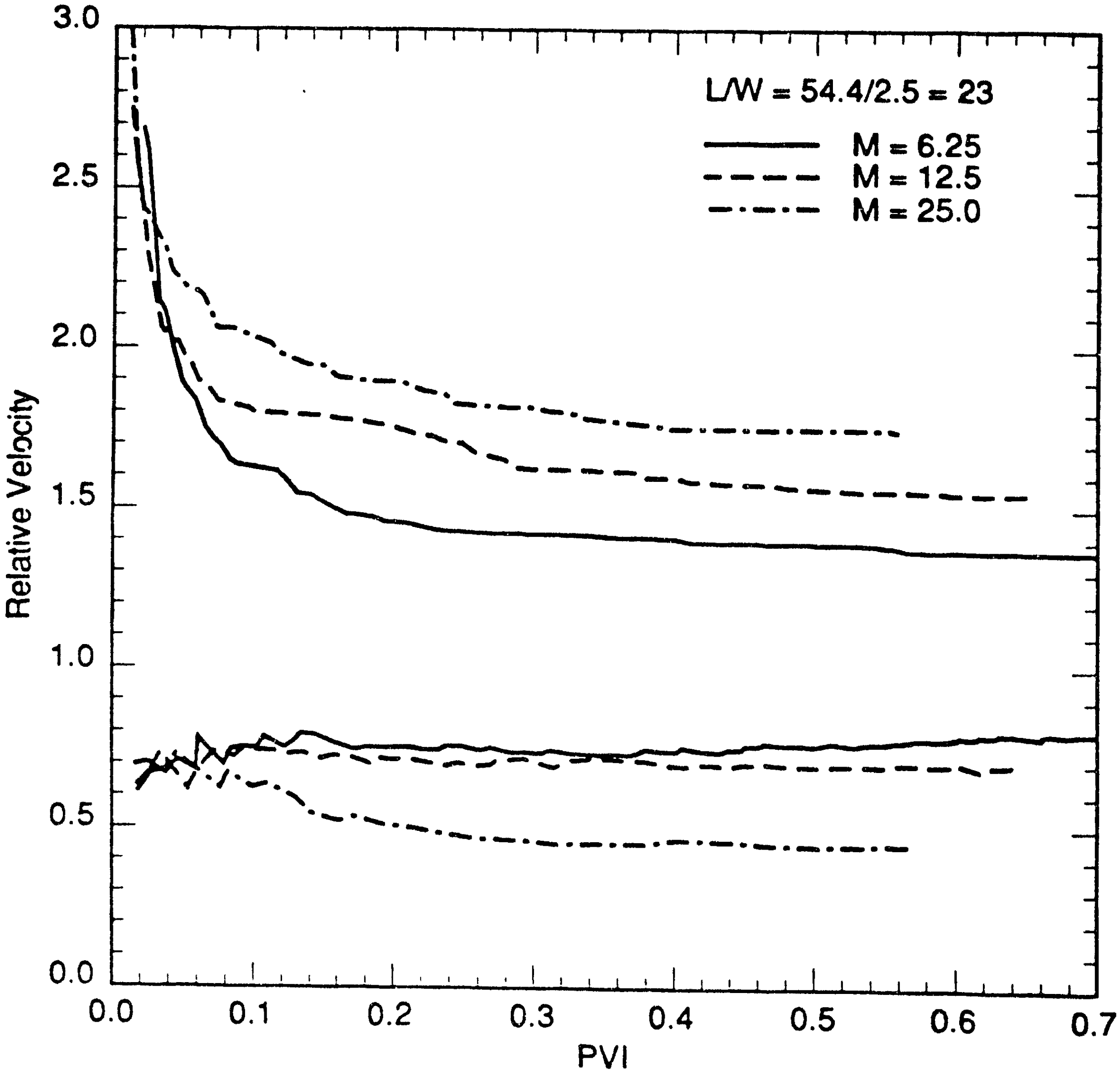

Figure 4.13: Velocities of the leading and trailing edges vs. PVI for M = 6.25, 12.5, and 25 in a system with L/W = 23.

level. The effective mobility ratio in these models is actually the velocity of the leading edge of the fingered zone. If this velocity is correct, the penetration length of the leading edge will be correct, and the prediction of breakthrough time will be accurate.

The velocities of the leading and trailing edges however were demonstrated here to vary with flow length. While the trailing edge velocity variations are small, the leading edge velocity variation with flow length is substantial and should be accounted for. This suggests that the fractional flow curve itself changes in the course of the displacement. Fig. 4.12 suggests that two distinctive regions may be delineated. In each region, one can assume a constant effective mobility ratio (i.e., constant fractional flow curve). As a result, the fractional flow curve used to predict recovery should account for these changes with flow length. Thus, for the empirical viscous fingering models to incorporate the L/W effect, the effective mobility ratio will have to be corrected according to Fig. 4.12. Fig. 4.13 may be used for detailed calibration of the fractional flow curve in the first region.

4.1.3 Conclusions

1. The influence of the outlet boundary on displacement behavior is negligible. In homogeneous and mildly heterogeneous media, the trailing edge moves leaving a fully swept region behind it. As a result, moving boundaries may be used without sacrificing the accuracy or resolution of the numerical simulation. This allows for the study of miscible unstable displacement behavior in long systems. Moreover, CPU time savings are significant.
2. The velocities of the leading and trailing edges of the fingered zone change with the flow length. However, they stabilize at nearly constant values at some value of injected pore volumes. The distance at which they stabilize increases as the mobility ratio increases.
3. Because the flow length at which the velocities of the leading and trailing edges stabilize is a smaller fraction of the domain's length for longer systems, the influence on breakthrough recovery and thereafter decreases as L/W increases.
4. In the absence of molecular diffusion, the leading edge velocity remains nearly constant even after long flow lengths. This suggests that dispersive growth will not occur even in long systems if the mobility ratio is sufficiently unfavorable.
5. The changes in the leading frontal velocity can be accounted for by delineating two regions. The velocity in each region may be assumed to be constant. This assumption is approximate for the first region.
6. The viscous fingering empirical models can account for the effects of L/W by using a fractional flow curve sensitive to the major changes in the effective mobility ratio (i.e., the velocity of the leading front).

4.2 Simulation of Three-Dimensional Viscous Fingering

Two-dimensional simulations proved adequate for linear flow in homogeneous systems and in nearly two-dimensional (thin slabs) domains. The structure and connectivity of the permeability field in real systems of interest, however, are far more complex due to their truly three-dimensional nature. As a result, a complete investigation of the interaction between viscous fingering and heterogeneity must incorporate the influence of the third dimension.

The effectiveness of the random walk particle-tracking method in the simulation of unstable miscible displacement in 2D was demonstrated by Araktingi [1], Araktingi and Orr [2] and Brock et al. [8].

The use of particle tracking is advantageous for the following reasons:

1. Numerical dispersion resulting from a direct numerical solution of the saturation equation is avoided.
2. The grid orientation effect is minimized since the particles' sensitivity to the grid is a function only of how well the pressure distribution in the flow domain is represented.
3. When physical dispersion is viewed as a random process at microscale, the use of random walkers is natural.
4. The ability of the random walk particle-tracking method to model the anisotropy in the dispersion tensor is superior to other methods.

The need for fine grid simulations to model unstable displacement was emphasized in the previous section. Even in two-dimensional flow, the grid numbers needed to properly model adverse mobility ratio displacements can be prohibitive. Numerical mesh sizes of 10,000 gridblocks may be needed for the simulation of displacements in nearly two-dimensional laboratory scale displacements. A corresponding three-dimensional simulation may yield numerical models having hundreds of thousands of gridblocks. Such systems simply cannot be contemplated on conventional uniprocessor computers.

However, parallel processing machines utilizing thousands of small processors operating in unison are well suited for such systems. The MasPar Single Instruction Multiple Data (SIMD) computer with up to 8K processors was used to implement a 3-D random walk particle-tracking simulator sensitive to the details of the underlying physics of dispersion, viscous instability and convection.

The MasPar system includes:

1. The data parallel unit (DPU) which consists of:
    - (a) An array of small processors, each with its own memory, referred to as the "PE array". A variable declared to be parallel is uniformly distributed to the individual processors in the PE array at the same memory location in each. All processors in the PE array execute an instruction simultaneously on the targeted parallel data item. Processors can access the memory of other processors through a network. It is easier for neighbors to communicate rather than a random collection of processors attempting to exchange information.
    - (b) A control unit of limited memory called the (ACU). The ACU holds singular variables and can be thought of as the controlling unit of the PE array.
2. The Front End: a fast uniprocessor workstation which provides capability to handle calculations more suited to uniprocessor machines.

The programming languages available fall into two categories:

1. A user transparent language in which declarations and communications are implicit. This language may be used to program the Front End and the DPU.
2. A low level (highly efficient and flexible) language in which variable declarations and communications must be provided explicitly. This provides for taking advantage of the underlying architecture, and it facilitates optimized performance for the problem at hand. This language can only be used to program the DPU. The code for the 3-D simulator was written using this low level programming language. Interactions with the Front End are made through calls between routines written in this language and a conventional one.

The concept of independent distributed memory is helpful in outlining the strengths of and difficulties in utilizing SIMD massively parallel computers to solve large problems. One clear objective is to keep all processors working productively as much as possible. Another objective is to minimize communications between the processors. As a result, from an optimization point of view, each class of problems must be handled differently in order to take full advantage of the extensive computational power available.

In developing the code for the 3D particle simulator, the following interrelated issues were of prime concern:

1. Mapping strategies. This refers to how one is to distribute the variables involved in the problem such that efficient operation of the PE array is achieved. Points of concern include among other things the coupling of the various variables one is solving for, and what information various parts of the problem need and where do they lie in the distributed memory.
2. Load balancing. Depending on the mapping strategy adopted for the particular problem and the actual physics of what is being modeled, some areas of the PE array may be doing too much of the work, while others are idle. For example, if one grids a reservoir with a gas cap, then most of the action in terms of phase behavior, etc., is taking place in a limited part of the whole grid. How then does one balance the load? Another example is a heterogeneous domain in which fingering is to be modeled. A streak and/or areas of high permeability see most of the action. If particles are mapped to the numerical grid, which in turn is mapped to the PE array, these areas of high permeabilities are bottlenecks because the processors responsible for the grid domain that is affected will be working extra hard while other processors wait for them to finish.
3. Communication structures. A certain amount of communication among the processors as well as with the Front End will be needed. This depends on the issues of mapping and load balancing and their relation to the physics of the problem being tackled. Streamlining the communications and finding schemes to add structure to them enhances the efficiency and may in fact be the determining factor in the success or failure in utilizing parallelism.
4. Virtualization. The size of the PE array is fixed for a machine, while the problem at hand can be of any size. For example, if you have a grid for the purpose of a numerical solution for an engineering problem, how do you fit your problem in the memory and what distribution strategy of the overall grid will you use? The numerical grid will then be folded over in a certain fashion to fit into the machine. How will things communicate then?

These items are interrelated and are being scrutinized by scientists and engineers involved in parallel computation. Massive parallel computation is the way of the future, and developments in the areas outlined in the above listing are shaping them into disciplinary natures.

The collection of algorithms implementing the three-dimensional particle-tracking model are designed such that optimum utilization of the machine's architecture and parallel constructs is achieved. Questions of load balancing, structures of communication, multiple mapping strategies, virtualization and their relation to the unstable flow problem were addressed. The efficiency of the iterative solver is being studied.

Details of the numerical implementation will be presented in subsequent reports. Displacements in three-dimensional domains with over half a million cells were performed at CPU times comparable to two-dimensional systems having a total number of gridblocks two orders of magnitude smaller. For example, injecting and tracking 300,000 particles for 150 steps on 128 by 64 grid takes more than 3 hours of CPU time on the Apollo 10000 machine, while it takes about a minute on the parallel machine.

A detailed study of the interaction between viscous instability and heterogeneity in 3D, now that efficient parallel low level code is at hand, is underway. The results of this study will be presented in the subsequent reports.

4.3 Compositional Particle Tracking and Viscous Fingering

Marco R. Thiele

In a 3-D, heterogeneous, multi-phase, multi-component environment, as may be present in a CO_2-flood, a complete understanding of viscous fingering remains a significant challenge. The complex relationship between viscous, gravity, capillary and dispersive/diffusive forces, the phase behavior of the system and the 3-D heterogeneity encountered in real-world reservoirs makes the problem a difficult one indeed.

Nevertheless, many investigators have been able to make substantial contributions by making simplifying assumptions, such as reducing the dimensionality of the system, isolating driving forces and, importantly, through experimental observation and validation. This has led to a number of different theories and models published in the literature. Notable efforts to simulate numerically the growth of viscous fingers in ideal miscible displacements have been undertaken by various authors. Christie and Bond [13] used a very refined mesh, obtaining good agreement with data of Blackwell et al [6]. King [34] used a statistical approach that generated fingers but did not match experimental observations very well [2]. Tan and Homsy [72] applied a Fourier spectral method, which yielded quite accurate solutions but computational limitations restricted consideration of flows with high transverse Peclet numbers. Araktingi and Orr [2] approached the problem using particle tracking. Their simulations showed clear examples of finger growth mechanisms such as shielding, spreading, tip-splitting, and coalescence. Efforts to include phase behavior in the study of viscous fingers have been more limited. They can be found in the work of Gardner and Ypma [23] and recently in the work of Chang et al. [11].

The approach to be followed here is that proposed by Araktingi and Orr [2], in which only viscous forces and the heterogeneity of the system were considered for simulation of a 2-D, cross-sectional ideal miscible displacement. Even though numerically intensive, the particle tracking method has a number of advantages. It does not require any perturbation, either in the permeability field or the pressure field, to initiate fingers. It is dispersion free in the classical sense, and it is appealing to intuition. Simulation of scaled flow visualization experiments by Brock and Orr [9] and by Tchelepi [52, Sec. 4.2] validated the model further as an alternative to the classical reservoir simulation approach.

In this investigation we propose to extend the particle tracking model by including effects of phase behavior. Most miscible floods rely on mass-transfer between phases to increase recovery. The objective then is to explore in detail how component partitioning affects displacement performance when viscous instability and viscous crossflow also contribute to transverse mixing. Gardner and Ypma [23] argued that such mixing reduces local displacement efficiency. Recent work by Chang et al. [11] on the other hand, suggests that in the case of CO_2 flooding, fingering can be attenuated considerably by the phase behavior of the system and may result in better recovery than would be obtained in an ideal miscible displacements in the same reservoir.

4.3.1 Compositional Particle Tracking

The central idea of the particle tracking method is to represent the physical process of fluid flow through porous media by a number of particles that move along streamlines. In particular, for the ideal miscible displacements modeled by Araktingi and Orr [2], the particles carry a finite volume allowing the concentration at each grid block to be determined by simply counting the number of particles within a block. The movement of the particles is dictated by the pressure field at every time-step, while longitudinal and transverse dispersion, representing subgrid heterogeneity, is modeled by scaled random movements of the particles. A detailed description of the technique is given in Araktingi [1].

In compositional particle tracking the idea of the random walk method is extended to include phase behavior effects. As in the case for ideal miscible displacements, under the assumption of no volume change on mixing as components transfer between phases, the overall material balance equation reduces to the continuity equation, which is solved for the pressure field.

The conservation equation for species i assuming no chemical reactions and adsorption/desorption is [37, pg. 29]

$$\frac{\partial}{\partial t}\left(\phi\sum_{j=1}^{N_P}\rho_j S_j \omega_{ij}\right) + \nabla\cdot\left(\sum_{j=1}^{N_P}\rho_j\omega_{ij}\vec{u}_j - \phi_j S_j \rho_j \vec{K}_{ij}\cdot\nabla\omega_{ij}\right) = 0 \qquad (4.5)$$

with $i = 1, N_c$ and where

ϕ = porosity

ρ_j = molar density of phase j

S_j = saturation of phase j

ω_{ij} = mole fraction of component i in phase j

u_j = Darcy velocity of phase j

$\vec{K}_{ik}$ = dispersion of component i in phase j

N_p = number of phases present

N_c = number of components present

Division by the pure component molar density ρ_i, and summation with respect to all components i leads to the overall material balance equation,

$$\frac{\partial}{\partial t}\left(\phi\sum_{j=1}^{N_P}S_j\left[\rho_j\sum_{i=1}^{N_c}\frac{\omega_{ij}}{\rho_i}\right]\right) + \nabla\cdot\left(\sum_{j=1}^{N_P}\vec{u}_j\left[\rho_j\sum_{i=1}^{N_c}\frac{\omega_{ij}}{\rho_i}\right] - \phi_j S_j \vec{K}_{ij}\cdot\nabla\left[\rho_j\sum_{i=1}^{N_c}\frac{\omega_{ij}}{\rho_i}\right]\right) = 0 \qquad (4.6)$$

Introducing the assumption of no volume change on mixing allows a crucial simplification of Eq. 4.6. No volume change on mixing simply states that phase volumes can be obtained as the sum of the volumes occupied by individual components, whose densities, ρ_i, are independent of the phase in which components appear. If that assumption is satisfied, it follows that

$$\rho_j\sum_{i=1}^{N_c}\frac{\omega_{ij}}{\rho_i} = 1 \qquad (4.7)$$

Substitution of Eq. 4.7 into the overall material balance Eq. 4.6 returns the continuity equation.

$$\nabla \cdot \sum_{j=1}^{N_p} \vec{u}_j = 0 \tag{4.8}$$

$$\vec{u}_j = -\lambda_{rj} k \nabla p \tag{4.9}$$

where

λ_{rj} = relative mobility of phase j

k = absolute permeability

p = pressure

As in the ideal miscible case then, the pressure field is easily obtained from Eq. 4.8. The principal difference lies in the definition and treatment of the particles. For compositional particle tracking the algorithm is:

1. Begin by defining the parameter ζ which has units of *[particles/mole]*. Assuming the injection rate remains constant, choose the number of particles to be injected per block at every time step. Note that this will result in no material balance error since the injected particles will represent exactly the injected moles. If instead ζ is fixed arbitrarily, the required number of particles for a given number of moles injected may not be an integer number. Thus,

$$\zeta = \frac{N_y N_{P_{inj}}}{q \Delta t \rho_{inj}} \left[\frac{\text{particle}}{\text{mole}}\right] \tag{4.10}$$

where

N_y = number of blocks at the injection face
$N_{P_{inj}}$ = number of particles to inject per block
q = injection rate
Δt = time step
ρ_{inj} = molar density of injected phase

2. With the initial overall composition known, perform a flash to determine the initial saturation of the system. If two phases are present the phase saturations are simply given by

$$S_v = \frac{1}{1 + \frac{L\rho_v}{V\rho_l}} \tag{4.11}$$

$$S_l = 1 - S_v \tag{4.12}$$

where

L, V = liquid and vapor phase mole fractions
$\rho_{l,v}$ = phase density given by Eq. 4.7

Using ζ then, the total number of particles in the system at time $t = 0$ may be determined from

$$N_{P_t} = \zeta V_{PV} \left(S_l \rho_l + S_v \rho_v\right) \tag{4.13}$$

where

N_{P_t} = total number of particles in the system

V_{PV} = pore volume of the system

3. Now inject a volume $q\Delta t$ and calculate the resulting pressure field from Eq. 4.8. Generate the particles representing the injected volume and place them, randomly, in the source blocks and move all particles according to their phase velocities. Note that newly injected particles stay in the injected phase until the next time step. The new position of a particle is given by Orr [52, pg. 194]

$$x_{new} = x_{old} + \frac{u_{jx}}{\phi}\Delta t + Z_1\sqrt{2\alpha_L|\vec{u}_j|\Delta t}\frac{u_{jx}}{|\vec{u}_j|} + Z_2\sqrt{2\alpha_T|\vec{u}_j|\Delta t}\frac{u_{jy}}{|\vec{u}_j|} \tag{4.14}$$

$$y_{new} = y_{old} + \frac{u_{jy}}{\phi}\Delta t + Z_1\sqrt{2\alpha_L|\vec{u}_j|\Delta t}\frac{u_{jy}}{|\vec{u}_j|} + Z_2\sqrt{2\alpha_T|\vec{u}_j|\Delta t}\frac{u_{jx}}{|\vec{u}_j|} \tag{4.15}$$

where

Z_1, Z_2 = Normally distributed random variables ($m = 0, \sigma = 1$)

α_L, α_T = Longitudinal and transverse dispersion coefficients

4. Once all particles have been moved, the number of particles of each component in each block is counted. The total number of moles in block *km* and the number of moles of component *i* are then simply given by

$$(n_i)_{km} = \left(\frac{N_{P_i}}{\zeta}\right)_{km} \tag{4.16}$$

$$(n_t)_{km} = \left(\frac{N_{P_t}}{\zeta}\right)_{km} \tag{4.17}$$

where

n_i = number of moles of component i

n_t = total number of moles

5. Now determine the overall compositions in block *km* from

$$(z_i)_{km} = \left(\frac{n_i}{n_t}\right)_{km} = \left(\frac{N_{P_i}}{N_{P_t}}\right)_{km} \tag{4.18}$$

6. With the overall compositions known, a flash calculation will return values for L and V at each block *km*. Using constant K-values this amounts to solving

$$\mathcal{F}(V) = \sum_{i=1}^{N_c} \frac{z_i(K_i - 1)}{1 + (K_i - 1)V} = 0 \tag{4.19}$$

where

$$V = \frac{n_v}{n_t} \tag{4.20}$$

$$L = 1 - V \tag{4.21}$$

7. Now use L and V to calculate the phase saturations from

$$S_v = \frac{1}{1 + \frac{L\rho_v}{V\rho_l}}$$

$$S_l = 1 - S_v$$

8. All particles can now be assigned to the correct phases since the amount present in each phase is known from the flash. Thus

$$N_{P_{il}} = n_l x_i \zeta \tag{4.22}$$

$$N_{P_{iv}} = n_v y_i \zeta \tag{4.23}$$

   where

   $N_{P_{il}}$ = number of particles of comp. i in the liquid phase
   $N_{P_{iv}}$ = number of particles of comp. i in the vapor phase
   n_l = number of moles in the liquid phase
   n_v = number of moles in the liquid phase
   x_i = mole fraction of comp. i in the liquid phase
   y_i = mole fraction of comp. i in the vapor phase

   The assignment of the particles to phases must be random within a block. The reason for this, of course, is that the distribution of the phases at a scale smaller than the grid-block cannot be resolved. In other words, the grid-block acts like a stirred tank.

9. Now update all transmissibilities using the new saturations and return to step 3 to calculate the new pressure field.

4.3.2 Discussion

As with other methods particle tracking has its advantages and disadvantages. Because it does not require a perturbation to initiate fingers, it is especially suited to study the growth and decay of viscous fingers in homogeneous media. By slowly increasing the heterogeneity of the system then, the transition from purely viscous dominated to heterogeneity dominated flow is well demonstrated, as Araktingi and Orr [2] showed. Unquestionably, the strong point of particle tracking lies in the absence of numerical dispersion. Numerical dispersion has the effect of smearing out such details as fingers, and thus it may interfere with or even prevent the growth of fingers. The lack of numerical dispersion is also the reason for its popularity in groundwater modeling, where grid-blocks can be so large that numerical dispersion completely overwhelms the physical dispersion needed for the model.

The main limitation, on the other hand, is the large number of particles and the associated numerical work and storage required. The computational requirements will increase when phase behavior is introduced because the smallest composition representable will always be carried by a single particle. Thus, the total number of particles needed to maintain a certain level of detail can become very large. This problem is associated, however, mainly with the availability of computing power and storage rather than with the physics the algorithm attempts to represent.

Testing the algorithm involves a two-step approach. First, computational results from the new model will be compared with the single phase results obtained by Araktingi and Orr [2]. This is easily done by choosing K-values that will always return a single phase. The performance of the portion of the model that couples phase equilibria to convective transport will be tested by simulating stable flow of three and four-component mixtures. The results of the simulations can be compared directly with the analytical solutions obtained in Chapter 3 for dispersion-free flow in one dimension. Thus, it is particularly useful that such solutions are available because they permit a detailed assessment of the accuracy of the numerical model. If the particle tracking method can be shown to model accurately both the viscous instability and the analytical solution for the chromatographic separations associated with development of miscibility, then the model can be used with confidence to explore the interactions of phase behavior, crossflow, and nonuniform flow due to fingering and heterogeneity.

4.4 Summary

In this chapter results of particle-tracking simulations to investigate the scaling of viscous fingering in linear flow are reported. Improvements to the two-dimensional code are described that reduce computational costs substantially without loss of accuracy. The linear-scaling calculations show that the simplified models that make use of a fractional flow expression [36, 19, 20] must be modified if they are to represent with reasonable accuracy the effects of variation in length-to-width ratio. The sensitivity of currently available fractional flow models of fingering to variables such as length to width ratio and also to the presence of heterogeneity suggests that significant improvements to such models will be needed if they are to yield accurate representations of field-scale fingering.

Also described in this chapter are efforts to extend the particle-tracking approach in two ways. The first is to allow computations in three dimensions. While the ideas behind that extension are straightforward, the implementation is not if computational costs are to be low enough to allow significant problems to be attacked. Additional extensions to include the effects of phase equilibrium are also underway. Those changes will permit an assessment of the importance of the interactions of phase behavior with crossflow during unstable flow in heterogeneous porous media.

5. Crossflow: Effects of Gravity, Capillary and Viscous Forces in Heterogeneous Porous Media

In this chapter, we examine the interplay of forces that drive flow between zones with differing permeability. Consider, for example, a nearly miscible flood in a system with two layers. Because the displacement is not quite miscible, two-phase flow occurs. The displacement proceeds more rapidly in the high permeability layer. Thus, the permeability difference creates differences in composition and saturation between the two layers. Those differences lead to crossflow. Differences in mobility induce viscous crossflow. Differences in phase density cause gravity segregation of the phases. Differences in saturation cause capillary-pressure differences that also drive crossflow, and composition variations will induce interfacial tension (IFT) gradients that contribute to that crossflow. Diffusion and dispersion will also contribute to transverse mixing. Because all the crossflow mechanisms will mix fluids of different compositions, the development of miscibility, described in detail for one-dimensional flow in Chapter 3, will also be affected. Thus, understanding of the scaling of crossflow is of considerable importance to the description of miscible flood performance.

In Section 5.1 we examine the combined effects of gravity and capillary crossflow. Results of experiments with equilibrated phases are reported, as are results for crossflow in systems with IFT gradients. We show that as IFT is reduced to modestly low levels (10^{-1} mN/m), there is a transition to gravity-dominated flow that produces very high displacement efficiency. In Section 5.2 we report results of flow visualization experiments that illustrate the scaling of the interaction of heterogeneity, dispersion, and gravity-driven crossflow. In addition, simple, limiting-case analyses of the flows described in Sections 5.1 and 5.2 are also given. The combination of experimental and theoretical results presented, therefore, provide a foundation of evidence on which additional experiments to examine more complex flows will be based.

5.1 Capillary Imbibition and Gravity Segregation in Low IFT Systems

David S. Schechter and Dengen Zhou

The transfer of fluid by some combination of capillary imbibition and gravity-driven flow is significant in a variety of oil recovery processes. In fractured reservoirs, for example, capillary imbibition has long been regarded as a primary mechanism for oil recovery during waterflooding. The high IFT associated with oil/water systems induces a correspondingly high capillary pressure which, in turn, provides the driving force for spontaneous imbibition into matrix blocks. Capillary crossflow during waterfloods in heterogeneous reservoirs is the basis for the vertical equilibrium assumption sometimes used to calculate pseudorelative permeability functions [84]. Some combination of capillary crossflow and gravity-driven flow undoubtedly operates during the near miscible conditions necessary for enhanced oil recovery (EOR) processes in heterogeneous reservoirs, though scaling of those contributions is largely uninvestigated. In EOR processes such as miscible or surfactant/polymer flooding, IFT's vary with the composition of the equilibrium phases generated during the flow process, as will density difference between phases. In near miscible gas injections, for instance, it would be expected that injection compositions should generate tie-lines in the two phase region near to the critical point where the IFT is negligible. With large values of IFT, capillary forces overcome gravitational forces thus preventing macroscopic phase separation within the confines of porous media. However, when the fluid phases are near the critical locus, the density difference may dominate and determine the phase distributions. The following experiments have been performed to quantify low IFT gravitational flow.

5.1.1 Scaling of Imbibition

Most experimental investigations of capillary crossflow have been aimed at the transfer of an imbibing phase into a rock matrix from a fracture. The experiments of Mattax and Kyte [42] and Kleppe and Morse [35], for example, reported results of experiments performed with fixed IFT. They showed that the time dependence of recovery depends on the matrix geometry and physical properties of the fluids. Kleppe and Morse argued that for a given rock type (k,ϕ), block size (L^2) and fluid properties (μ_w, μ_o, σ), the time scale for imbibition is given by

$$t_d = t\sqrt{\frac{k}{\phi}}\left[\frac{\sigma\cos\theta}{\mu_w \mathrm{L}^2}\right] \tag{5.1}$$

According to the scaling implied by Eq. 5.1, displacements in which values of t_d are equal should show equivalent recovery. Key assumptions for this scaling relation are that the flow is governed by capillary forces and gravity forces are negligible. According to Eq. 5.1, if the IFT (σ) is reduced, the time required to recover a given fraction of the oil increases. Hence, recovery rate decreases with the IFT when capillary imbibition dominates the flow. Experimental investigations of the effect of changes in IFT have been limited, however. Cuiec et al. [14] performed imbibition experiments in low permeability chalk samples. They found that lowering the IFT between the imbibing brine phase and the oil phase in the chalk sample reduced the rate of oil recovery, in accordance with the scaling theory of Eq. 5.1. Effects of gravity-driven flow have been largely ignored in the analysis of the scaling of such flows, although Van Golf-Racht [78] suggested that gravity may govern the displacement for large matrix blocks or low capillary pressure.

More literature is found regarding gravity stabilized gas injections in the presence of oil and connate water. Gravity drainage in this case may be highly efficient in the ultimate recovery of the oil phase. Residual oil saturations as low as 3% have been measured in the presence of connate water [17]. Other experimental efforts have determined that film drainage after breakthrough during gas drive experiments may substantially contribute to the final oil recovery [25, 48]. Pavone et al. [58] recently conducted low IFT gravity drainage experiments which indicated that flow occurred in two distinct regions. The oil phase rapidly drained during bulk flow when the saturation of the gas phase was still low. As the gas saturation increased, there was a sharp break in the drainage recovery curve in which oil continued to drain, but at a much slower rate. The film drainage mechanism was observed to increase recovery by as much as 20%. Thus, an understanding of the relative permeability behavior of the oil phase becomes crucial in order to model such drainage experiments [58, 22].

In this section, we report experimental imbibition and drainage results demonstrating that both gravity and capillary forces can be important when the IFT is moderately low, and that there is a transition from capillary-dominated to gravity stabilized imbibition as the IFT is reduced in a ternary oil/water/alcohol system.

5.1.2 Experimental Observations

A well-described ternary fluid [47] system consisting of isooctane (IC8), brine (2 wt.% $CaCl_2$) and isopropanol (IPA) was used for this study. Imbibition experiments were performed with equilibrium phases on three tie lines as shown in Fig. 5.1.

Properties of the phases are reported in Table 5.1. The three tie lines showed significantly different properties. For IC8 and brine mixtures containing no IPA, the IFT is 38.1 mN/m (tie

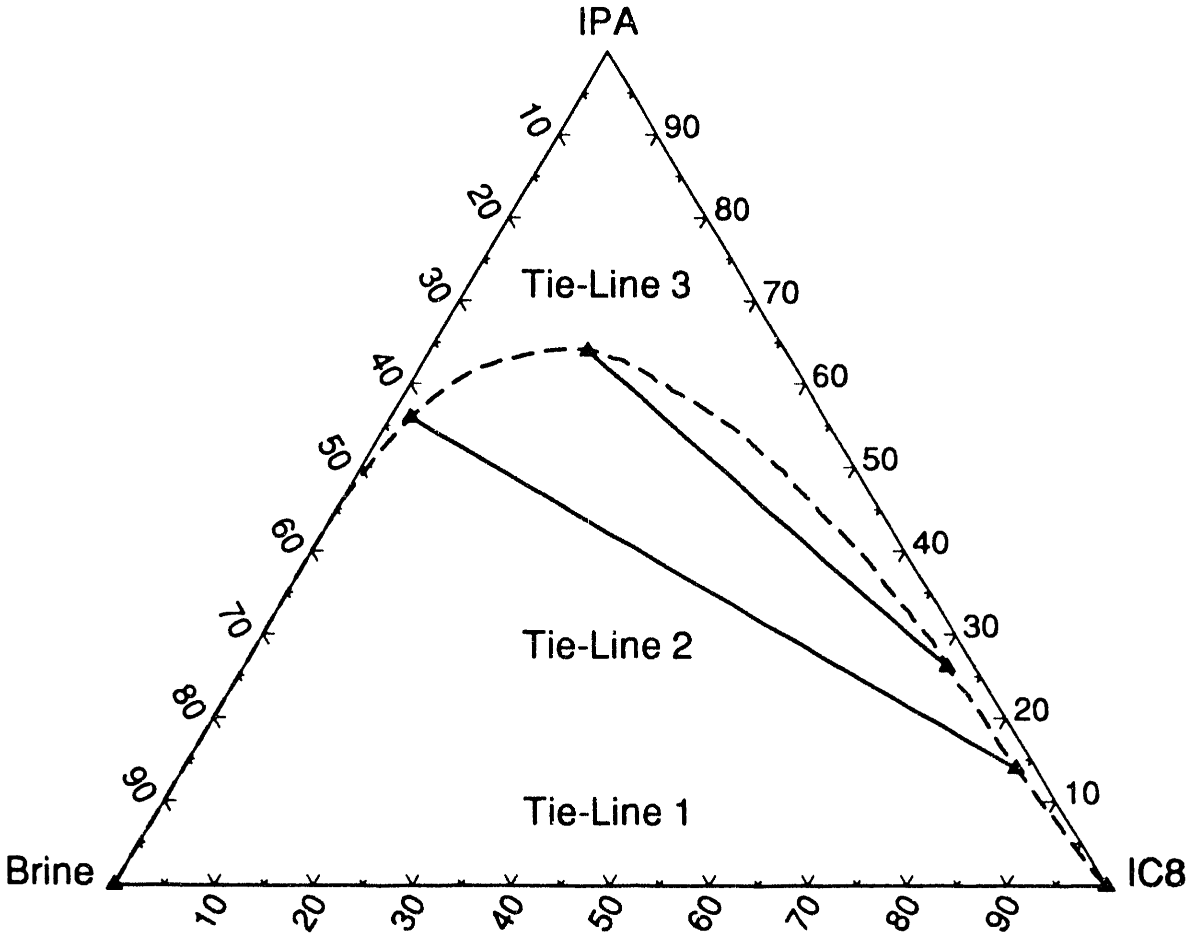

Figure 5.1: Phase diagram for IC8/brine/IPA system.

Table 5.1: Phase Properties for Three Equilibrium Tie-Lines

Tie Line	$\Delta\rho$ (g/cm^3)	IFT (mN/m)	Viscosity Ratio (μ_w/μ_o)
1	0.33	38.1	2.0
2	0.21	1.07	6.25
3	0.11	0.10	3.71

Table 5.2: Core Properties (Diameter of each core = 6.35 cm)

Sample	Permeability (md)	Length (cm)	Porosity (ϕ)	Pore Volume (cm^3)
Indiana Limestone	15	61	0.158	305
Berea Sandstone	100	57	0.187	335
Berea Sandstone	500	57	0.213	385
brown Sandstone	700	61	0.184	353

line 1 in Fig. 5.1). For equilibrated mixtures on tie-lines 2 and 3, the IFT's are reduced to 1.0 and 0.1 mN/m respectively. Thus, the IFT's differed by two orders of magnitude, while the density difference ($\Delta\rho$) was a factor of three lower on tie line 3 than on tie line 1. In addition, two experiments were performed with oil and water phases that were not in equilibrium.

The cores used in this study were all obtained from Cleveland Quarries Co. Properties of the cores are given in Table 5.2.

The experimental procedure consisted of vacuum saturation of the cores with either nonequilibrated or equilibrated oil phase. This was accomplished in a core holder equipped with an overburden sleeve. The core was then transferred to a plexiglass cell with an annular space of 0.08 cm between the side of the core and the wall (Fig. 5.2).

The air in the annulus was displaced by the nonwetting phase until the entire core was immersed in the nonwetting fluid. After 24 hrs. of immersion, the wetting phase was introduced into the bottom of the cell, and the nonwetting phase was quickly displaced from the annular space until the core was completely immersed in the wetting phase. Flow was discontinued and the entrance and exit valves were closed. The core was allowed to remain completely immersed in the wetting phase until oil production was complete. The produced oil collected in the top of the chamber. At various intervals, this oil was flushed and the volume measured.

Imbibition Experiments with Equilibrated Fluids

Figs. 5.3–5.6 are recovery curves for each of the cores investigated. Each plot shows observed behavior for the high, intermediate and low values of IFT. Fig. 5.3 demonstrates that as IFT was reduced, the rate of imbibition slowed in the 15 md limestone core.

At high IFT, the brine rapidly imbibed into the core with completion of imbibition occurring after four hours. During that experiment at high IFT, oil droplets were observed to exit from the lateral faces of the core. At the intermediate IFT, drops were observed to exit the core from both the lateral and the top face of the core. The final recovery was slightly higher than that of the high IFT case although imbibition occurred more slowly over several days. At low IFT there was a substantial increase in total oil produced, but completion required approximately 40 days. For the limestone core, rate behavior is therefore in qualitative agreement with Eq. 5.1.

The recovery curves for the 100 md Berea core are shown in Fig. 5.4. The trend in rate behavior shown in Fig. 5.4 differs sharply from that implied by Eq. 5.1. In this case, the high IFT brine imbibed more slowly than either the intermediate or the low IFT brines. Initially, the recovery rate was greatest at the intermediate IFT. For the first two days, the low IFT experiment showed a lower rate than the intermediate IFT case, but a much larger fraction of the oil originally in place (%OOIP) was eventually recovered at low IFT. In the high IFT experiment, nearly 60% of the oil was recovered, but the recovery rose to 95% for imbibition of the low IFT brine.

A similar trend was observed for the 500 md Berea core as shown in Fig. 5.5. The high IFT case produced the smallest fraction of OOIP, while the intermediate IFT produced more oil

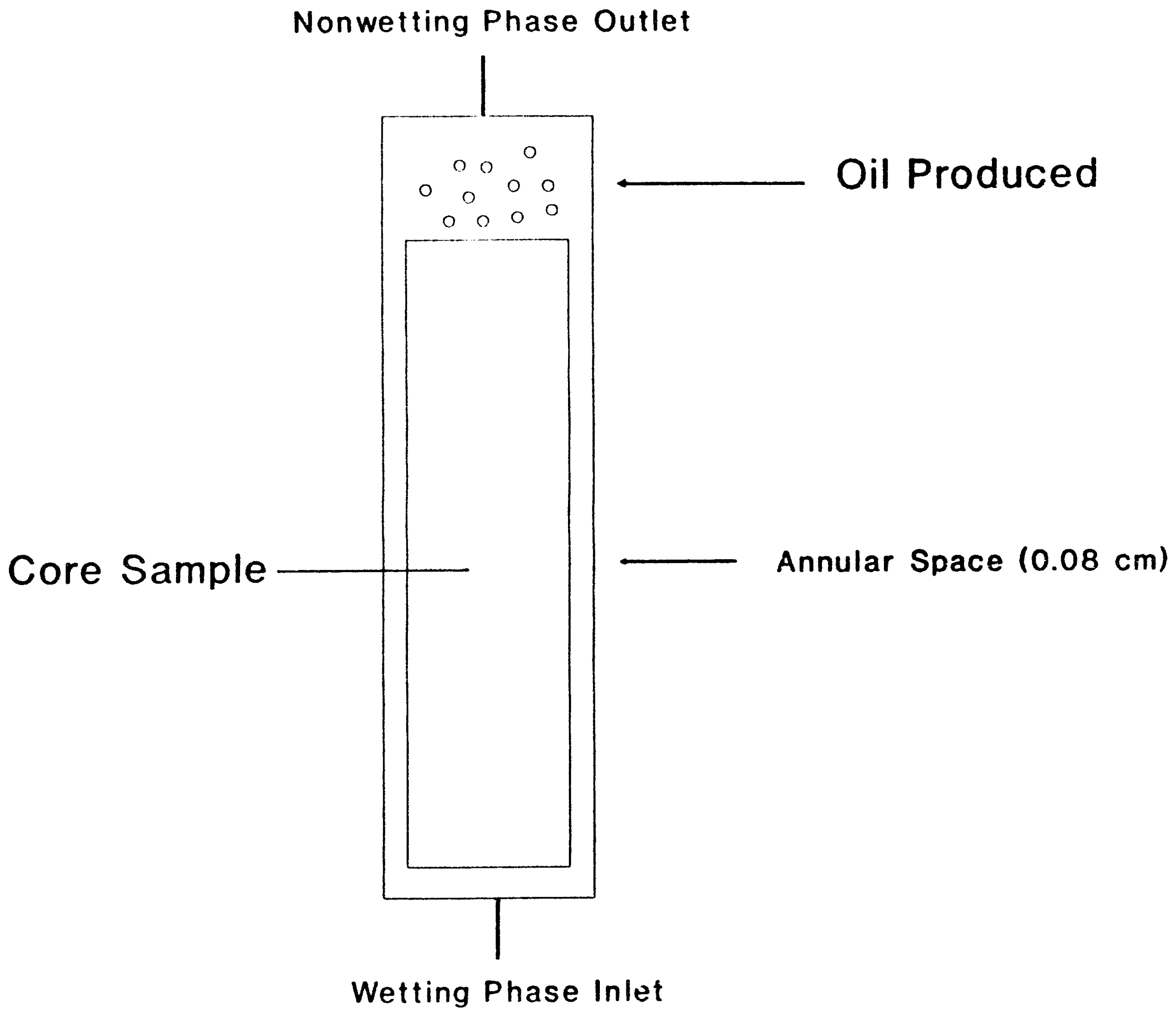

Figure 5.2: Schematic of plexiglass imbibition cell.

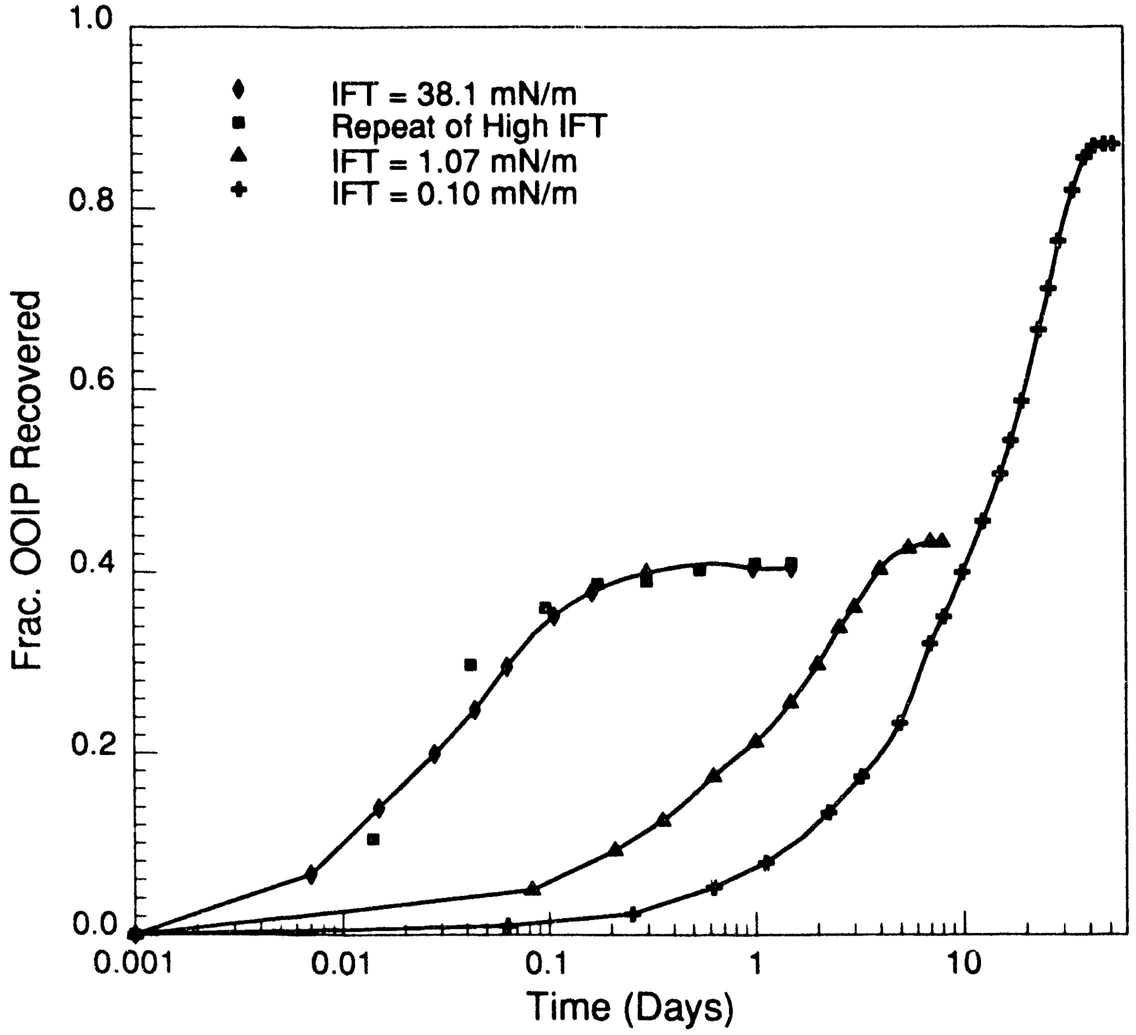

Figure 5.3: Oil recovery for 15 md Indiana Limestone.

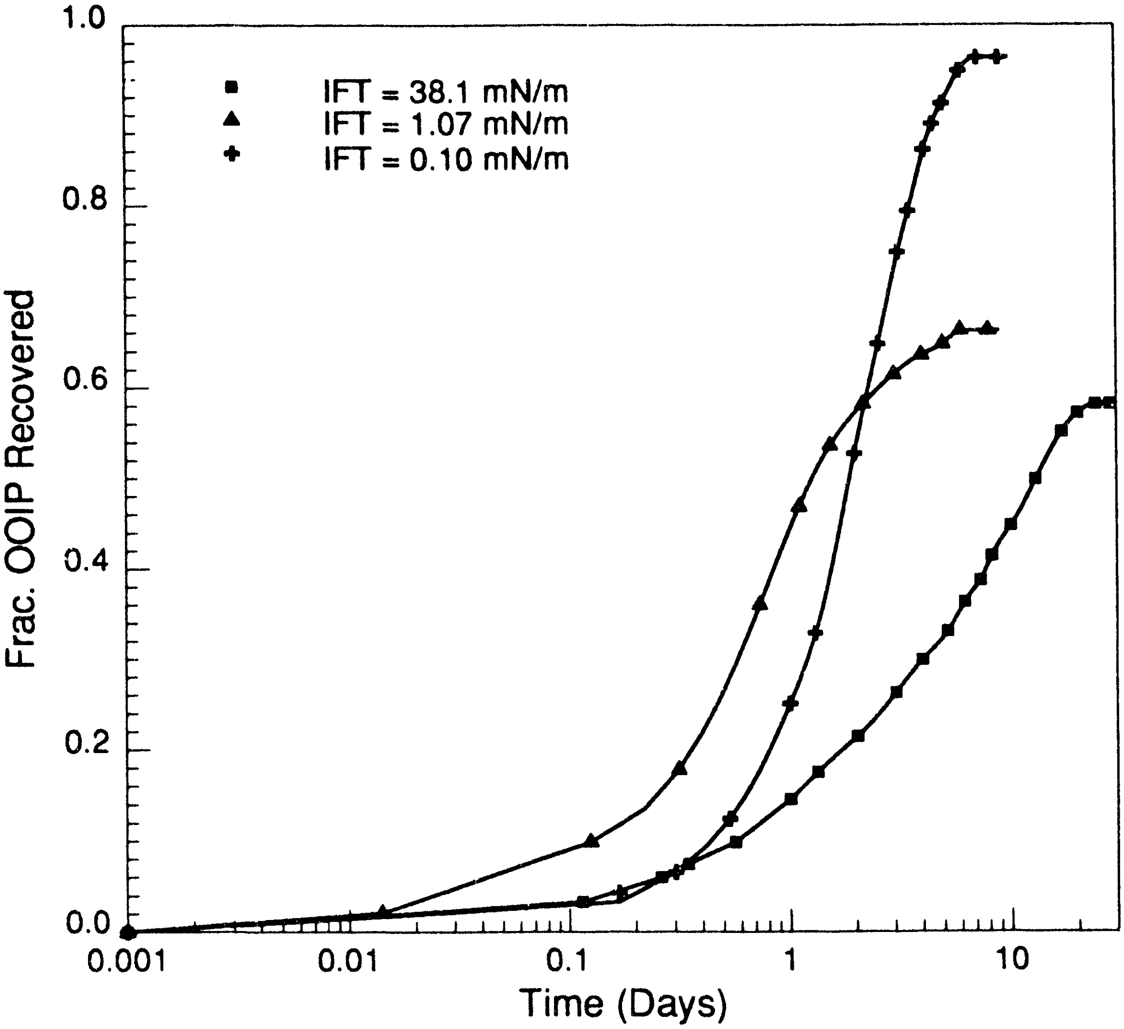

Figure 5.4: Oil recovery from 100 md Berea sandstone core.

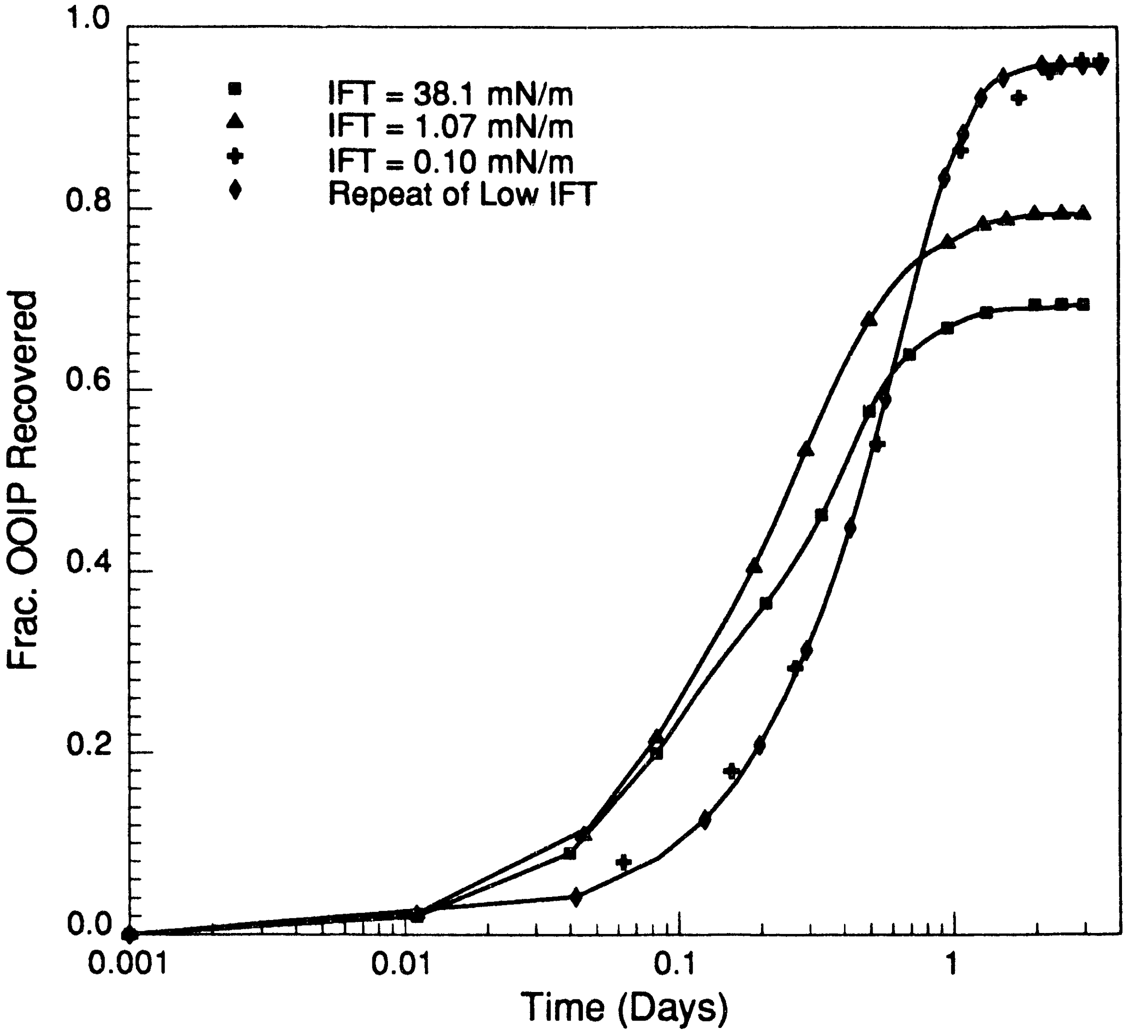

Figure 5.5: Oil recovery from 500 md Berea sandstone core.

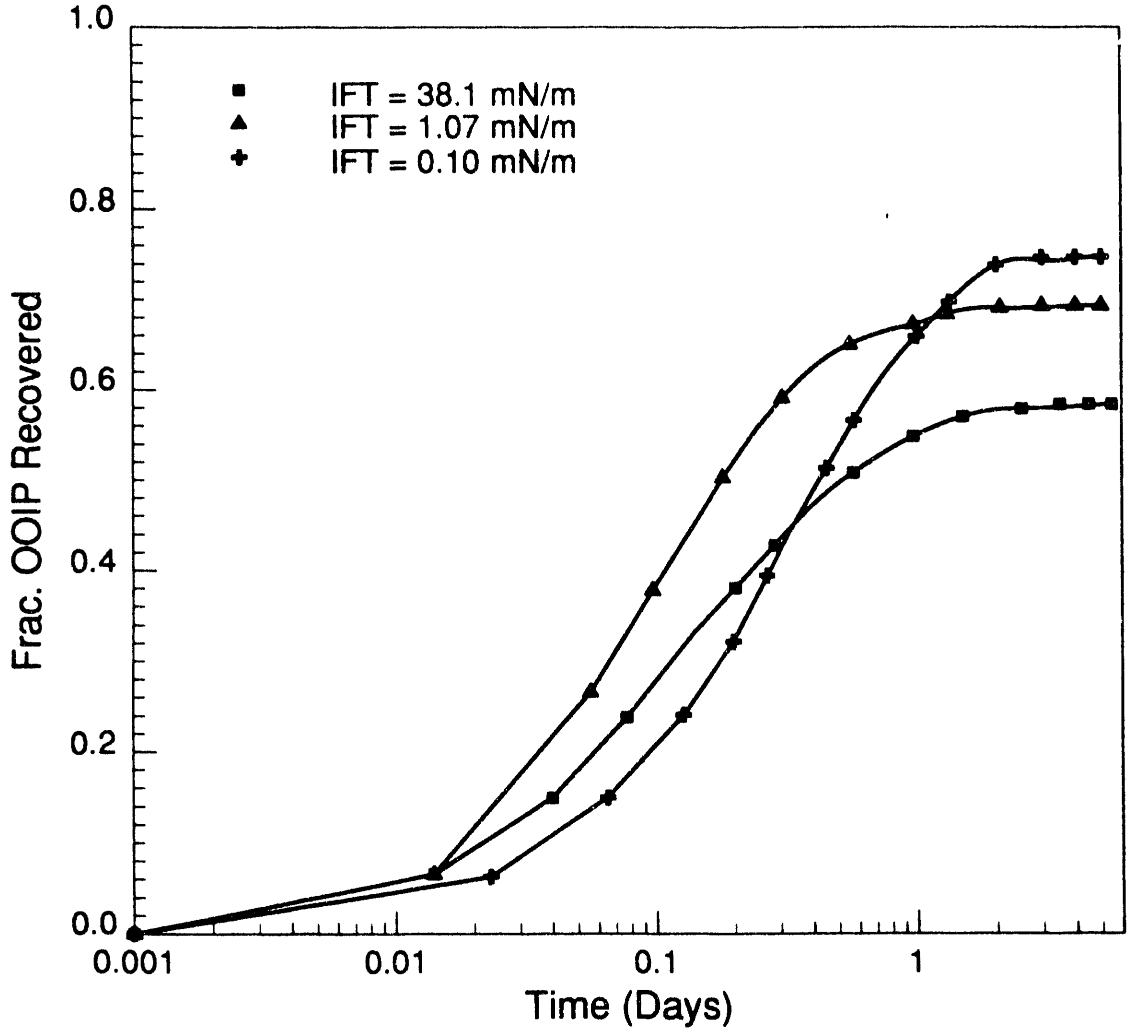

Figure 5.6: Oil recovery from 700 md brown sandstone core.

at a faster rate. In the low IFT case again oil was produced slowly during the first part of the experiment, but recovery eventually equaled and then exceeded the amount of oil produced in the intermediate and high IFT experiments. As with the 100 md Berea, final recoveries exceeded 90% in the low IFT case. To test repeatability of the measurements, the low IFT experiment was performed again. As Fig. 5.5 shows, recovery behavior observed in the two experiments differed only slightly.

Fig. 5.6 shows recovery curves for the brown sandstone core. The trend was similar to that of the Berea cores except the final recoveries were lower. The external surface of that core appeared to be much more heterogeneous, which may account for the lower recovery.

An important change in the flow behavior was observed for the intermediate and low IFT experiments in the three sandstone cores. Oil was no longer produced from all faces as was the case at high IFT. Instead, the oil produced in these experiments was a result of cocurrent flow in which oil droplets exited the core only from the top face.

One additional experiment was performed to evaluate the importance of gravity effects at

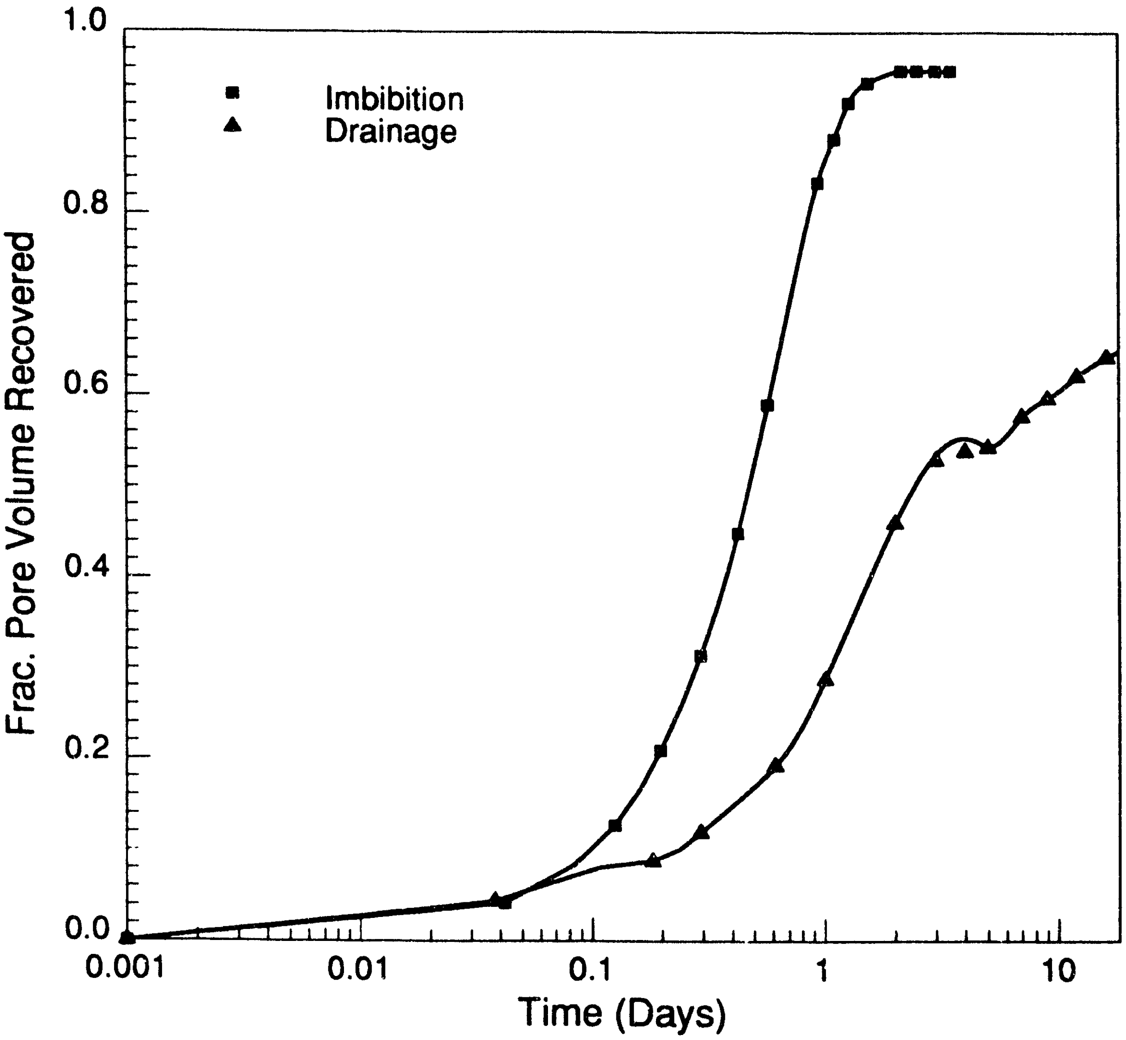

Figure 5.7: Spontaneous imbibition and drainage in 500 md Berea, IFT = 0.1 mN/m.

low IFT in the 500 md Berea sandstone core. The curve labeled "imbibition" in Fig. 5.7 is the low IFT recovery curve shown in Fig. 5.5. In the other experiment, the core was saturated with preequilibrated brine phase and immersed in the preequilibrated oil phase at low IFT. It is generally accepted that clean sandstone is strongly water wet for the refined oil system used here. However, the low IFT imbibition curves shown in Fig. 5.3-5.6 suggest that if the capillary forces that act to oppose an increase in oil saturations are small, the aqueous phase could drain spontaneously under the force of gravity. Fig. 5.7 verifies this idea. It shows that at low IFT 65% of the aqueous (presumably wetting) phase drained from the core. Thus, in that relatively high permeability core, gravity forces were sufficient to overcome capillary forces when the IFT was 0.1 mN/m. The drainage curve is characterized by a break in recovery after 45% of the wetting phase had been recovered. At this point, film drainage occurred over the course of several days and was responsible for 20% of the recovery. This data agrees with the observations of Pavone et al. [58], but it must be pointed out that there is a fundamental difference in the two sets of experiments. In gravity stabilized gas injections connate water is always the wetting phase and oil forms a thin film between the gas and water phases whereas in the drainage experiment in Fig. 5.7, the wetting phase is the draining phase. We expect some differences in the drainage experiments presented in this paper to that of the gravity stabilized gas injections of Pavone due to the interactions of the draining film. In our case, there are only two phases, and the film that is draining also interacts with the solid surface. In gas injections, the oil film which drains exists between the wetting water phase and the gas phase so there is no interaction of the oil with the solid.

Imbibition Experiments with Nonequilibrium Fluids

Two experiments were performed to investigate nonequilibrium effects on imbibition. In the first case, the core was saturated with pure IC8 and contacted with wetting phase in the annulus which had a high concentration of IPA. Unlike equilibrium studies, in which the volume of oil produced equaled the volume of wetting phase imbibed, the oil phase produced in nonequilibrium experiments contained IPA that partitioned from the imbibing brine phase. Therefore, the effluent oil phase was analyzed by gas chromatography to establish the quantity of IC8 actually produced.

Fig. 5.8 shows the results of three displacements in the 500 md Berea core. The equilibrium curve was taken from the low IFT experiment shown in Fig. 5.5. In one experiment the core was saturated with pure IC8 and immersed in a 70% solution of IPA in brine. The rate of recovery exceeded that of the equilibrium case. The minimum IFT possible in the nonequilibrium case was about 0.2 mN/m. In the second experiment, the core was saturated with an IC8 solution containing 40% IPA. It was then immersed in pure brine. In that experiment the rate of recovery and the final amount of nonwetting phase produced was greatly reduced.

5.1.3 Analysis of Recovery Mechanisms

Conventional interpretations of imbibition generally regard capillary pressure as the driving force behind imbibition. For low IFT immiscible phases, one would expect a decrease in capillary forces and therefore slower mobilization of the nonwetting phase during imbibition, as Eq. 5.1 indicates. According to the experimental results outlined here, this is not necessarily the case. Indeed, reduction of the equilibrium IFT apparently enhanced the rate as well as final recovery in the high permeability sandstone cores used.

Cuiec et al. [14] observed that reducing the IFT resulted in a decrease of imbibition rates. Their results were obtained in tight chalk with permeabilities between 1 and 3 md. The results presented, however, cover a wider range of permeabilities. The analysis given below suggests that gravity segregation dominated flow in the high permeability sandstone cores and that capillary forces were more important in the limestone core and the low permeability chalk cores of Cuiec et al. We argue that the change in displacement behavior occurs because there is a crossover from capillary to gravity driven imbibition which is dependent on the average pore size, the pore size distributions, and the phase behavior of the fluids considered. Therefore, we suggest that imbibition can occur in three differing regimes: capillary dominated, gravity dominated, and a region where both forces affect imbibition.

The transition from capillary to gravity dominated flow occurs because IFT's decrease more rapidly near a critical point than do phase density differences. As Fig. 5.1 indicates, tie line 3 is much closer to the plait point in the IC8/brine/IPA system than are the other two tie lines. According to critical scaling [66, 64] arguments, the IFT (σ) between two phases near a critical point may be scaled as the distance of the chemical potential of one phase to some reference chemical potential at the critical point according to

$$\sigma = \sigma^* \left[\frac{\mu_r - \mu_{rc}}{\mu_{rc}} \right]^\gamma \tag{5.2}$$

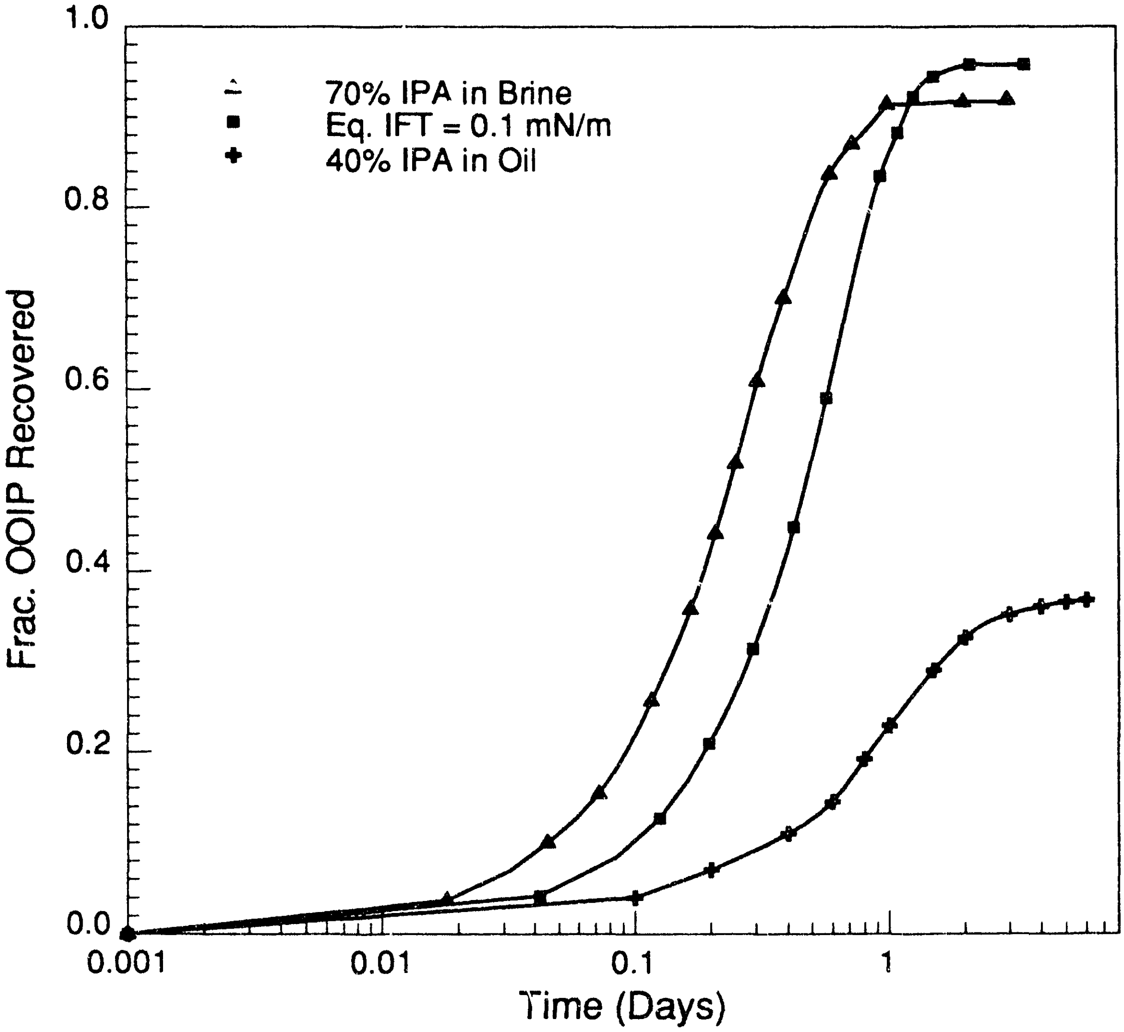

Figure 5.8: Imbibition of nonequilibrium fluids.

Here, γ is the scaling exponent for IFT. It has a theoretical value of 1.26 [66].

Similarly, the density difference ($\Delta\rho$) between the two phases is also determined by a power law dependence of the form

$$\Delta\rho = \Delta\rho^{*}\left[\frac{\mu_r - \mu_{rc}}{\mu_{rc}}\right]^{\beta} \tag{5.3}$$

where β, the scaling exponent for density difference, is approximately 0.33 [66].

Combination of these two equations shows that the IFT is related to the density difference by

$$\sigma = \sigma^{*}\left[\frac{\Delta\rho}{\Delta\rho^{*}}\right]^{\gamma/\beta} = \sigma^{*}\left[\frac{\Delta\rho}{\Delta\rho^{*}}\right]^{3.8} \tag{5.4}$$

If Eq. 5.4 is correct, a plot of log σ vs. log $\Delta\rho$ will be linear with a slope equal to the ratio of the two scaling exponents, approximately 3.8. Fig. 5.9 is a plot of IFT/$\Delta\rho$ data taken from various experimental measurements for alcohol/oil/water systems. The reasonable agreement of critical scaling theory with experimental measurements confirms that density differences decline more slowly as the critical point is approached than do IFT's. Hence, it is also reasonable to expect that there will be a transition from flow which capillary forces dominate to flow in which gravity forces are more important.

Capillary Pressure Dominated Imbibition

We begin with a simple limiting-case model of flow controlled by capillary forces [52]. For a given water-wet porous medium, pore sizes vary considerably. Hence, the aqueous wetting phase imbibes into the small pores and forces the oil out of the larger pores. Due to the randomness of the spatial distribution of various size pores, water can imbibe into the rock from all faces in contact with the aqueous phase. In addition, oil can flow out of the matrix from all available faces. Fig. 5.10(a) is a schematic diagram of this flow situation. If the length of the core is much larger than the diameter, it is reasonable to assume oil and water flow is radial. For radial countercurrent flow, the time required to recover a fraction R amount of the oil is shown [65] to be

$$t = \frac{(1+M)\Delta S\phi r_o^2}{\Delta P_c\lambda_o k}\left(R + (1-R)\ln(1-R)\right) \tag{5.5}$$

Use of Eq. 5.5 requires that ΔP_c and λ_o be known. However, the ratio of times for two different recoveries is independent of those physical properties, and is given by

$$t_{rc} = \frac{t_1}{t_2} = \frac{R_1 + (1-R_1)\ln(1-R_1)}{R_2 + (1-R_2)\ln(1-R_2)} \tag{5.6}$$

Gravity-Dominated Imbibition

When gravity effects are much larger than capillary effects, another limiting case solution can be constructed. Here we assume that displacement is piston-like, that is, the flow is considered to be cocurrent, not countercurrent [7]. In other words, all the aqueous phase enters the core at the base and the oil exits the core at the top, as is shown in Fig. 5.10(c). In this case, the relationship between time and the normalized recovery is [65]

$$t = \frac{\phi\Delta S L^2}{L\Delta\rho g k\lambda_o}\left((1+M)R - M\ln(1-R)\right) \tag{5.7}$$

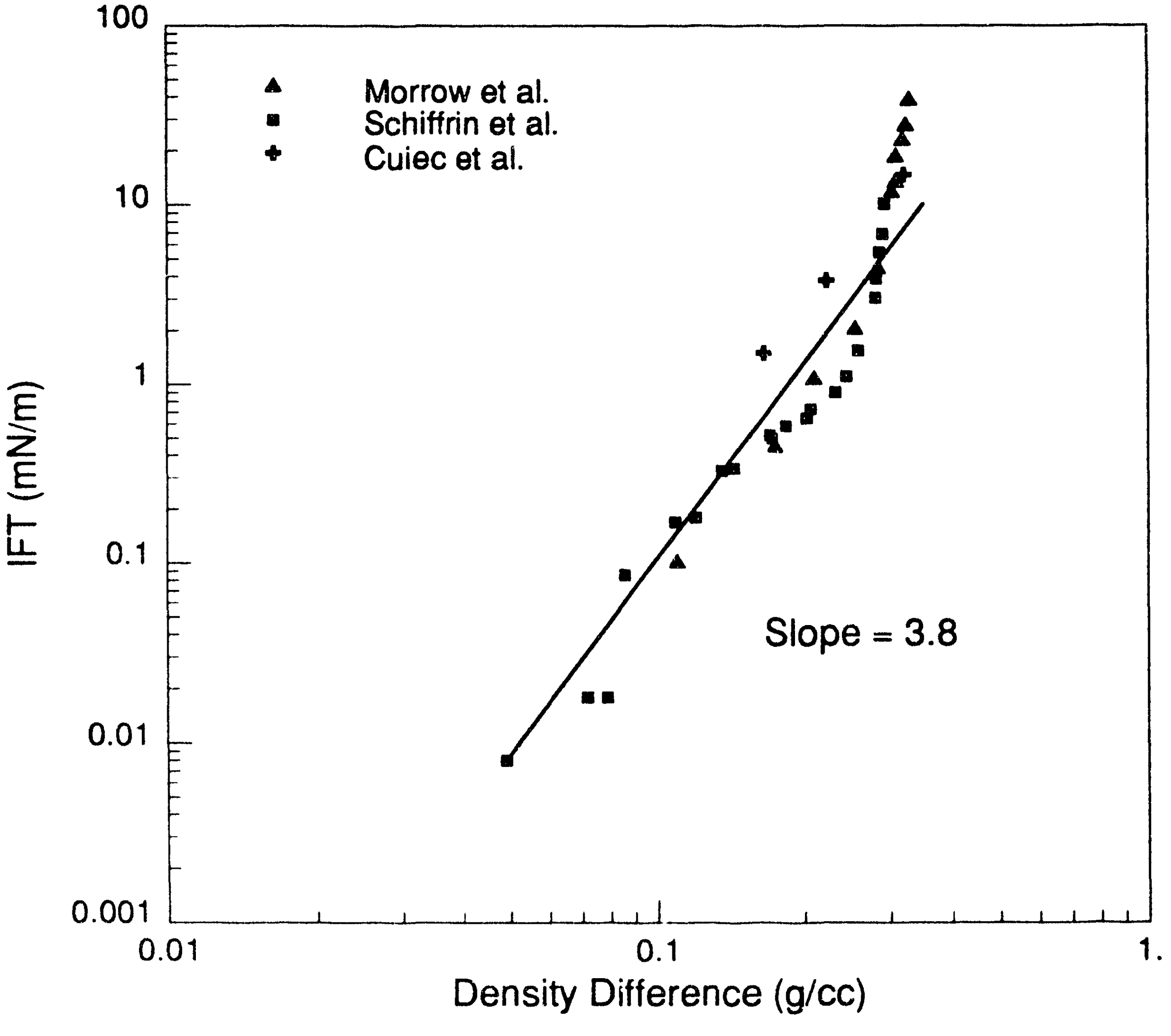

Figure 5.9: Comparison of critical scaling with experimental measurements of IFT vs. density difference.

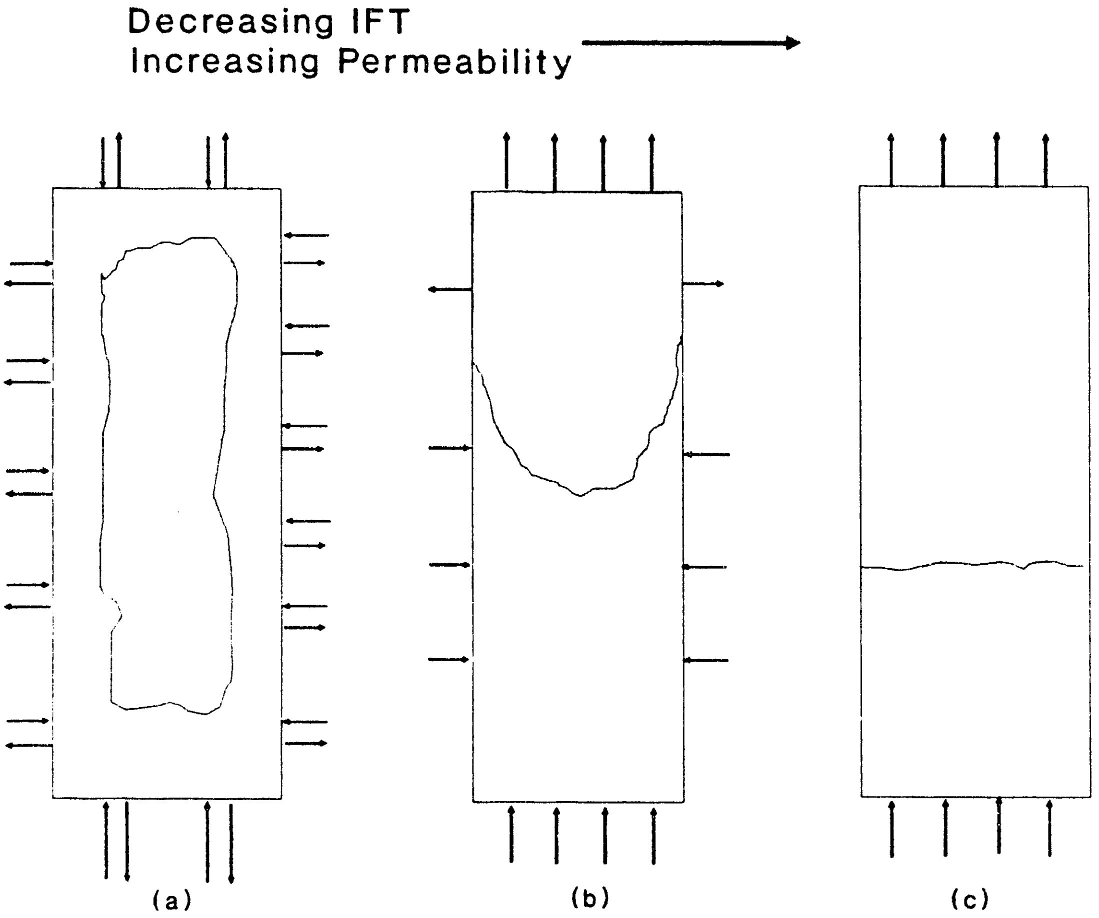

Figure 5.10: Transition from countercurrent to cocurrent flow.

In the gravity dominated case, then, the time ratio for two different recoveries is

$$t_{rg} = \frac{t_1}{t_2} = \frac{R_1 - \frac{M}{(1+M)}\ln(1 - R_1)}{R_2 - \frac{M}{(1+M)}\ln(1 - R_2)} \tag{5.8}$$

Eq. 5.8 includes the mobility ratio, but for the case M $\gg$ 1, the value of $\frac{M}{1+M}$ is of order one.

Scaling of Capillary and Gravity Forces

The discussion given above is for two limiting cases. In the experiments described, some combination of capillary and gravity forces presumably acted as illustrated in Fig. 5.10(b). For both of the limiting cases, the time ratios given by Eqs. 5.6 and 5.8 are not strongly dependent on the physical properties of the core. They are influenced much more by whether the flow is cocurrent or countercurrent. To examine the scaling of these processes, we used the time at 75 and 25 percent of normalized recoveries to obtain t_{rg} and t_{rc}. For capillary dominated flow according to Eq. 5.6, the calculated ratio t_{rc} is 11.78. The ratio in the gravity dominated case is 3.97 from Eq. 5.8. Fig. 5.11 shows the experimental time ratios for the four cores at the three different IFT's. It is clearly seen that with increasing IFT, the flow behavior approaches the capillary dominated limit with values of t_{re} near 10. At low IFT's, the values of t_{re} are close to 4. For the intermediate IFT cases, the time ratio is between 4 and 10, which suggests that both capillary and gravity forces affected the flow process. It should be noted that t_{re} only describes the shape of the curve, not the absolute recovery rate. Because both forces were contributing, the recovery rate was higher than when either capillary or gravity forces dominated. Thus, the experimentally observed dependence of recovery rate on IFT's is consistent with the idea that a transition from capillary to gravity-driven flow occurs as the IFT is reduced.

The displacement data shown in Figs. 5.3–5.6 also demonstrate a strong dependence of total recovery on IFT. Fig. 5.12 shows the remaining oil saturations at different inverse Bond numbers. This behavior is very similar to capillary desaturation behavior [12]. The effect of gravity on the reduction of residual saturation is indicated by the Bond Number $N_B = (R^2 \Delta\rho g/\sigma)$. Morrow and Songkran [46] determined that for low IFT systems, buoyancy forces may play a significant role in displacement mechanisms. The reduction of residual saturation for random packings of equal-size spheres was correlated with the inverse Bond Number, N_B^{-1}. They reported that residual saturation was unaffected for inverse Bond numbers above approximately 200. Estimation of the particle radius from the Kozeny-Carman equation and calculation of the Bond number (see Table 5.3) shows that reduction of the IFT to the low value of 0.1 mN/m gives inverse Bond numbers low enough to account for recovery of more oil in the 100 md case. For greater values of permeability (500 and 700 md), only a moderate reduction in IFT is required to decrease the inverse Bond number to values that increase final recovery. Morrow and Songkran demonstrated that on the microscopic level, the hydrostatic pressure due to gravitational forces would supplement imbibition pressures and prevent snap-off and entrapment of a blob. Thus, as the ratio of gravity to capillary forces is increased, a blob that would have been trapped in the capillary dominated case can continue to flow if the gravitational forces are more important.

Nonequilibrium Imbibition

The results of the nonequilibrium experiments are consistent with the idea that IFT gradients strongly influenced the flow. For example, when a core is saturated with pure IC8 and contacted with an aqueous phase containing a high IPA concentration, the IPA must transfer to the oil phase as the aqueous front imbibes and contacts the oil. With increasing penetration, the

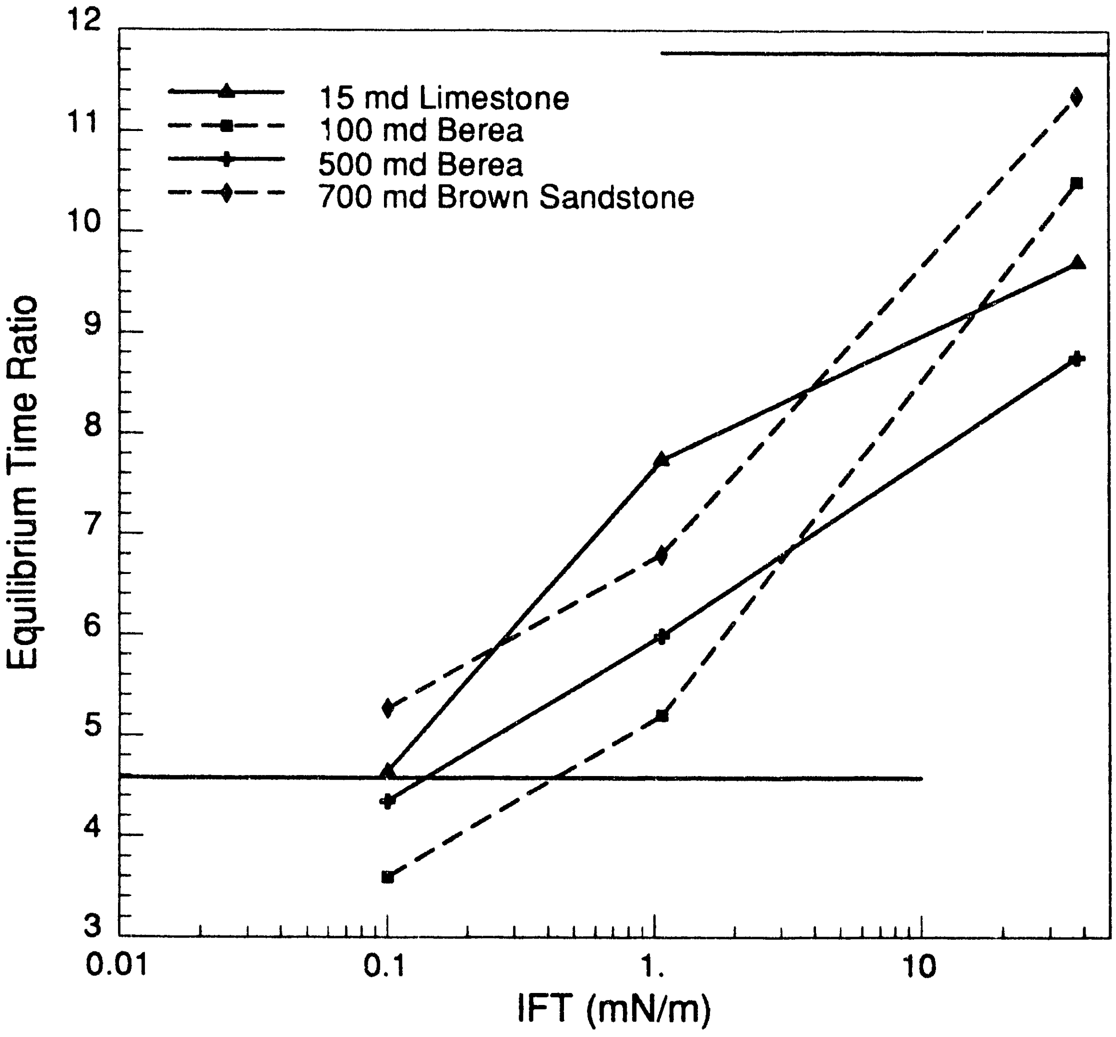

Figure 5.11: Time ratios for four cores at three values of IFT.

Table 5.3: Inverse Bond Numbers for Core Displacements.

k (md)	N_B^{-1} $\Delta\rho = 0.33$ g/cm^3 $\sigma = 38.1$ mN/m	N_B^{-1} $\Delta\rho = 0.21$ g/cm^3 $\sigma = 1.07$ mN/m	N_B^{-1} $\Delta\rho = 0.11$ g/cm^3 $\sigma = 0.1$ mN/m
15	9.7×10^5	4290	760
100	2.6×10^5	1150	200
500	7900	350	60
700	3500	150	30

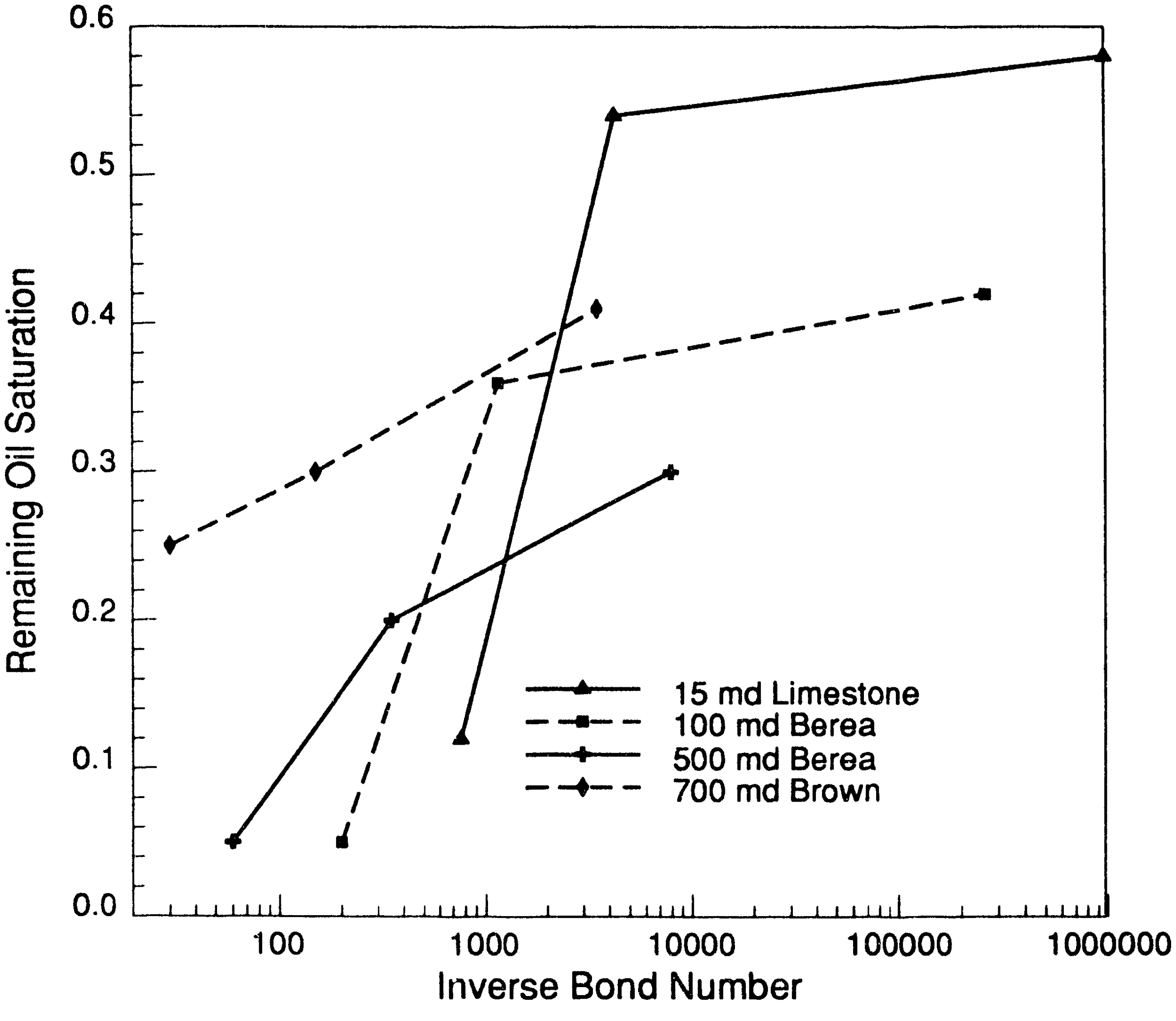

Figure 5.12: Remaining oil saturations for different Bond numbers.

concentration of alcohol in the aqueous phase must decline. More and more IPA partitions into fresh oil encountered by the aqueous phase. Hence, the IFT between the oil and water must be largest in the interior of the core, where most of the IPA has been removed from the brine, and smallest at the exterior, where the IPA concentration is high.

The effect of such an IFT gradient can be seen from a simple model of the imbibition process. We assume that the oil will flow from the larger pores at the surface of the core as the water penetrates the smaller pores in the interior. The driving force for imbibition in this nonequilibrium case is, therefore

$$P_{cn} = 4\left(\frac{\sigma_i}{D_i} - \frac{\sigma_o}{D_o}\right) \tag{5.9}$$

According to Eq. 5.9, P_{cn} (nonequilibrium capillary pressure) is greater than P_c for the equilibrium case because $\sigma_i/\sigma_o > 1$. We have assumed here that the medium is large enough that on the surface of the medium, the oil and water phases are in equilibrium, while at the water front there is no alcohol in either phase. Therefore, the IFT's at the outlet and on the water front are constants. Thus the surface tension gradients which are developed as the brine/alcohol phase continue to penetrate into the core significantly enhance imbibition rates by a Marangoni effect. Eq. 5.9 also explains the low recovery seen in Fig. 5.8 for the case in which the core was initially saturated with an IC8/IPA solution. As brine containing no IPA imbibes and begins to accumulate IPA, the IFT is lower at the advancing front in contrast with the higher IFT at the face of the core. In this case the surface tension gradient is no longer in the favorable direction, and the ensuing recovery is greatly reduced.

5.1.4 Discussion

The experimental results and limiting-case analyses given here indicate that the transport of fluid by gravity-driven flow can be quite rapid if the IFT is moderately low, and that substantial reductions in residual oil saturations are also possible. Those mechanisms will play a role in multicontact miscible (MCM) flood processes in heterogeneous reservoirs, because the interaction of phase behavior and flow in MCM displacement generates reservoir fluid compositions near a critical point [53]. For example, CO_2 or other miscible injection gas may invade unswept lower permeability layers above by gravity segregation in the region of pore space where IFT's are low. In reservoirs with sufficient vertical relief, it may also be possible to take advantage of near-miscible displacement conditions to enhance gravity drainage with moderately low IFT's, even if the reservoir pressure or injection gas composition required for miscibility is out of reach. The use of IFT gradients to enhance recovery from fractured reservoirs is another possibility that should be explored further. For example, a recently reported analysis of diffusion of nitrogen into a core saturated with a hydrocarbon mixture indicated that IFT induced capillary pressure gradients resulted in unexpected saturation profiles [27]. The potential for improved displacement process designs and more accurate predictions of the performance of EOR processes indicates that additional investigation of the scaling of capillary and gravity and compositional effects is needed.

5.1.5 Conclusions

1. Reduction of the IFT for imbibing fluids may increase or decrease the rate of imbibition substantially depending on the relative contribution of capillary and gravity forces.
2. Only a moderate reduction in IFT is required to induce a crossover from capillary-driven to gravity stabilized imbibition in high permeability sandstones.

3. The crossover from capillary to gravity imbibition is characterized by an optimal IFT in which both forces contribute, and the rate of imbibition into the matrix is greatest.
4. Imbibition at high IFT and low permeability occurs due to countercurrent flow whereas at low IFT and high permeability, oil is recovered by cocurrent flow.
5. In gravity stabilized cocurrent flow at low IFT, total recoveries may be very high due to suppression of entrapment mechanisms.
6. Nonequilibrium imbibition may significantly enhance or reduce the rate of imbibition depending on the direction of the surface tension gradient.

5.2 Visualization of Gravity Segregation and Viscous Crossflow in Miscible Displacement in a Two-layered Model

Dengen Zhou

Many factors influence the displacement performance of a miscible flood. According to the accepted description of development of miscibility, phase behavior acts to generate high local displacement efficiency in the zone swept by the injected fluid. The fraction of a reservoir swept at a given time in a flood is determined partly by injection and production well patterns, permeability variations in the rocks, gravity segregation, and viscous fingering arising from an unfavorable ratio of displaced oil mobility to injected fluid mobility. Understanding the relative importance of such factors is a key part of scaling the performance of a miscible flood. This section describes such an experimental study to investigate the relative importance of gravity segregation, dispersion and viscous crossflow in a layered system.

5.2.1 Experimental Apparatus and Procedures

In order to study gravity segregation, dispersion, and viscous crossflow in layered porous media, visualization experiments were performed in a pack of glass beads with two layers. The model shown in Fig. 5.13 was packed in such a way that the flow in the inlet and outlet is uniformly distributed across the inlet face. The two layers were created with beads of two diameters (0.23 and 0.46 mm) resulting in a permeability ratio of 4 to 1. The permeability estimation and packing procedure has been fully discussed by Brock [8]. The experimental apparatus and procedures have also been reported in detail [8].

A series of experiments was initiated to study the effects of viscosity ratio, flow rates and density difference. In the first system, isooctane (IC8) and isopropanol (IPA) were used as the displacing and displaced fluids. These two components form a nearly ideal mixture. The properties of the fluids are listed in Table 5.4.

Table 5.4: Properties of Fluids Used

	component	viscosity cP	density g/cc
displacing	IC8	0.47	0.68
displaced	IPA	2.73	0.78

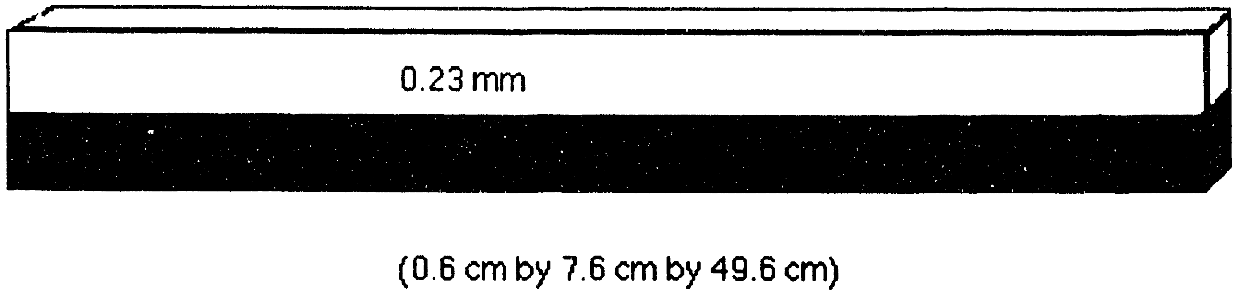

Figure 5.13: Schematic diagram of the two-layered model

In order to visualize the fluid distributions, C_8 was dyed with Oil Red, which was chosen to ensure that there would be no chromatographic separation between the injected fluid and the dye. The displacements were then recorded on video tape.

5.2.2 Experimental Results

To demonstrate the effects of gravity segregation on the flow behavior of these two fluids, two sets of experiments were conducted. In the first case, the model was oriented horizontally, thereby eliminating most gravity effects on the crossflow between the two layers. In the second set, the model was placed vertically. In this case, gravity forces may aid or resist crossflow depending on the arrangement of these two layers. Results from these two sets of experiments are reported separately below.

Flow in the Horizontal Model

Four flow rates (0.3, 1.0, 2.0, 4.0 ml/min.) were employed to study the effects of flow rate on crossflow behavior. Figs. 5.14–5.17 are the fluid distributions at different times. The black indicates the C_8 (the injected fluid), and the white represents the oil (IPA, the displaced fluid). There were clear indications of crossflow between these two layers. As Figs. 5.16 and 5.17 show, there was a sharp corner in the front in the low permeability layer at the injection rates of 2.0 and 4.0 ml/min. It resulted from the contrasting flow directions ahead and behind the front in the low permeability layer. Crossflow occurred from the low permeability layer to the high permeability layer behind the front while crossflow occurred in the opposite direction in the region ahead of the front. The displacement in both layers was piston-like for this moderate viscosity ratio (5.5). When the flow rate was decreased from 4.0 ml/min. to 1.0 ml/min., the crossflow from the high permeability layer to the lower permeability layer increased gradually. However, when the flow rate was reduced to 0.3 ml/min., a significant increase in crossflow was observed, as Fig. 5.14 shows.

Flow in the Vertical Model

There are two possible arrangements of the model in the vertical position, with the low permeability layer above or below the high permeability layer. The injected fluid in this system was less dense than the displaced fluid. The first arrangement of the model allows maximum crossflow, because the gravity force aids the crossflow. In the results reported in this section, displacements were performed with the low permeability layer above the high permeability layer to achieve maximum crossflow. Before conducting a displacement, special care was taken to fill the

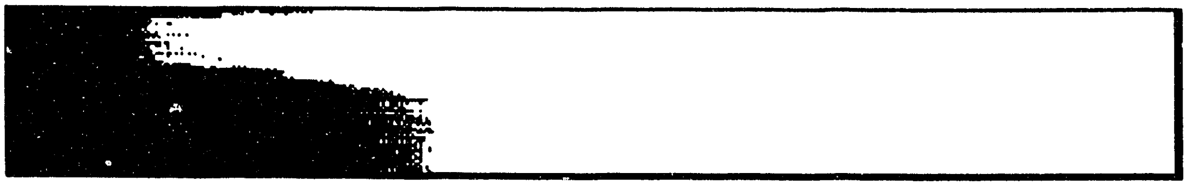

PYI = 0.10

PYI = 0.35

PYI = 0.50

Figure 5.14: Fluid distributions in the horizontal model at different times (Injection rate = 0.3 ml/min.).

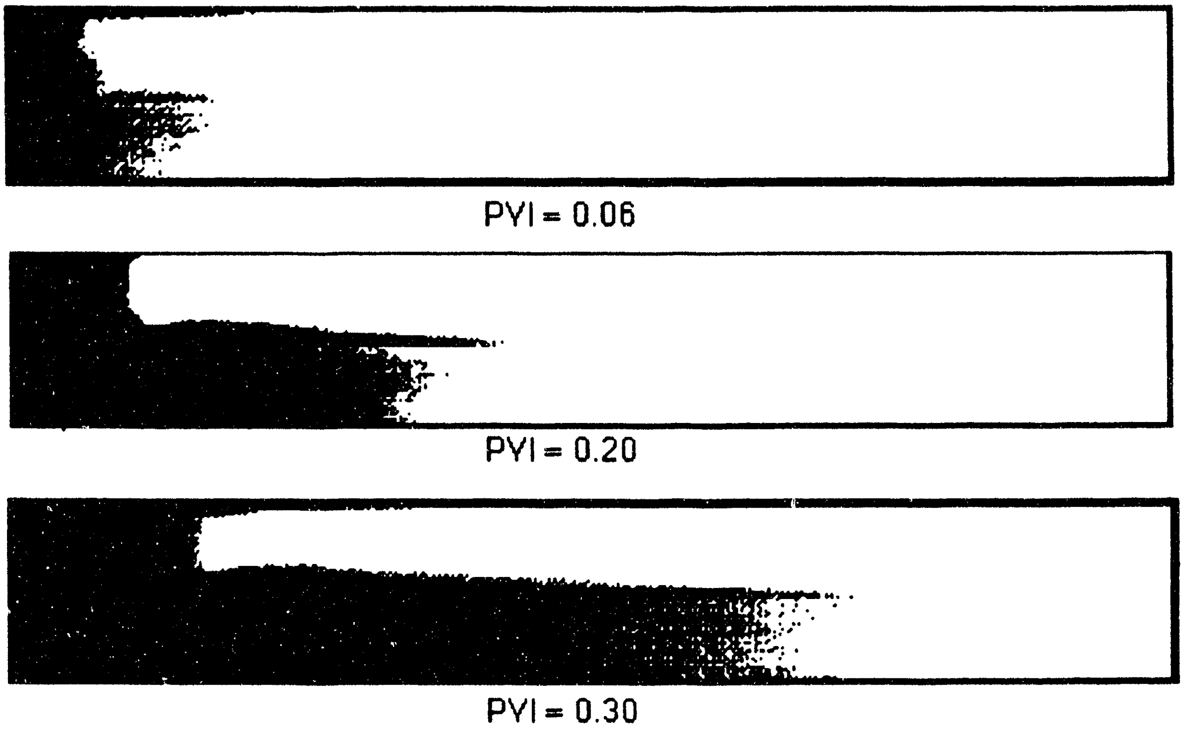

Figure 5.15: Fluid distributions in the horizontal model at different times (Injection rate = 1.0 ml/min.).

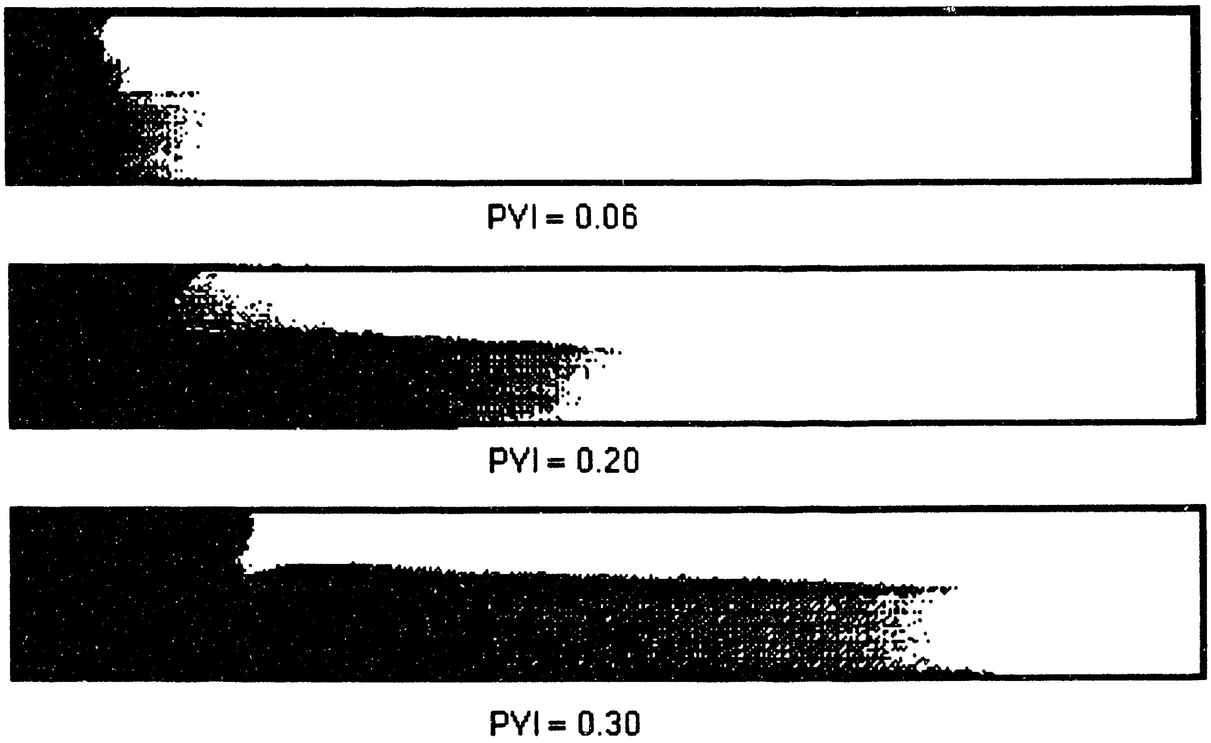

Figure 5.16: Fluid distributions in the horizontal model at different times (Injection rate = 2.0 ml/min.).

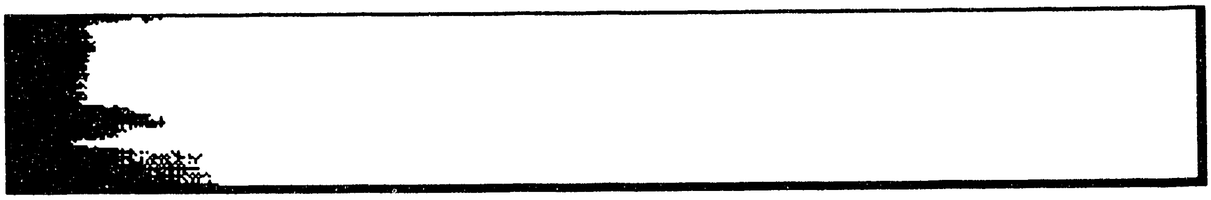

PYI = 0.06

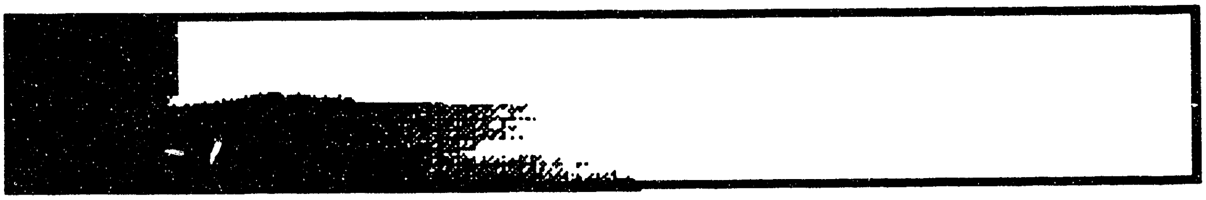

PYI = 0.20

PYI = 0.30

Figure 5.17: Fluid distributions in the horizontal model at different times (Injection rate = 4.0 ml/min.).

header with the injected fluid. This allowed the displaced fluid to be uniformly distributed within the header.

Figs. 5.18–5.20 show the flow patterns of different flow rates at different times. Fig. 5.18 shows the fluid distributions when the injection rate was 0.5 ml/min. IPA flowed from the upper layer to the lower layer and some fingering occurred even though IPA is 5.5 times more viscous than IC8. This was due to a gravity-driven instability. There were two dominant fingers in the displacement. One was in the low permeability (upper) layer, a normal gravity tongue. The other finger in the high permeability layer was diluted by the crossflow from the low permeability layer and cannot be described as normal gravity override. The gravity tongue in the low permeability layer dominated the displacement process in this experiment.

Increasing the injection rate to 1.0 ml/min. changed the picture of the fluid distributions substantially, as Fig. 5.19 shows. The displacing fluid formed a single finger in the high permeability layer, and the displacing fluid crossflowed from the higher permeability layer. Small fingers developed in the region of crossflow from the high permeability layer to the low permeability layer. These fingers were tilted at an angle of about 50^o from the horizontal. The gravity override in the low permeability layer was much less significant than in the previous case. Under the gravity tongue, crossflow occurred from the low permeability to the high permeability layer. In the high permeability layer, the crossflow of IPA from the low permeability layer improved the sweep efficiency. A further increase of the injection rate to 4.0 ml/min. resulted in the thinning of the main finger and earlier breakthrough than at the rate of 1.0 ml/min., as Fig. 5.20 indicates. At a flow rate of 4.0 ml/min., fingering occurred at an angle of about 36^o. Crossflow of the displacing fluid from high permeability layer was less significant than at the lower injection rate (1.0 ml/min.).

5.2.3 Discussion

In this work, the experiments were designed to show the relative importance of gravity effects, dispersion and viscous crossflow in layered systems. Gravity effects on crossflow were nearly eliminated in the first setup. If the model can be considered as two dimensional, at least, only dispersion and viscous crossflow would be responsible for the observed behavior in the horizontal model. With different flow rates, the relative importance of dispersion and viscous crossflow could then be illustrated. In the vertical case, gravity effects are added, and hence, the effects of gravity-driven crossflow can be distinguished by comparing displacement patterns with those due solely to dispersion and viscous crossflow in the horizontal experiments.

Viscous Crossflow

If we eliminate the effects of diffusion and gravity forces, crossflow is only due to the pressure difference between these two layers. To show how viscous crossflow occurs, we assume there is an impermeable film between the two layers that does not allow any crossflow. We further assume that the flow in both layers is piston-like. The pressure in each layer at a given time is shown in Fig. 5.21 for the model used in this work. The injection rate was 0.3 ml/min. It is clear that behind the front in the low permeability layer, the pressure is higher. The pressure is lower ahead of the front. Thus, there would be crossflow from the low permeability layer to the higher one behind the front and vice versa ahead of the front. This explains why there are sharp corners near the front of the low permeability layer.

If there is no crossflow, the velocity distribution in each layer before breakthrough can be expressed as

$$\frac{v_1}{v_2} = \frac{k_1}{k_2} \frac{\mu_1 l_2 + \mu_2(L - l_2)}{\mu_1 l_1 + \mu_2(L - l_1)} \tag{5.10}$$

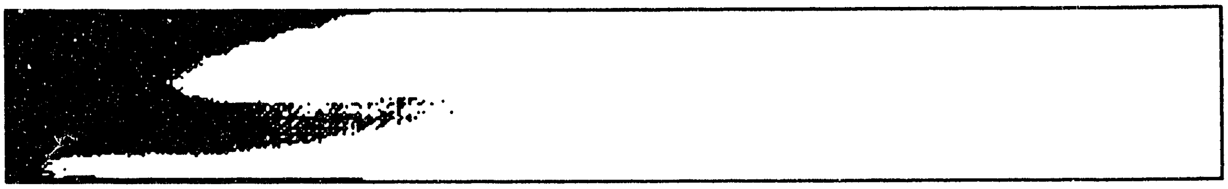

PYI = 0.10

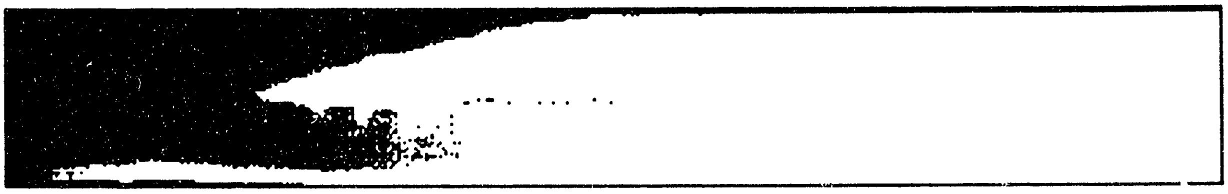

PYI = 0.20

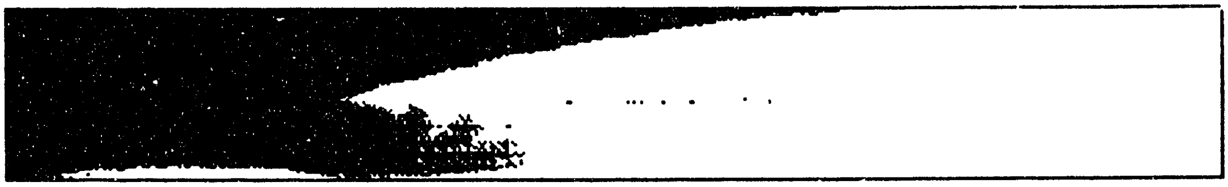

PYI = 0.30

Figure 5.18: Fluid distributions in the vertical model at different times (Injection rate = 0.5 ml/min.).

PYI = 0.10

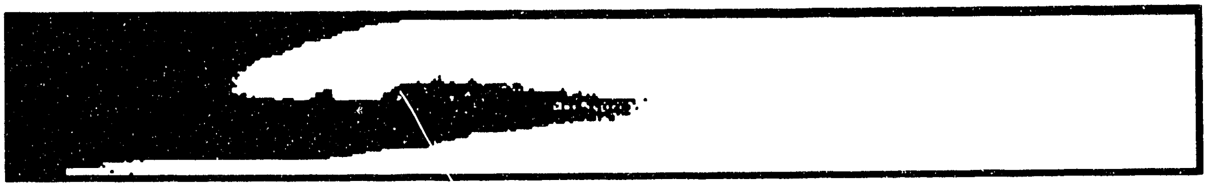

PYI = 0.20

PYI = 0.30

Figure 5.19: Fluid distributions in the vertical model at different times (Injection rate = 1.0 ml/min.).

PYI = 0.10

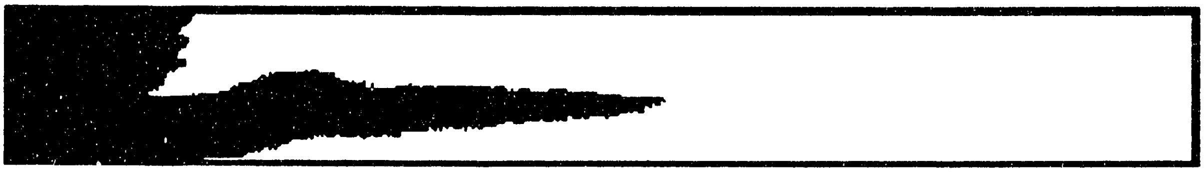

PYI = 0.20

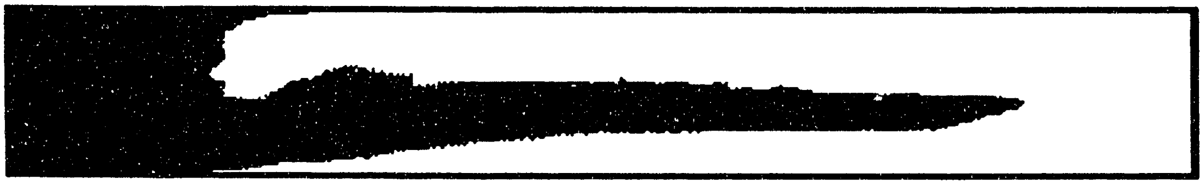

PYI = 0.30

Figure 5.20: Fluid distributions in the vertical model at different times (Injection rate = 4.0 ml/min.).

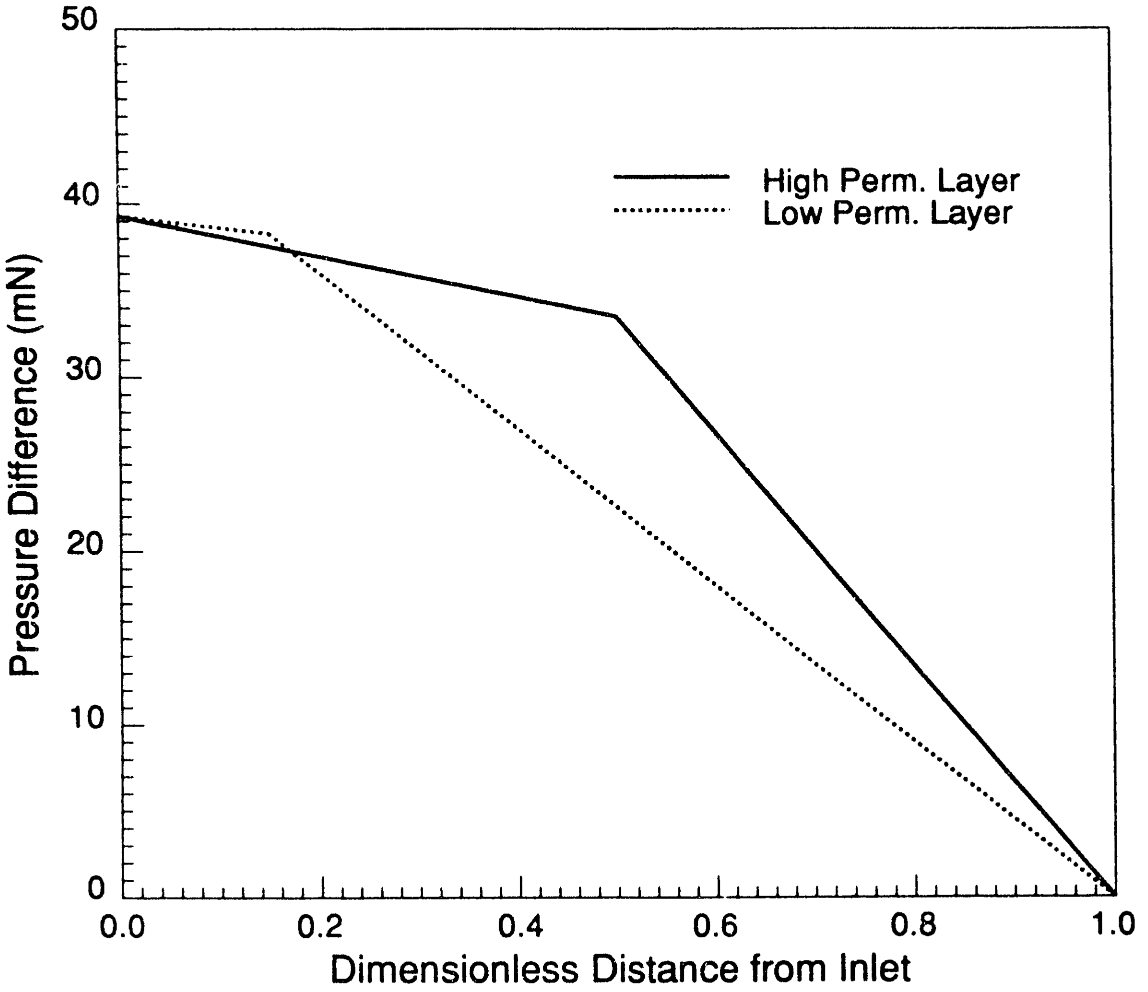

Figure 5.21: Pressure distribution in a horizontal two-layered system.

where v_1 and v_2 are the velocities of the fluids in layer 1 and 2, k_1 and k_2 are the permeabilities of layer 1 and 2, l_1 and l_2 are the distances of the fronts in layer 1 and 2, L is the length of the medium, and μ_1 and μ_2 are the viscosities of the displacing and displaced fluid.

The front positions in these layers may be obtained from the above equation as

$$1 + \frac{(\mu_1 - \mu_2)l_1}{\mu_2 L} = \left(1 + \frac{(\mu_1 - \mu_2)l_2}{\mu_2 L}\right)^{\frac{\phi_2 k_1}{\phi_1 k_2}} \tag{5.11}$$

where ϕ_1 and ϕ_2 are the porosities of the layers. If we increase the injection rate, the velocity in each layer increases proportionally, and thus the pressure in each layer increases linearly. Therefore the viscous crossflow at a given injected pore volume is not influenced by injection rates. The same conclusion was obtained from particle-tracking simulations [8]. From Figs. 5.14–5.17 we can see that the displacements were close to piston-like at injection rates of 0.5 to 4.0 ml/min., although some small fingering was observed in the 4.0 ml/min. case. As the injection rate decreased, more crossflow occurred. In the next section, we consider to what extent dispersion and gravity forces were responsible.

Dispersion and Model Thickness Effects

The convection-dispersion equation describes the conservation of the displacing component in one dimensional miscible displacement,

$$\frac{\partial C}{\partial t_d} + \frac{\partial C}{\partial x_D} - \frac{1}{N_{Pe}} \frac{\partial^2 C}{\partial x_D{}^2} = 0 \tag{5.12}$$

where t_D and x_D are dimensionless time and distance, C is the concentration of the displacing fluid, and N_{Pe} is the Peclet number defined as

$$N_{Pe} = \frac{uL}{\phi K_l} \tag{5.13}$$

where L is the length of the medium, ϕ is the porosity and K_l is the longitudinal dispersion coefficient.

With a given N_{Pe}, Eq. 5.12 can be solved with appropriate boundary conditions. The relative importance of the dispersion effects is reflected by the Peclet number, which depends on the flow rates for a given medium and the longitudinal dispersion coefficient K_l. K_l is given by Lake [37]

$$K_l = \frac{D_o}{\phi F} + C_2 \left(\frac{v D_p}{D_o} \right)^{\beta} D_o \tag{5.14}$$

where ϕ is the porosity of the medium, F is the tortuosity factor of the medium, D_o is the binary molecular diffusion coefficient between the miscible displacing and displaced fluids, β is a constant between 1.0 and 1.25, v is the interstitial velocity, and C_2 is a constant. D_p is the particle diameter of the medium.

At low flow rates, the second term of the above equation is negligible. K_l is independent of flow rates. For fast displacements, the second term is more significant, and K_l can be approximated as

$$K_l \cong \alpha v \tag{5.15}$$

For fast displacements, K_l is linearly related to the injection rate. Therefore the Peclet number is independent of injection rates. Hence, the solution of Eq. 5.12 is not influenced by changing the flow rates. For low injection rates, the Peclet number is proportional to the rate. For small Peclet numbers, therefore, dispersion affects the solution of Eq. 5.12. To show the difference of the flow rates of crossflow and injection, we can calculate the ratio of the maximum crossflow rate, v_c, to the injection rate in the high permeability layer as

$$\frac{v_c}{v_1} = \left(1 - \frac{\mu_1 l_1 + \mu_2 (L - l_1)}{\mu_1 l_2 + \mu_2 (L - l_2)} \right) \frac{l_2 k_h}{H k_1} \tag{5.16}$$

where H is the length of the crossflow, and k_h is the permeability in the crossflow direction. The rate of crossflow depends on the front position of the high permeability layer. For the system used in this work, the maximum crossflow rate can be calculated at different injection times. The highest Peclet number at $x_D = 0.28$ is about 500. The mixing length due to dispersion at a Peclet number of 500 is about 0.5 mm ($D_o = 10^{-5} cm^2/s$, F= 2.5). In the same time about 1.0 cm of crossflow had occurred in the experiment of 0.3 ml/min. injection. This difference is substantial, and hence we conclude that dispersion alone is not sufficient to cause the large amount of crossflow indicated in Fig. 5.14, for example.

The other possible reason for this increase in crossflow at low injection rate is gravity segregation due to the density difference between fluids operating over the thickness of the model.

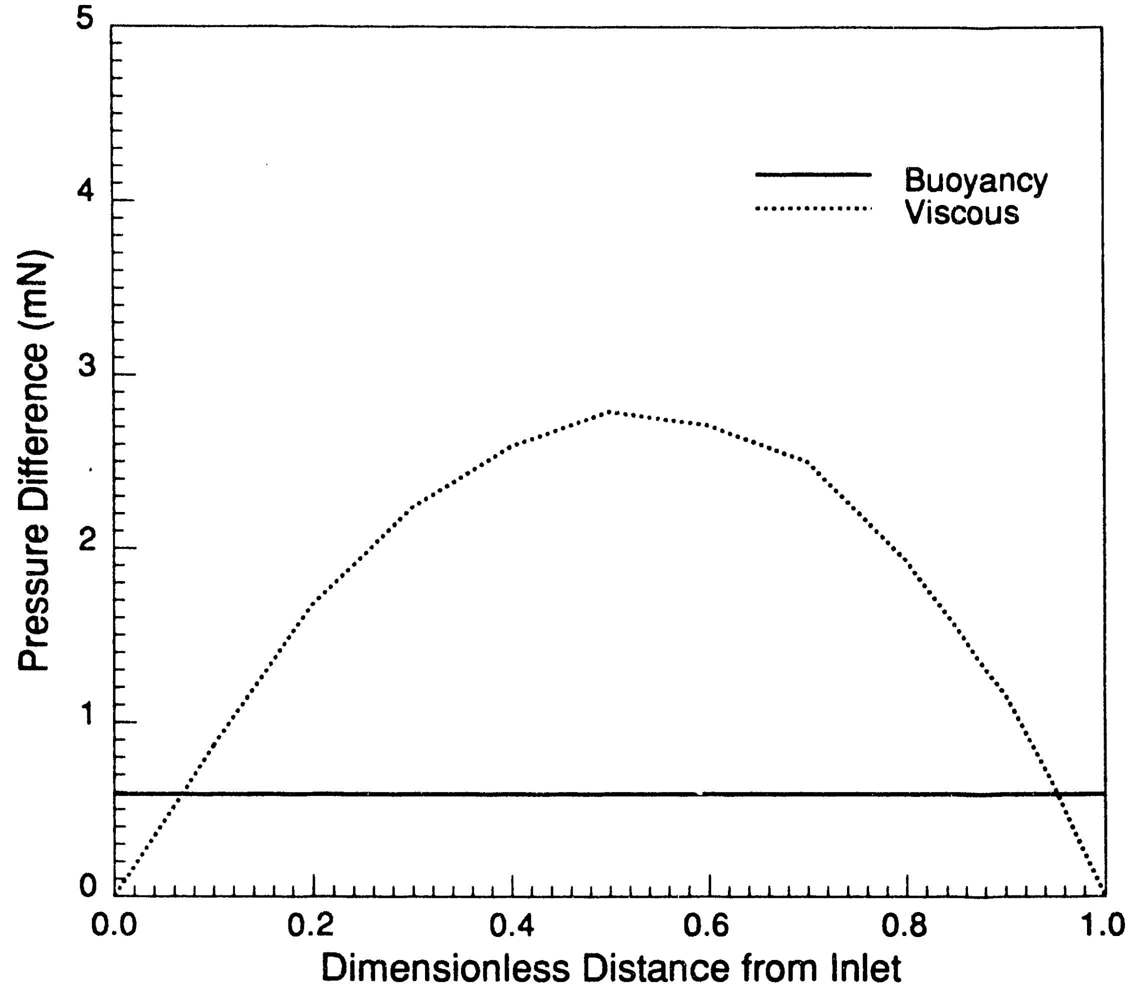

Figure 5.22: A comparison of the buoyancy force with the viscous cross pressure difference between the two layers.

Although the model used here is only 6 mm thick, the pressure difference due to the hydraulic head can be comparable to the viscous crossflow pressure difference between the two layers, as Fig. 5.22 shows. The viscous crossflow pressure difference in Fig. 5.22 was calculated from Eq. 5.10. The hydraulic head is much smaller than the pressure difference due to viscous crossflow when the displacement front in the high permeability layer is in the middle of the medium. However, the viscous pressure difference shown in Fig. 5.22 is the maximum value, since no crossflow was assumed. For a given front position in the medium, the crossflow pressure difference varies from zero to the maximum value, which occurs at the location of the displacement front in the high permeability layer. For other locations, the viscous pressure difference will be much smaller, and hence for significant portions of the flow length, the crossflow pressure difference will be comparable to the buoyancy driving force for crossflow. Hence, the model used here should not be considered as two-dimensional when the model is horizontally positioned. Additional experiments are planned to study the relative importance of dispersion and gravity segregation across the model thickness.

Gravity Effects in the Vertical Model

Gravity may influence the displacement in two ways. First, the ratio of the gravity force to the viscous force determines the tongue development. When injection rates are not too small, a single finger develops in the high permeability layer, the fluid distributions are unstable, and the buoyancy force redistributes the fluids in the medium. To show the relative importance of the gravity force compared with viscous forces, we assume that at the beginning of the process, the model was placed horizontally and after a certain amount of injection, the model is placed vertically. The pressure profile in these two layers before and after the rearrangement is shown in Fig. 5.23. It is clear that when the model is vertically oriented, there is an additional hydraulic pressure difference which aids the crossflow ahead of the front in the low permeability layer. The ratio of the hydraulic head to the pressure difference across the section is

$$\frac{p_1 - p_2}{\Delta\rho g h} = \frac{2\mu_2 l_1 Q}{k_2 A \Delta\rho g h}\left(\frac{f}{k_r} - 1\right)\frac{1}{1+f} \tag{5.17}$$

where A is the cross-sectional area of the medium, k_r is the ratio of k_1 to k_2, h is the thickness of the low permeability layer and f is defined as

$$f = \frac{\mu_1 l_1 + \mu_2(L - l_1)}{\mu_1 l_2 + \mu_2(L - l_2)} \tag{5.18}$$

According to Eq. 5.17, at the injection rate of 1.0 ml/min., the hydraulic head can be as much as 70 percent of the transverse pressure difference. Only 17 percent of the transverse pressure difference, however, is contributed by the buoyancy forces at the injection rate of 4.0 ml/min. Therefore, more crossflow occurs due to the buoyancy force at low injection rates. This explains the reason for the variations in fingering angle at different flow rates.

Future Work

Based on the current observations, one can see that gravity segregation in layered systems can improve the sweep efficiency significantly in some cases. The work reported here was performed with two-component, first contact miscible fluids. However, for processes such as CO_2 injection, phase behavior will also be involved. In such displacements, variations in the permeability of the reservoir, mass transfer, and the chromatographic separations that are inherent to multicontact miscible displacement will all interact, as Pande's work showed [54]. Pande's work did not include dispersion and gravity segregation effects, however. As the displacements show here, gravity segregation can also be a substantial contributor to crossflow. Dispersion and gravity segregation will cause concentration variations, and hence, there will be variations of densities and the interfacial tensions of phases in each layer. Those variations, in turn, will affect the flow behavior of fluids in the system. In order to gain a better understanding of those complex interactions, phase behavior will be included in future experimental work. This can be done with the fluids used here. The IPA-C_8-brine ternary system has been well described [47]. A possible arrangement would be to use a mixture of brine and IPA as the displaced phase and C_8 as the displacing phase. It is similar to the CO_2 injection process, in that the injected phase is the nonwetting phase and is less viscous. The concentration of the dyed C_8 can be measured by digitizing the image of the video tape [8].

To scale these observations to reservoirs, we need to study quantitatively the effects of crossflow due to dispersion, viscous forces and gravity segregation. A detailed simulation of those processes would be very helpful in defining the parameters representing those processes. The extended particle-tracking simulator described in Chapter 4 will be used to perform such simulations.

5.2.4 Conclusions

Flow visualization experiments performed to investigate crossflow driven by viscous and gravity forces lead to the following conclusions:

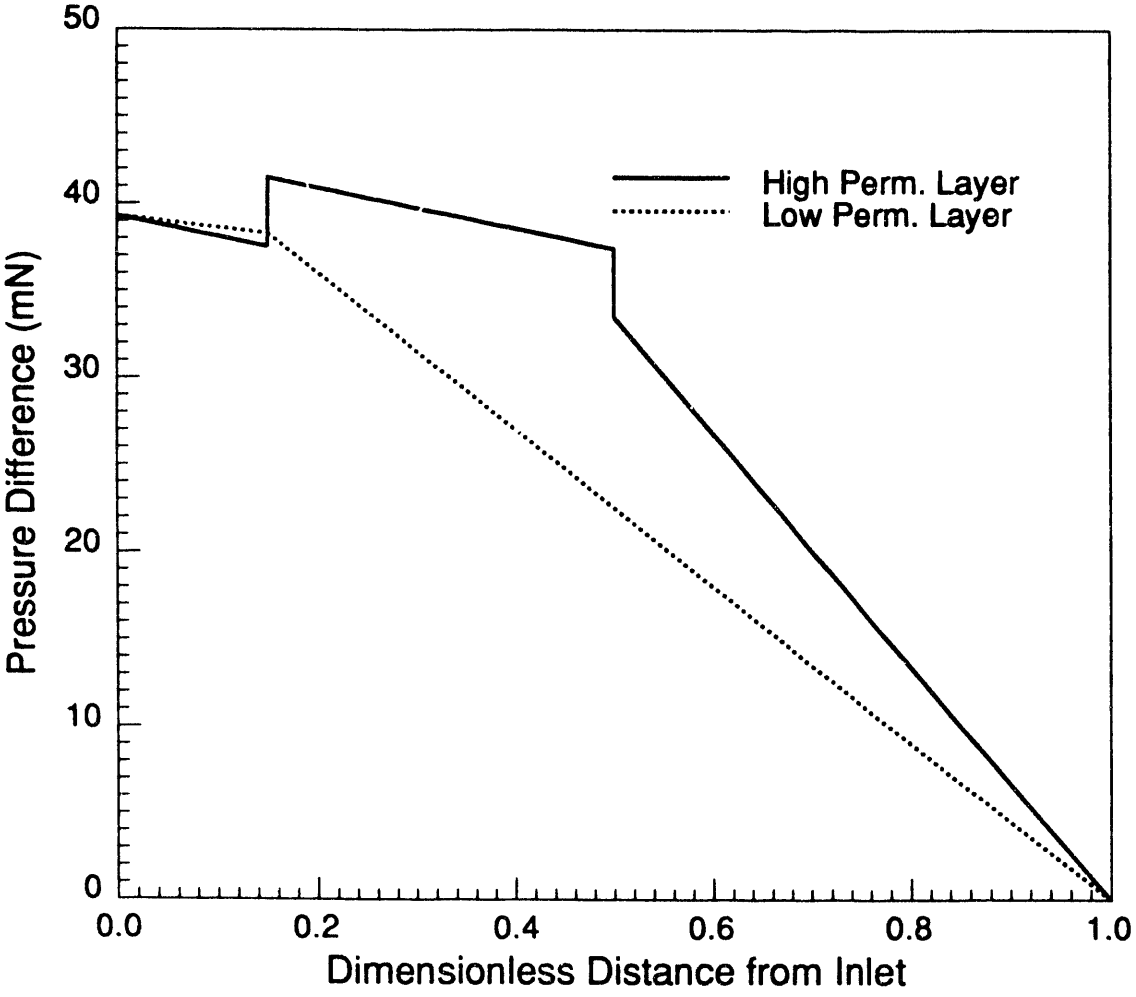

Figure 5.23: Pressure distribution in a vertical two-layered system.

1. The direction of the viscous crossflow can be observed directly in two dimensional displacements in which the two-layer flow model is horizontal. Low viscosity fluid leaves the high permeability layer ahead of the displacement in the low permeability layer. The crossflow direction is reversed behind that front. In the absence of gravity effects, viscous crossflow is insensitive to displacement rate.
2. When the two-layer model is oriented as a vertical cross section, with the high permeability layer below, gravity forces augment transverse transport of low density, low viscosity injected fluid. Gravitational instabilities can induce transverse fingering in such cases.

5.3 Summary

The experimental results and simple, limiting case analyses of transport mechanisms and rates reported in this chapter illustrate how capillary and gravity-driven crossflow can move fluid between regions of differing permeability. The coreflood experiments of Section 5.1 show that there is a significant interaction of gravity-driven flow with capillary imbibition. When interfacial tension (IFT) is high, capillary crossflow dominates, residual saturations are typical of flow at low capillary number, and oil recovery rate is controlled by countercurrent flow of oil and water. When IFT is low, on the other hand, gravity maintains segregated flow, snap-off of residual oil droplets is suppressed, and recovery can be much higher than when IFT is high. Those results are important for scaling of miscible floods, because any successful multicontact miscible (MCM) flood will generate composition paths that pass near a critical point (see Chapter 3). Hence, low IFT's will exist within the transition zone during MCM displacements. Furthermore, that transition from capillary to gravity-dominated flow begins at only moderately low IFT's, even for permeabilities as low as 15 md. Thus, transverse transport of fluids between layers of high and low permeability is likely to be controlled by gravity forces in part of the transition zone and by some combination of capillary and gravity forces elsewhere. Composition, and hence IFT, gradients will also exist. As a result, substantial quantities of crossflow are possible in reservoirs with sufficient vertical permeability.

The first-contact miscible displacements of Section 5.2 also show how complex the flow and mixing patterns can be when low density solvent is injected into a layered system with low permeability above high permeability. In such displacements, viscous and gravity forces controlled the scaling of crossflow. At low injection rates, gravity-driven crossflow leads to significant override even in the low permeability layer. At high rates, viscous forces dominate, and most of the injected fluid enters the high permeability layer. At intermediate rates, viscous crossflow and gravity segregation both contribute to transverse flow, and hence there is an optimum rate at which the adverse effects of heterogeneity are minimized. In effect, the high permeability layer is used to deliver fluid to the low permeability layer by crossflow, which is more rapid than the corresponding longitudinal flow in the low permeability layer. In such displacements, however, there will be considerable transverse mixing of oil and solvent, as the experiments of Section 5.2 show. In MCM displacements, substantial interaction of chromatographic compositional effects (Chapter 3) with crossflow can be expected. For such systems, therefore, a detailed compositional representation of the flow will be required if the details of the scaling behavior of heterogeneity and crossflow are to be understood.

6. Summary

This report outlines research results in four areas that involve physical mechanisms that play pivotal roles in the performance of gas injection processes:

1. Characterization of crude oils and prediction of multicomponent phase equilibrium,
2. Development of miscibility in multicomponent systems,
3. Viscous fingering in homogeneous and heterogeneous porous media, and
4. Crossflow driven by capillary, gravity, and viscous forces.

All four areas contribute in important ways to determine the performance of a miscible flood in a given reservoir. Furthermore, the individual physical mechanisms act (and interact) on different length and time scales, a fact that greatly complicates the analysis of scaling behavior. For example, phase equilibrium operates on relatively short-length scales. Molecular diffusion insures that phases are equilibrated at the pore scale. At the microscopic scale then, the calculation of phase equilibrium with an equation of state is completely appropriate. The experimental approaches described in Chapter 2 show how compositional information about a crude oil can be acquired efficiently by chromatography and mass spectrometry methods and how that information can be used to build a characterization of the oil for equation-of-state calculations of phase equilibria.

The next step beyond the strictly local pore scale is the extension to flow lengths in one space dimension. That step is taken in Chapter 3, where the interplay of phase equilibrium and two-phase flow is examined. The analysis of the flow behavior of four-component systems by the method of characteristics reveals a very important aspect of the development of miscibility that cannot be discerned from the traditional analysis of three-component systems. Development of multicontact miscibility requires that some key tie-line approach a critical point. In ternary systems, that can only happen if the initial oil or the injected fluid composition lies on the extension of a critical tie line. The theory of Chapter 3 shows that as components are added, additional tie lines come into play, and hence miscibility can also develop if any one of them approaches a critical tie line. That theory explains, for example, the behavior of condensing/vaporizing gas drives. It also indicates why calculation techniques that use criteria based on the requirement that the initial oil or injected fluid lie on a critical tie line sometimes fail [41, 28].

The extension of scales to the second and third space dimensions adds considerable complexity to the flow behavior as the results presented in Chapters 4 and 5 show. Now, nonuniform flow arises from heterogeneities in porosity and permeability and from the hydrodynamic instability that causes viscous fingering. That nonuniform flow inevitably reduces displacement efficiency, as the particle-tracking calculations described in Chapter 4 and elsewhere [52, 1, 8, 2, 9] show, but that is not the only important mechanism. If there is any nonuniform flow (and the mobilities of all the fluids are not the same), then crossflow will also occur. Crossflow can be driven by capillary forces, gravity, viscous forces and, more slowly, by diffusion and dispersion. Whatever the combination of driving forces, crossflow will induce mixing of fluid in regions where flow is rapid with fluid in adjacent zones. That mixing will deliver injected gas to areas that would be reached only much more slowly by longitudinal flow. Furthermore, the transverse mixing causes two-phase flow even in displacements that would be multicontact miscible (MCM) in one-dimensional flow [23, 54, 55, 56, 57]. It is unlikely, therefore, that MCM floods in real reservoirs are strictly single phase. Instead, the combination of dispersion and crossflow with phase behavior means that two phases will be present.

While the presence of two-phase flow appears at first to be a negative response to crossflow, calculations reported previously for two-layer flow indicate the opposite. Recovery is actually more rapid when crossflow is present than it is when layers are isolated [55, 56, 57], even though the crossflow moves the process composition path back into the two-phase region. The existence of two-phase flow actually alters local mobility distributions enough to improve displacement performance. Thus, crossflow is likely to be beneficial in many miscible floods.

If two phases are really present in field-scale miscible floods, then analysis of scaling behavior and crossflow must include capillary phenomena. The results of Chapter 5 have important implications for the design of miscible floods, therefore. They show that if interfacial tensions (IFT's) are only moderately low, gravity forces can move significant quantities of both the wetting and nonwetting phases. Furthermore, a combination of modestly low IFT and gravity leads to faster initial crossflow than that observed for either capillary or gravity-driven crossflow alone. It is clear from the analysis of crossover tie lines in Chapter 3 that low IFT's in the required range will be created by the chromatographic interaction of phase equilibria with two-phase flow, which insures that some tie line will be near a critical point. Furthermore, the experimental observations for crossflow induced by IFT gradients suggest that local concentration gradients will contribute to crossflow in ways that have not been explored previously.

The combination of thermodynamic, mathematical, and experimental results reported here, therefore, indicates that many design opportunities exist to harness the beneficial effects of crossflow in the design of miscible displacement processes. For example, a combination of phase behavior, low IFT's and gravity drainage could be used effectively in fractured reservoirs. In addition, the use of horizontal wells opens many avenues for more advantageous use of gravity forces along the lines suggested in Chapter 5. Furthermore, the recognition that the full interplay of compositional behavior, nonuniform flow and crossflow determine process-scaling behavior is an essential step toward effective use of improved descriptions of reservoir heterogeneities that are now being produced. While much remains to be understood as the implications of the results presented here are explored further, it is clear that substantially improved descriptions of the way miscible floods operate in real reservoirs are on the way.

References

[1] Araktingi, U.G.: *Viscous Fingering in Heterogeneous Porous Media*, PhD dissertation, Stanford University, Stanford, CA (1988).

[2] Araktingi, U.G. and Orr, F.M., Jr.: "Viscous Fingering in Heterogeneous Porous Media," paper SPE 18095 presented at the 1988 SPE Annual Technical Conference and Exhibition, Houston, TX, October 2-5.

[3] Baker, L.E., Pierce, A.C. and Luks, K.D.: "Gibbs Energy Analysis of Phase Equilibria," *Soc. Pet. Eng. J.* (October 1982) **22**, 731-742.

[4] Bartle, K.D., Clifford, A.A. and Jafar, S.A.: "Measurement of Solubility in Supercritical Fluids Using Chromatographic Retention: the Solubility of Fluorene, Phenanthrene, and Pyrene in Carbon Dioxide," *J. Chem. Eng. Data* (1990) **35**, 355-360.

[5] Bartmann, D. and Schneider, G.M.: "Experimental Results and Physico-Chemical Aspects of Supercritical Fluid Chromatography with Carbon Dioxide as the Mobile Phase," *J. Chromatography* (1973) **83**, 135-145.

[6] Blackwell, R.J., Rayne, J.R. and Terry, W.M.: "Factors Influencing the Efficiency of Miscible Displacement," *Trans., AIME* (1959) **216**, 1-8.

[7] Bourbiaux, B.J. and Kalaydjian, F.J.: "Experimental Study of Cocurrent and Countercurrent Flows in Natural Porous Media," paper SPE 18283 presented at the 1988 SPE Annual Technical Conference and Exhibition, Houston, TX, October 2-5.

[8] Brock, D.C.: *An Experimental Investigation of Viscous Fingering in Heterogeneous Porous Media*, PhD dissertation, Stanford University, Stanford, CA (1990).

[9] Brock, D.C. and Orr, F.M., Jr.: "Flow Visualizations of Viscous Fingering in Heterogeneous Porous Media," paper SPE 22614 presented at the 1991 SPE Technical Conference and Exhibition, Dallas, TX, October 6-9.

[10] Brock, D.C, Tchelepi, H.A.I.M and Orr, F.M., Jr.: "Viscous Fingering and Gravity Segregation During Miscible Displacement in Heterogeneous Porous Media," (October 1990) 11th International Workshop and Symposium on Enhanced Oil Recovery sponsored by the International Energy Agency and the Institut Francais du Petrole, Rueil-Malmaison, France.

[11] Chang, Yih-Bor, Lim, M.T., Pope, G.A. and Sepehrnoori, K.: "Carbon Dioxide Flow Patterns Under Multiphase Flow, Heterogeneous Field Scale Conditions," paper SPE 22654 presented at the 1991 SPE Annual Technical Conference and Exhibition, Dallas, TX, October 6-9.

[12] Chatzis, I. and Morrow, N.R.: "Correlation of Capillary Number Relationships for Sandstone," *Soc. Pet. Eng. J.* (October 1984) **5**, 555-562.

[13] Christie, M.A. and Bond, D.J.: "Detailed Simulation of Unstable Processes in Miscible Flooding," *Soc. Pet. Eng. Res. Eng.* (November 1987) **2**, No. 4, 514–522.

[14] Cuiec, L.E., Bourbiaux, B. and Kalaydjian, F.: "Imbibition in Low-Permeability Porous Media: Understanding and Improvement of Oil Recovery," paper SPE 20259 presented at the 1990 7th Annual Symposium on Enhanced Oil Recovery, Tulsa, OK, April.

[15] Deo, M.D., Nutakki, R. and Orr, F.M., Jr.: "Schmidt-Wenzel and Peng-Robinson Equations of State for Carbon Dioxide-Hydrocarbon Systems: Binary Interaction Parameters and Volume Translation Factors," paper SPE 18796 presented at the 1989 California Regional Meeting, Bakersfield, CA, April 5–7.

[16] Dougherty, E.L.: "Mathematical Model of an Unstable Displacement," *Trans., AIME, 222* (1963) 155–163.

[17] Dumoré, J.M. and Schols, R.S.: "Drainage Capillary Pressure Functions and the Influence of Connate Water," *Soc. Pet. Eng. J.* (1974) 437–444.

[18] Dumoré, J.M. Hagoort, J. and Risseeuw, A.S.: "An Analytical Model for One-Dimensional, Three-Component Condensing and Vaporizing Gas Drives," *Soc. Pet. Eng. J.* (April 1984) **24**, 169–179.

[19] Fayers, F.J.: "An Approximate Model with Physically Interpretable Parameters for Representing Miscible Viscous Fingering," *Soc. Pet. Eng. Res. Eng.* (May 1988) **3**, 551–558.

[20] Fayers, F.J., Blunt, M.J. and Christie, M.A.: "Accurate Calibration of Empirical Viscous Fingering Models," *Revue de L'Institut Francais du Pétrole* (September 1990).

[21] Firoozabadi, A. and Aziz, K.: "Analysis and Correlation of Nitrogen and Lean-Gas Miscibility Pressure," *Soc. Pet. Eng. Res. Eng.* (November 1986) 575–82.

[22] Foulser, R.W.S., Naylor, P. and Seale, C.: "Relative Permeabilities for the Gravity Stable Tertiary Displacement of Oil by Nitrogen," (October 4–6 1989) 10th International IEA Symposium on Enhanced Oil Recovery, Stanford, CA.

[23] Gardner, J.W. and Ypma, J.G.J.: "An Investigation of Phase-Behavior/Macroscopic-Bypassing Interaction in CO2 Flooding," *Soc. Pet. Eng. J.* (October 1984).

[24] Gasem, K.A.M. and Robinson, R.L. Jr.,: "Solubilities of Carbon Dioxide in Heavy Normal Paraffins (C_{20}–C_{44}) at Pressures to 9.6 MPa and Temperatures from 323 to 423 K," *J. Chem. Eng. Data* (1985) **30**, 53–56.

[25] Hagoort, J.: "Oil Recovery by Gravity Drainage," *Soc. Pet. Eng. J.* (1980) 139–150.

[26] Helfferich, F.G.: "Theory of Multicomponent, Multiphase Displacement in Porous Media," *Soc. Pet. Eng. J.* (February 1981) **271**, 51–62.

[27] Hu, H., Whitson, C.H. and Qi, Y.: "A Study of Recovery Mechanisms in a Nitrogen Diffusion Experiment," (May 21–23 1991).

[28] Jensen, F. and Michelsen M.L.: "Calculation of First Contact and Multiple Contact Minimum Miscibility Pressures," *IN SITU* (January 1990) **14**, No. 1, 1–17.

[29] Jhaveri, B.S. and Youngren, G.K.: "Three-Parameter Modification of the Peng-Robinson Equation of State to Improve Volumetric Predictions," *Soc. Pet. Eng. Res. Eng.* (August 1988) 1033–1040.

[30] Johansen, T. and Winther, R.: "Mathematical and Numerical Analysis of a Hyperbolic System Modeling Solvent Flooding," (September 1990) Second European Conference on the Mathematics of Oil Recovery, France.

[31] Johns, R.T.: personal communication (1991).

[32] Katz, D. and Firoozabadi, A.: "Predicting Phase Behavior of Condensate/Crude-Oil Systems Using Methane Interaction Coefficients," *J. Pet. Tech.* (November 1978) 1649–55.

[33] Kesler, M.G and Lee, B.I.: "Improve prediction of enthalpy of fractions," *Hydrocarbon Processing* (March 1976) **55**, 153–158.

[34] King, M.J.: "Viscous Fingering Utilizing Probabilistic Simulation," paper SPE 16708 presented at the 1987 SPE Annual Technical Conference and Exhibition, Dallas, TX, September.

[35] Kleppe J. and Morse, R.A.: "Oil Production from Fractured Reservoirs by Water Displacement," paper SPE 5084 presented at the 1974 SPE Annual Meeting, Houston, TX, October 6–9.

[36] Koval, E.J.: "A Method for Predicting the Performance of Unstable Miscible Displacements in Heterogeneous Media," *Trans., AIME* (1963) **228**, 145–154.

[37] Lake, W.L.: *Enhanced Oil Recovery*, first edition, Prentice Hall, Engelwood Cliffs, NJ 07632 (1989).

[38] Lax, P.D.: "Hyperbolic Conservation Laws II," *Comm. Pure and Applied Math.* (1957) **10**, 537–566.

[39] Lee, S-T, Lo, H. and Dharmawardhana, B.T.: "Analysis of Mass Transfer Mechanisms Occurring in Rich Gas Displacement Process," paper SPE 18062 presented at the 1988 SPE Annual Technical Conference and Exhibition, Houston, TX, October 2-5.

[40] Lohrenz, J., Grey, B.C. and Clark, C.R.: "The Viscosity of Pure Substances in Dense Gaseous and Liquid Phases," *J. Pet. Tech.* (1964) 1171–1176.

[41] Luks, K.D., Turek, E.A. and Baker, L.E.: "Calculation of Minimum Miscibility Pressure," *Soc. Pet. Eng. Res. Eng.* (November 1987) 501–506.

[42] Mattax, C.C. and Kyte, J.R.: "Imbibition Oil Recovery from Fractured Water Drive Reservoirs," *Soc. Pet. Eng. J.* (1972) 177–184.

[43] McHugh, M. and Paulaitis, M.: "Solid Solubilities of Naphthalene and Biphenyl in Supercritical Carbon Dioxide," *J. Chem. Eng. Data* (1980) **25**, 326–329.

[44] Metcalfe, R.S. and Yarborough, L.: "The Effect of Phase Equilibria on the CO2 Displacement Mechanism," *Soc. Pet. Eng. J.* (August 1979) 242–252.

[45] Monroe, W.W., Silva, M.K., Larsen, L.L. and Orr, F.M. Jr.: "Composition Paths in Four-Component Systems: Effect of Dissolved Methane on 1D CO_2 Flood Performance," *Soc. Pet. Eng. Res. Eng.* (August 1990) 423–432.

[46] Morrow, N.R. and Songkran, B.: "Effect of Viscous and Buoyancy Forces on Nonwetting Phase Trapping in Porous Media," *Surface Phenomena in Enhanced Oil Recovery*, D. Shah (ed.), Plenum Press, New York City, NY (1982) 387–411.

[47] Morrow, N.R., Chatzis, I. and Taber, J.J.: "Entrapment and Mobilization of Residual Oil in Bead Packs," *Soc. Pet. Eng. Res. Eng.* (1988) **3**, 927–935.

[48] Nectoux, A.: "Equilibrium Gas-Oil Drainage: Velocity, Gravitational and Compositional Effects," (October 27–29 1987).

[49] Newley, T.M.J. and Merrill R.C. Jr.: "Pseudocomponent Selection for Compositional Simulation," *Soc. Pet. Eng. Res. Eng.* (November 1991) **6**, No. 4, 490–496.

[50] Nutakki, R.: *Phase Behavior Calculations for Systems with Hydrocarbons, Water, and* CO_2, PhD dissertation, Stanford University, Stanford, CA (1991).

[51] Orr, F.M., Jr.: "Reservoir Characterization for the CO_2 Enhanced Oil Recovery Process—Final Report," No. DE-AC21-85MC22042, U.S. Department of Energy, Bartlesville, OK (1989).

[52] Orr, F.M., Jr.: "Scale-Up of Miscible Flood Processes," Annual Report No. U.S. DOE Grant No. DE-FG21-89MC26253, U.S. Department of Energy, Bartlesville, OK (1991).

[53] Orr, F.M., Jr., Johns, R.T. and Dindoruk, B.: "Miscibility in Four-Component Vaporizing Gas Drives," paper SPE 22637 presented at the 1991 SPE Annual Technical Conference and Exhibition, Dallas, TX, October 6–9.

[54] Pande, K.K.: *Interaction of Phase Behaviour with Nonuniform Flow*, PhD dissertation, Stanford University, Stanford, CA (December 1988).

[55] Pande, K.K. and Orr, F.M., Jr.: "Interaction of Phase Behavior, Reservoir Heterogeneity and and Crossflow in CO_2 Floods," paper SPE 19668 presented at the 1989 SPE Annual Technical Conference and Exhibition, San Antonio, TX, October 8–11.

[56] Pande, K.K. and Orr, F.M., Jr.: "Analytical Computation of Breakthrough Recovery for CO_2 Floods in Layered Reservoirs," paper SPE 20177 presented at the 1990 SPE Annual Technical Conference and Exhibition, Tulsa, TX, April 22–25.

[57] Pande, K.K. and Orr, F.M., Jr.: "Effects of Permeability Heterogeneity on Miscibility Development in Condensing Gas-Drive Processes," paper SPE 22635 presented at the 1991 SPE Annual Technical Conference and Exhibition, Dallas, TX, October 6–9.

[58] Pavone, D., Bruzzi, P. and Verre, R.: "Gravity Drainage at Low IFT," (October 1989) 5th European Symposium on Enhanced Oil Recovery, Budapest.

[59] Peneloux, A., Rauzy, E. and Freze, R.: "A Consistent Correction for Redlich-Kwong-Soave Volumes," *Fluid Phase Equilibria* (1982) **8**, 7–23.

[60] Peng, D.Y. and Robinson, D.B.: "A New Two-Constant Equation of State," *Ind. Eng. Chem. Fund.* (1976) **15**, 59–64.

[61] Rathmell, J.J., Stalkup, F.I. and Hassinger, R.C.: "A Laboratory Investigation of Miscible Displacement by Carbon Dioxide," paper SPE 3483 presented at the 1971 SPE Annual Meeting, New Orleans, LA, October.

[62] Reid, R.C., Prausnitz, J.M. and Sherwood, T.K.: *The Properties of Gases and Liquids*, third edition, McGraw-Hill, New York, NY (1977).

[63] Rhee, H., Aris, R. and Amundson, N.R.: *First-Order Partial Differential Equations: Volume I*, Prentice-Hall, Englewood Cliffs, NJ (1986).

[64] Satherly, J. and Schiffrin, D.: "The Measurement of Low IFT Values for Enhanced Oil Recovery," (August 1986) Progress Report to U.K. DOE, Winfrith.

[65] Schechter, D.S., Zhou, D. and Orr, F.M., Jr.: "Capillary Imbibition and Gravity Segregation in Low IFT Systems," paper SPE 22594 presented at the 1991 SPE Annual Technical Conference and Exhibition, Dallas, TX, October 6–9.

[66] Shang-keng, M.: *Modern Theory of Critical Phenomena*, Benjamin Cummings, Reading, Mass. (1976).

[67] Smoller, J.: *Shock Waves and Reaction-Diffusion Equations*, first edition, Springer-Verlag, New York, NY 10010 (1983).

[68] Stalkup, F.I.: "Displacement Behavior of the Condensing/Vaporizing Gas Drive Process," paper SPE 16715 presented at the 1987 SPE Annual Technical Conference and Exhibition, Dallas, TX, September.

[69] Stalkup, F.I.: "Effect of Gas Enrichment and Numerical Dispersion on Compositional Simulator Predictions of Oil Recovery in Reservoir Condensing and Condensing/Vaporizing Gas Drives," paper SPE 18060 presented at the 1988 SPE Annual Technical Conference and Exhibition, Houston, TX, October.

[70] Stalkup, F.I., Jr.: "Miscible Displacement," Monograph 8, Soc. Pet. Eng. of AIME, New York (1983).

[71] Stessman, A.N.: "Phase Behavior of Means Crude Oil and Carbon Dioxide," Master's thesis, Stanford University, Stanford, CA (1991).

[72] Tan, C.T. and Homsy, G.M.: "Simulation of Nonlinear Viscous Fingering in Miscible Displacements," *Phys. Fluids* (June 1988) **31**, No. 6, 1330–1338.

[73] Tchelepi, H. and Orr, F.M., Jr.: "Particle-Tracking Simulations of Viscous Fingering: Boundary Conditions and Scaling," Industrial Affiliates Meeting, SUPRI-C, Stanford Univ. (May 1991).

[74] Todd, M.R. and Longstaff, W.J.: "The Development, Testing and Application of a Numerical Simulator for Predicting Miscible Flood Performance," *Trans., AIME*, *253* (1972) 874–882.

[75] Tsai, F.-N. and Yau, J.-S.: "Solubility of Carbon Dioxide in *n*-Tetracosane and in *n*-Dotriacontane," *J. Chem. Eng. Data* (1990) **35**, 43–45.

[76] Twu, C.H.: "An Internally Consistent Correlation for Predicting the Critical Properties and Molecular Weights of Petroleum and Coal-Tar Liquids," *Fluid Phase Equilibria* (1984) **16**, 137–150.

[77] Van Deemeter, J.J. and Zuiderweg, F.J. and Kinkenberg, A.: "Longitudinal Diffusion and Resistance to Mass Transfer as Causes of Nonideality in Chromatography," *Chem. Eng. Sci.* (1956) **5**, 271–289.

[78] Van Golf-Racht, T.: *Fundamentals of Fractured Reservoir Engineering*, Elsevier (1981).

[79] Van Ness, H.C. and Abbott, M.M.: *Classical Thermodynamics of Nonelectrolyte Solutions With Applications to Phase Equilibrium*, McGraw-Hill, San Francisco (1982).

[80] Walsh, B.W. and Orr, F.M. Jr.: "Prediction of Miscible Flood Performance: The Effect Of Dispersion on Composition Paths in Ternary Systems.," *IN SITU* (1990) **14**, No. 1, 19–47.

[81] Walsh, M.P.: "Minimum Miscibility Pressure Calculations Including Effects of Three Phase Equilibria," (May 1991) Sixth European Symposium on Improved Oil Recovery, Norway.

[82] Wattenbarger, R.C.: personal communication (1991).

[83] Whitson, C. and Michelsen, M.: "The Negative Flash," (April 1989) Fifth International Conference on Fluid Properties and Phase Equilibria for Chemical Process Design, Banff, Alberta, Canada.

[84] Yokoyama, Y. and Lake, L.: "Miscibility in Four-Component Vaporizing Gas Drives," paper SPE 10109 presented at the 1981 SPE Annual Technical Conference and Exhibition, San Antonio, TX.

[85] Yonker, C.R., Gale, R.W. and Smith, R.D.: "Effects of Pressure on Retention in Supercritical Fluid Chromatography," *J. Phys. Chem.* (1987) **91**, 3333–3336.

[86] Zauderer, E.: *Partial Differential Equations of Applied Mathematics*, second edition, Wiley-Interscience, New York, NY (1989).

[87] Zick, A.A.: "A Combined Condensing/Vaporizing Mechanism in the Displacement of Oil by Enriched Gas," paper SPE 15493 presented at the 1986 SPE Annual Technical Conference and Exhibition, New Orleans, LA, October.

*U.S.GPO:1992-661-026/60023

END

DATE FILMED

7/8/92